



TECHNISCHE  
UNIVERSITÄT  
DARMSTADT

# The FuN Screen – A Versatile High-Throughput Assay for Nanopore Engineering

Vom Fachbereich Biologie der Technischen Universität Darmstadt zur Erlangung des akademischen Grades  
Doctor rerum naturalium genehmigte Dissertation von

Wadim Weber

1. Referent: Prof. Dr. Viktor Stein
2. Referent: Prof. Dr. Gerhard Thiel



TECHNISCHE  
UNIVERSITÄT  
DARMSTADT

# The FuN Screen – A Versatile High-Throughput Assay for Nanopore Engineering

Vom Fachbereich Biologie  
der Technischen Universität Darmstadt

Zur Erlangung des Grades  
Doctor rerum naturalium  
(Dr. rer. nat.)

Dissertation

Von Wadim Weber

Erstgutachter: Prof. Dr. Viktor Stein  
Zweitgutachter: Prof. Dr. Gerhard Thiel

Darmstadt 2020

---



Weber, Wadim: The FuN Screen – A Versatile High-Throughput Assay for Nanopore Engineering  
Darmstadt, Technische Universität Darmstadt  
Jahr der Veröffentlichung der Dissertation auf TUpriints: 2021  
URN: urn:nbn:de:tuda-tuprints-195132  
Tag der mündlichen Prüfung: 09.12.2020

Veröffentlicht unter CC BY-SA 4.0 International  
<https://creativecommons.org/licenses/>



---

Give up the thought that you have control.  
You don't. The best you can do is adapt, anticipate,  
be flexible, sense the environment and respond.

-Frances Arnold

---

---

---

## Table of Contents

---

Table of Contents	i
Acknowledgements - Danksagung	1
Zusammenfassung	2
Abstract	2
Introduction	3
Motivation for this Project	3
Synthetic Biology – from Protein Engineering to Nanopore Applications	3
Nanopore Engineering	4
Synthetic Organic Nanopores	4
DNA Nanopores	4
Peptide Nanopores	5
Protein Nanopores	6
Assay Systems for Protein Nanopores	8
Electrophysiological Characterization in Reconstituted Lipid Bilayer Membranes	8
Stochastic Sensing in Reconstituted Lipid Bilayer Membranes	9
Fluorescence Based Optical Read-outs	10
Genetic Screening Systems for Nanopores	12
Medium-Throughput Hemolytic Activity Assay	12
Medium to High-Throughput Membrane Integrity Dependant Fluorescent Change	12
High-Throughput Growth Related Screening	13
Ultra-High-Throughput Screening using Liposome Display	13
Pores in Detail: Holins and Holin-like Proteins	15
Mechanism of Holin Action and Timing	16
Pore Forming Proteins in Detail	18
The Diversity of Holins and Holin-like Proteins	21
Genetically Encoded Fluorescent Proteins	22
Using Biosensors as Tools for Nanopore Engineering and Vice Versa	24
Results	25
Design Principle of the FuN Screen	25
FuN Screen: A Method to Investigate Pore Function and Behaviour	33
Truncation Analysis of S <sup>2168</sup>	37
In Vitro Bilayer Measurements of Selected Variants	40
Examination of the Charged N-Terminus of S <sup>2168</sup>	42
Microfluidic Microscopy Measurements with the FuN Screen	44
Colony Based FuN Screen with Airbrush Technology	48
Model Selection with Fluorescence Activated Cell Sorting (FACS)	49
Library Construction and Screening of Alternative Antiholin Variants	51
Conclusion	57
Outlook	58
Holins – Potential Ancestors of Transporter Systems	58



---

Developing new Biosensors with the FuN Screen	60
Material and Methods	63
Supplementary	87
References	101
List of Abbreviations	116
List of Figures	119
List of Tables & Equations	120
Own Work	122
Declaration – Ehrenwörtliche Erklärung	123

---

## Acknowledgements - Danksagung

---

An dieser Stelle möchte ich mich bei allen Personen bedanken, die mich in den Jahren meiner Promotion begleitet haben und ohne die diese Arbeit nicht möglich gewesen wäre.

Mein besonderer Dank gilt **Prof. Dr. Viktor Stein** für die Möglichkeit Teil einer neu gegründeten Arbeitsgruppe zu sein und dem Bereitstellen eines spannenden Themas. Die Chance ein Labor mit aufzubauen und maßgeblich mit meiner Forschung beitragen zu können, sowie die Freiheit eigene Ideen umzusetzen und dabei stets unterstützt und gefördert zu werden war einmalig und hat mich persönlich stark vorangebracht.

Zudem gilt mein Dank **Prof Dr. Gerhard Thiel** für die Übernahme des Korreferats, sowie für die Unterstützung innerhalb des Projekts bei jeglichen Anliegen.

Meinem Kollegen **Jan Ranglack** danke ich für den vielen Input und für das wahnsinnige Wissen, sodass man mit er für fast jede Frage eine Antwort parat hatte.

Außerdem möchte ich **Markus Röder** danken, der die Grundsteine der Arbeit gelegt und auch später noch bei wichtigen Experimenten geholfen hat. Zudem danke ich allen Studierenden, die bei mir eine Abschlussarbeit getätigt haben und somit eine maßgebliche Rolle in dieser Arbeit spielten. Dazu gehören: **Isabell Gregorz, Robin Maatz, Tobias Probanowski** und **Janine Christin Pleitner**. Besonders **Philipp Kemp** und **Theresa Wörmann** möchte ich auch noch zusätzlich für die lustige und interessante Zeit im Labor danken.

Zudem möchte ich **Dr. Markus Langhans** und **Prof. Dr. Tobias Meckel** danken, die bei mir unter anderem das Interesse für die Mikroskopie, Bildanalyse als auch das Klonieren geweckt haben. Hierzu haben auch **Alexander Krömmelbein** und **Robert Lehn** beigetragen, mit denen man immer ein Schwätzchen halten konnte.

**Dr. Oliver Rauh, Tobias Schulze** und **Dr. Kerri Kukovetz** möchte ich besonders für die Hilfe am Bilayer danken. Ohne euch wären die Messungen nicht möglich gewesen.

Einen großen Dank möchte ich meinem langjährigen Freund **Dr. Tobias Winterstein** aussprechen, der mich seit Anbeginn des Studiums begleitet hat und mit dem das iNAPO Projekt umso besser war.

Außerdem gilt mein Dank allen anderen **iNAPO** Mitgliedern, die dazu beigetragen haben, dass das Projekt so erfolgreich war, sowie für die netten Stammtische. Insbesondere möchte ich hier **Lena Müller, Ivana Duznovic, Mario El Houry** und **Sarah Schneider** danken.

Meinen Eltern **Erika** und **Andrej Weber**, sowie meiner Schwester **Nicole Weber** danke ich für die fortwährende Unterstützung vom Anfang meines Studiums bis hin zur Promotion.

Meiner langjährigen Freundin **Karen Lischka** möchte ich sagen: Vielen Dank, dass du für mich da warst und bist. Gerade gegen Ende der Promotion warst du eine große Hilfe!

---

## Zusammenfassung

---

In den letzten Jahren sind Nanoporen zu einem wichtigen Werkzeug in der Biotechnologie geworden, vor allem in der Biosensorik und DNA-Sequenzierung. Die Fähigkeit Nanoporen mit maßgeschneiderten Eigenschaften und Funktionen zu konstruieren, ist der Schlüssel zu ihrer biotechnologischen Entwicklung und liefert neue grundlegende Erkenntnisse über ihre Wirkungsmechanismen. Bis heute wurden die meisten konstruierten Nanoporen mit rationalen, struktur-basierten Ansätzen realisiert, während genetische Durchmusterungsverfahren nicht weit verbreitet sind. Um diese technologische Lücke zu schließen, wurde ein Durchmusterungsverfahren entwickelt, das auf genetisch kodierten fluoreszierenden Proteinsensoren basiert und eine hochauflösende und quantitative Analyse der Funktion von Nanoporen in *E. coli* ermöglicht.

Die Leistungsfähigkeit dieses Verfahrens wurde durch die Analyse molekularer Merkmale und Funktionen des Bakteriophagen Pinholins S<sup>2168</sup> in hochauflösenden genetischen Durchmusterungen auf verschiedenen Plattformen demonstriert und durch hochauflösende elektrische Aufzeichnungen ergänzt. Diese Klasse von Membranpeptiden ist Teil des Lebenszyklus des Bakteriophagen und sehr effizient bei der Initiierung der Zelllyse. Die detaillierte Analyse der ersten Transmembrandomäne demonstrierte die Schlüsselfunktionen einzelner Aminosäuren, bei denen vor allem positiv geladene Reste zur Nanoporen Stabilisierung beitragen. Darüber hinaus wurden mehrere verschiedene Nanoporen mit diesem System getestet, um die Erweiterbarkeit des Verfahrens für weitere Anwendungen zu zeigen.

---

## Abstract

---

In recent years, nanopores have become an important tool in biotechnology especially in biosensing and DNA sequencing. The capacity to engineer nanopores with tailored properties and functions is key to their biotechnological development and provides new fundamental insight into their mechanisms of action. To date, most construction efforts have been realised with rational, structure-guided approaches while genetic screening systems are not widely used. Addressing this technological gap, a genetic reporter assay was developed based on genetically-encoded fluorescent protein sensors to enable a high-resolution, quantitative read-out of nanopore function in *E. coli*. The capacity of this assay was demonstrated by dissecting molecular features and functions of the bacteriophage pinholin S<sup>2168</sup> in high-resolution genetic screens on different platforms and complemented with high-resolution electrical recordings. This class of membrane peptides is part of the bacteriophage life cycle and very efficient in cell lysis initiation. Detailed analysis of the first transmembrane domain revealed key functions of single amino acids with positively charged residues as main regulators of nanopore stabilization. In addition, several different nanopores were tested with this system and demonstrated the expandability of the screen for further application.

---

## Introduction

---

### Motivation for this Project

This project aims to devise new strategies to engineer protein nanopores with tailored properties and functions and subsequently develop them for different biotechnological applications. In recent years, nanopores have become an important tool in biotechnology and basic research (Dal Peraro & van der Goot, 2016) such as biosensing (Nehra et al., 2019), DNA sequencing (Ayub & Bayley, 2016), single molecule studies (S. Wang et al., 2018) and catalytic reactions (Willems et al., 2017). The capacity to engineer nanopores with tailored properties is key to their biotechnological development and also helps dissect the mechanisms behind nanopore formation and function. The majority of nanopores are engineered by rational, structure-guided approaches while genetic screening systems are not widely used. The few that have been developed are frequently limited in terms of throughput or rely on expensive equipment (Cosentino et al., 2015; Fujii et al., 2013; Wloka et al., 2016). Addressing this technological gap, the specific goal of this project is to develop a genetic reporter assay featuring genetically-encoded fluorescent protein sensors that enable a quantitative fluorescent read-out, but also high throughput screening of nanopore function. Furthermore, the capacity of the reporter assay is demonstrated by re-engineering the structural and functional properties of bacteriophage derived nanopores – so called holins – and evaluate their suitability as elementary building blocks in nanopore engineering.

### Synthetic Biology – from Protein Engineering to Nanopore Applications

Synthetic biology (SynBio) is a multidisciplinary field which aims to devise systematic approaches to engineer new biological functions either by adopting and re-designing components from nature or engineering parts, devices and systems entirely from scratch (Benner & Sismour, 2005; Cameron et al., 2014; Smolke, 2018). One major focus concerns the construction of proteins with tailored properties and functions.

When protein engineering emerged in the beginning of the 1980s, solving structures with X-ray crystallography provided the foundation to understand the principles of enzyme functions. Back then, the exploration of functional groups and their activity in enzymes was achieved with chemical modifications that had limited range and poor specificity (Brannigan & Wilkinson, 2002). A real game changer was site-directed mutagenesis. First reported for single amino acid exchange in tyrosyl-transfer RNA synthetase (Winter et al., 1982) and  $\beta$ -lactamase (Dalbadie-McFarland et al., 1982; Sigal et al., 1982), this technique later became powerful enough to modify whole loops (Jones et al., 1986) and domains (Neuberger et al., 1984). The problem with rationally introduced mutations was the huge impact on stability or activity of proteins and it resembled more a trial-and-error approach than a goal-oriented pipeline. In the following years, new iterations of mutagenesis methods have arisen, with one of them being directed evolution. By creating a high number of variants and only selecting for the most suitable ones, several proteins could be tailored with desired functions (Arnold, 1998; K. Chen & Arnold, 1993; Cramer et al., 1998; Stemmer, 1994; Winter & Milstein, 1991). Over time, DNA libraries became a lot easier to build, but one major challenge remained through all these years: The ability to select a library for certain variants is based on the linkage between the genotype (DNA) and the phenotype (function).

A suitable screening system has to be established for every new protein or function and multiple tuning cycles have to be done to selectively enrich the library with the desired variants (Arnold, 2019). Protein engineering grew big in the last few decades, among other things driven by the decreasing cost for DNA synthesis and sequencing, progress in computational methods such as the ROSETTA project (Simons et al., 1999) or advances in gene manipulation like CRISPR/Cas9 (Cong et al., 2013; Jinek et al., 2012). Despite the fact that membrane proteins represent 20-30% (Krogh et al., 2001) of the proteasome of most organisms and around 40% of drug targets (Overington et al., 2006) the engineering efforts on

---

membrane protein pores were lagging behind. This changed rapidly, when researching groups discovered the potential of nanopores (Branton et al., 2008).

## Nanopore Engineering

Nanopore engineering represents an emerging research area that has rapidly grown since the 1990s and paved the way for a range of biotechnological applications. Millions of years of evolution created highly specific protein nanopores that execute key roles in a broad range of physiological processes such as transport of membrane-impermeable solutes, control of membrane potential or mediation of pathogen-related functions (Schmidt, 2016). Nanopores can adopt a range of functional structures. For example, they can comprise highly selective ion channels or just toxic open barrels for cell content release. This broad range of properties provides an extensive toolbox that can be exploited and re-engineered for specialized applications. Prominent examples include third and fourth-generation DNA sequencing technology (Feng et al., 2015; Suzuki, 2020) but also highly specific biosensors for analytical and biomedical applications (S. Wang et al., 2018; Willems et al., 2017). Nanopores can be derived from a number of different substrates including synthetic organic compounds, DNA, peptides and proteins that form aqueous channels across lipid bilayers.

### Synthetic Organic Nanopores

Synthetic molecules offer the widest repertoire of building blocks for pores. Examples include ion channels based on crown ethers coupled to leucines forming an  $\alpha$ -helix that spans the lipid bilayer (Meillon & Voyer, 1997). From there on, several other artificial channels based on macrocycles (Gokel & Negin, 2013), synthetic oligomeric  $\beta$ -barrels (Sakai et al., 2008), water-selective aquaporin analogues (Barboiu & Gilles, 2013) or carbon nanotubes (Geng et al., 2014) followed. These pores offer a great biomimetic platform, which for example allows the detection of organic molecules in complex matrices that effectively mimic the function of a tongue (Litvinchuk et al., 2007).

Even though these pores seem optimal, the freedom of design has several disadvantages. Building pores larger than a few nanometres that remain stable for several hours is challenging due to the lack of generic architectural principles. In addition, synthetic pores often adopt their functional conformation only following membrane insertion, making it difficult to obtain structural data (Stefan Howorka, 2017).

### DNA Nanopores

The most recent trend in the field of nanopores are DNA pores, which are based on modularity of interconnected DNA duplexes (Burns et al., 2013; Langecker et al., 2012). This makes the *de novo* design of complex structures up to tens of nanometres fairly easy, compared to synthetic nanopores or peptides and proteins (Y.-J. Chen et al., 2015; Pinheiro et al., 2011; Rothmund, 2006). The assembly of nucleotides into duplexes in these DNA ‘origami’ structures is well known, predictable and easy to fulfil (Rothmund, 2006). With the software caDNAno it is possible to create bundles of parallel duplexes to form functional pores (Douglas et al., 2009), that can later be coupled with lipid anchors like cholesterol (Göpfrich et al., 2015), porphyrin (Seifert et al., 2015) or tocopherol (Krishnan et al., 2016) to enable bilayer insertion. Alternatively, the DNA backbone can be chemically modified by removing the negative charges in the phosphates (Burns et al., 2014). The Howorka lab could demonstrate how DNA can be used to create a ligand-gated ion channel (Burns et al., 2016) by creating a DNA-based lid on top of a channel blocking the current. A matching DNA ligand can then hybridize the lid and open the channel for a constant ion current flow.

Nevertheless, DNA also has its limitations. The structure itself fluctuates more than protein pores and often the ionic current flows both through the pore as well as along the DNA walls and gaps (Maingi et al., 2015; J. Yoo & Aksimentiev, 2015). The lipid anchors can also alter the bilayer by reorganizing the

interface to the pore wall leading to small water-filled gaps and pores in the membrane (Göpfrich et al., 2016; Maingi et al., 2015).

## Peptide Nanopores

Peptide pores usually consist of up to 50-100 amino acids and frequently exert antibiotic function. Their short length constitutes a key advantage, which renders them easier to make and modify. For instance, they can readily include residues that extend beyond the 20 amino acids provided by the genetic code (e.g. D-amino acids) either by non-ribosomal biosynthesis (Reimer et al., 2016) or even entirely built from non-biogenic amino acids via solid-phase synthesis (Montenegro et al., 2013). This leads to completely new scaffolds and functions that can be explored.

Natural pore-forming peptides include the antibiotic gramicidin from *Bacillus brevis*. Gramicidin is 15 residues in length and features alternating L- and D-amino acids that assemble into a  $\beta$ -helix with all residues pointed outwards (Ketchum et al., 1993). This contrasts protein  $\beta$ -barrels, where sequential amino acids alternate between an inward and outward orientation. Gramicidin spans only one membrane leaflet due to its short length but can form a membrane penetrating channel when two half-channels dimerize (**Figure 1**) (Cifu et al., 1992).

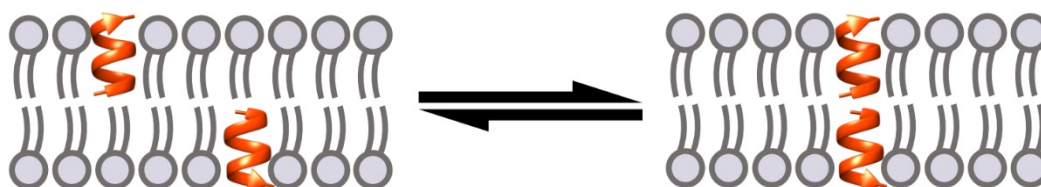


**Figure 1 Gramicidin A forming a dual  $\beta$ -helix ion channel in a lipid bilayer.** The antibiotic gramicidin from *Bacillus brevis* assembles into a  $\beta$ -helix, which spans only one membrane leaflet. When two half-channels dimerize, a transient membrane penetrating channel is formed. Adapted from (Blake et al., 2008); PDB: 1MAG.

Driven by the imminent need to identify and develop new antibiotics, the basic design principle of gramicidin was used to generate alternating D-L peptide rings that stack on top of each other via hydrogen-bonds. These 'nanotubes' showed a broad range of antibacterial activity and are advantageous when it comes to synthesis and bioavailability (Montenegro et al., 2013). By attaching different chemical or biochemical moieties at the C-terminal end of synthetic gramicidin channels, label-free sensing of catalytic activity at single molecule level could be achieved (Cornell et al., 1997; Mayer & Yang, 2013). With functional azide or chemical protecting groups one could also track cycloaddition and hydrolysis reactions (Blake et al., 2008; Mayer & Yang, 2013), while coupled substrates were used for phosphatase and protease activity measurement (Macrae et al., 2009).

Another antibiotic peptide, alamethicin from *Trichoderma viride*, folds into an  $\alpha$ -helix with standard L-amino acids and non-proteinogenic amino acid residues like 2-aminoisobutyric acid (Leitgeb et al., 2007). When alamethicin is inserted into the membrane, it forms ion-selective channels of four to twelve subunits (Pieta et al., 2012). Artificial versions of alamethicin were used to generate more stable synthetic channels (Molle et al., 1996). An important step in peptide engineering was the computational design of *de novo* pores like the four-helix transmembrane Zinc transporter (Joh et al., 2014) or helices that undergo pore formation in a pH-dependent fashion and can be used to deliver and release cargo (Y. Zhang et al., 2015). These peptides have a huge potential in medical application, for instance in the intracellular delivery of drugs.

But there are also drawbacks. The transient nature of the peptides leads to unstable and poorly defined pores, which can be solved by attaching organic scaffolds (Sakai et al., 2008). Mahendran *et al.* redesigned the C-terminal D4 domain of the polysaccharide transporter Wza from *Escherichia coli* with a consensus sequence and subsequently stabilized the pore with cyclodextrin (Mahendran et al., 2017).

---

Later on, the same technique was utilized on  $\alpha$ -helical porin Acj from *Corynebacterium jeikeium* (Krishnan R et al., 2019).

In the end, the benefits of peptide pores outweigh their downsides by being accessible via solid-phase synthesis, having a wide chemical parameter space and their ability to easily insert into the membranes because of their small size (Stefan Howorka, 2017). Difficulties in building large or complex nanopore structures are currently being addressed by computational *de novo* designs (Joh et al., 2014; Thomson et al., 2014) and the variety of pore forming peptides in nature is immense.

## Protein Nanopores

The largest class used in the nanopore field are protein nanopores. They are mainly used for DNA sequencing (Ayub & Bayley, 2016), single-molecule studies (S. Wang et al., 2018) and demonstrate potential for sensing a wide range of different analytes (Stefan Howorka, 2017; Nehra et al., 2019; Varongchayakul et al., 2018). Many protein nanopores have naturally evolved to form defined and stable channels across biological membranes that facilitate rational engineering. Their modular organisation composed of a defined combination of  $\alpha$ -helices or  $\beta$ -sheets makes them easy to finetune at defined positions via amino acid exchange on a genetic level (Stefan Howorka, 2017). Consequently, one can fuse functional domains (Moreau et al., 2008) or remove undesired and interfering parts (M. Chen et al., 2008) to enhance pore stability (Soskine et al., 2012). In addition, protein pores can be chemically modified for example by placing organic molecules into the cavity (Gu & Bayley, 2000), covalently modifying the amino acid side chains or incorporating non-natural amino acids (Spicer & Davis, 2014). Also, whole parts of the polypeptides can be replaced with synthetic pendants via expressed protein ligation, a technique to fuse recombinant proteins with synthetic peptides (Focke & Valiyaveetil, 2010; J. Lee & Bayley, 2015). In some cases, it is even possible to synthesize a complete pore by fusing several synthetic fragments together (Clayton et al., 2004; Kochendoerfer et al., 1999).

The very first application for nanopores was single stranded DNA characterization (Kasianowicz et al., 1996) and DNA sequencing is still to this day an important implementation (Cherf et al., 2012; Deamer et al., 2016; Manrao et al., 2012; Quick et al., 2016). In nanopore sequencing, single stranded DNA molecules translocate through the channel with a narrow cavity leading to ionic current blockades, which create an electrical read-out pattern representing the single bases. This method is label-free and can read very long DNA strands, even with altered bases that are methylated or hydroxymethylated cytosine (Laszlo et al., 2013). The company Oxford Nanopores Technologies invented a portable stick called MinION and made it possible to sequence DNA everywhere (Bowden et al., 2019; Quick et al., 2016). However, the accuracy of nanopore sequencing is less precise compared to sanger sequencing (S. Wang et al., 2018).

Furthermore, protein nanopores can be engineered to detect a range of alternative analytes beyond DNA and quantify their interaction by means of stochastic sensing (Bayley & Cremer, 2001; Stefan Howorka & Siwy, 2009). The analyte typically binds to a defined region within the pore lumen which in turn modulate the conductance of a nanopore (Bayley & Cremer, 2001). First attempts were made by introducing histidine patches inside the lumen of  $\alpha$ HL in order to detect metal cations (Braha et al., 1997). Alternatively, docking  $\beta$ -cyclodextrin made it possible to distinguish between small molecular weight drugs and other biomedically relevant compounds (Gu et al., 1999, 2001; Kang et al., 2006).

In order to turn a nanopore into a sensor, it is crucial to modify the pore lumen with a molecular receptor. In this regard, cysteine residues are generally preferred which can be genetically encoded and selectively modified at mild reaction conditions to preserve protein function. In this way, a range of molecular receptors such as single stranded DNA oligonucleotides were coupled to cysteines and enabled hybridization of complementary strands (S. Howorka et al., 2001) or chemical polymers that have been functionalized with peptide ligands to detect proteins (Movileanu et al., 2000). Several other chemical modifications and reactions were successfully examined in pores, like the photochemical isomerization of diazo dyes (Banghart et al., 2004; Ludwig & Bayley, 2006), organo-arsenic reactions (Shin et al., 2007), the kinetic reaction of quinones (Lu et al., 2010) or the reversible bond formation along multiple cysteines creating a small molecule walker (Pulcu et al., 2015).

In cell biology and biotechnology, nanopores have also been developed into a powerful resource to control membrane permeability. In particular, nanopores can be used to control cell behaviour in response to a molecule or ion flux or mediate the controlled exchange of cargo. Banghart *et al.* redesigned the Shaker potassium channel entrance with an azobenzene linker which undergoes a wavelength dependent cis-trans photoisomerization (Banghart *et al.*, 2004). Upon remote optical triggering, they were able to control neuronal excitability. For larger cargos, the 3-nm-wide MscL channel was equipped with multiple spiropyran chromophores which react with a light-induced charge separation which in turn leads to pore opening or closing (Koçer *et al.*, 2005). Apart from light, several pores were developed that could be controlled by other external stimuli. There exists a version of  $\alpha$ HL with a lumen-anchored, temperature-sensitive polypeptide, that changes its conformation upon thermal changes (Jung *et al.*, 2006) and a 49-Arg rich  $\alpha$ HL, which collapses and reopens depending on the applied voltage and therefore works like a diode (Maglia *et al.*, 2009).

With initial efforts focussing on bacterial toxins such as  $\alpha$ -hemolysin ( $\alpha$ HL) from *Staphylococcus aureus* (Song *et al.*, 1996), more recently, several additional protein nanopores were engineered. This includes *Mycobacterium smegmatis* porin A (MspA) (Faller *et al.*, 2004), cytotoxic cytolysin A (ClyA) expressed by virulent *Escherichia coli* and *Salmonella enterica* strains (M. Mueller *et al.*, 2009), the hetero-oligomeric *Nocardia farcinica* porin A and B (Nfp) (Singh *et al.*, 2012), aerolysin from *Aeromonas hydrophilia* (Payet *et al.*, 2012; Piguët *et al.*, 2018), CsgG (curli specific gene G) pore from *Escherichia coli* (Goyal *et al.*, 2014) or the actinoporin fragaceatoxin C from *Callorhynchus milii* (FraC). These nanopores share several functional and structural features. They have well-characterized 3D structures available with detailed information about their size and geometry (Figure 2). Notably, despite their large oligomeric structure, they readily insert into membranes. Furthermore, once they are in a bilayer, they show uniform opening states with a low probability of stochastic structural fluctuation and are therefore well suited for nanopore engineering (Stefan Howorka, 2017; Varongchayakul *et al.*, 2018).

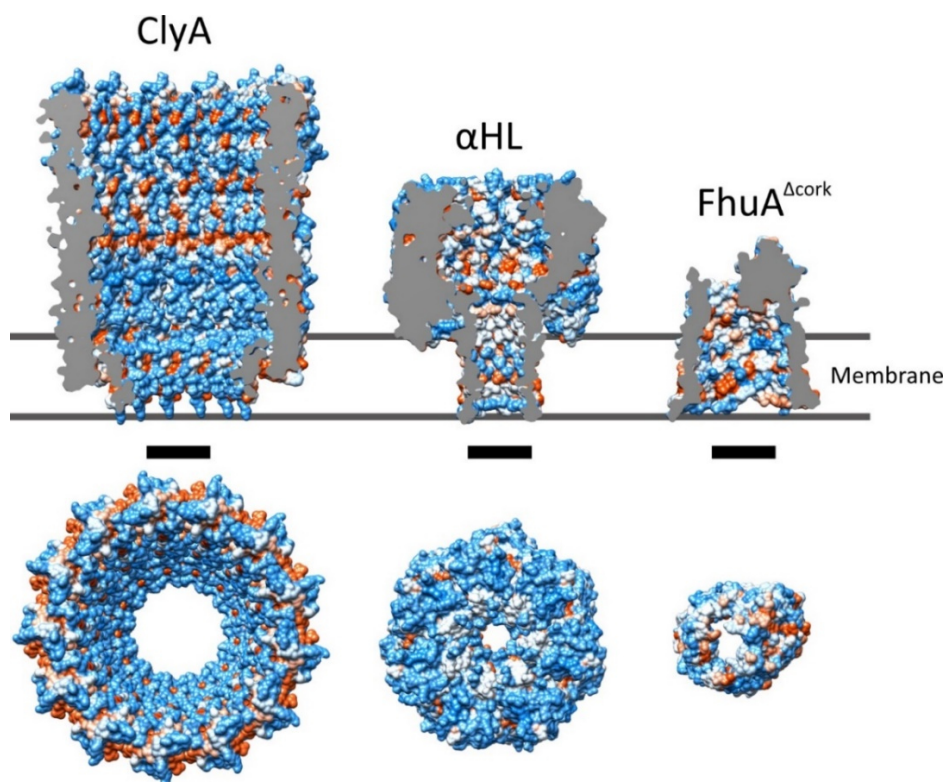


**Figure 2 Demonstration of the size of different Nanopores.** ClyA: The large cytotoxic cytolysin A pore expressed by virulent *Escherichia coli* and *Salmonella enterica* strains got engineered for protein detection.  $\alpha$ HL:  $\alpha$ -hemolysin from *Staphylococcus aureus* was the first pore used for DNA sequencing due to its narrow cavity and easy expression. FhuA: The *Escherichia coli* ferrichrome outer membrane transporter is derived from a single peptide chain and has a prominent cork domain for channel control (here shown without the cork to present the pore size). Red represents a hydrophobic surface, while blue stays for a hydrophilic surface. Scale Bar: 3 nm.

---

Other prominent nanopores comprise the outer membrane proteins F and G (OmpF/OmpG) from *Escherichia coli* (Cowan et al., 1992; Liang et al., 1999) and the ferrichrome outer membrane transporter (FhuA) (Bonhivers et al., 1998). Compared to large oligomeric toxins, these pores are formed solely by a single polypeptide chain. FhuA stands out with its characteristic cork domain that has its unique way of channel control (Thakur & Movileanu, 2018). Together with ion channels like the potassium channels KscA from *Streptomyces lividans* (Doyle et al., 1998; Thompson et al., 2008), the Shaker K<sup>+</sup> channel (Banghart et al., 2004; Schoppa & Sigworth, 1998) or the large conductance mechanosensitive ion channel MscL from *Mycobacterium tuberculosis* (G. Chang et al., 1998; Hindley et al., 2019), a variety of pore scaffolds can be exploited while new ones are being continuously discovered and engineered.

One of the greatest strengths of protein nanopores is the huge genetic diversity and its subsequent existing variety of functional modules. The combination of different existing protein modules can lead to outstanding designs with new functions. On a genetic engineering level, whole domains like a G-protein coupled receptor or a substrate binding protein for ligand detection were combined with a potassium channel to generate new channels (Moreau et al., 2008; Schönrock et al., 2019)

Despite many advantages, there are also some limitations for protein nanopores. Proteins can be immunogenic, which limits their use in therapies. In addition, the computational *de novo* design of protein nanopores still constitutes a significant challenge (Stefan Howorka, 2017). Furthermore, it is difficult to predict structural changes while engineering proteins, especially when whole domains are removed or combined. To tackle those problems, appropriate assay and screening systems for nanopores were developed.

## Assay Systems for Protein Nanopores

Considering the hydrophobic nature of protein nanopores, the majority of nanopore assays are based on electrophysiological measurements in reconstituted membrane bilayers. Although these measurements provide ultra-high-resolution read-outs, their throughput is generally limited. The following chapter presents a summary of basic assay systems that are available to experimentally characterise proteins nanopores with different read-outs and discusses their relative advantages and disadvantages.

### Electrophysiological Characterization in Reconstituted Lipid Bilayer Membranes

In nature, a lipid bilayer membrane forms a stable barrier between two cellular compartments. Prominent examples include the plasma membrane which defines cellular integrity and intracellular membranes that define organelles and provide reaction enclosures. Communication and exchange of matter is generally achieved through membrane proteins that mediate the passage of ions and solutes across this otherwise impermeable membrane barrier.

The idea to characterise individual membrane ion channels embedded in natural lipid bilayer membranes via single channel current recordings was developed 50 years ago (Hladky & Haydon, 1970; P. Mueller et al., 1962; Neher & Sakmann, 1976). The most widespread technique is the black lipid membrane (BLM) technique. Here, two chambers filled with an adequate buffer are separated by a Teflon foil with a small 50-100  $\mu\text{m}$  hole (**Figure 3**) (Montal & Mueller, 1972). A symmetric or asymmetric membrane patch can then be spread of the hole either by pipetting the buffer up and down or painting with an air bubble (Braun, Baer, et al., 2014; Gutschmann et al., 2015). In the final step, pore forming proteins can be added in the vicinity of the membrane patch covering the Teflon hole resulting in membrane insertion. An electrical field can then be applied across the membrane in order to generate a recordable ion current that will vary as a function of the opening state of the nanopore. Notably, extremely low currents in the picoamperes (pA) range and conductance in the picosiemens (pS) range can be distinguished in this way (Zakharian, 2013) and provide information on the size, gating and ion selectivity of a nanopore. Due to the nature of ion channels, most of them are able to control the flow of ions via opening and closing in response to various stimuli such as voltage, ion current or neurotransmitters (Stefan Howorka & Siwy, 2009) which can be easily tested in this setup. Given its

extremely high resolution, the BLM technique remains a potent and widely used method to characterize pores in reconstituted lipid bilayers.

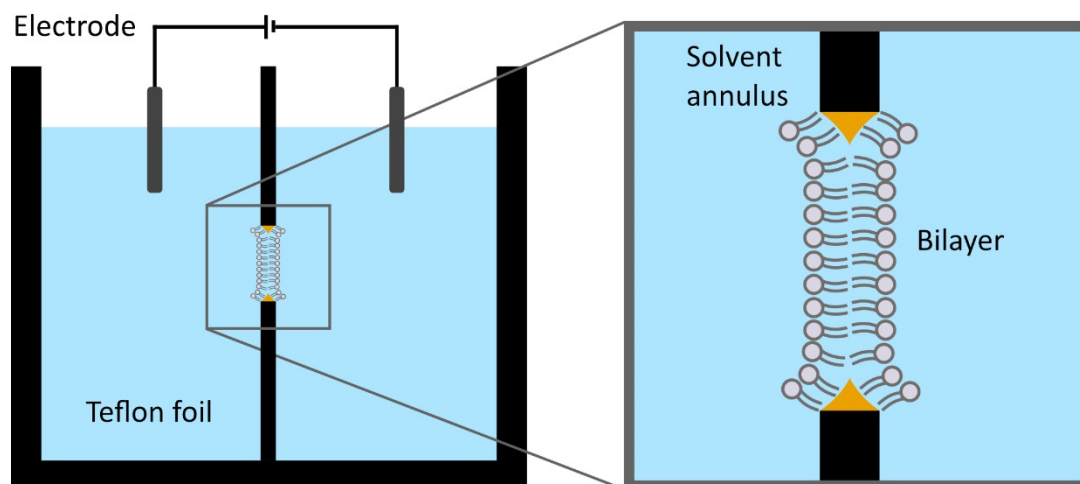


**Figure 3 Structure of a bilayer chamber used in electrophysiological measurements.** A typical bilayer chamber is composed of two sites separated by a Teflon foil with a small hole of about 50-100  $\mu\text{m}$ . The hole gets covered by a lipid bilayer, which was reconstituted in an organic solvent (remains are present in the solvent annulus). One or several pores can then be added to the side with the ground electrode.

### Stochastic Sensing in Reconstituted Lipid Bilayer Membranes

Nanopores and their interactions with a target analyte can be quantified by means of stochastic sensing. Stochastic sensing is based on the quantitative analysis of ion current blockades generated through interactions between an analyte and the protein pore. As soon as the analyte passes through the pore, the ionic current is interrupted and distinct read-outs can be detected in electrical recordings (**Figure 4**). This method is extremely sensitive and enables the detection of single molecules passing through the pore and across the bilayer membrane. Considering the binding of an analyte is reversible, it is possible to record the frequency of binding events which correlates with the concentration of an analyte (Bayley & Cremer, 2001). Furthermore, given the exquisite sensitivity of the BLM technique, the experimental resolution is extremely high and can show different blocking patterns depending on the molecular or conformational state of an analyte (**Figure 4**) (Shi et al., 2017).

One prominent example where stochastic sensing is applied in the context of a nanopore sensor includes sequencing DNA. In this case, every time single-stranded DNA threads through the nanopore, the current flow is blocked in a distinctive fashion upon passage of different nucleotides through the nanopore (L. Liu & Wu, 2016). In addition, DNA was used as a receptor in various applications monitoring DNA/RNA hybridization (Y. Wang et al., 2011), DNA/RNA aptamer binding (Kawano et al., 2011), DNA-metal-ion binding (Wen et al., 2011) or DNA-protein interactions (Smeets et al., 2009). Most recently, the sequencing of peptides and proteins has caught the attention of scientists. The idea is the same as for DNA, but the sequence space with 20 natural amino acids is more complex. Initial experiments with peptides demonstrated the potential (Ji et al., 2016; Mahendran et al., 2012) but the tertiary structure of proteins still remains a challenge (Restrepo-Pérez et al., 2018).

Beyond low-throughput, the BLM technique also carries several other drawbacks. In particular, the reconstitution of lipid bilayer depends on organic solvents that can potentially mimic the behaviour of a pore. In addition, synthetic lipids are preferred due to their stability as natural lipid membranes often turn out to be fragile.

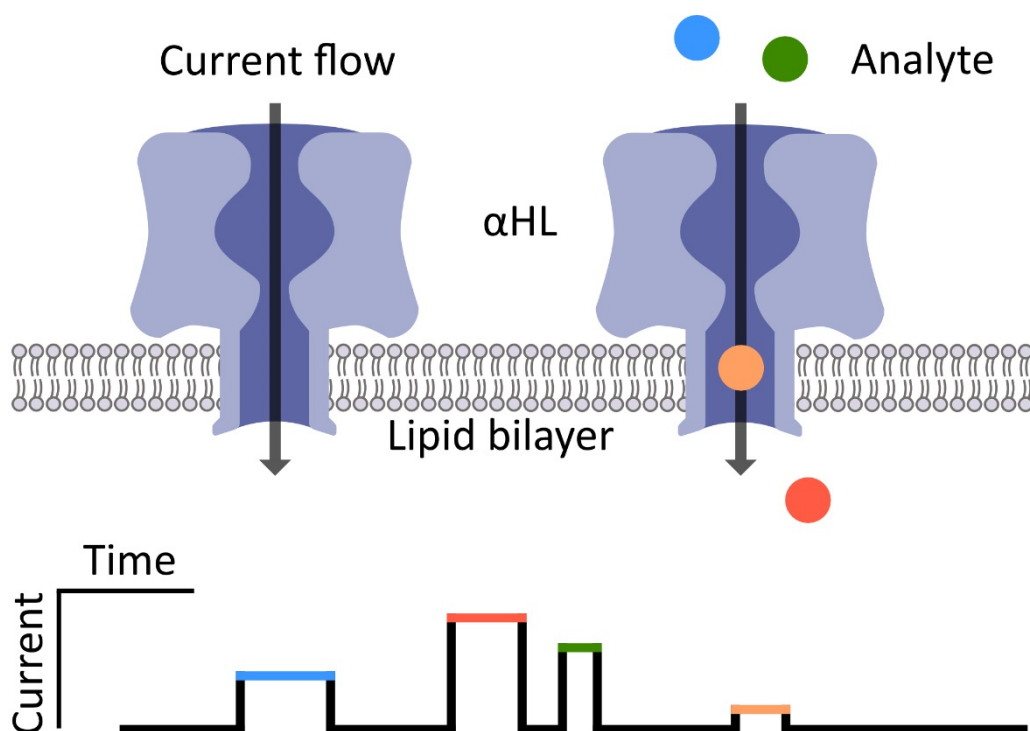


**Figure 4** Schematic overview of different analytes passing a protein pore. When  $\alpha$ HL inserts into a bilayer and voltage is applied, a constant current flow through the pore can be measured. As soon as an analyte molecule like DNA nucleotides or peptides passes the pore, the current gets blocked. This leads to a characteristic time dependent current pattern for every molecule.

### Fluorescence Based Optical Read-outs

Apart from classic ion-current read-outs, alternative methods have been developed to assay nanopores. First attempts focussing on membrane transporters dated back to 1983 and were termed ‘optical single transporter recording’ (OTSR) (R. Peters, 1983). This method was then adapted for whole cells containing isolated transmembrane pores (R. Peters et al., 1990). Briefly, intact membranes were isolated and attached to transparent test compartments. Two fluorescent solutes with similar properties are then added in one of the two compartments, but only one of the solutes can translocate through the pore. The transport characteristics of pores can then be analysed by a time-dependent fluorescence increase in one chamber, with a control signal in the other compartment (Reiner Peters, 2003).

Today, fluorescent read-outs have developed into a powerful toolbox that combines high-throughput with high-resolution data on nanopore functions. For example, Kleefen *et al.* introduced a silicon chip for multiplex analysis of membrane channels and transporters in lipid membranes without the requirement for surface modification or even organic solvents (Kleefen et al., 2010). A silicone nitrate chip was fabricated containing 2025 nanopores with femtoliter compartments, filled with fluorescent molecules and sealed with suspended lipid bilayers (Figure 5). These molecules could then exit through a nanopore in the membrane and thus generate an optical read-out. By using two different fluorescent dyes of which only one is able to pass the pore, one could distinguish between a real pore and membrane rupture. Later on, these chips have been optimized with alternative materials such as silicon dioxide and provide up to 14000 functional cavities that can be observed with high resolution CCD cameras (Diederichs et al., 2018; Kusters et al., 2014). As a proof of concept, antibodies were used to prevent  $\alpha$ HL pore formation, which demonstrates the potential medical applications like drug screening for therapeutic antibodies (Kusters et al., 2014). Despite the huge parallelization in silicon chips, this system does not offer actual high-throughput in terms of library screening, as the linkage between genotype and phenotype is not given. The statistical evaluation on the other hand is large, due to the sheer number of cavities.

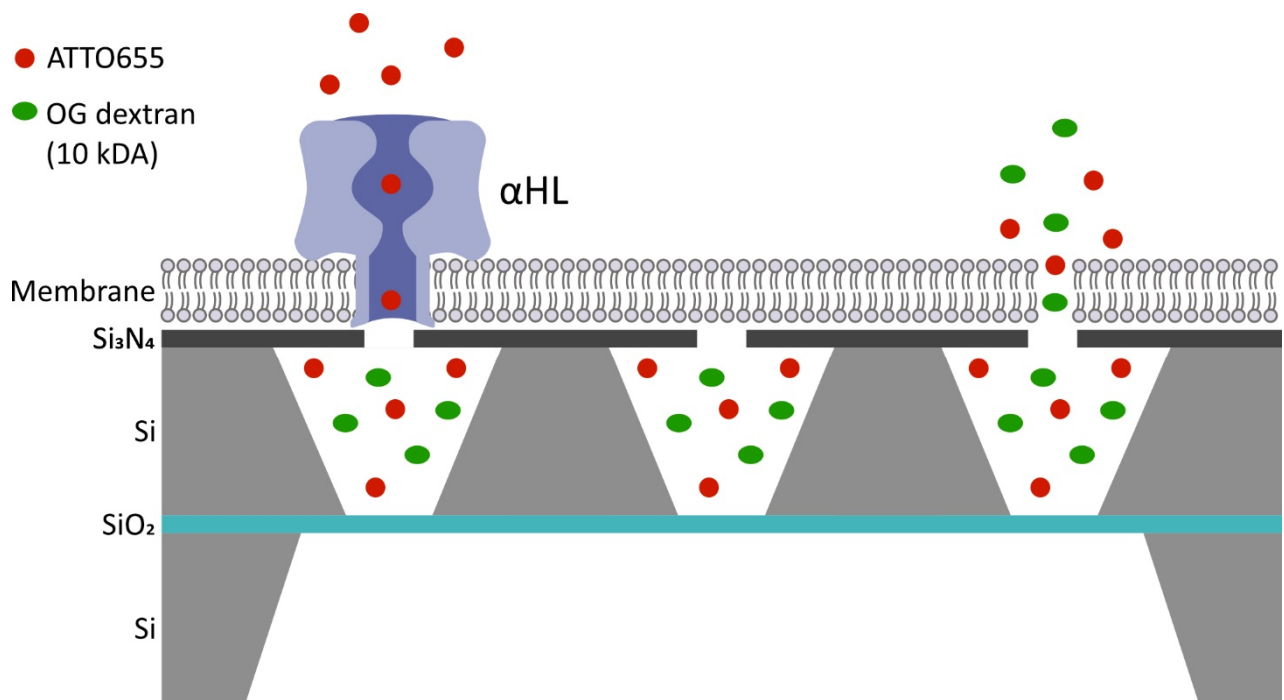


**Figure 5 Schematic drawing of a modern chip with possible scenarios during  $\alpha$ -hemolysin mediated transport.** When  $\alpha$ -hemolysin is inserted correctly, only the red fluorescent dye ATTO655 can pass the pore. If the membrane stays unpunctured, both dyes stay inside the cavity, otherwise both dyes can escape the compartment. Adapted from Diederichs et al., 2018.

Looking for alternatives to sequencing DNA by electrophysiological means - which is technically challenging - optical read-out was realized based on dyes that increase their fluorescence upon binding a specific ligand (S. Huang et al., 2015). A single droplet interface bilayer filled with the  $\text{Ca}^{2+}$  dependent dye Fluo-8 was placed on an agarose film with  $\text{Ca}^{2+}$ . As long as the pore adopted an open state, a bright spot at the location of each protein can be measured by total internal reflection microscopy. Every time DNA passes the membrane, the spot turns off and the time it stays in this condition can then be interpreted similar to electrophysiological measurements. Every droplet contains around  $\sim 10^4$  nanopores per  $\text{mm}^2$  and by creating an array of 2500 bilayers in a hydrogel chip, different samples can be loaded into specific bilayers suitable for high-throughput recordings. Unfortunately, this technique suffers in temporal resolution with a limitation of  $\sim 2$  ms, which could be improved by today's very fast sCMOS detectors. Also, the data acquisition is finite by virtue of  $\text{Ca}^{2+}$  accumulation in the droplets and therefore, the background fluorescence increases over time. Still, this approach is very promising, as it demonstrates the high-throughput capabilities of nanopore screening systems based on fluorescence.

---

## Genetic Screening Systems for Nanopores

While electrophysiological measurements provide high-resolution data on the function of individual nanopores, the throughput of such measurements is generally limited. This means, in order to engineer more complex functional properties, it is necessary to develop suitable high-throughput screening and selection systems. While creating libraries is simple, the subsequent screening of variants with desired properties is challenging. This particularly applies to nanopores that require a membrane environment to be functionally expressed (Carpenter et al., 2008). The following selection provides an overview of the genetic screening and selection systems that have been developed to assay nanopores in high-throughput.

### Medium-Throughput Hemolytic Activity Assay

Most of the nanopores that are used for sensing applications today are derived from organisms with hemolytic activity. They are usually secreted as water-soluble monomers that assemble in lipid bilayers to form cylindrical oligomeric pores. The first screening system exploited erythrocytes as substrates for nanopore formation. In 1995, Walker and Bayley started to identify key residues for membrane binding, oligomerization and pore formation activity of  $\alpha$ HL by Cys mutagenesis and chemical modifications (Walker & Bayley, 1995). They mixed the modified monomers with rabbit red blood cells and monitored the optical density (OD) over time which generally decreased in response to the hemolytic activity of  $\alpha$ HL.

Nearly 30 years later, this method was used to tune the size and other key functional properties of cytolysin A (ClyA) from *Salmonella typhi* (Soskine et al., 2013). The hemolytically active ClyA has a large opening of 7 nm at the top and 3.8 nm at the bottom, which makes it an ideal candidate to detect and analyse proteins (Soskine et al., 2012). But there are also drawbacks associated with ClyA nanopores which tends to assemble into hetero oligomeric states that suffer from low solubility and predominantly form inclusion bodies when overexpressed in *E. coli*. Addressing these limitations, functional properties of ClyA were modified by means of directed evolution. In the first few rounds, the soluble expression was increased by error-prone PCR and growing the colonies on horse-blood agar. The second stage included activity screening in crude lysates with horse erythrocytes in microtiter plates, making it a medium-throughput system with about  $10^2$ - $10^3$  variants being screened each cycle. In the final, stage selected candidates were purified, oligomerization was verified by blue native PAGE and favourable variants were measured in *in vitro* bilayers.

While this screening method led to some stable forms of ClyA, the procedure is rather time consuming. In the first step of the hemolytic activity screen, ClyA yielded a large number of false positives since pore formation itself is a broad criterion. Furthermore, this assay is entirely dependent on hemolytic pores that need to be exported into the extracellular media and restrict the approach to specific classes of pores.

### Medium to High-Throughput Membrane Integrity Dependant Fluorescent Change

Determination of cell viability is a central measuring tool in all kinds of assays. Usually, cellular integrity collapses following cell death and one can stain the exposed DNA of the cells with various fluorescent dyes like propidium iodide or sytox green (Krishan, 1975; Nicoletti et al., 1991; Rathinakumar et al., 2009). These dyes provide information about the membrane integrity and can even be used in flow cytometry (Yasir et al., 2019). One application of these dyes is the screening for antimicrobial peptides (AMP), mostly used to target the outer membrane of bacteria. The problem here is the lack of specificity as dyes can react to every kind of cell death independent of pore formation (Rathinakumar et al., 2009; Roth et al., 1997). Also, they are not capable of detecting changes in ion permeability which can inhibit and kill bacteria by damaging the transmembrane potential (Te Winkel et al., 2016).

---

In this regard, voltage dependent dyes like 3,3' -Dipropylthiadicarbocyanine (DiSC<sub>3</sub>(5)) are more specific. They react to membrane potential changes and are extremely sensitive. It is even possible to calculate the voltage in membrane potential changes (Te Winkel et al., 2016). However, these dyes are expensive and tend to be released rapidly into the medium upon depolarization disqualifying them for long-term measurements.

### High-Throughput Growth Related Screening

Alternatively, functional nanopores can be screened using genetic complementation assays. In 2015, Cosentino *et al.* engineered a blue-light-inducible potassium channel 1 (BLINK1) by recombining the plant LOV2-J $\alpha$  photosensory module with the small viral potassium channel Kcv while optimising the connecting linkers (Cosentino et al., 2015). To screen for blue-light inducible Kcv channels, they used a growth based genetic screening system in a yeast strain that was deficient in the endogenous potassium uptake system. Following transformation with plasmids carrying variants of the BLINK1 channel, only colonies with a functional channel could grow upon blue-light illumination.

Although this approach featured a modular protein engineering strategy and therefore only a few constructs were generated, this screening system is considered as high-throughput as it is principally possible to examine 10<sup>4</sup>-10<sup>5</sup> colonies per selection cycle. Another advantage is the accuracy as the selection condition is very tight and therefore only few false positives can accumulate.

### Ultra-High-Throughput Screening using Liposome Display

Protein nanopores can also be engineered entirely *in vitro* obviating any toxic effects associated with nanopore function. In one example, Fujii *et al.* reported a liposome display for the *in vitro* evolution of  $\alpha$ HL (Fujii et al., 2013, 2014). Liposome display is based on cell-sized artificial liposomes made from water-in-oil emulsions. In each liposome, the cell-free transcription and translation PURE system (Shimizu et al., 2001), a single molecule of DNA and a fluorescent probe together with the HaloTag protein are encapsulated. While the fluorescent dye is needed to calculate the size of the liposomes, the HaloTag protein is used to capture its counterpart, the HaloTag ligand which is labelled with another fluorophore. After the translation of  $\alpha$ HL, numerous proteins are incorporated into the liposomes rendering them porous. The content of the liposomes is designed to stay inside, while the externally added HaloTag ligand that is labelled with AlexaFluor488 can diffuse through the pores into the liposomes and is covalently bound until the point of saturation. This increase in fluorescence can then be sorted by fluorescence-activated cell sorting (FACS) followed by extraction and PCR amplification of the corresponding DNA (Figure 6). With this method, a variant of  $\alpha$ HL was successfully engineered which exhibits a 30-fold increase in pore forming ability compared to wildtype  $\alpha$ HL. The library used on this screening had an overall diversity of 10<sup>7</sup> variants.

Two years later, liposome display was used to enhance the EmrE pore of *E. coli*, a multidrug transporter which is able to translocate toxic cationic compounds like tetraphenylphosphonium or ethidium bromide (Uyeda et al., 2016). The idea was to use the EmrE transporter as a biosensor to detect various toxic chemicals, for example with the contact droplet method (Funakoshi et al., 2006; Hwang et al., 2008). Library screening was performed on the ethidium bromide import and after only three rounds, the activity of the new transporter was already higher compared to the wildtype variant.

Liposome display can be considered as an ultra-high-throughput system with a very high accuracy. False positives are sorted out in several screening cycles and the modularity of the system makes it suitable for most transmembrane pores as it allows the exchange of single components to fit the desired application. The only downside is its dependency on very expensive equipment.

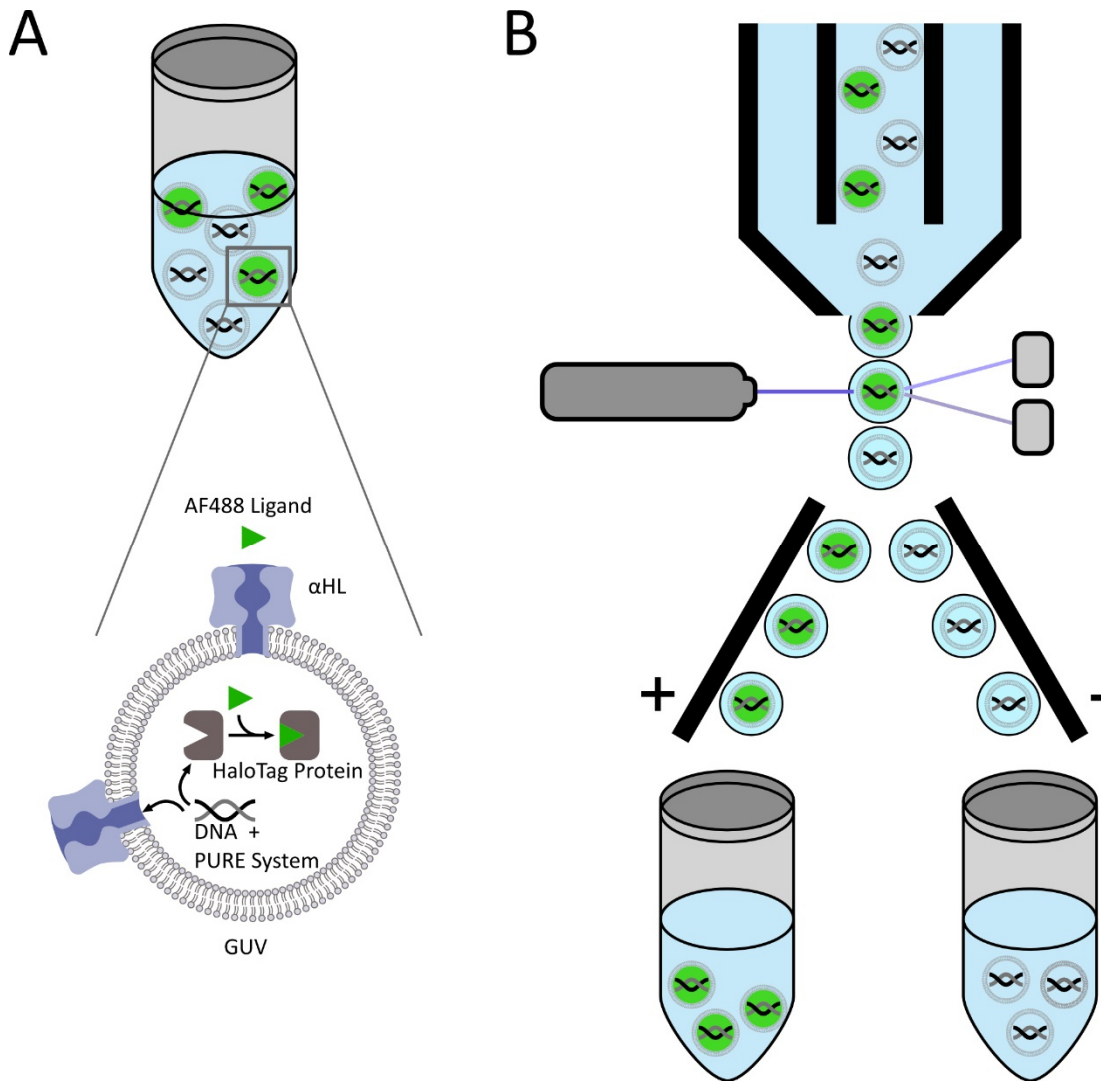


**Figure 6 Schematic overview of the in vitro evolution of  $\alpha$ HL in the liposome display technique.** (A) A DNA library generated by random mutagenesis of the wildtype  $\alpha$ HL is encapsulated in giant unilamellar vesicles (GUV) with around one copy per liposome, together with the PURE expression translation system and the HaloTag protein. When  $\alpha$ HL is expressed, the AF488 ligand can penetrate the membrane and accumulate in the liposomes. (B) GUVs with high fluorescence signals can be separated via FACS and the recovered genes can be used for another round of selection. Adapted from Fujii et al., 2013, 2014.

## Pores in Detail: Holins and Holin-like Proteins

A promising but not yet fully explored class of nanopores are holins. Holin comprise a family of small membrane pore forming peptides or proteins that play a crucial role in the bacteriophage life cycle by permeabilizing the inner membrane of their bacterial host before activating a cascade of reactions that eventually trigger cell lysis and the release of new bacteriophages (Milton H. Saier & Reddy, 2014). Holins feature between one and four transmembrane domains and their characteristic fast and reliable oligomeric pore formation makes them a promising scaffold for nanopore engineering and evolutionary studies. One theory suggests that  $\alpha$ -helical hairpins are stabilized by hydrophobic interactions of two amphiphilic  $\alpha$ -helices facing each other; upon interaction with the membrane one of the two  $\alpha$ -helices might spread on the membrane surface and interact with the lipid bilayer (Mulkiđjanian et al., 2009). The protein then turns inside out and forms a membrane pore (Figure 7). Starting with pores that were built of amphiphilic  $\alpha$ -helices, an evolutionary theory suggests that membrane proteins could have evolved via multiple gene duplications and replacements of polar with non-polar amino acids leading to multi-helix membrane proteins found today (Mulkiđjanian et al., 2009; M. H. Saier Jr, 2000). The simplicity of these peptides also renders them favourable for many biotechnological applications like the cell lysis for content release (S.-Y. Park et al., 2011) or in medical applications as antimicrobial agents (Rajesh et al., 2011; Roach & Donovan, 2015).

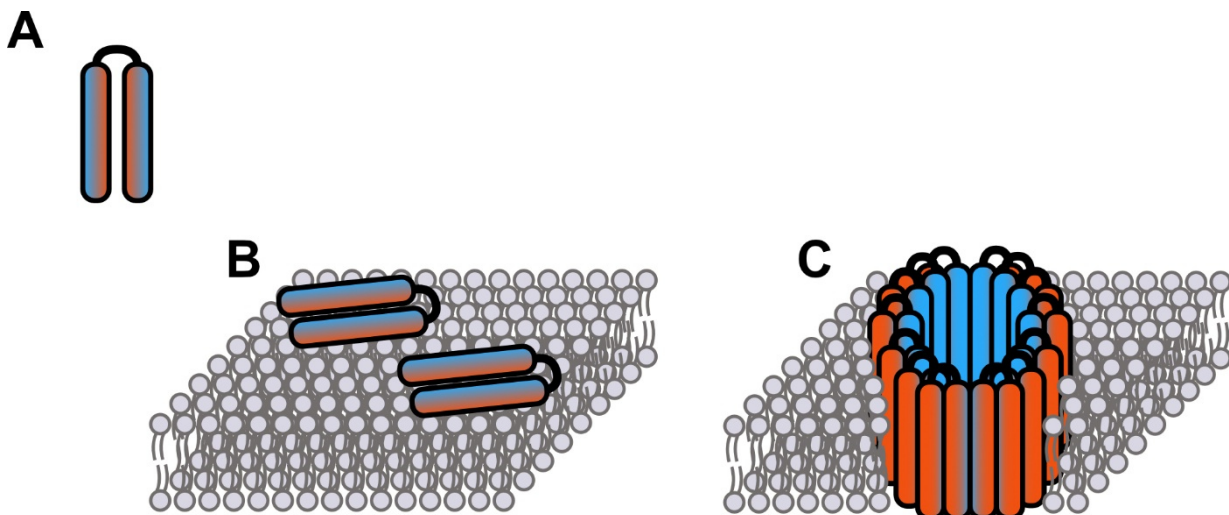


**Figure 7** Insertion theory of a folded water soluble  $\alpha$ -helical hairpin into the lipid membrane by 'inside-out' transition. Blue represents the hydrophilic and red the hydrophobic surface. (A) The soluble  $\alpha$ -helical hairpin spreads and accumulates (B) on the membrane surface by interacting with the lipid bilayer. (C) When a critical mass is reached, the protein turns inside-out and inserts into the membrane. Adapted from Mulkiđjanian et al., 2009.

Until 2014, 58 families of holins were found and 21 of them were subdivided by Saier and Reddy (Reddy & Saier, 2013; Milton H. Saier & Reddy, 2014) in seven superfamilies where members are homologous but distantly related (**Table 1**). With modern genomic sequencing bioinformatic methods, several new putative holins joined the transporter classification database (Milton H. Saier Jr et al., 2016).

**Table 1 Characteristics of holin superfamilies.** Adapted from Saier and Reddy (Milton H. Saier & Reddy, 2014).

Superfamily	Family (TC number (Milton H. Saier Jr et al., 2006))	Organismal type	Avg. size (mean of amino acids $\pm$ SD)	Number of transmembrane domains
I	1.E.11	<i>Firmicutes, Actinobacteria, Proteobacteria</i>	97 $\pm$ 38	2
II	1.E.1, 1.E.6, 1.E.7, 1.E.25, 1.E.50	<i>Proteobacteria</i>	78 $\pm$ 14	1/2
III	1.E.2, 1.E.3, 1.E.4, 1.E.5, 1.E.20, 1.E.34, 1.E.41	<i>Proteobacteria, Actinobacteria, Archaea, Synergistetes, Deinococcus/Thermus</i>	114 $\pm$ 23	3
IV	1.E.10, 1.E.16, 1.E.19, 1.E.14	<i>Firmicutes, Actinobacteria, Fusobacteria</i>	156 $\pm$ 94	3/4
V	1.E.21, 1.E.29	<i>Firmicutes, Chloroflexi, Actinobacteria</i>	98 $\pm$ 17	3/4
VI	1.E.12, 1.E.26	<i>Firmicutes, Chloroflexi, Fusobacteria, Tenericutes, Thermotogae, Deinococcus/Thermus</i>	132 $\pm$ 21	1
VII	1.E.36	<i>Actinobacteria</i>	105 $\pm$ 40	2/4

### Mechanism of Holin Action and Timing

Bacteriophage induced cell lysis of gram-negative bacteria such as *E. coli* is a highly regulated process which ensures a sufficient amount of time to assemble phage particles before causing cell death and triggering their release. This process requires the destruction of three layers of the bacterial cell envelope: (i) the inner membrane, (ii) the peptidoglycan cell wall, and (iii) the outer membrane (Silhavy et al., 2010). The lysis process is mainly regulated by three types of proteins: Holins, endolysins and spanins (Ryland Young, 2014) which are often encoded in adjacent or clustered genes titled as ‘lysis cassette’ (Ry Young, 2002). When the lysis pathway is stimulated at the end of the infection cycle of double stranded DNA phages, holins, endolysins and spanins accumulate in an inactive form in the host cell until a specific time is reached. The holins initiate cell lysis which leads to the permeabilization of the inner membrane (Ry Young, 2013). Scientists distinguish between two lysis pathways: canonical and non-canonical. The canonical pathway is composed of holins which form pores from  $>340$  nm to  $\sim 1$   $\mu$ m in diameter and release active endolysins from the cytoplasm into the periplasm to perform hydrolysis. In the non-canonical pathway pinholins depolarize the membrane with small pores and release membrane-tethered inactive SAR-(signal-anchor-release) endolysins into their active form in the

periplasm (Q. Sun et al., 2009; M. Xu et al., 2004; Ryland Young, 2014). In the final step, the outer and inner membrane connecting spanins collapse both membranes which finally leads to the disruption of the cell (**Figure 8**) (Kongari et al., 2018).

The triggering itself is solely dependent on pore formation and the depolarization of the membrane resulting in a collapse of the proton motive force (PMF) (Gründling et al., 2001; T. Pang et al., 2013; Ryland Young, 2014). This process can be divided into three steps (**Figure 8**). In the beginning, holins accumulate in an inactive form in the inner membrane until a critical concentration of holins is reached and the first ‘rafts’ appear. These rafts comprise a few, but relatively large accumulations of holins in the canonical pathway or numerous small ones in the non-canonical pinholin pathway (Ry Young, 2013). As a second step, a few pores assemble in those rafts which slightly depolarizes the membrane. Membrane depolarization then triggers a sudden cascade of pore formation which ultimately leads to a complete collapse of the PMF (White et al., 2011).

To avoid premature cell lysis, holin genes often feature a complementary antiholin which is encoded by a second reading frame (Ry Young, 2002). Antiholins are negative regulators of their holin counterparts and delay the triggering to ensure a sufficient phage count. Most antiholins contain positive charges at the N-terminus and therefore are less likely to penetrate the membrane due to a PMF sensitive block of the first transmembrane domain which plays a critical role on pore formation (Ry Young, 2013).

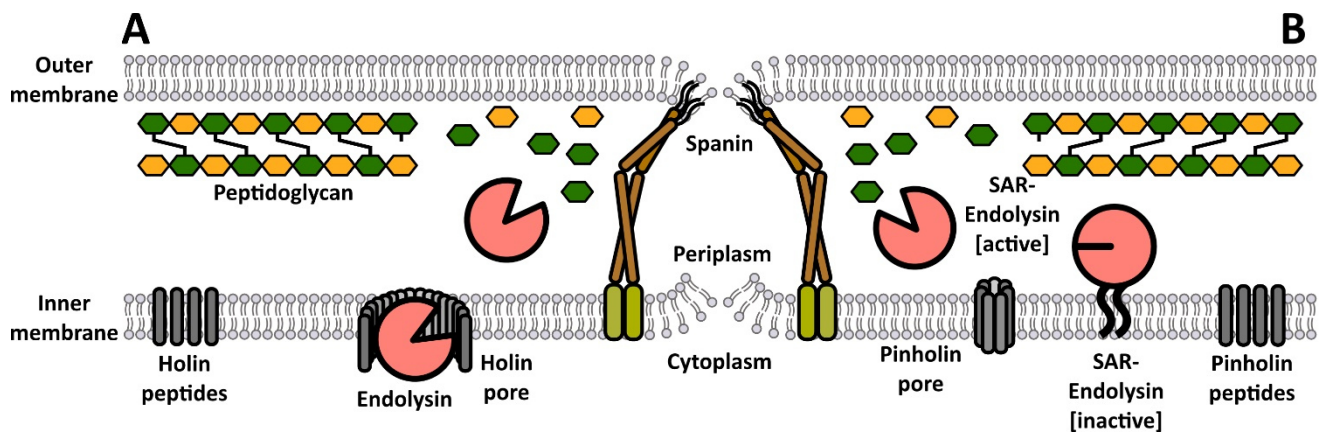


**Figure 8 Overview of the pore forming mechanisms of canonical and non-canonical holins. (A)** In the canonical holin pathway, active endolysins (cytoplasm), spanins (periplasm) and pore forming peptides (inner membrane) accumulate harmlessly in the cell. At a certain point, triggering leads to sudden pore formation, releasing endolysins into the periplasm to destroy the peptidoglycan. Spanins then can collapse the outer membrane to open up the cell. **(B)** In the non-canonical holins SAR-endolysins are exported as inactive versions in the periplasm and anchored to the inner membrane. Similar to the canonical pathway, spanins and pore forming peptides accumulate in the membrane until the triggering point. Many small pores are formed, leading to the collapse of the PMF, which in turn releases the SAR-endolysins into their active form. With the help of spanins, the cell is then disrupted.

## Pore Forming Proteins in Detail

### S<sup>105</sup> Holin

One of the best studied holin systems is the canonical  $\lambda$  phage S<sup>105</sup> holin, whose name also represents its length (Raab et al., 1986; To & Young, 2014). It is one of the products of the S gene, the other being the S<sup>107</sup> antiholin and consists of three transmembrane domains. During the bacteriophage's life cycle, both the holin and the antiholin accumulate harmlessly as heterodimers in a ratio of about 2:1 in the membrane (Ry Young, 2013). The additional positive charge at the N-terminus of the S<sup>107</sup> antiholin delays pore formation until a critical concentration of holins is reached. Small lesions occur and lead to the depolarisation of the membrane, which in turn removes the barrier for a topological change of the first transmembrane domain (TMD1). Inactive holin-antiholin heterodimers suddenly become fully active, producing 1-3 pores per cell with an average of about >340 nm up to 1  $\mu$ m in size (Figure 9) (To & Young, 2014). The openings are large enough to let endolysins of around 18 kDA pass through the membrane to hydrolyse the peptidoglycan layer, but also proteins up to 500 kDA are able to diffuse (I.-N. Wang et al., 2003). The pore formation itself is precisely timed and occurs under defined laboratory conditions around 50 minutes after induction of the lambda prophage (C. Y. Chang et al., 1995). It was even shown that the S<sup>105</sup> holin is functional in other life domains, for example in yeast (Garrett et al., 1990) or mammalian cells (Agu et al., 2007).

Arguably, the most critical structure of the S<sup>105</sup> holin is its first transmembrane domain. In truncation studies, the  $\Delta$ TMD1S<sup>105</sup> variant was defective in lysis and insensitive to membrane depolarization and the truncated  $\Delta$ TMD1S<sup>107</sup> antiholin was not able to detain pore formation (White et al., 2010).

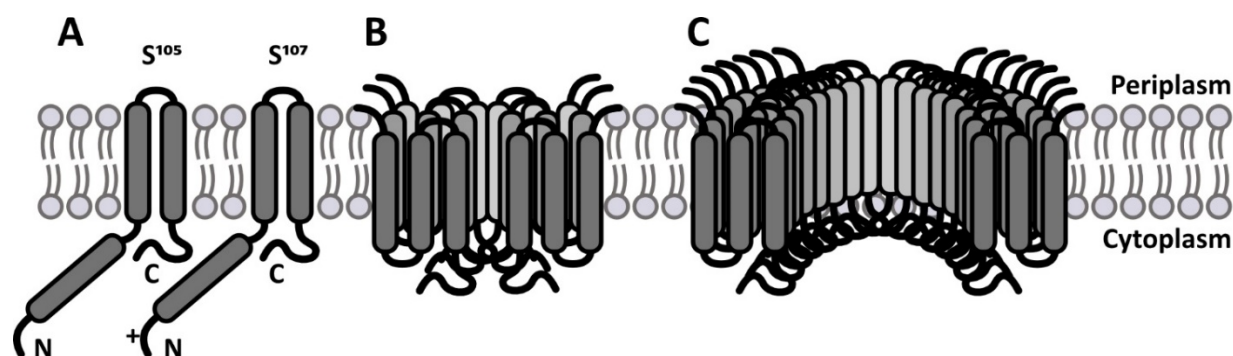


**Figure 9** Illustration of S<sup>105</sup> pore formation and topology. (A) In the beginning, S<sup>105</sup> and S<sup>107</sup> accumulate harmlessly in the membrane as inactive dimers. (B) When a critical point is reached, first rafts appear inducing small lesions that reduce the PMF. (C) As soon as the membrane potential is completely collapsed, 1-3 large pores appear in the membrane.

### S<sup>2168</sup>

A related, yet different way of cell lysis is performed by the non-canonical phage 21 and its S<sup>2168</sup> pinholin (T. Pang et al., 2009). It is composed of two transmembrane domains while its cognate antiholin S<sup>2171</sup> features additional positive charges at the N-terminus. The pinholin also accumulates along with its S<sup>2171</sup> antiholin in the membrane until a specific time point. As soon as triggering occurs, up to 7000 peptides form about 10<sup>3</sup> heptameric pinholes per cell, with an estimated diameter of ~2 nm (Ry Young, 2013). These defined pores in turn collapse the PMF and depolarise the membrane (Figure 10). Subsequently, signal-anchor release (SAR) endolysins which are coupled in an inactive form to the periplasmic site of the membrane, are released and refold into their active state (T. Park et al., 2006). In contrast to the S<sup>105</sup> holin, the TMD1 is dispensable for pore formation (T. Pang et al., 2009). The model predicts a predominant TMD1-TMD2 interaction as long as both helices remain in the membrane. Self-association of the TMD2 begins as soon as TMD1 exits the membrane into the periplasm. Interplay between TMD1 helices on the periplasmic site might then further accelerate TMD2-TMD2 pore forming (T. Pang et al., 2010a).

Recently, groups started to chemically synthesize and characterise the S<sup>2168</sup> pinholin with biophysical methods (Ahammad et al., 2019, 2020; Drew et al., 2019). They show that the TMD1 seems to be

anchored to the membrane after externalization, which suggests that the TMD1 can both inhibit and stabilise nanopore formation.

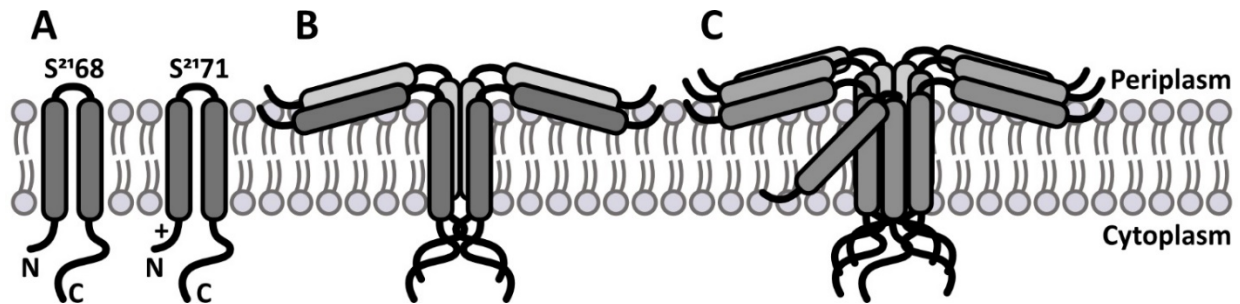


**Figure 10 Illustration of S<sup>2168</sup> pore formation and topology.** (A) S<sup>2168</sup> and S<sup>2171</sup> accumulate harmlessly in the membrane, mostly associated as dimers. (B) First rafts appear after a certain time, inducing small lesions that reduce the PMF. (C) As soon as the membrane potential has completely vanished, up to 10<sup>3</sup> heptameric pinholes per cell can be observed.

### T4 Holin

In addition to the canonical and non-canonical lysis pathways, there is also third class of holins with slightly different architectures and mechanisms. The T4 holin of T4 bacteriophages functions similar to the S<sup>105</sup> holin by forming large  $\mu\text{m}$ -sized pores for endolysins to exit (Ramanculov & Young, 2001a) but its topology and its control mechanism through antiholins is completely different. The T4 holin only features one transmembrane domain with its short N-terminus located in the cytosol and a large periplasmic C-terminus (Ramanculov & Young, 2001b). In comparison, holins usually have two or more transmembrane domains that are critical for their flipping mechanism. In contrast, the large C-terminal tail of T4 holin plays an inhibitory role in nanopore formation which is regulated by the periplasmic antiholin RI and the cytoplasmic RIII (Figure 11) (Y. Chen & Young, 2016). They do not have any similarities with the T4 holin, which makes them special in the greater context of the holin family. Both proteins are responsible for a superinfection state, where they can extend the length of the bacteriophages vegetative cycle (Rutberg & Rutberg, 1965).

Given its unique regulatory mechanism based on soluble domains, this T4 holin could provide valuable starting points to engineer post-translational control of nanopore formation. Truncation and mutation experiments so far suggest that the TMD combined with the short N-terminal domain are responsible for membrane permeabilization and periplasmic C-tail is a regulatory module for lysis timing (Ramanculov & Young, 2001a).

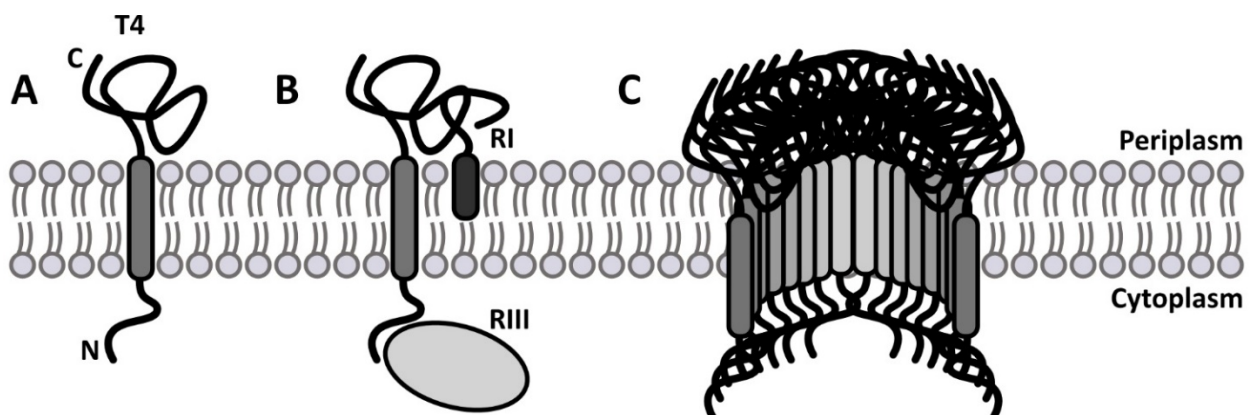


**Figure 11 Illustration of T4 pore formation and topology.** (A) The T4 holin consists of only one TMD and accumulates in the membrane with its C-terminus protruding into the periplasm. (B) When the host gets superinfected and the vegetation cycle is prolonged, the antiholins RI and RIII interact with the C- and N-tail respectively and inhibit pore formation. (C) Pore formation of T4 holins is similar to the canonical holins with undefined large pores.

---

## HokB/TisB

Another class of pores similar to holins are the persistence-inducing toxins like HokB or TisB. These pores are found in persister cells, phenotypic variants of isogenic bacterial populations, that are able to survive treatment with high doses of antibiotics. As soon as the antibiotic is removed, persister cells are able to regrow and form a new antibiotic sensitive population (Michiels et al., 2016). Recent findings suggest that resistant mutants can emerge from this cell population (Fauvart et al., 2011; Levin-Reisman et al., 2017; Sebastian et al., 2017). Mediators of persistence are toxin-antitoxin (TA) modules. These feature a stable toxin that targets essential cellular functions and an unstable antitoxin that inhibits the toxins (Wilmaerts et al., 2018). Usually, the antitoxin reacts to environmental changes and as soon as it is downregulated, the toxin becomes active (Lobato-Márquez et al., 2016). Overall, there are six types of TA modules, one of which features membrane localized toxins that are able to collapse the membrane potential (Brantl & Jahn, 2015). Both TisB and HokB form pores which then drop the PMF and ATP levels and thus induce a dormant state (Gurnev et al., 2012; Wilmaerts et al., 2019). Paradoxically, an antimicrobial peptide manages to protect the cell from being killed by other toxins. However, the detailed mechanisms are still unknown (Balaban et al., 2013).

The functional properties of HokB and TisB nanopores have also been studied by *in vitro* bilayer measurements. This included mutations of key residues and blocking the pores with different sizes of polyethylene glycol or even FACS studies with voltage dependent membrane dyes (Gurnev et al., 2012; Wilmaerts et al., 2018). The increasing clinical relevance of multi-resistant bacteria also makes those persistence pores a promising target for the development of antibiotics.

## Kcv ion channels

The Kcv potassium channels belong to the most common group of ion channels which occur in every living organism (Littleton & Ganetzky, 2000). Their main task is to transport  $K^+$  rapidly and selectively across the membrane in the direction of their electrochemical gradient. They regulate the resting potential in many cells but are also able to process higher tasks like the secretion of insulin in a glucose mediated cascade pathway and dysfunctions in those channels can lead to diseases such as diabetes (Tarasov et al., 2006). The KcvNTS channel used in this study has a tetrameric structure and is composed of four identical subunits which form a stable pore (Braun, Lachnit, et al., 2014; Pagliuca et al., 2007). Their specificity for  $K^+$  results from its selectivity filter module, a highly conserved consensus sequence. The carboxylic groups of the four subunits in the selectivity filter mimic a hydrate shell, therefore no energy is needed for the ions to switch from a hydrated state into the protein pore (Roux, 2017). In nature, these channels are used by *Chlorella* viruses to attack the hosts membrane in order to reduce the cell turgor which makes it easier for the virus to inject its DNA (Thiel et al., 2011).

## BM2 proton channel

The influenza BM2 channel is a proton porter that consists of 4 transmembrane helices forming a pore in the viral envelope. It gets activated during cell entry by receptor mediated endocytosis and the following endosomal acidification. BM2 channels then mediate a further pH drop which in turn leads to the weakening of electrostatic interactions of several matrix proteins. The subsequent release of ribonucleoprotein complexes is the starting point of viral replication (Pielak & Chou, 2011).

---

## The Diversity of Holins and Holin-like Proteins

Interestingly, holins and holin-like proteins are also encoded in a range of alternative species, including bacteria (Milton H. Saier & Reddy, 2014). Those bacterial holins for instance play a critical role in biofilm formation by mediating cell lysis and the release of genomic DNA which comprises a key structural component of the biofilm matrix (Ranjit et al., 2011). Another example is the involvement of holins in bacterial gene transfer, where the bacterial donor transfers encapsulated DNA in phage-like particles via a lysis cassette, similar to the ones found in bacteriophages, to the recipient (Matson et al., 2005). Furthermore, in bacteria holins have been shown to play a role in stress response (Ahn et al., 2012), release of toxins (Degnan & Moran, 2008) and bacterial sporulation and spore germination (Real et al., 2005). In recent studies, the *Bacillus subtilis* YsbA and its two-component regulatory system LytST were found to have a metabolic function by regulating the import and export of pyruvate in and out of the cytosol (Charbonnier et al., 2017; van den Esker et al., 2017a).

In plants, LrgB-domain containing proteins that have homologies to the CidA/CidB and LrgA/LrgB putative holin system in *Staphylococcus aureus* were found in the leaf chloroplasts envelope and are predicted to be plastidic glycolate/glycerate transporters (PLGG1) involved in photorespiration (Pick et al., 2013; Yang et al., 2012). But also in programmed cell death, LrgAB protein is suggested to function as a holin, similar to the Bcl-2 family proteins that are involved in the apoptosis in animals (J. Wang & Bayles, 2013). Homologues can be found in cell-walled fungi, stramenopiles and plants. This diversity of organisms shows that they seem to carry out a variety of biochemical functions (Milton H. Saier & Reddy, 2014).

Even animal programmed cell death is similar to a functional holin system. Mitochondria in animal cells react to apoptotic signals with outer membrane permeabilization which in turn initiates a series of proteolytic events by releasing cytochrome C and other mitochondrial proteins into the cytosol called the 'caspase cascade' (Danial & Korsmeyer, 2004; Jiang & Wang, 2004; Newmeyer & Ferguson-Miller, 2003). The membrane permeabilization is mainly controlled by Bcl-2 family proteins, containing the proapoptotic Bax and Bak protein and the antiapoptotic proteins Bcl-2 and Bcl-x<sub>L</sub>. Similar to antiholins, the antiapoptotic proteins inhibit permeabilization by suppressing the proapoptotic proteins which can be compared to holins (Galonek & Hardwick, 2006). Pang *et al.* demonstrated the link between Bax/Bak and  $\lambda$  phage holin by exchanging the holin with either Bax or Bak (X. Pang et al., 2011). In both cases the proapoptotic proteins displayed a similar function in pore formation.

---

## Genetically Encoded Fluorescent Proteins

For the development of a genetic screening system to assay nanopore function in high-throughput, genetically encoded fluorescent sensors can provide valuable tools to monitor the nanopore-dependent flux of a ligand across the membrane. To this end, a range of different biosensors have been created throughout the years to detect and understand biological signalling events (Constantinou & Polizzi, 2013; Fehr et al., 2005; Merckx et al., 2013; Newman et al., 2011; Palmer et al., 2011). This includes indicators for  $\text{Ca}^{2+}$  (Mank & Griesbeck, 2008; Miyawaki et al., 1997; Nakai et al., 2001), reporters of cyclic nucleotide levels (Klarenbeek et al., 2011; Russwurm et al., 2007) or kinase activation indicators (Schleifenbaum et al., 2004; J. Zhang et al., 2001).

Every genetically encoded protein biosensor is based on three main components. It starts with the receptor domain which is able to bind an analyte of interest. Usually, this function is performed by allosteric binding domains like the calmodulin and the myosin light chain M13 (Akerboom et al., 2009) which can bind  $\text{Ca}^{2+}$  or the FRB and FKBP12 system which can associate in the presence of rapamycin (Banaszynski et al., 2005). Alternatively, periplasmic binding proteins like the glutamate binding component GltI from the ABC transporter complex for glutamate and aspartate can be used (Marvin et al., 2013).

The second biosensor component is the actuator domain. This module produces a detectable signal output which is often an increase or decrease in fluorescence (Newman et al., 2011), but can also be accomplished by enzyme activity (Guntas et al., 2005; Stein & Alexandrov, 2014) or by electrical current readout from redox reactions (Guo et al., 2016). Fluorescent biosensors are either based on intramolecular Förster resonance energy transfer (FRET) between two fluorescent proteins or a single fluorescent protein which is either a split version or a circularly permuted fluorescent protein. The FRET variant which relies on the transfer of energy from a donor to acceptor chromophore after distance alteration between two fluorescent proteins provides favourable ratiometric output. But it also has several drawbacks like its limited detection range of only two orders of magnitude of the analyte concentration and a restricted dynamic range because of the distance of the chromophores between the two spatially bound large beta-barrel proteins (Ast et al., 2017; San Martín et al., 2013; Tsien, 1998).

On the other hand, single fluorescent biosensors can achieve a large dynamic and detection range and have a high signal-to-noise ratio (Ast et al., 2017; Nagai et al., 2001). Usually, those sensors are based on circularly permuted GFP (cpGFP), a variant of GFP where the native N- and C-terminus are connected via a short linker and new N- and C-termini were created in the beta sheet near the chromophore (Baird et al., 1999; Ohba et al., 2013). The fluorescence of this opened up barrel can then be restored once the new N- and C-terminus get spatially reunited, for example by a conformational change of domains connected to these termini.

The third important building block of biosensors is the connection between the actuator and the sensing domain, better known as linker. In naturally occurring multi-domain proteins, the single modules are connected via oligopeptides and the combination and biophysical abilities of the amino acids in these linkers lead to individual characteristics (Sørensen & Kjaergaard, 2019). The functional range of linkers is wide and becomes even more important in the context of multi-domain assembly for artificial proteins (George & Heringa, 2002; Lin & Liu, 2016; Gräwe et al., 2020). For example, flexible linkers are based on small or hydrophilic amino acids like glycine-serine repeats and are often used to minimise negative impact on fold or structure, but also allow free interactions between two domains (X. Chen et al., 2013). Rigid linkers containing  $\alpha$ -helical structures or multiple proline residues provide a fixed distance between the domains which allows them to maintain their independent functions without interacting (X. Chen et al., 2013; George & Heringa, 2002).

The combination of a receptor and an actuator connected with the right set of linkers can lead to powerful biosensors for different applications such as the genetically encoded  $\text{Ca}^{2+}$  indicators for optical imaging (GECO).  $\text{Ca}^{2+}$  indicators were among the first generation of biosensors and were constantly improved over the years, demonstrating the usability and importance of such tools (Miyawaki et al., 1997; Nagai et al., 2001; Zhong & Schleifenbaum, 2019). The allosteric binding receptor is based on calmodulin (CaM) and the calmodulin binding peptide (CBP) derived from the myosin light chain kinase (M13). In the presence of  $\text{Ca}^{2+}$ , CaM binds the ions and changes its conformation. The M13 domain can

then associate with CaM, causing the receptor to transition to an even more compact state. While in the original design, this change of conformation was detected by FRET, a more integrated version based on circularly permuted fluorescent proteins was created (Zhao et al., 2011) and is based on the deprotonation of the chromophore, when both domains at the N- and C-terminus associate upon ligand binding (Figure 12).

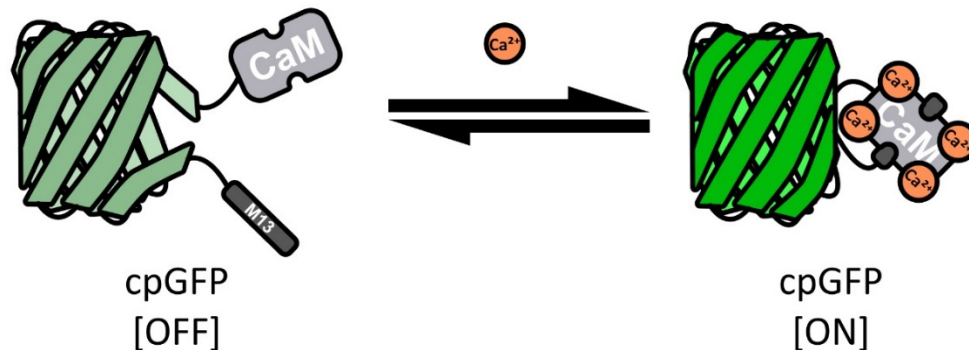


**Figure 12 Principle of the circularly permuted GFP based biosensor G-GECO.** In the presence of Ca<sup>2+</sup> ions, the calcium binding domain Calmodulin (CaM) associates with the myosin light chain kinase derived peptide M13. This reversible process reunites the N- and C-terminus of the cpGFP, leading to a deprotonation and a subsequent fluorescence signal upon excitation.

Main requirements for a reporter unit like cpGFP are an intense fluorescent signal with a high dynamic range, but also a dim OFF-state and, if possible, with a ratiometric read-out. These technical requirements frequently cannot be fulfilled within one single protein sensor, but one kind of sensor can be modified in various ways to generate a subset of sensors for a single analyte that can be used in different applications. In 2011, Zhao *et al.* expanded the palette of genetically encoded calcium sensors by exporting the protein into the periplasm where the Ca<sup>2+</sup> concentration can be environmentally controlled and measuring the intensity change after EGTA addition (Zhao et al., 2011). They improved the green version (G-GECO1), made a blue (B-GECO1) and red (R-GECO1) variant and managed to engineer a ratiometric sensor (GEX-GECO1) which exhibits a large Ca<sup>2+</sup> dependant change in the excitation ratios of 400 nm and 488 nm.

---

## Using Biosensors as Tools for Nanopore Engineering and Vice Versa

Few attempts have been made so far to develop screening systems for genetically encoded fluorescent sensors in combination with pores or with other membrane permeabilizers. Litzlbauer *et al.* exploited the ability of *E. coli* cells to maintain a very low in vivo concentration of calcium of about  $90 \text{ nm} \pm 10 \text{ nm}$  (Gangola & Rosen, 1987) and screened for diversified  $\text{Ca}^{2+}$  sensitive FRET sensor in a large-scale colony approach by permeabilizing the membrane with poly-L-lysine and ionomycin (Litzlbauer *et al.*, 2015). The combination of both treatments allows  $\text{Ca}^{2+}$  to surpass the membrane and screen for a sufficient FRET sensor variant.

In 2017, Majumder *et al.* used G-GECO1 to sense external  $\text{Ca}^{2+}$  concentrations in artificial cells (Majumder *et al.*, 2017). They co-expressed G-GECO1 and MscL, a mechanosensitive membrane protein that is able to sense osmotic pressure in a cell free transcription-translation system and afterwards incorporated this solution into double emulsion vesicles. By adding  $\text{Ca}^{2+}$  to the outside medium, the osmotic change opened up the pores and the vesicles showed increased fluorescence. However, this method requires the addition of EGTA, since the transcription and translation system requires up to 1 mM  $\text{Ca}^{2+}$  which is enough to activate the G-GECO.

The goal of this study was to develop a functional nanopore screen based on genetically encoded GECOs and pore proteins to visualize the influx of  $\text{Ca}^{2+}$  ions which is dependent on the characteristics of the nanopores. For this purpose, a subclass of pores was chosen with a special focus on the pinholin S<sup>2168</sup>. Starting with colony-based and microtiter plate screening, the system was stepwise adjusted until it was possible to use it in a high-throughput manner. After gaining insights into different pore mechanisms, this system was further exploited to be able to screen for biosensors instead of pores - making it a versatile and powerful tool in tailored nanopore and biosensor development for biotechnological applications.

---

## Results

---

### Design Principle of the FuN Screen

The functional nanopore (FuN) screen aims to provide a new screening system for the *in vivo* analysis of pore forming peptides that is compatible with a range of different assay formats from low-throughput and high-resolution to high-throughput and low-resolution. To this end, a genetic screening system in *E. coli* was designed that is based on three main components: the input signal (ion), a transducer (nanopore) and the output signal (biosensor). The cell itself acts as a compartment which separates the input signal from the biosensor and provides a link between the genotype and phenotype.

In the initial configuration, the screening system was developed using genetically encoded calcium indicators for optical imaging (GECO) (Zhao et al., 2011) as biosensors. It features an integrated biosensor design with a circularly permuted fluorescent protein that is fused to calmodulin (CaM) and the calmodulin binding peptide (CBP) M13 to its N- and C-terminus respectively. Upon binding of  $\text{Ca}^{2+}$ , CaM binds M13 which results in a change in the microenvironment of the fluorophore and modulates its fluorescent properties. The GFP variant of the sensor (G-GECO1) is a stable version with an intensity change from the unbound to the bound state of 25x in the purified form, a theoretical brightness around half ( $17.2 \text{ mM}^{-1}\text{cm}^{-1}$ ) of the original eGFP ( $33.54 \text{ mM}^{-1}\text{cm}^{-1}$ ) and a  $K_d$  of 749 nM. It is soluble and was originally screened in *E. coli* by transporting the protein to the periplasm where the calcium concentration can be environmentally controlled.

The screen was verified with three different classes of small membrane peptides and protein nanopores that insert into the membrane independently of a signal sequence. This includes holins, persistence inducing toxins and small viral potassium channels. While holins were an integral focus of this work and included mechanistic studies to dissect their mechanism of action, persistence inducing toxins feature greater clinical relevance as they mediate the efflux of antibiotics in multi-resistant bacteria. Nevertheless, both classes have the ability to form (defined and undefined) pores out of small peptides in common and are quite unspecific regarding their ion flow through the pore. In contrast, small viral potassium channels like the KcvNTS are highly specific for  $\text{K}^+$  and are therefore a viable negative control. In the elementary protocol, the FuN screen relies on the expression of the sensor protein followed by the induction of a nanopore. This leads to a permeabilization of the inner cytoplasmic membrane enabling a ligand to flow into the cytoplasm (Figure 13) and in turn increases fluorescence of the biosensor. Depending on the kinetics of the fluorescent signal it is possible to infer information on the formation and function of the nanopore (Figure 13)

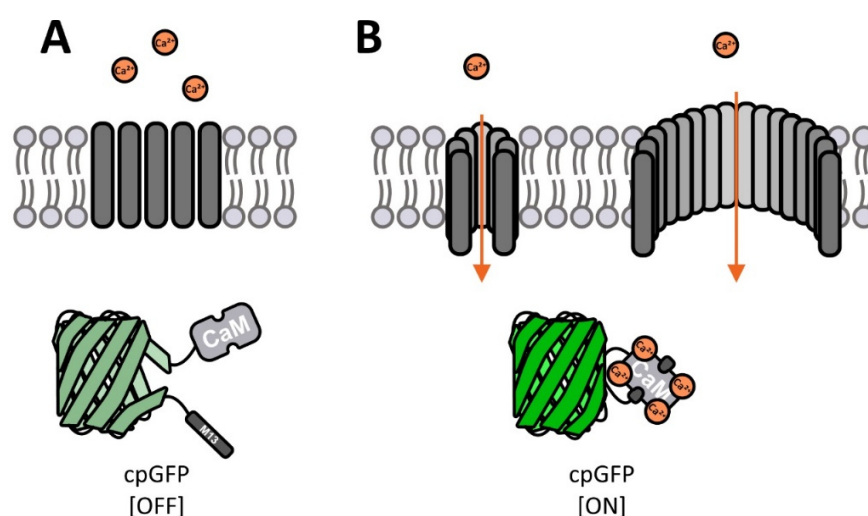


**Figure 13 Principle of the FuN screen.** The screen is composed of three main components: the input signal (ion), a transducer (nanopore) and the output signal (biosensor). (A) In the beginning the biosensor G-GECO1 is expressed in a dim state because of the low  $\text{Ca}^{2+}$  concentration in *E. coli* cells. As soon as nanopores are induced, they begin to accumulate in the membrane and (B) upon a certain point pores start to form. This allows  $\text{Ca}^{2+}$  to pass the membrane and activate the G-GECO1. Pores with different sizes can be measured with this platform.

To realise the FuN screen, a co-expression system was devised to express the nanopore and the biosensor from two independent plasmids. The most crucial step in the development of the FuN screen was the design of the plasmid backbone carrying the pore. This is because of the toxic nature of these proteins and the leakiness of the majority of recombinant expression systems. Furthermore, several additional criteria had to be fulfilled: Both plasmids must have different antibiotic selection markers and compatible origin of replication (ori) classes. The compatibility of the ori is an important factor. Even though plasmids with the same ori were co-transformed without complications in some cases (Velappan et al., 2007), the literature describes two main issues with incompatible oris in the same cell: the replication and the partitioning problem. The bacterial origin of replication machinery has a negative feedback regulation system which involves antisense RNA or iterons that inhibit the replication when the copy number gets too high (Novick, 1987). In the case of two compatible plasmids, different negative regulation systems control plasmid replication by using unique replication machinery. In the contrary case of incompatible plasmids (same ori class) the negative regulation system cannot distinguish between them which leads to a significantly lower copy number of both plasmids (del Solar et al., 1998). In addition, there is also a problem with low copy plasmids using the same ori while plasmid partitioning. Generally, the partitioning system in bacteria is a controlled mechanism which does not rely on chance and ensures that compatible plasmids are passed on equally to the daughter cells (Schumacher, 2012). In the case of incompatible oris, the asymmetric plasmid loss occurs frequently over time, either from outcompeting or because there is simply not enough time during cell division for correct partitioning (Diaz et al., 2015). While most of the previously mentioned problems do not interfere in single variant transformation, massive problems can occur during library transformation due to the partial loss of variants.

To overcome these limitations, two compatible plasmids were taken and engineered to the point they showed the best possible signal. Starting with the plasmid coding for the G-GECO1 biosensor, the pPRO24 system was chosen (S. K. Lee & Keasling, 2005, 2006). This plasmid uses the pBAD (arabinose inducible promoter) backbone and carries the class A ori pBR322 and F1 (described as high copy) with an ampicillin resistance (Guzman et al., 1995). In pPRO24 protein expression is based on the *prpBCDE* promoter ( $P_{prpB}$ ) which is controlled by the *prpR* transcription factor. This encodes for a positive regulator of the *prpBCDE* promoter and naturally regulates the propionate catabolic genes (Figure 14). Furthermore, the expression system is based on the endogenous  $\sigma^{54}$ -dependent RNA polymerase and can be activated by up to 50 mM propionate. In addition, it has a similar tuneable expression pattern like the pBAD plasmid, but without the dependency of a sugar source for activation.

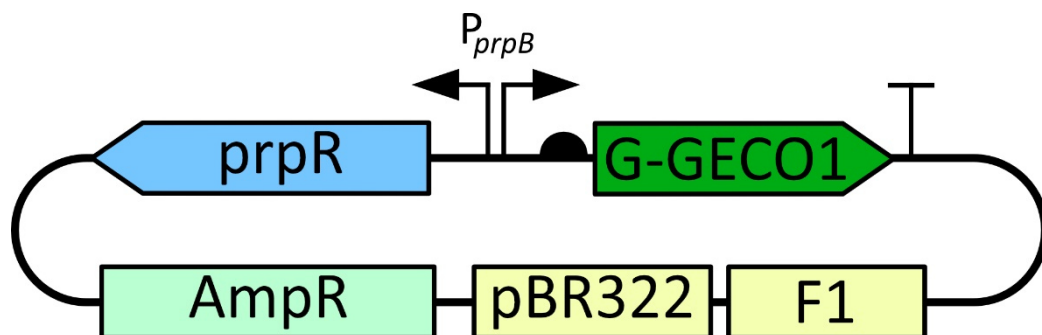


**Figure 14 Schematic overview of pPRO24 carrying the gene for G-GECO1.** The pPRO24 plasmid is controlled by the  $P_{prpB}$  promoter which is positively regulated by *prpR* in the presence of propionate. It carries an ampicillin resistance and is described as a high copy plasmid with its class A pBR322 and F1 ori.

The plasmid underlying the expression of nanopore is based on the pACYCT2 backbone (Ponchon et al., 2013). This plasmid carries the low copy class B ori p15A and a chloramphenicol resistance. To achieve tight control of nanopore expression, the original  $P_{tac}$  promoter and RBS site were swapped with different combinations of the isopropyl- $\beta$ -D-thiogalactopyranosid (IPTG) inducible T7 promoter ( $P_{T7}$ ) and different ribosome binding sequences (RBS) that varied in their expression strength. This promoter needs a T7 RNA polymerase to be active and is controlled by the LacI repressor which is also encoded on this

plasmid. It is crucial to prevent leakiness of the promoter/repressor system in order to maintain cell viability. For this purpose, the whole expression cassette was flanked by two terminators before the promoter and three terminators after the multiple cloning site (Mairhofer et al., 2015). Furthermore, the single mutation W220F was introduced into the *lacI* gene which leads to a tighter control and a better IPTG titration curve for the T7 promoter (Figure 15) (Gatti-Lafranconi et al., 2013). The plasmid was finally termed pCTRL2.

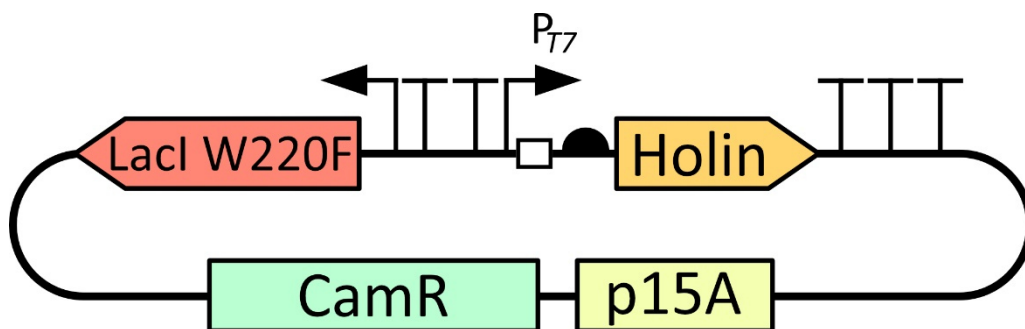


**Figure 15 Schematic overview of pCTRL2 carrying the gene for a holin.** The pCTRL2 plasmid is controlled by the  $P_{T7}$  promoter which is inhibited by the *LacI* repressor. It carries a chloramphenicol resistance and is described as a low copy plasmid with its class B p15A ori. Several terminators before and after the expression cassette were introduced together with a single mutation in the *lacI* gene to reduce leaky expression to a minimum.

In the next step, the expression strength of the newly designed plasmid pCTRL2 was tested. Three T7 promoter strengths were chosen from the literature and combined with three different RBS sequences which can be found in Table 2. The goal was to find the right combination which provides the best signal to noise ratio without interfering in colony growth, due to leaky expression. Detailed sequences of every combination can be found in the material and methods section. Three ribosome binding sites were chosen: a strong RBS and two RNA thermometer (RNAT) RBS variants. The RNAT RBS variants form temperature sensitive secondary structures in the 5' untranslated region of the mRNA and were considered to potentially have another regulating mechanism in addition to the inductor. Furthermore, the T7 expression cassette from the pET system was also used as a reference for strong expression.

**Table 2 Promoter and RBS systems used in this work.**

Promoter/RBS	Description	Reference
T7.03	Transcription efficiency on mRNA level is about 3% compared to the T7.100 promoter.	Imburgio et al., 2000
T7.14	Transcription efficiency on mRNA level is about 14% compared to the T7.100 promoter.	Imburgio et al., 2000
T7.100	Transcription efficiency was set to 100% as this is the most efficient consensus sequence.	Imburgio et al., 2000
sRBS	Strong ribosome binding site.	Elowitz & Leibler, 2000
U6	RNA thermometer, which is described to be fully active at 37°C.	Neupert et al., 2008
U9	RNA thermometer, which is described to be slightly active at 30°C and fully active at 37°C.	Neupert et al., 2008
T7.wt.sRBS	Expression cassette from the pET24(+) vector, which features a different spatial design.	Rosenberg et al., 1987; Studier et al., 1990

Expression tests were performed with the orange fluorescent protein mKO<sub>k</sub> (Figure 16) All possible combinations of the T7 promoter and RBS proved inferior to the classic expression cassette used in pET24 plasmids (T7.wt.sRBS). In addition, three of the combinations with the RNAT variants T7.03.U6, T7.14.U6, T7.14.U9 did not produce any detectable protein product in spectrophotometric measurements at all (Supplementary Figure 1). Although the T7.14 promoter is stated to be stronger compared to the T7.03 promoter as judged by mRNA transcripts levels (Imburgio et al., 2000), the fluorescent output of the T7.03.sRBS cassette is higher compared to the T7.14.sRBS variant. Nevertheless, for further comparisons the T7.03/14/100.sRBS and T7.wt.sRBS variants were chosen due to their grading strength which could be useful for potential different applications.

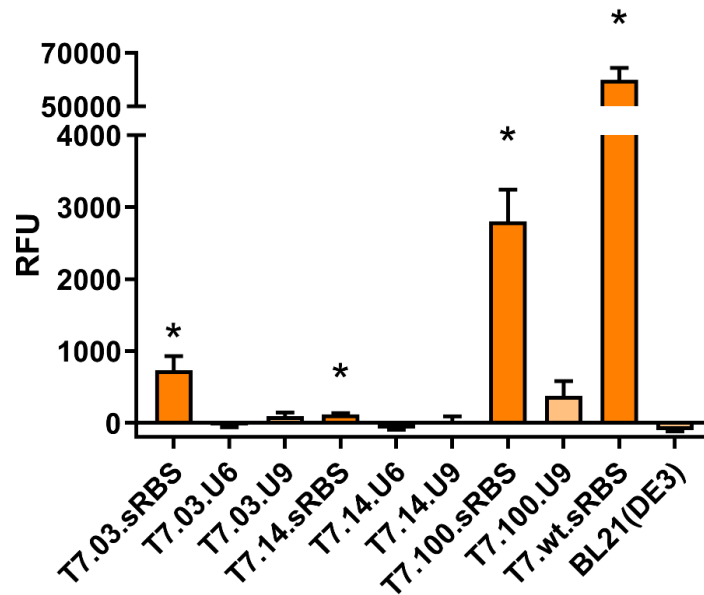


**Figure 16 Endpoint fluorescence measurements for different promoter and RBS combinations 200 min after induction.** Variants with the sRBS showed a favourable distribution in expression strength and were chosen for further experiments (dark orange, marked with an asterisk). Besides the T7.100.U9 and T7.03.U9 variant every other RNAT combination lacked detectable fluorescence comparable to the BL21(DE3) control without plasmid. Bar graphs represent mean values with SD indicated as error bars; n=3.

In the next step, the selected set of promoter strengths were evaluated in the context of the biosensor. Two colours for the genetically encoded Ca<sup>2+</sup> indicator for optical imaging were chosen (red - R-GECO1 and green - G-GECO1) and combined with one nanopore under each of the selected expression cassettes from Figure 17 (Supplementary Figure 2). For this purpose, four nanopores with different properties were used. This includes three different holins S<sup>2168</sup>, T4 and S<sup>105</sup> (Supplementary Figure 2) that were described as unselective pores (Ramanculov & Young, 2001a; Ryland Young, 2014) and the viral ion channel KcvNTS which is selective for K<sup>+</sup> (Thiel et al., 2011). In addition, the KcvNTS (composed of four subunits) and S<sup>2168</sup> (composed of seven subunits) pores are known to be small channels with defined pore size compared to S<sup>105</sup> and T4 that form large pores and induce cell lysis. This selection takes several properties of different pores into account and also provides a control to verify the assay conditions. The corresponding OD<sub>600nm</sub> growth curves can be found in the supplementary data (Supplementary Figure 3; Supplementary Figure 4)

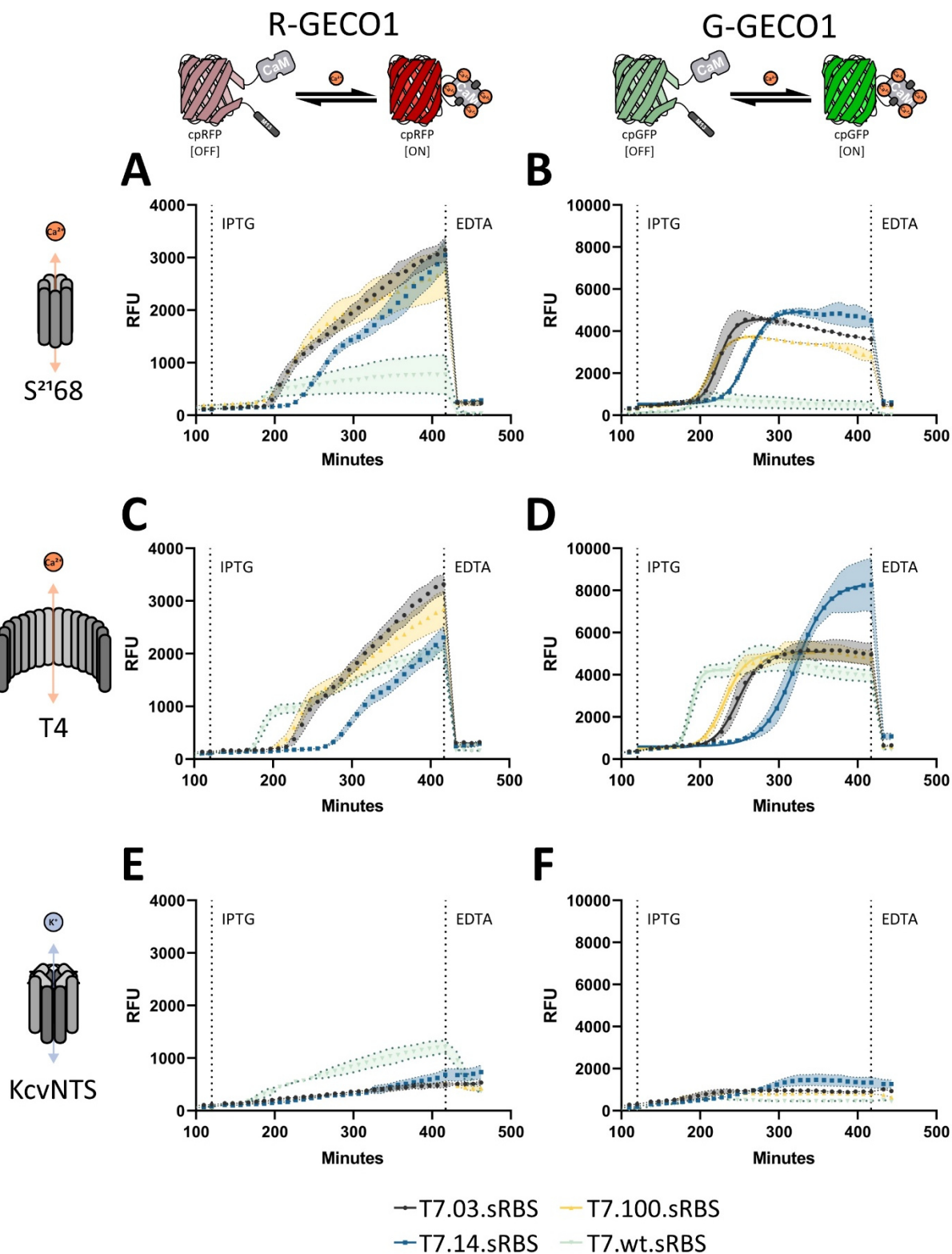


**Figure 17** Fluorescence measurement over time of the three pores  $S^{2168}$ , T4 and KcvNTS in combination with R-GECO1 or G-GECO1. Sensors were expressed for 113 minutes followed by nanopore induction marked by the IPTG line and EDTA addition to diminish the signal. **(A-B)** For  $S^{2168}$  the strongest promoter T7.wt.sRBS inhibits cell growth and leads to a weak signal in both R-GECO1 and G-GECO1 while the weakest promoter shows a late answer to induction. T7.03.sRBS, as well as T7.100.sRBS show a similar signal. **(C-D)** T4 holin expressions shows a more straightforward pattern, with T7.wt.sRBS as the strongest version, followed by T7.03.sRBS/T7.100.sRBS and a delayed pore formation for the T7.14.sRBS variant with a higher signal in the end with G-GECO1. **(E-F)** KcvNTS does not show a signal for any promoter strength with G-GECO1, but a slightly linear increase in fluorescence for the T7.wt.sRBS variant with R-GECO1. Data points represent mean values with SD indicated as error area; n=3. Legend at the bottom refers to all graphs.

First of all, the nanopores S<sup>2168</sup>, T4 and S<sup>105</sup> (**Figure 17 B, D; Supplementary Figure 2**) triggered distinct signal patterns depending on their expression strength while the negative control KcvNTS did not show a significant change in fluorescence due to its selectivity for K<sup>+</sup> ions. Furthermore, it is noteworthy that R-GECO1 triggers a different signal pattern (**Figure 17 A, C, E**) compared to G-GECO1 (**Figure 17 B, D, F**). The signal turned out weaker even though the spectrophotometer gain setting was higher. In addition, the curve itself has no distinct sigmoidal pattern like in the G-GECO1 measurements. This is presumably because R-GECO1 has a very slow maturation time which leads to a prolonged signal increase from newly formed active biosensor proteins. It is known that red fluorescent proteins often have higher maturation times or lack brightness and photostability compared with their green fluorescent equivalents (Eason et al., 2017). Advantages primarily concern fluorescent microscopy studies in deep tissue due to their longer excitation and emission wavelength. In the context of the FuN screen, these features are however not needed so the sensor of choice was G-GECO1.

The right promoter strength was decided by several factors, which had to be considered for further experiments. First of all, it is critical that leaky expression of the toxic nanopores is kept to a minimum to ensure sufficient colony growth when used in library experiments. At the same time, nanopores need to be expressed sufficiently fast to be detected within an adequately short time frame. This particularly applies to spectrophotometric measurements in microtiter plates where the growth medium containing the cells evaporates over time. Furthermore, the cells should have enough time to produce the biosensor before they die due to the nanopores. These preferences dismiss the strongest promoter T7.wt.sRBS and the weakest promoter T7.14.sRBS as they are either too leaky inhibiting growth or too weak leading to a delayed signal, respectively. Even though the two other remaining promoters T7.03.sRBS and T7.100.sRBS seem to produce a similar signal pattern in the FuN screen (**Figure 17**), they do show differences in overall protein production when tested with a fluorescent protein (**Figure 16**). For the FuN screen, T7.100.sRBS was chosen because of its low-to-medium strength which ensures a suitable amount of nanopore production without being overly toxic. Depending on the specific application, the protein expression may have to be tuned individually.

In the next step, an equation was used to fit and quantify the fluorescent signal curves generated by different nanopores. With this approach individual parameters from different nanopores can be compared in a quantitative fashion. Due to the sigmoidal shape of the following non-linear regression equation was used (**Equation 1**)

**Equation 1** Non-linear regression equation used to fit sigmoid curves.

$$f(x) = a + \frac{b}{1 + e^{\frac{-(x-c)}{d}}}$$

**Figure 18** shows a typical sigmoidal curve to demonstrate the fitting parameters. The values a and b define the bottom and top borders of the curve. C provides information about the inflection point and is defined as the half-time (in minutes) needed to reach the maximum value and d describes the steepness of the curve (in RFU\*minutes<sup>-1</sup>) with a larger value indicating a shallow curve. These parameters will be referred to as T<sub>1/2</sub> (c) and steepness (d). It is important to note that there was no normalization performed on the cell density, due to the partly lysing nature of some pores. This usually resulted in curves with false signal rise because of the quotient of a stable fluorescence signal and the decreasing absorption. Instead pores with known properties and curve shape were used as controls.

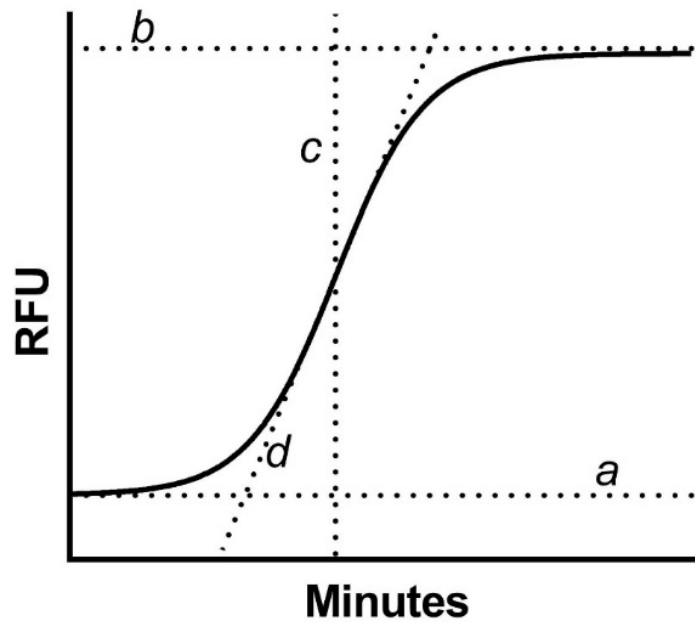


**Figure 18 Example sigmoidal curve for parameter explanation.** The sigmoidal curve was fitted with the **Equation 1**. The parameters *a* and *b* define the bottom and top border of the curve, while *c* marks the inflection point referred to as half-time and *d* describes the steepness of the curve, with a larger value indicating a shallow curve.

The last parameter to optimise assay conditions was the timing of induction. For the first experiments, the cells were diluted to an  $OD_{600nm}$  of 0.1 before the expression of the biosensor was induced for 110 min at 30°C followed by nanopore induction. At the time of 110 min, the cells had reached an  $OD_{600nm}$  of about  $\sim 0.4$  which is described to be in the optimal range of the T7 expression system (Angius et al., 2018; Studier, 1991). To test whether a delayed induction of the nanopore improves the signal, induction times were shifted every 30 minutes and the resulting signal and cell density were compared (Figure 19; Supplementary Figure 5).

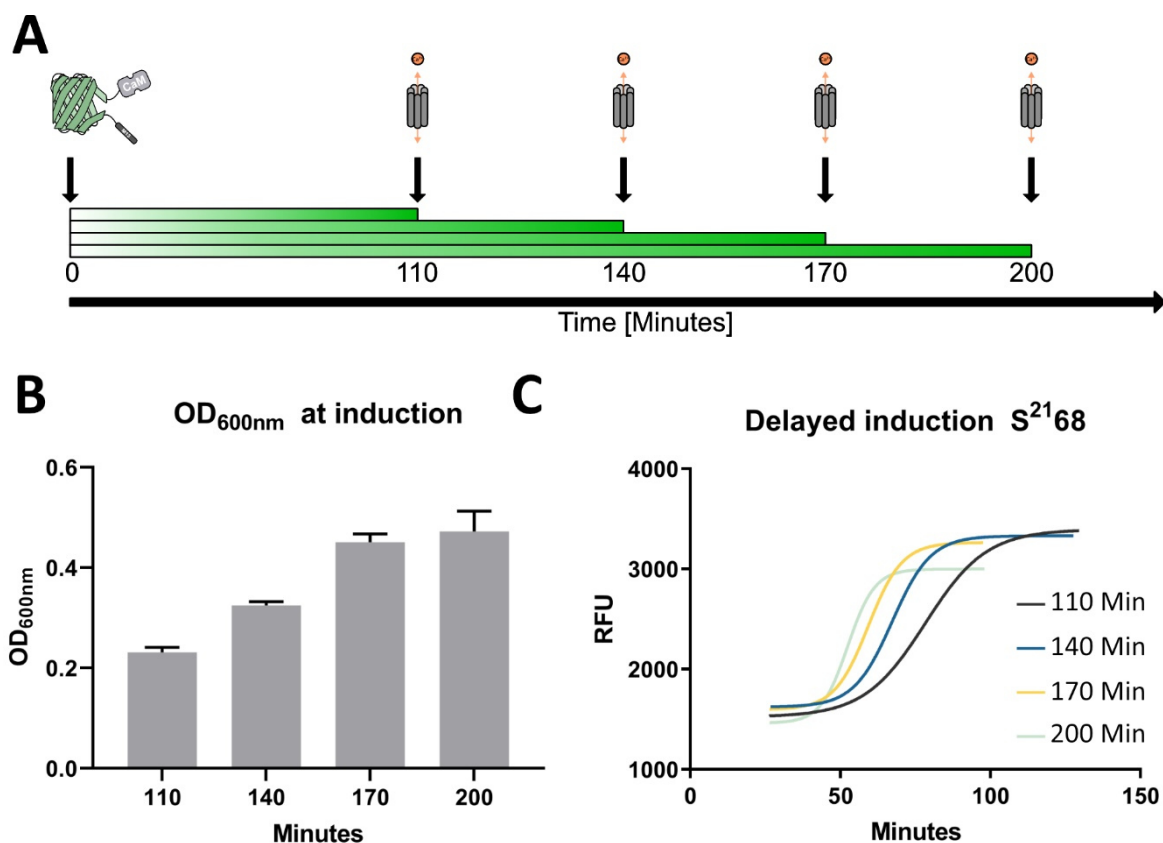


**Figure 19 Variation of induction times leads to different signal patterns.** (A) Schematic illustration of the shifted pore induction timepoints. G-GECO1 was induced at an  $OD_{600nm}$  of 0.1 and the subsequent nanopore induction was done at 110, 140, 170 or 200 minutes. (B) The  $OD_{600nm}$  at the nanopore induction varied from 0.2 to 0.5. This number has to be multiplied by  $\sim 2$  to get the corresponding  $OD_{600nm}$  from UV-vis measurements in cuvettes. (C) Fluorescence measurements over time from different starting points were plotted by setting the induction point to 0 minutes and comparing the signal after induction. The maximum signal does not change, but the kinetics of the sigmoidal curves vary. The later the nanopore is induced the faster the signal rises. Graph bars represent mean values with SD indicated as error bars;  $n=3$ . Error bars missing in (C) for better visibility.

Varying the timing of induction demonstrated some interesting behaviour. First of all, the maximum fluorescence for  $S^{2168}$  does not change too much which is generally favourable. It seems that the early induction of the biosensor combined with cells in their lag to logarithmic growth phase do not produce significantly different amounts of sensor (Figure 19 B, C). Nevertheless, the sigmoidal curve kinetics show a large variation depending on induction timing. Cells induced 200 minutes after biosensor expression show an early reaction with a steeper curve compared to cells that were induced at 110 minutes. The later the cells were induced, the earlier the signal rose. This seems to diminish small differences in the kinetics of different nanopores and therefore decreases the overall dynamic range (Supplementary Figure 5). In addition, a cell density of  $OD_{600nm}$  0.4 is preferred for induction. Therefore, all following FuN screen assays were performed at 110 minutes for nanopore induction if not stated otherwise.

---

## FuN Screen: A Method to Investigate Pore Function and Behaviour

After parameters and assay conditions were optimised, the FuN screen was applied to characterise individual nanopores. A variety of pores were chosen to demonstrate the general utility of the assay and the measuring time between two cycles was reduced from 10 minutes to 3 minutes to increase the resolution.

The first category are small defined nanopores with S<sup>2168</sup> as its representative. This pinholin forms heptameric pores with an opening of about 2 nm for ion release and subsequent membrane depolarization (Ry Young, 2013). It is predicted that the TMD1 flips over the lipid bilayer to form stable pores, but the domain is not mandatory for pore formation. Furthermore, the antiholin S<sup>2171</sup> and the mutated S<sup>2171</sup>-M4A which lacks the second reading frame were tested with this assay (**Figure 20 A**). A rather special variant used in this work was the <sup>SGS-ΔTMD1</sup>-S<sup>2168</sup> and its counterpart <sup>TVMV-ΔTMD1</sup>-S<sup>2168</sup> (**Figure 20 E**). Both are truncated versions of S<sup>2168</sup> with only the second TMD left and the additional N-terminal amino acid sequence S-GS (GS is the linker sequence) or the TVMV protease recognition sequence SSSGGS-ETVRFO/S-GS (SSSGGS and GS are linker sequences) (Nallamsetty et al., 2004). These candidates were used in experiments for posttranslational activation of nanopores by proteolytic cleavage at an N-terminal recognition site. The idea behind this was to express unfunctional nanopores that can be easily activated at a defined time point. Unfortunately, the TVMV protease was not able to cleave its recognition site probably due to its inaccessibility (Data not shown). Nevertheless, these pores served as a positive/negative control that are either capable (<sup>SGS-ΔTMD1</sup>-S<sup>2168</sup>) or incapable (<sup>TVMV-ΔTMD1</sup>-S<sup>2168</sup>) of cell perforation.

The second category are nanopores which form undefined large pores for cargo release like the S<sup>105</sup> holin (C. Y. Chang et al., 1995) and T4 holin (Ramanculov & Young, 2001a) or are used by the persister-cells to induce a dormant state by dropping the PMF and ATP level in the case of HokB (Wilmaerts et al., 2018) and TisB (Gurnev et al., 2012 (**Figure 20 B, C**)). It is predicted that some pores are capable of cell lysis as they are sufficiently large to collapse the cellular integrity (Ramanculov & Young, 2001a).

All negative controls used in this work were grouped in the last category (**Figure 20 D**). Two different pore systems known to be selective for ions other than Ca<sup>2+</sup> were chosen. KcvNTS is a small viral K<sup>+</sup> selective channel with a high open probability (Thiel et al., 2011) and BM2 is a viral proton porter (Mandala et al., 2020). In addition, the expression strain BL21(DE3) carrying only the plasmid for the G-GECO1 sensor was also considered, as it lacks the plasmid for toxic nanopore expression.

It is important to note that the overall fluorescence decreased in this assay as the fluorescent signal was measured every 3 minutes which causes greater bleaching of the G-GECO1 fluorophore compared to the 10 minutes cycle from **Figure 17**. However, the resolution of the assay increased which becomes even more important for extremely fast forming nanopores used in later experiments.

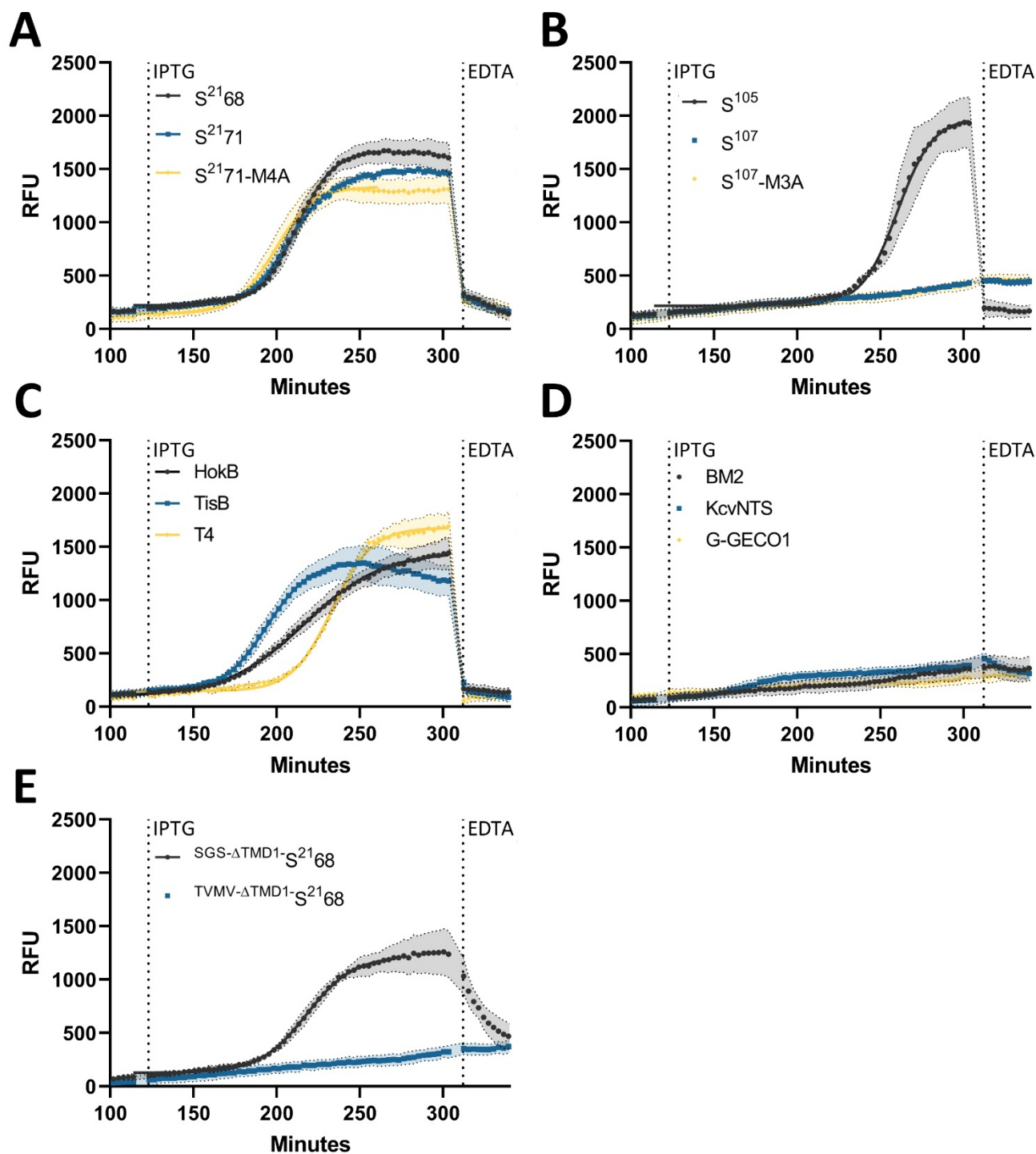


**Figure 20** FuN screen verification with a variety of different nanopores. Sensors were expressed for 113 minutes followed by nanopore induction marked by the IPTG line and EDTA addition at 312 minutes to diminish the signal. (A) Pinholin measurements with  $S^{2168}$ , the antiholin  $S^{2171}$  and  $S^{2171}$ -M4A show nearly no difference in signal increase, while (B) the canonical  $S^{105}$  holin is the only active variant compared to its antiholin variants  $S^{107}$  and  $S^{107}$ -M3A. (C). The T4 Holin has a steep but delayed signal pattern and from the persistence inducing pores TisB has a faster and steeper signal increase then HokB (D) All controls which are not able to transport  $Ca^{2+}$  over the membrane like BM2 and KcvNTS do not show any signal similar to the BL21(DE3) cells producing only the G-GECO1 sensor. (E) The truncated variant  $SGS-\Delta TMD1-S^{2168}$  has a slightly different signal compared to  $S^{2168}$  and is the only variant showing a prolonged signal decrease after EDTA addition.  $TVMV-\Delta TMD1-S^{2168}$  does not induce pore formation. Data points represent mean values with SD indicated as error area;  $n=3$ .

---

The FuN screen test with different nanopores was successful as it clearly demonstrated a signal increase in combination with pore induction, but also gave rise of distinct fluorescent signals based on the properties of individual nanopores. For example, S<sup>2168</sup> is known to have an antiholin in the natural system which is able to delay pore formation with its N-terminal charged residue Lys. Nevertheless, the TMD1 is not essential for pore formation (T. Pang et al., 2009). The FuN screen shows that the S<sup>2168</sup>, S<sup>2171</sup> and the S<sup>2171</sup>-M4A pinholins have a similar signal output, with S<sup>2171</sup>-M4A being a little bit faster due to its better ability to grow (**Figure 20 A**; **Supplementary Figure 6**). Even the truncated variant <sup>SGS-</sup> $\Delta$ TMD1-S<sup>2168</sup> has a similar, but slightly slower fluorescence increase compared to the wildtype S<sup>2168</sup> (**Figure 20 A, E**). The fact that the addition of EDTA does not immediately quench the fluorescent signal but required about 30 minutes suggests that pores formed by this variant are transient and not stable. TMD1 is predicted to be a stabilizing anchor which floats on the membrane and prevents pore disruption (Ahammad et al., 2019, 2020; Drew et al., 2019). Furthermore, the OD<sub>600nm</sub> does not decrease after induction, but remains stable over a long period suggesting that cells maintain their integrity which makes them favourable for applications like fluorescent activated cell sorting (FACS) (**Supplementary Figure 6**). However, pore formation can be blocked by introducing additional amino acids possibly rendering the N-terminus impassable through the membrane as seen with <sup>TVMV-</sup> $\Delta$ TMD1-S<sup>2168</sup>. Due to the fact that S<sup>2168</sup> is one of the best described peptide nanopores with intriguing mechanisms of pore formation and retention, it is the main subject in the following chapters. In particular, it is used to demonstrate the capacity of the FuN screen across different assay formats and in library selection experiments.

The other category of nanopores used in this assay were holins which are known to form large undefined pores. S<sup>105</sup> was one of the first canonical holins described in the literature which consists out of three TMDs (Raab et al., 1986). In contrast to the previously mentioned pinholin S<sup>2168</sup>, the TMD1 in S<sup>105</sup> plays a crucial role in nanopore formation. Only if this TMD1 enters the periplasm, pore formation can be induced (White et al., 2010). This behaviour can be observed in the FuN screen with S<sup>105</sup> being active after induction while the antiholin S<sup>107</sup> and S<sup>107</sup>-M3A do not show any signal increase (**Figure 20 B**). A similar pattern can be seen for the class III holin T4 which also seems to form large pores (**Figure 20 C**). In contrast to the S<sup>105</sup> holin, T4 has only one TMD and is predicted to insert via its C-terminal tail into the membrane while the N-terminus is located in the cytoplasm. Both S<sup>105</sup> and T4 holin seem to lyse the cells rapidly after pore formation due to their extreme large pores up to 1  $\mu$ m, which is nearly half of the cell size of *E. coli* (**Supplementary Figure 6**) (To & Young, 2014).

The persistence inducing nanopores HokB and TisB fulfil function in a similar fashion as mediators of persistence in toxin-antitoxin (TA) modules. Pore formation of these peptides usually leads to a drop in the PMF and ATP levels. Moreover, TisB is described to be anion selective at mild expression conditions (Gurnev et al., 2012). In this screen, TisB does not show anion selectivity and has the fastest signal increase compared to the other nanopores while the HokB signal is slower and the curve has a rather shallow steepness (**Figure 20 C**).

A screening system is only as good as its negative controls, therefore the two pore systems BM2 and KcvNTS were compared together with cells lacking a plasmid for pore induction. BM2 pores are natural proton porters (Mandala et al., 2020) and the channel KcvNTS is a K<sup>+</sup> selective ion channel (Thiel et al., 2011). All three variants did not show any signal increase upon induction (**Figure 20 D**). Judging by the growth curves, it can be seen that the OD<sub>600nm</sub> of cells transformed with the T7.100.sRBS plasmid with KcvNTS plateaued after induction, but not with BM2 (**Supplementary Figure 6**). The promoter strength has to be higher for BM2 to be able to kill the cells properly as demonstrated with the T7.wt.sRBS promoter (**Supplementary Figure 2**; **Supplementary Figure 4**). This demonstrates that the promoter strength in this artificial system needs to be optimized depending on the identity of the nanopore.

The following table summarizes the pore forming propensities of individual pores in terms of  $T_{1/2}$  and steepness (**Table 3**). Lower  $T_{1/2}$  and steepness values represent fast nanopore formation with a steep signal increase. Higher  $T_{1/2}$  and steepness values indicate slow nanopore formation with a shallow curve.

**Table 3**  $T_{1/2}$  and steepness values from the fitted curves from **Figure 20**. Data points represent mean values with  $\pm$ SD; n=3.

Nanopore	$T_{1/2}$	Steepness
S <sup>2168</sup>	212 $\pm$ 0.4	11.19 $\pm$ 0.35
S <sup>2171</sup>	208.4 $\pm$ 0.4	13 $\pm$ 0.37
S <sup>2171</sup> -M4A	198.9 $\pm$ 0.67	11.52 $\pm$ 0.61
SGS- $\Delta$ TMD1-S <sup>2168</sup>	217.9 $\pm$ 0.59	14.12 $\pm$ 0.52
S <sup>105</sup>	260.2 $\pm$ 0.73	10.68 $\pm$ 0.59
HokB	216.6 $\pm$ 0.85	23.65 $\pm$ 0.88
TisB	194 $\pm$ 0.69	12.82 $\pm$ 0.64
T4	233.3 $\pm$ 0.43	11.99 $\pm$ 0.38

Overall, this system showed a significant response to different nanopores and seems to be suitable for screening pores to penetrate the *E. coli* inner membrane. Some of the measured pores showed extreme lysis capability as judged by OD<sub>600nm</sub> values (S<sup>105</sup>, T4, HokB) while others kept cellular integrity intact (**Supplementary Figure 6**). Lysis systems are well known in the literature and are used in auto-lysis cassettes. These cassettes usually feature a holin, an endolysin and a spanin to coordinate cell lysis. (Cárcel-Márquez et al., 2019). While the FuN screen uses only the pores, the mechanical stress induced by rapid orbital culture shaking can be sufficient to disrupt the cells for certain variants. A systematic test was performed to compare the capacity of individual pores to lyse cells, by analysing the total fluorescence in the supernatant and the cell pellet three hours after induction (**Figure 21**).

The results clearly show that only S<sup>105</sup>, T4 and HokB featured fluorescence in the supernatant which generally correlated with decreasing absorption measurements following induction of the nanopore. Moreover, the graph demonstrates that G-GECO1 on its own and nanopores that are not permeable to Ca<sup>2+</sup> (TVMV- $\Delta$ TMD1-S<sup>2168</sup>, BM2, KcvNTS, S<sup>107</sup>-M3A) only have a weak fluorescence signal overall. On the other hand, S<sup>107</sup> has a very high fluorescence even though it did not show an increase in the spectrophotometer measurements 200 minutes after induction (**Figure 20 B**). However, prolonged measurements of S<sup>107</sup> for up to 600 minutes showed that this antiholin has an extremely delayed signal increase (**Supplementary Figure 7**). In addition, shear forces generated by pipetting can destabilise cells and seem to be sufficient to break the fragile membrane resulting in a stronger signal compared to other variants.

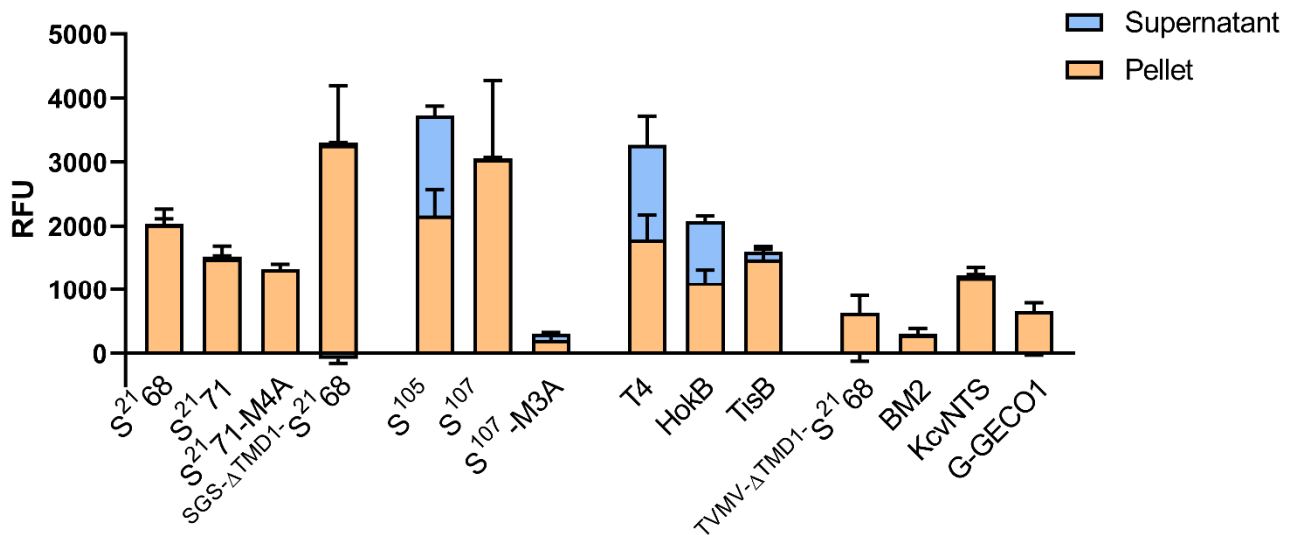


**Figure 21 Total fluorescence measurements of the supernatant and the cell pellet 3 hours after nanopore induction.** The nanopores S<sup>105</sup>, T4 and HokB which indicate cell lysis in OD<sub>600nm</sub> measurements show a distinct fluorescence signal in the supernatant. Negative controls, as well as all other nanopores either do show a weak signal or retain the fluorescence in the cell pellet. Data points represent mean values with SD indicated as error bars; n=3.

## Truncation Analysis of S<sup>21</sup>68

Once the assay was verified with different nanopores, the system was used to dissect the genetic features that underlie the formation of the S<sup>21</sup>68 pore in greater detail. S<sup>21</sup>68 is a unique holin and interesting in many ways. As previously described, it forms pores independent of its TMD1 which has been primarily suggested to stabilize the pore and retain the heptameric structure. The externalization of the TMD1 is therefore an important step towards the formation of stable nanopore (Ahammad et al., 2019; T. Pang et al., 2010a). One way to study the role of the TMD1 and its single amino acid (AA) functions is to truncate the sequence and compare the resulting pore formation kinetics. The truncation was performed in increments of two amino acids starting with residue 68 and ending with 38 (**Figure 22 A**). It is important to note that the first Met from S<sup>21</sup>68 was included in the numbered count while for all following truncations the additional Met was not. All new variants were compared relative to the wildtype S<sup>21</sup>68 and S<sup>21</sup>71 variants as well as the S<sup>21</sup>71-M4A mutation (**Figure 22 B**). Representative curves of selected variants are shown in **Figure 22 C, D**. All remaining curves can be found in **Supplementary Figure 8** and **Supplementary Figure 9**.

The truncation experiments once again demonstrated the high resolution of the FuN screen and provided more detailed information about the role of the TMD1. While the truncation of the Asp from S<sup>21</sup>68 to S<sup>21</sup>66 did not change the signal output, the deletion of Lys and Ile to S<sup>21</sup>64 caused a large functional shift towards a faster and steeper response (**Figure 22**). This signal output is sustained for all variants from S<sup>21</sup>64 to S<sup>21</sup>48 and the curves seem to be nearly identical (**Supplementary Figure 8**). Interestingly, there is another transition point beginning with S<sup>21</sup>48 from which the signal starts to become slower again (**Figure 22 A; Supplementary Figure 8**).

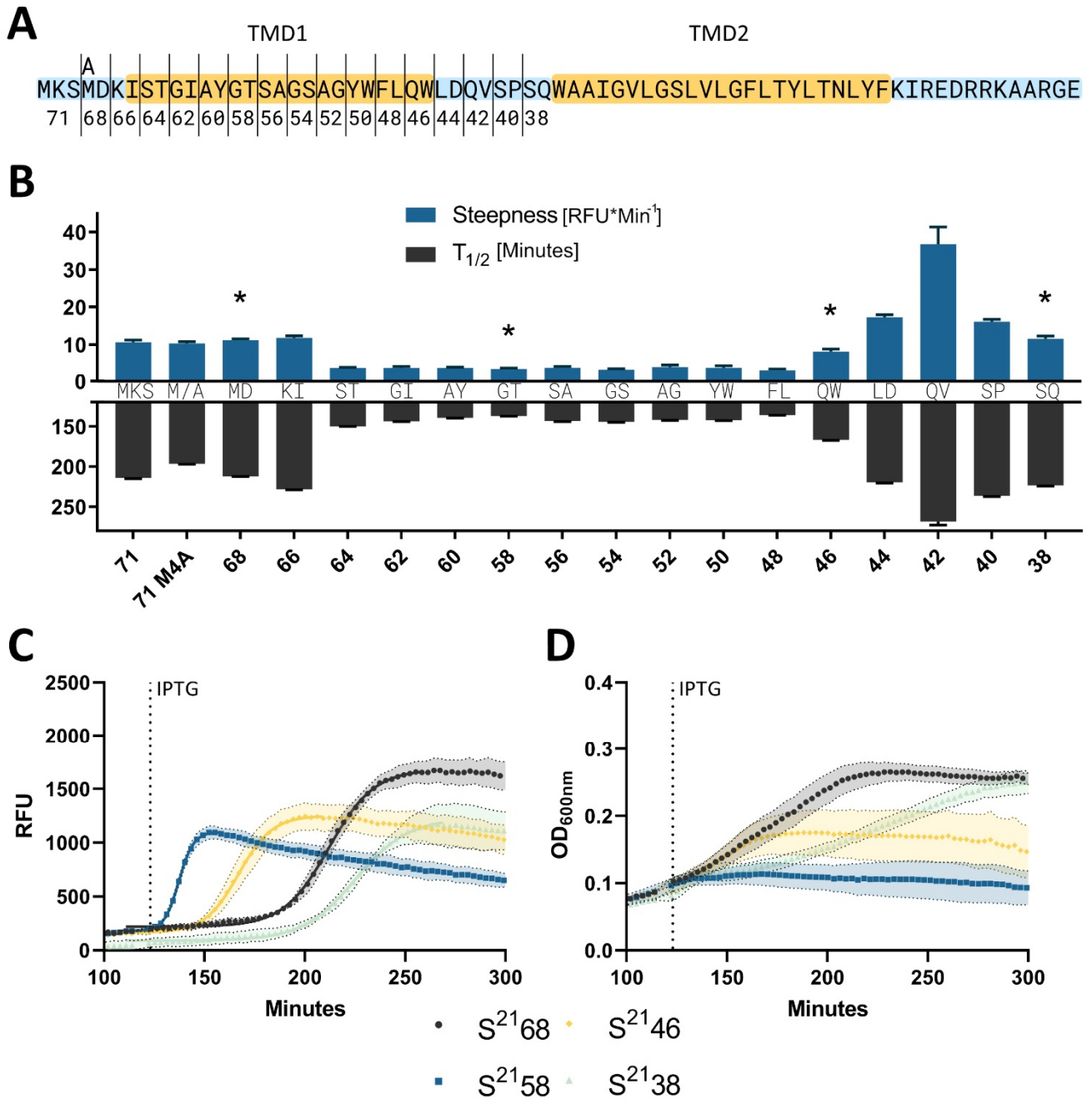


**Figure 22 Truncation experiments of the first transmembrane domain of S<sup>21</sup>68.** (A) Amino acid sequence of S<sup>21</sup>68 with the denoted truncation sites. (B) Steepness and T<sub>1/2</sub> measurements of the truncated variants reveal two transition points, one between S<sup>21</sup>66 and S<sup>21</sup>64 to a faster and steeper signal increase and one between S<sup>21</sup>48 and S<sup>21</sup>46 where the signal rise gets slower again. The variant S<sup>21</sup>42 had extremely delayed pore forming activity. (C) Representative curves of the variants marked with an asterisk in (B) show the detailed kinetic of pore formation and (D) the stagnating absorption measurements confirm that strong variants like S<sup>21</sup>58 lead to a fast cell death compared to slow variants like S<sup>21</sup>38. Bar graphs and data points represent mean values with SD indicated as error area or bars; n=3. Legend at the bottom refers to all graphs from (C) and (D).

To rationalise these results, the screening data was compared to the distribution of amino acids in transmembrane proteins which critically contribute to their structural integrity. Notably, database analysis of transmembrane proteins from a variety of genomes revealed global trends that can be used to rationalise the behaviour of individual mutants in this screen. In one example, Mbaye *et al.* investigated the frequency of aliphatic, aromatic, polar and charged amino acids in different regions of the membrane bilayer (Figure 23) (Mbaye *et al.*, 2019). To this end, the membrane was roughly divided into the two interfacial regions defined by the phospholipid head groups, the hydrophobic core as well

as the aqueous region outside of the bilayer (**Figure 23 A**) (Sharpe et al., 2010). Notably, a systematic bioinformatic analysis demonstrated that distinct regions in a transmembrane protein are usually occupied with distinct amino acids depending on the membrane region they form contact with. The hydrophobic core contains mostly aliphatic residues while the aqueous region around the lipid bilayer contains polar and charged residues. In contrast, aromatic amino acids on the other hand seem to accumulate mostly in the interfacial region (**Figure 23 B**).

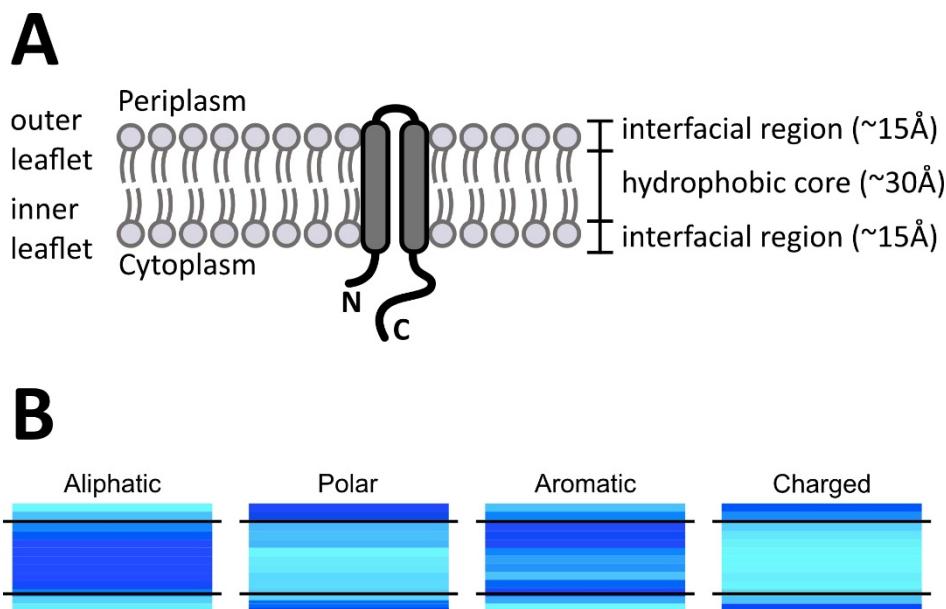


**Figure 23** Schematic illustration of the different lipid bilayer regions and the amino acids groups occurrence in those areas. (A) The membrane has a hydrophobic core flanked by two interfacial regions separating the bilayer from the aqueous solution. The two transmembrane domains from the S<sup>2168</sup> pinholin remain in the membrane in their inactive form. (B) Frequencies of the different amino acid groups in the bilayer. Dark blue indicates higher frequencies and lighter blue lower frequencies. Adapted from Mbaye et al., 2019.

S<sup>2168</sup> seems to maintain most of the rules stated for single amino acids in small multi-pass transmembrane proteins. It has a charged N- and C-tail, a polar loop between the two TMDs and mostly aliphatic amino acids in the core as well as aromatic residues near the interfacial region (**Figure 22 A**; **Figure 23 A**). According to literature, this peptide accumulates as inactive dimers in the membrane with intramolecular TMD1-TMD2 interactions as long as both helices remain in the membrane. Whenever TMD1 exits the membrane into the periplasm, intermolecular association between several TMD2 begins to dominate and are accelerated by interactions of TMD1 on the periplasmic site (T. Pang et al., 2010a). N-terminal truncation disturbs the classic interactions and leads to new forms of pore behaviour. The first truncation to S<sup>2166</sup> does not considerably change the kinetics of pore formation as the Lys maintains contact with the membrane. But as soon as all charged residues are removed and only the TMD1 residues remain (S<sup>2164</sup> to S<sup>2148</sup>) the rate at which pores form immediately accelerates (**Figure 22 B**; **Supplementary Figure 8**). It seems that the barrier for the flipping mechanism of the TMD1 is based on charged residues. Starting from S<sup>2146</sup>, the pore forming activity decelerates again and even yields a variant like the S<sup>2142</sup> which seems to have a very poor pore forming ability.

There can be several reasons for this phenomenon. On the one hand side, the polar amino acids from the connecting loop between TMD1 and TMD2 form a new barrier when exposed after truncation. On the other hand, pore formation itself may slow down due to the missing stabilization of TMD1 and the peptides float on or in the membrane with only short association timings. Therefore, the peptide concentration becomes the new limiting factor for nanopore formation. In both theories the N-end rule could also affect the rate of pore formation as exposure of distinct N-terminal amino acids may cause degradation of the pore forming peptides by the proteasome. For instance, amino acids like Arg, Lys, Phe, Leu, Trp and Tyr have a very short half-life of about two minutes and are degraded very fast when they are not buried in the membrane (Varshavsky, 1997). In addition, bacterial proteins are usually expressed with an N-terminal formyl-methionine which is removed more efficiently when the second

---

amino acid is small and uncharged like Ala but inefficient for bulky and charged amino acids like Arg (Hirel et al., 1989).

### In Vitro Bilayer Measurements of Selected Variants

To investigate specific pore forming abilities by a complementary technique, ultra-high-resolution *in vitro* bilayer measurements were performed. To ensure maximum purity and full-length peptides, chemically synthesized holin peptides were used. Representative variants were chosen beginning with the full length S<sup>2168</sup>, the fast variant S<sup>2158</sup> and the slow pore forming S<sup>2138</sup> (**Figure 24**). The *in vitro* bilayer measurements provided great detailed insight into the pore forming abilities of the different variants.

Full length S<sup>2168</sup> was difficult to assay as the addition of the right amount of peptide was crucial. This means, there was an optimum between too much peptide (bilayer breaks) and not enough peptide (no signal). In addition, and this applies to all variants, the signal generally disappeared over time but could be re-established by further peptide addition. The traces after signal appearance were generally unstable, especially compared to ion channel measurements. This is hardly surprising given the transient nature of these nanopores. Nevertheless, S<sup>2168</sup> did show some distinct signals, especially in the positive voltage range while at negative voltages, the current was rather low and around 0 to -10 pA (**Figure 24 A, B**). It seems that at -100 mV single peptides from the predicted heptameric structure fluctuate in and out of the pore and +100 mV leads to a more stable pore formation with distinct states.

In contrast, the truncated S<sup>2158</sup> variant on the other hand that displayed a fast and steep increase in the fluorescent signal in the FuN screen showed an extremely broad pattern in the current output (**Figure 24 C, D**). Notably, the S<sup>2158</sup> variant tended to insert more easily into the bilayer and it was impossible to detect single pore events. As soon as pores formed, the signal always displayed an offset usually known from leaky bilayers or punctured Teflon foils. Moreover, the histogram shows that at -100 mV several spikes of conductance states exist. In contrast, at +100 mV there is only one prominent spike at around ~14 pA.

The last variant S<sup>2138</sup> was the most peculiar one. First of all, it had to be diluted up to 1:1000 due to its severe tendency to insert into the bilayer. Yet, it showed no real stable pore like behaviour, but more of a random puncturing antimicrobial peptide pattern (**Figure 24 E, F**). It did not show reasonable current flow at +100 mV and a very transient pore formation with very short states at -100 mV.

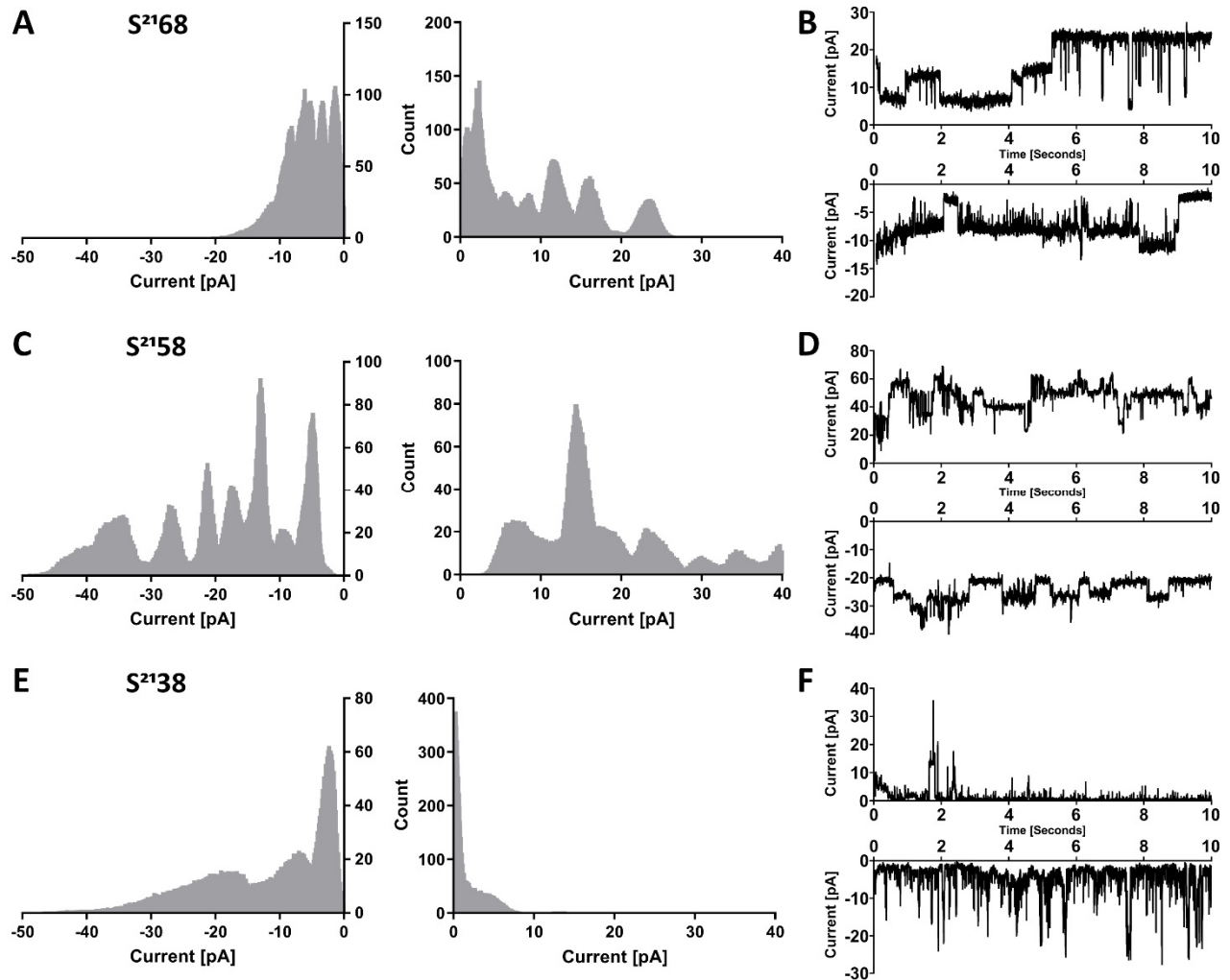


**Figure 24 Lipid bilayer measurements with selected and chemically synthesized variants.** (A) Histogram count of the current measurements and (B) representative I/V data of S<sup>2168</sup> reveals stable states at +100 mV and an overall low conductance at -100 mV. (C) The S<sup>2158</sup> histogram and (D) bilayer tracks show the various unstable but partly high conductance states this variant displayed. (E) S<sup>2138</sup> count histogram of the current states and (F) bilayer tracks demonstrate the unstable pore formation at -100 mV and only a transient one at +100 mV. Histograms calculated from three different experiments with at least six measurements (voltage protocol -100 mV to +100 mV vice versa for 10 seconds) per experiment.

With the results from the FuN screen (Figure 22) and the *in vitro* bilayer measurements from selected variants (Figure 24), a number of conclusions can be drawn. First of all, S<sup>2168</sup> forms a transient pore. Even though this pinholin is able to remain for a certain period in a defined state it still transitions fluently. One has to keep in mind that the bilayer system is artificial and the lipid composition is not the same as in natural *E. coli* membranes. The truncation of the first few amino acids to S<sup>2158</sup> led to a large shift in the FuN screen towards a faster kinetic which could also be demonstrated in the bilayer recordings. Removal of charged residues from the N-terminus rendered membrane insertion easier and the signal showed a large distribution with opening states nearly twice as large as the one for S<sup>2168</sup> (Figure 24 A, C). Nanopore formation in this variant does not seem to have any control mechanism as it fluctuates between several conductance states. Interestingly, every truncation variant inside of the TMD1 does show a similar signal pattern in the FuN screen which changes rapidly with the variants S<sup>2146</sup> and S<sup>2144</sup> (Figure 24 B; Supplementary Figure 8). This means, as soon as the last few hydrophobic amino acids are removed and the first polar residues are exposed, the ability to form pores is rapidly abolished. In addition, pore forming peptides underlie different kinds of pore forming scenario theories (Figure 25) (Brogden, 2005).

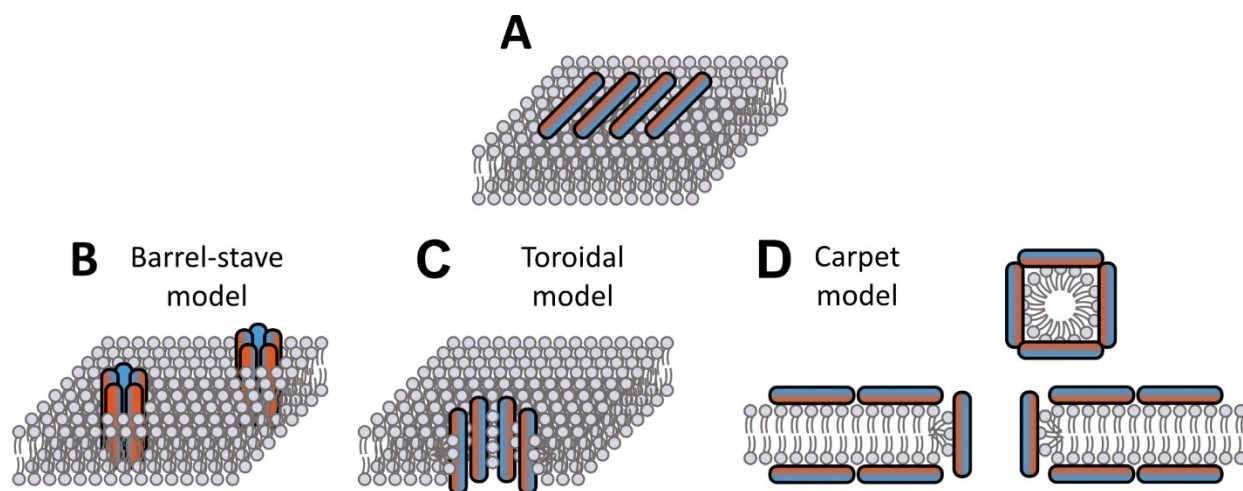


**Figure 25 Schematic illustration of the different antimicrobial peptide pore forming models.** Blue represents the hydrophilic and red the hydrophobic surface (A) Peptides usually float on the membrane and statistically insert into the bilayer. (B) In the barrel-stave model, peptides aggregate into the membrane so that the hydrophobic regions align outside and the hydrophilic regions align inside the pore. (C) The toroidal model stands for attached peptides that aggregate and bend the lipid bilayer, so that the water core consists of the peptides and the headgroups of the lipid. (D) In the carpet model peptides disrupt the membrane by orienting parallel to the surface of the bilayer and forming a carpet like layer, where sometimes a patch of the membrane gets isolated leading to perforation. Adapted from Brogden, 2005.

According to these models, S<sup>2168</sup> and S<sup>2158</sup> form barrel-stave pores while S<sup>2138</sup> behaves more like the toroidal model with its spiky current traces. It is also difficult to explain single variants and their behaviour right out of the FuN screen, such as the very slow S<sup>2142</sup> variant. It could be that the additional Trp from S<sup>2146</sup> is essential for transition as it is known to enable fast bilayer penetration (W. Zhang et al., 2006). But also, the Asp demonstrated in the S<sup>2144</sup> variant seems to be important and could be a part of the negative-not-inside/negative-outside rule which suggest that negative residues are more likely to occur on the periplasmic site and therefore seem to be able to penetrate the lipid bilayer (Baker et al., 2017; Killian & von Heijne, 2000).

Due to the novelty of this assay, changes in the two parameters  $T_{1/2}$  and steepness and their direct linkage to pore activity needs to be examined with care. Nevertheless, the combination of the newly invented FuN screen and the validation through the established *in vitro* bilayer system demonstrate the capability of the screen to study pore behaviour *in vivo*.

### Examination of the Charged N-Terminus of S<sup>2168</sup>

The truncation experiments revealed that the charged N-terminus of S<sup>2168</sup> with its Asp and Lys critically affects pore formation rate. Previous studies suggest that negatively charged residues occur in the periplasm while positive charges remain in the cytoplasm (Baker et al., 2017; von Heijne, 1986, 1989). To test this hypothesis in the context of S<sup>2168</sup> pinholin, the two amino acids Asp and Lys were exchanged individually with every other amino acid except Met and Cys. The latter two amino acids were excluded to prevent the initiation of translation from an alternative start codon and the formation of disulfide bonds, respectively. Changes in pore formation timing and steepness were compared to S<sup>2168</sup> as a control and plotted in a heatmap where blue means slower and orange means faster pore formation relative to the control (Figure 26).

Mutations of the Asp mostly led to slower or similar pore formation except for the two aliphatic amino acids Ile and Leu as well as the aromatic residue Phe (Figure 26 A). It seems that these three hydrophobic amino acids are able to diminish the retarding effect of the following Lys and allow a faster TMD1 transition over the membrane.

The mutation of Lys on the other hand accelerated pore formation for nearly every amino acid except for the positively charged Arg (Figure 26 A). Arg is usually enriched at the lipid-water interface and

presumably stabilizes proteins. This is also known as snorkel-like behaviour (Saha et al., 2017). These results clearly indicate the important role of Lys for the exact timing of pore formation which is required in the context of the bacteriophage lysis system and it also shows that it cannot simply be exchanged with the bulky structured and positively charged amino acid Arg.

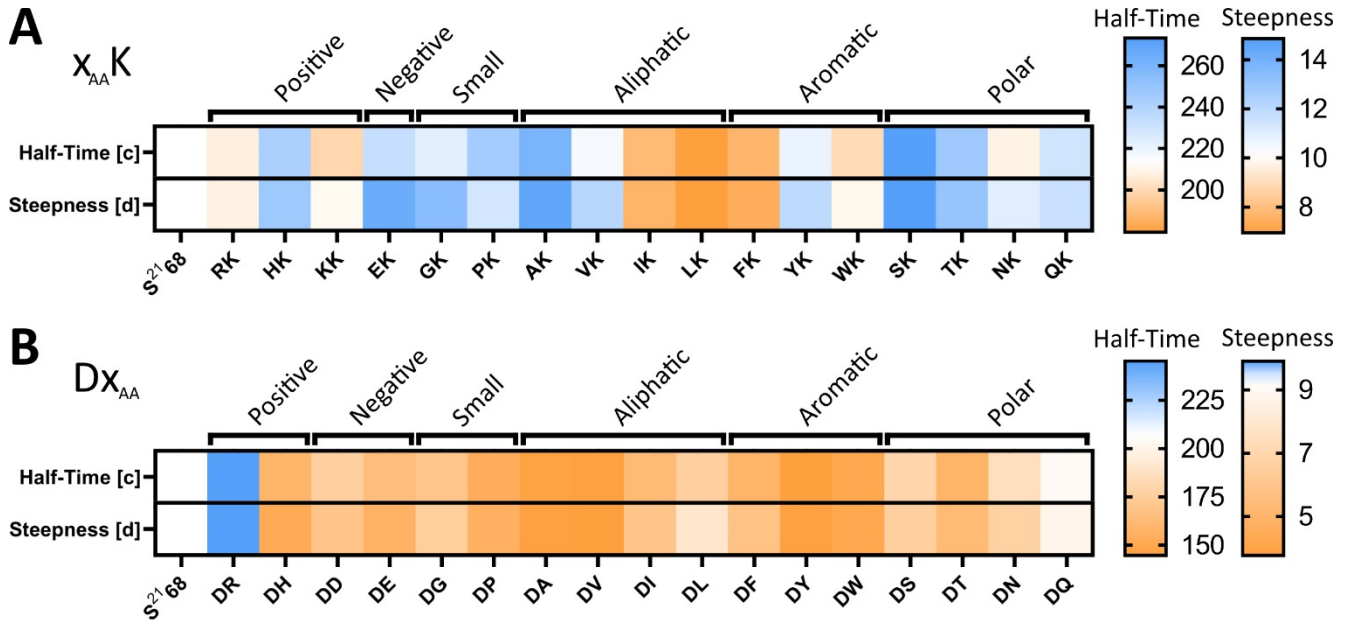


**Figure 26 Individual mutations of the two N-terminal amino acids Asp and Lys.** (A) Exchange of Asp to Ile, Leu and Phe led to faster pore formation compared to other mutations which either have slower timings or remain similar. (B) The mutations of Lys to any other amino acid except Arg leads to a large acceleration of pore formation. Heatmap colour code is normalized on  $S^{2168}$  (white) with slower timings in blue and faster timings in orange. Data points represent median values with 95% CI; n=3.

Even though the pinholin  $S^{2168}$  is one of the best studied holins, most studies focussed on the interaction of TMD1 and TMD2 (T. Pang et al., 2010a, 2010b, 2013). Recent biophysical studies also propose the model of transmembrane flipping and show that additional positively charged amino acids can prevent this interaction (Ahhammad et al., 2019, 2020; T. Pang et al., 2013). It seems that truncation studies and systematic changes of single residues were not performed due to the lack of simple assay systems and were either investigated using infecting bacteriophages or artificial liposome analysis of synthesized variants.

The FuN screen shows that single amino acid exchanges can be resolved within this assay and it reveals many new information regarding the pore forming ability of mutated variants of  $S^{2168}$ . To demonstrate the further potential of this screen, several other platform technologies were used in combination with the FuN screen. The goal was to show the universal applicability of the screen: from low-tech agar plates to expensive high-tech FACS measurements. Advantages and disadvantages of each technology are discussed as applicable.

## Microfluidic Microscopy Measurements with the FuN Screen

In recent years, microfluidic microscopy measurements became popular in the synthetic biology community. Not only do they provide single cell analysis on the microscopic level, they also allow the precise control and manipulation of injected fluids (e.g. gradients). Only very small volumes are required to conduct experiments which allows the efficient use of expensive substances at small scale. Furthermore, multiplexing (Araz et al., 2013), automation (Watson & Senyo, 2019) and the capacity for high-throughput analysis (Midkiff & San-Miguel, 2019; H.-Y. Wang & Lu, 2006) makes this technology attractive. In addition, different parameters can be measured or applied such as pressure (Cheung et al., 2012), magnetic fields (Lo et al., 2008) or electrical fields (Garcia et al., 2016).

For single cell studies microfluidic devices such as the ‘mother machine’ allow the tracking of individual cells for many generations by providing fresh medium under homeostatic growth conditions over a long period of time (P. Wang et al., 2010). In these devices cells can exit the individual chambers during cell division which keeps the cell in the log phase of growth. The chip used in this study comes from the Schaerli lab and follows another design, but the basic principle for cell tracking remains the same (Santos-Moreno et al., 2020). Cells are trapped in small chambers on the sides of a tunnel (Figure 27). Constant flow with fresh medium can be adjusted and induction can be timed precisely which allows the tracking of living cells for several days (Santos-Moreno et al., 2020; P. Wang et al., 2010).

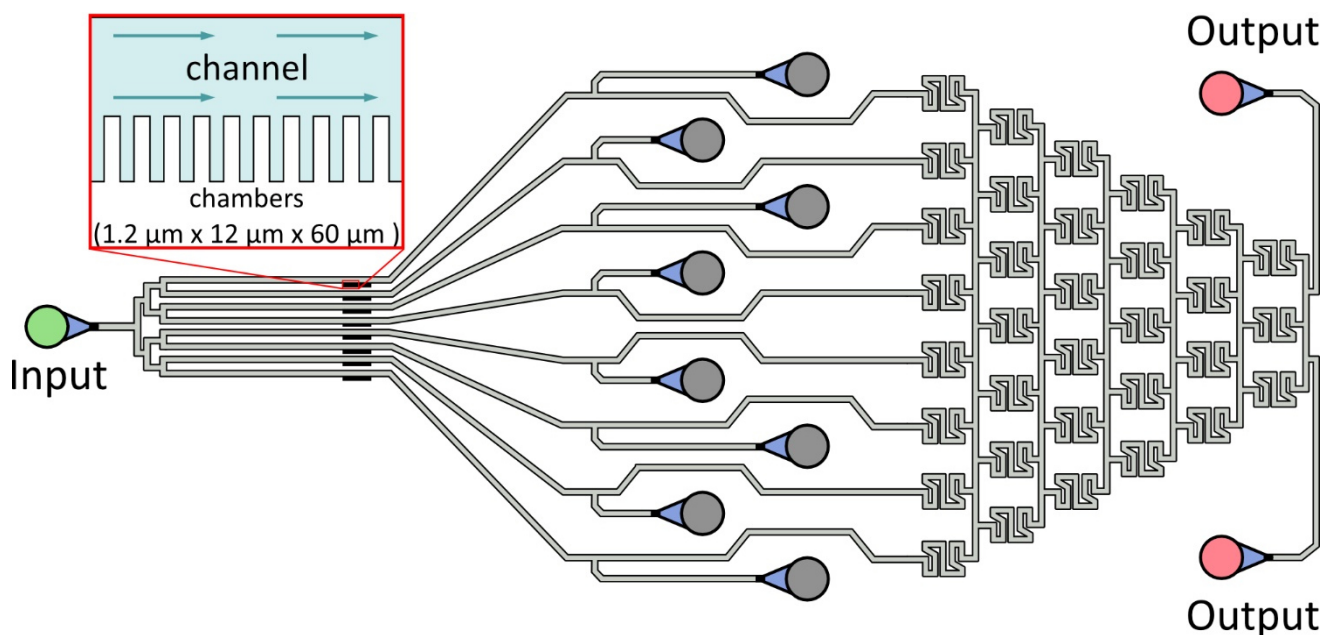


**Figure 27** Illustration of the microfluidic device used to validate the FuN screen. Cells, fresh medium and inducers are applied through the input valve and exit the device through the output valves. Once *E. coli* cells enter the chambers ( $1.2 \times 12 \times 60 \mu\text{m}$ ; H x W x L), they start to fill the room and excess cells exit through the channel. The tree-like design downstream can be used to generate a concentration gradient, but this feature was not used in this study

This microfluidic device was used to study the formation of nanopores at the level of single cells in the FuN screen. The following representative variants were chosen:  $S^{2168}$  and its truncations  $S^{2158}$ ,  $S^{2146}$  and  $S^{2138}$  (Figure 28), the T4 holin for lysis demonstration (Supplementary Figure 10) and the KcvNTS ion channel as a negative control (Supplementary Figure 10). After the cells were loaded into the chambers, the assay was performed identical to the spectrophotometric measurements with 113 minutes G-GECO1 induction followed by nanopore expression. Cells were observed for a total of 16 hours. While in spectrophotometer measurements the signal is averaged over all cells in a cavity, the biggest advantage of microscopic measurements is the investigation of single cell behaviour after induction. Furthermore, the fluorescence signal can be tracked, for instance whether it remains in the cytoplasm or leaves the cells and thus provides additional information on cellular integrity.

---

The signal from S<sup>21</sup>68 measurements showed a very evenly distributed signal over all cells in the field view (**Figure 28 A**). Cells were able to divide for a moment after induction and at a certain point every motion stopped and the fluorescence signal started to rise rapidly. This description applies to all variants except the potassium channel KcvNTS (**Supplementary Figure 10**). Here, the cells stop dividing and the signal does not rise immediately, but requires a longer period of time. It seems that the perforated and dead cells are not able to hold Ca<sup>2+</sup> back for too long. In contrast to the negative control, the T4 holin reacts with an accelerated signal rise which is followed by an exceptionally fast signal decrease (**Supplementary Figure 10**). These results suggest once again that T4 forms comparatively large pores which leads to a quick release of the cell inner content. Furthermore, the variants S<sup>21</sup>58, S<sup>21</sup>46 and S<sup>21</sup>38 emit a signal similar to their spectrophotometric measurements, but the response is relatively heterogeneous from cell-to-cell (**Figure 28 B, C, D**). For example, there are single cells that show a large increase in signal while other cells stop dividing but do not show any fluorescent signal and many other cells displaying intermediate signals. Usually this is not surprising, as cells within populations vary greatly in their characteristics such as stress resistance (Heins et al., 2019). But compared with the microscopy images from S<sup>21</sup>68 the variation is immense and could be more dependent on the pore formation rather than the natural heterogeneity. Another fact that has to be considered is the different cell density in each cavity. Biochemical interactions between individual cells in confined environments do show different behaviour in cell morphogenesis and order depending on the density (Cho et al., 2007; Volfson et al., 2008). It remains unclear, which of the possible explanations applies here or if it is an interplay of multiple factors.

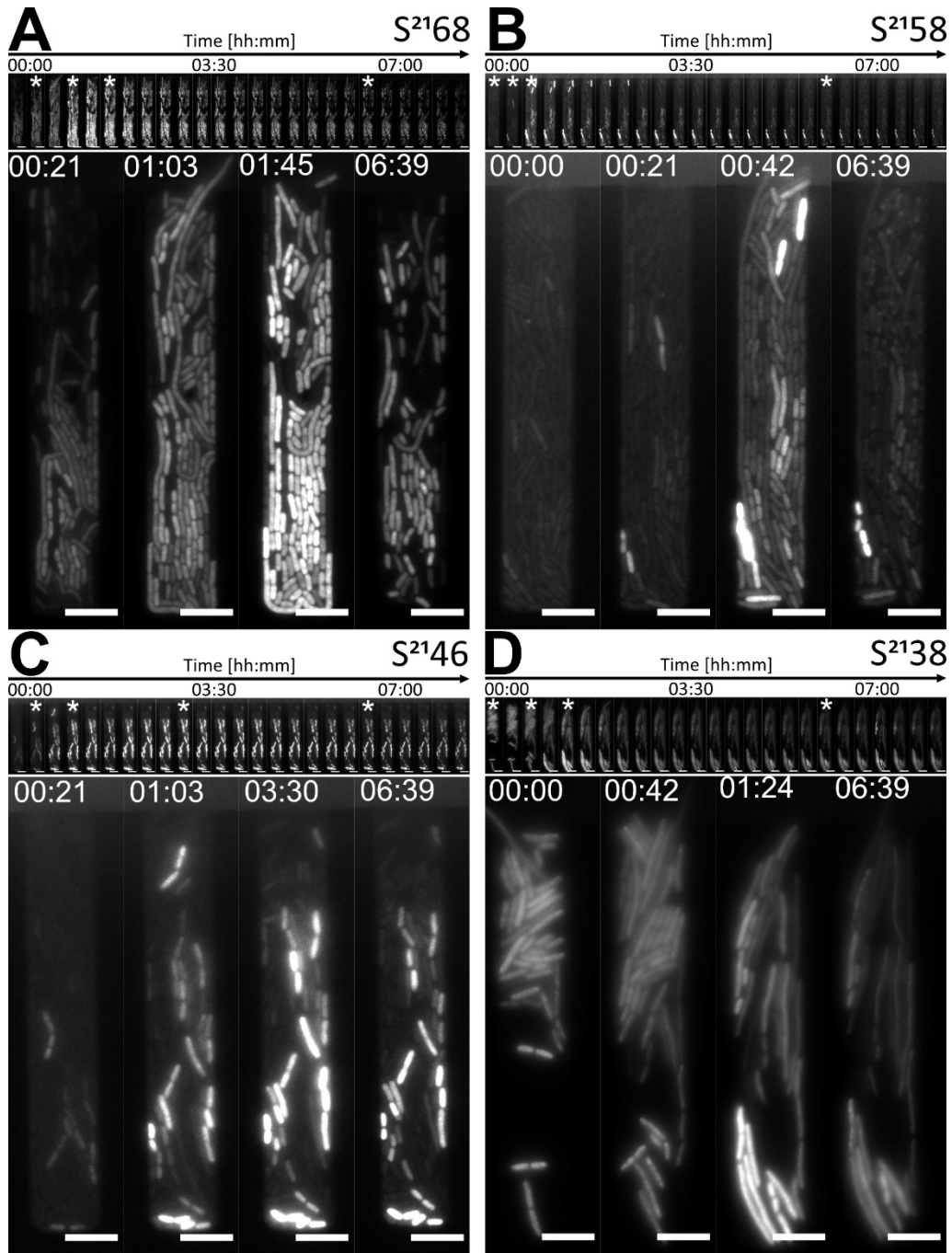


**Figure 28** Microfluidic microscopy measurements of the pinholin  $S^{2168}$  and the truncation variants  $S^{2158}$ ,  $S^{2146}$  and  $S^{2138}$ . The images in the top bar are 21 minutes apart and show a time window of 08:24. Representative images marked with an asterisk are shown enlarged below. Scale bar 5  $\mu\text{m}$ . (A) Cells with  $S^{2168}$  reveal a homogeneous signal distribution after cell death and perforation. (B)  $S^{2158}$  leads to a fast signal increase of a few cells, while (C)  $S^{2146}$  and (D)  $S^{2138}$  display slower signal increase

For a better comparison, the signal outputs from the spectrophotometer and the microscopy measurements were plotted in one graph. Most variants displayed similar kinetics in both assays with a few exceptions. Notably, KcvNTS,  $S^{2168}$ ,  $S^{2158}$  and  $S^{2148}$  were comparable in their behaviour after induction (Figure 28 A, B, C; Supplementary Figure 10), but  $S^{2138}$  and T4 did not exhibit matching curves (Figure 28 D; Supplementary Figure 10). These two holin variants seem to show a delayed kinetic in the spectrophotometer measurements. A possible explanation could be the premature induction of those variants in the microfluidic setup due to fluctuations in the flow control primarily based on leakages in the chips of unused outlets (Figure 27). This sometimes led to different medium flow in the single channels even though the overall flow remained stable.

Another noteworthy observation is the oscillating signal from S<sup>2158</sup> shortly after it reached its maximum (Figure 29 B). It seems that pore formation leads to spikes in Ca<sup>2+</sup> uptake and release. Potentially this phenomenon could be based on the transient nature of S<sup>2158</sup> where pores are formed temporarily and the cells are able to export Ca<sup>2+</sup> for a short period of time after nanopore induction.

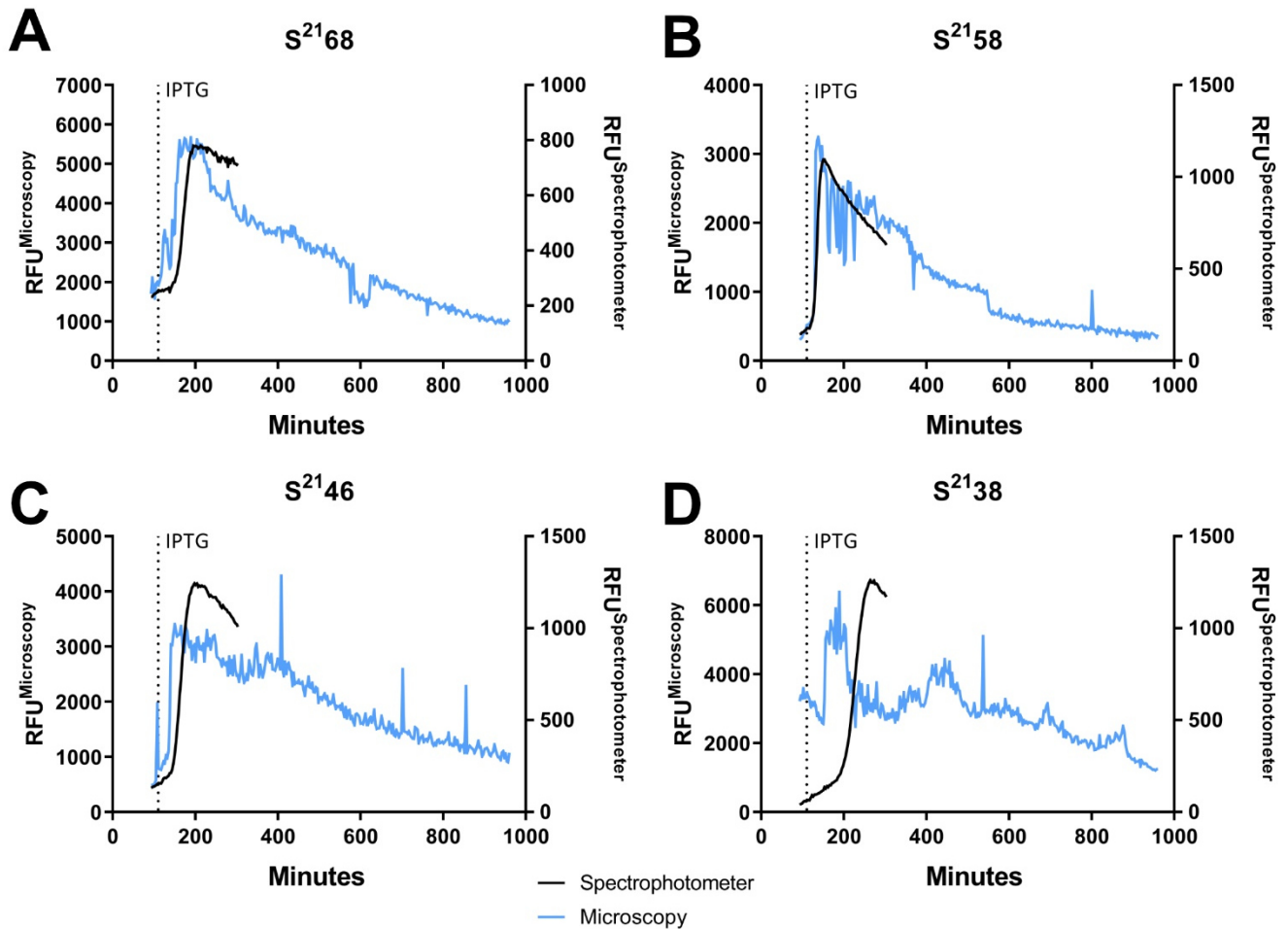


**Figure 29** Comparison of spectrophotometer and microscopy measurements of the pinholin S<sup>2168</sup> and the truncation variants S<sup>2158</sup>, S<sup>2146</sup> and S<sup>2138</sup>. While (A) S<sup>2168</sup>, (B) S<sup>2158</sup> and (C) S<sup>2146</sup> display matching curves from the different measurement methods, (D) S<sup>2138</sup> does show a premature signal rise in the microfluidic setup probably due to faulty flow control. Data points for spectrophotometer measurements represent mean values; n=3. Data points from microscopy measurements represent the max grey value of the whole cavity from Figure 28.

To summarise, microfluidic microscopy observations provide another level of detail compared to spectrophotometric analysis. Even though the overall signal output is comparable, single cell behaviour can be different and subject to stochastic effects. Furthermore, fluorescence changes can be studied in depth in a spatial manner and medium manipulation is a lot easier. However, the technical equipment for microfluidic measurements is expensive and the throughput as with most high-resolution techniques is limited.

## Colony Based FuN Screen with Airbrush Technology

Spectrophotometric, microfluidic and *in vitro* bilayer measurements are great technologies for the validation of the FuN screen, but are often not available in every laboratory. To provide a low-tech alternative which can also be performed at low cost, a classic colony screening method was chosen. For this method, cells are spread on agar plates, grown overnight and induced with a dispenser. This method is often used for the screening of fluorescent proteins or sensors and can be done just by eye (Shaner et al., 2013; Zhao et al., 2011).

The FuN screen on colony basis is performed differently than before to ensure best signal output. First of all, the concentration of the inducers was ten times higher for the G-GECO1 and 100 times higher for the nanopores. Furthermore, the expression times were adjusted to 180 minutes for the biosensor and 240 minutes for the nanopore, with an image acquisition every 60 minutes. This guaranteed an overall sufficient expression and an adequate signal-to-noise ratio. The data was summarized in a heatmap with total fluorescence measurements from a sector of each agar plate and variant (Figure 30 A). At 0 minutes after induction, the signal of all truncations remains the same. This changes after 60 minutes where the signal of the variants in the region S<sup>21</sup>64 to S<sup>21</sup>48 begins to rise and continues up to 240 minutes. At the last recorded time point, the variants S<sup>21</sup>68 and S<sup>21</sup>66 also start to exhibit a signal. If the colonies are examined side by side, one can even distinguish brighter variants by eye without the need of expensive equipment (Figure 30 A; Supplementary Figure 11). In addition, the number of colonies that can be screened is significantly higher with 10<sup>3</sup>-10<sup>4</sup> compared to microtiter plates with 10<sup>2</sup>. At the same time, the application of the inducer is simple rendering this screening method a viable alternative. Otherwise, it can be readily used in combination with spectrophotometric and bilayer measurements as a pre-sorting step to filter undesired variants.

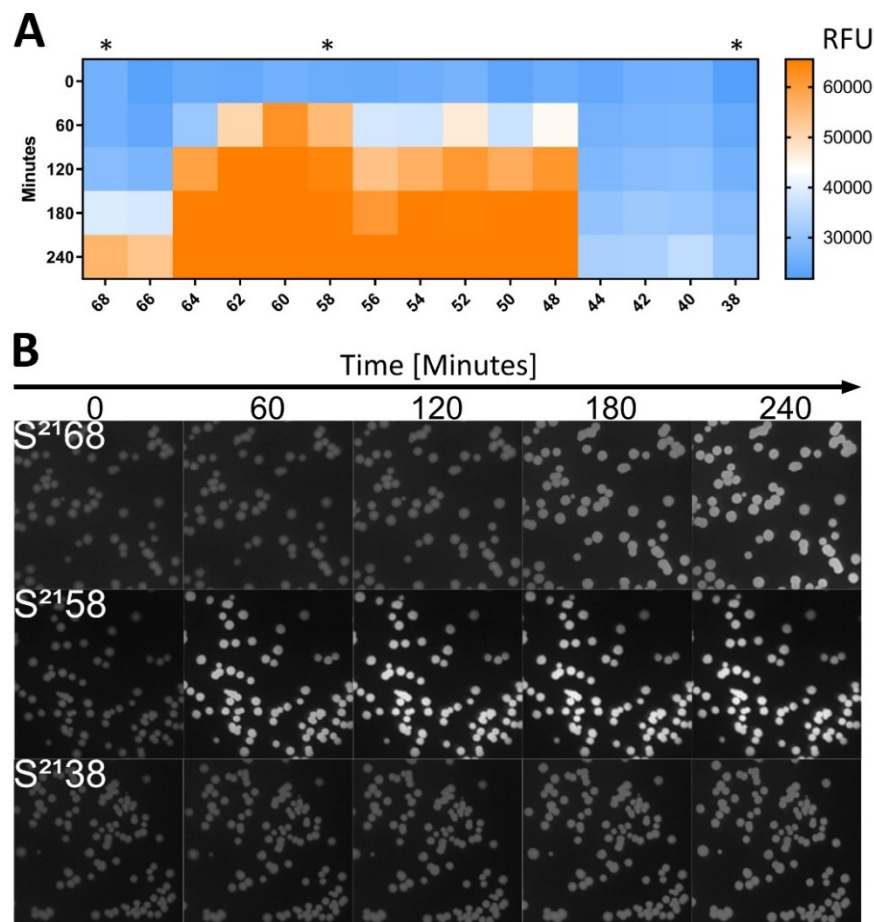


**Figure 30 Colony screening on agar plates. (A)** The heatmap demonstrates a faster fluorescence rise for the variants S<sup>21</sup>64 to S<sup>21</sup>48, followed by S<sup>21</sup>68 and S<sup>21</sup>66 over time. **(B)** Detailed view of variants marked with an asterisk from A. Heatmap colour code represents the max grey value from a sector of an agar plate.

---

## Model Selection with Fluorescence Activated Cell Sorting (FACS)

The last platform on which the FuN screen was tested was fluorescence activated cell sorting (FACS). This method provides ultra-high-throughput with up to  $10^6$ - $10^7$  variants and is a useful tool in library screening for endpoint measurements similar to the ones from the colony screen. Furthermore, one can infer additional information about the integrity and the viability of *E. coli* simply by comparing forward scatter (FSC) and backscatter (BSC). Here, FSC is a measure for cell size and BSC a measure for internal cell complexity like granularity. Alternatively, one can use fluorescent dyes such as propidium iodide which are able to stain dead cells (Tripathy et al., 2017). This work aimed to evaluate if the fluorescence output generated by the pore-dependent influx of  $\text{Ca}^{2+}$  and subsequent activation of the G-GECO1 was sufficient as a sorting condition and to examine if the DNA can be retrieved from the sorted cells.

For this purpose, the pore forming model peptide  $\text{SGS-}\Delta\text{TMD1-S}^{2168}$  and the negative control  $\text{TVMV-}\Delta\text{TMD1-S}^{2168}$  were chosen in combination with the T7.wt.sRBS promoter. Apart from their favourable functional properties, the biggest advantage of  $\text{S}^{2168}$  derived pores is that cellular integrity remains intact. For instance,  $\text{OD}_{600\text{nm}}$  measurements demonstrated a long and stable time window where the absorption does not change (**Supplementary Figure 6**) and the addition of EDTA which diminishes the signal of all other holins in an instant required up to 30 minutes to decrease the calcium signal to the baseline (**Figure 20 E**). This indicates that  $\text{SGS-}\Delta\text{TMD1-S}^{2168}$  is able to perforate the membrane without damaging the whole cell. The negative control  $\text{TVMV-}\Delta\text{TMD1-S}^{2168}$  on the other hand is 12 amino acids longer and does not lead to an increased signal or cell death within the first two hours after induction (**Supplementary Figure 4**). The assay conditions were the same as for the spectrophotometer measurements. Three different groups were prepared for the model selection: a positive and negative control, as well as a 1:10 mixture of positive to negative control. Electroporation was performed with the  $\text{SGS-}\Delta\text{TMD1-S}^{2168}$  and  $\text{TVMV-}\Delta\text{TMD1-S}^{2168}$  individually to have a positive and a negative control respectively. The model library was prepared out of a 1:10 ( $\text{SGS-}\Delta\text{TMD1-S}^{2168}$  to  $\text{TVMV-}\Delta\text{TMD1-S}^{2168}$ ) DNA mix and transformed by electroporation. This mixture was then sorted according to the fluorescence signal to separate the positive from the negative control.

Cell sorting was performed 1 hour after induction. To this end, recordings of 100.000 cells were first performed to get an impression of the different populations. According to the FSC against BSC dot plots (**Supplementary Figure 12**) cells looked reasonable, so in the next step gating was set according to the positive and the negative controls. The cells were pre-sorted with the first gate according to the FSC against fluorescence dot plots shown in purple (**Figure 31 A-C**), followed by a stricter second gate (teal) set in the histogram (**Figure 31 D-I**). Moreover, a high purity mode was selected for both sorts which ensured that only droplets with non-conflicting adjacent neighbour droplets were collected.

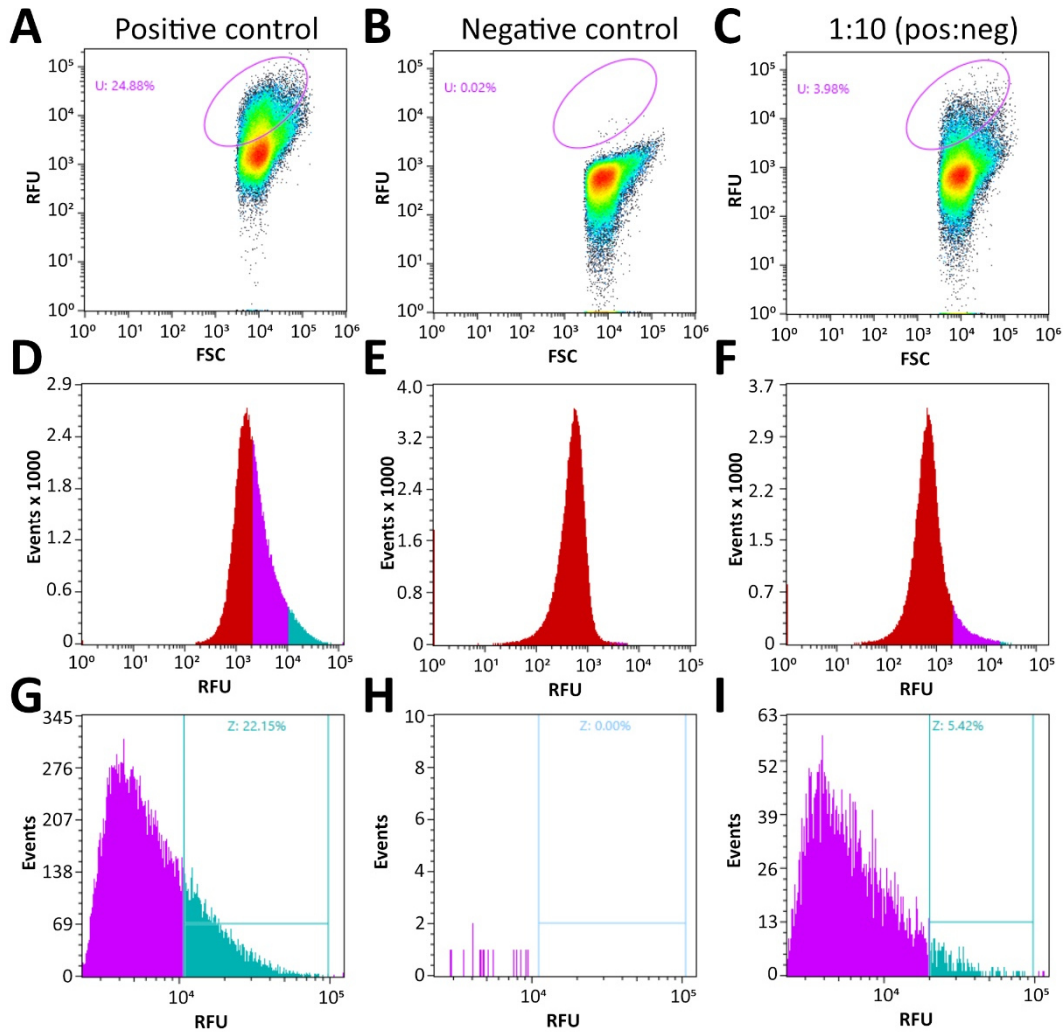


**Figure 31 FACS dot plots and histograms of the sorting conditions for the model selection with *SGS-ΔTMD1- $\zeta$ 2168* and *TVMV-ΔTMD1- $\zeta$ 2168* under the *pCTRL.wt.sRBS* promoter. (A-B) Fluorescence against forward scatter dot plots show the signal distribution of positive and negative control, as well as the 1 (positive) to 10 (negative) mixture. First sorting gate was set with the purple circle. (D-E) Fluorescence histogram demonstrates the event count of non-selected cells (red) compared to the purple selection gate. (G-I) To ensure tight selection conditions, another final sorting gate (teal) for the top (I)5.42% of the previous purple gate was set.**

In the end, the sorting yielded about 18500 events in total from which not every event is necessarily a cell. A colony PCR was performed on the cells from the positive and negative control, the 1:10 mix before sorting and the post selected cells (Figure 32). The positive control could be enriched after selection, even though the negative control still remained in the sample.

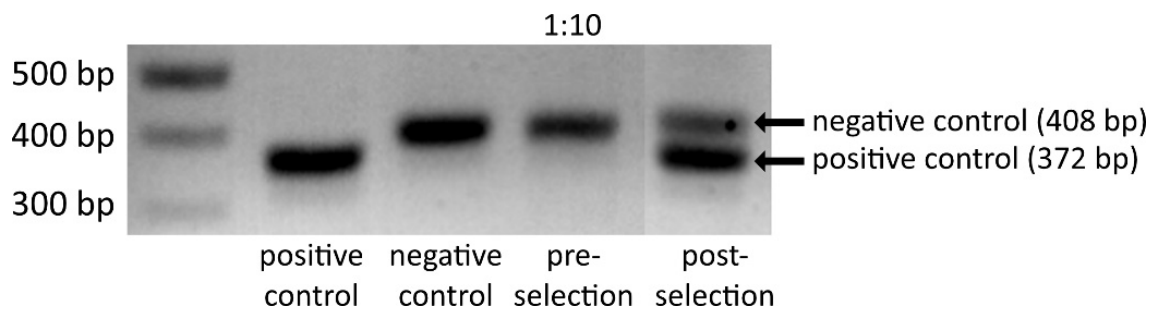


**Figure 32 Colony PCR of the model selection steps compared to the positive and negative control. Colony PCR on the preselection of the 1:10 positive to negative control mixture only reveals the negative control, while the postselection shows the accumulation of the positive control.**

Fluorescence activated cell sorting in combination with the FuN screen was successful and, once again, proves its robustness and compatibility across different assay formats. It is important to understand that not every type of nanopore can be examined by any assay format. For example, the T4 holin tends to disrupt the cell and would therefore not be suitable for FACS analysis. On the other hand, every non-lysing variant could potentially be used. In contrast to spectrophotometric measurements, a defined time point has to be chosen for sorting so this method is more suitable to sort functional versus non-functional nanopores rather than for detailed kinetic comparisons.

## Library Construction and Screening of Alternative Antiholin Variants

In the final set of experiments, the FuN screen was applied to screen a library of 8000 mutants. S<sup>2171</sup> is predicted to be able to retain pore formation long enough to prevent premature lysis (Ry Young, 2013). The key driving factor underlying this inhibition seems to be an additional positive charged Lys which prevents early flipping of TMD1 and stable nanopore formation. It seems that the pore forming process can be controlled by changing the N-terminal residues. Based on this information and the high-resolution provided by the FuN screen, the three amino acids following the first Met at the N-terminus of the antiholin S<sup>2171</sup> were randomly mutated leading to 8000 possible variants (**Table 4**). The idea was to examine the pore forming behaviour based on the amino acid composition and positioning.

**Table 4** Mutated amino acids of the S<sup>2171</sup>-library.

Name	N-terminal sequence
S <sup>2171</sup>	M K S M D K ( . . . )
S <sup>2171</sup> -library	M X X X D K ( . . . )

One of the most important things in a library screen is the spread of functional properties that can be experimentally resolved. Usually, when random or semi-rational changes are applied, most of the new variants are worse than the original while beneficial mutations are rare (Arnold, 1998). These beneficial mutations can be enriched by selection as long as the rate of false positives is low. This bottleneck heavily relies on the screening assay conditions. When the assay is not able to resolve beneficial mutations from undesired ones, then it is either not suitable for library screening or it takes a long time to find the right residues.

One important parameter in the FuN screen concerns the strength of protein expression by the promoter. To meet the right condition for a library screen, two different promoter strengths were compared to identify the best possible dynamic range by which variants with different propensities to form nanopores could be experimentally resolved. To this end, two S<sup>2171</sup> libraries were cloned, one with the strong T7.wt.sRBS and the other with the T7.100.sRBS promoter. Both libraries were treated equally with the standard FuN screen protocol. To be able to compare the distribution, the steepness was plotted against the T<sub>1/2</sub> (**Figure 33 A**) and the two parameters were also compared individually in a dot plot to demonstrate their range (**Figure 33 B, C**).

The distribution in the steepness against T<sub>1/2</sub> plot shows the accumulation of the T7.wt.sRBS variants in the lower left corner with only a few variants outside while the data points of T7.100.sRBS have a wider spread (**Figure 33 A**). At a closer look on the individual parameters visualized with a dot plot, T7.wt.sRBS data points are quite narrow together compared to the T7.100.sRBS which show a favourable distribution along the T<sub>1/2</sub> as well as the steepness (**Figure 33 B, C**). The dynamic range of the weaker T7.100.sRBS is therefore more suitable for this library and can examine small changes in pore formation, while the strong expression of the T7.wt.sRBS promoter provides less information.

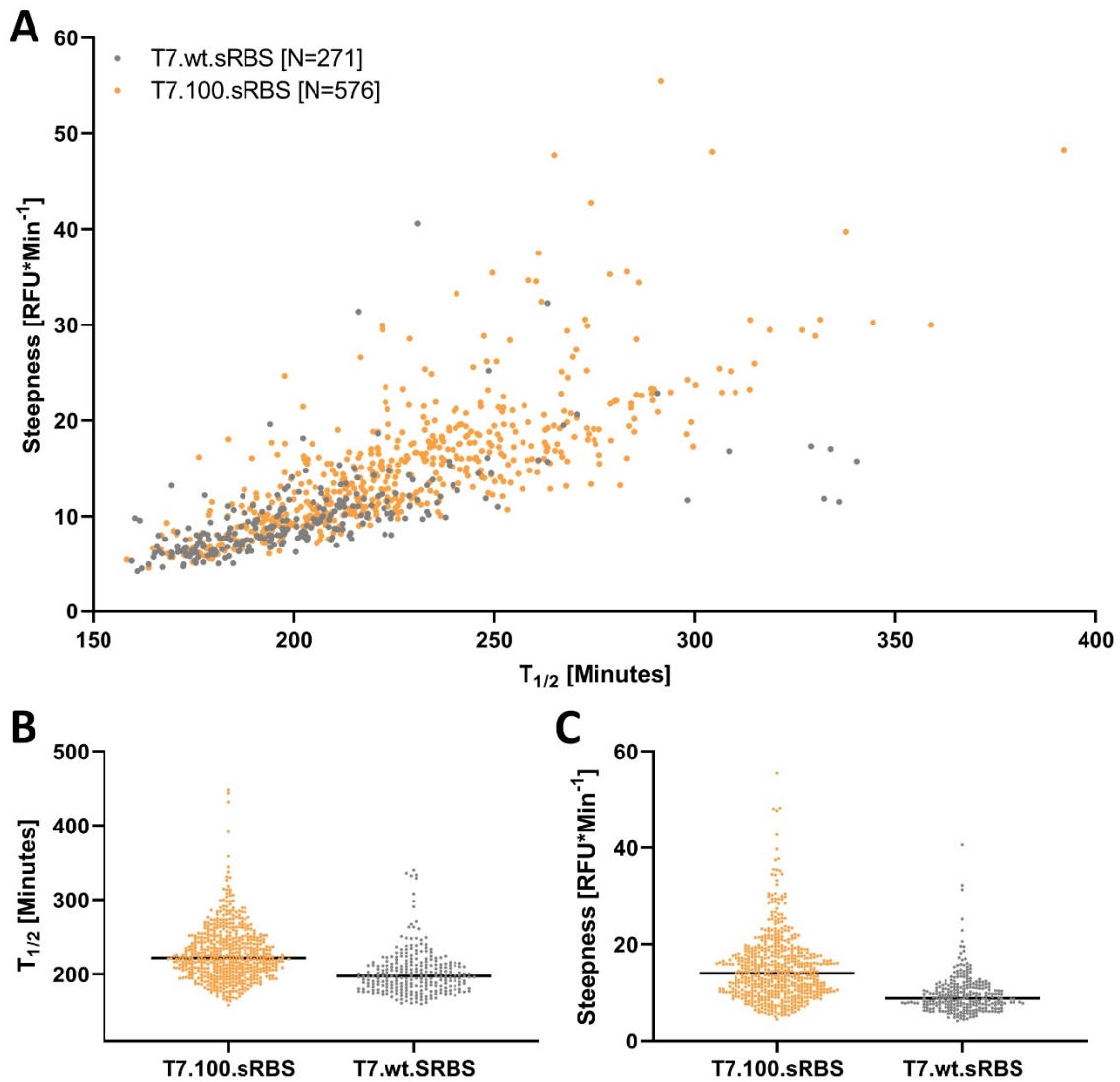


**Figure 33 Comparison of the promoter strength of T7.wt.sRBS and T7.100sRBS with the S<sup>2171</sup>-library.** (A) Steepness plotted against the T<sub>1/2</sub> shows the accumulation of T7.wt.sRBS (grey) variants in the lower left corner, while the T7.100.sRBS (orange) is more distributed on the whole scale. (B) T<sub>1/2</sub> and (C) steepness dot plots demonstrate the wide dynamic range of the T7.100.sRBS promoter. Black line annotates the median with 95% CI. Total count of measured variants was for T7.wt.sRBS N=271 and for T7.100.sRBS N=576.

After the T7.100.sRBS promoter was chosen, individual variants were randomly picked for sequencing around the control S<sup>2171</sup>-M4A which has a mutation of the second Met to prevent alternative reading frames. This selection condition should provide a broad picture of the library and the amino acid distribution. **Figure 34** contains the steepness against T<sub>1/2</sub> plot with the S<sup>2171</sup>-M4A control, the whole 576 screened library and the 173 sequenced variants.

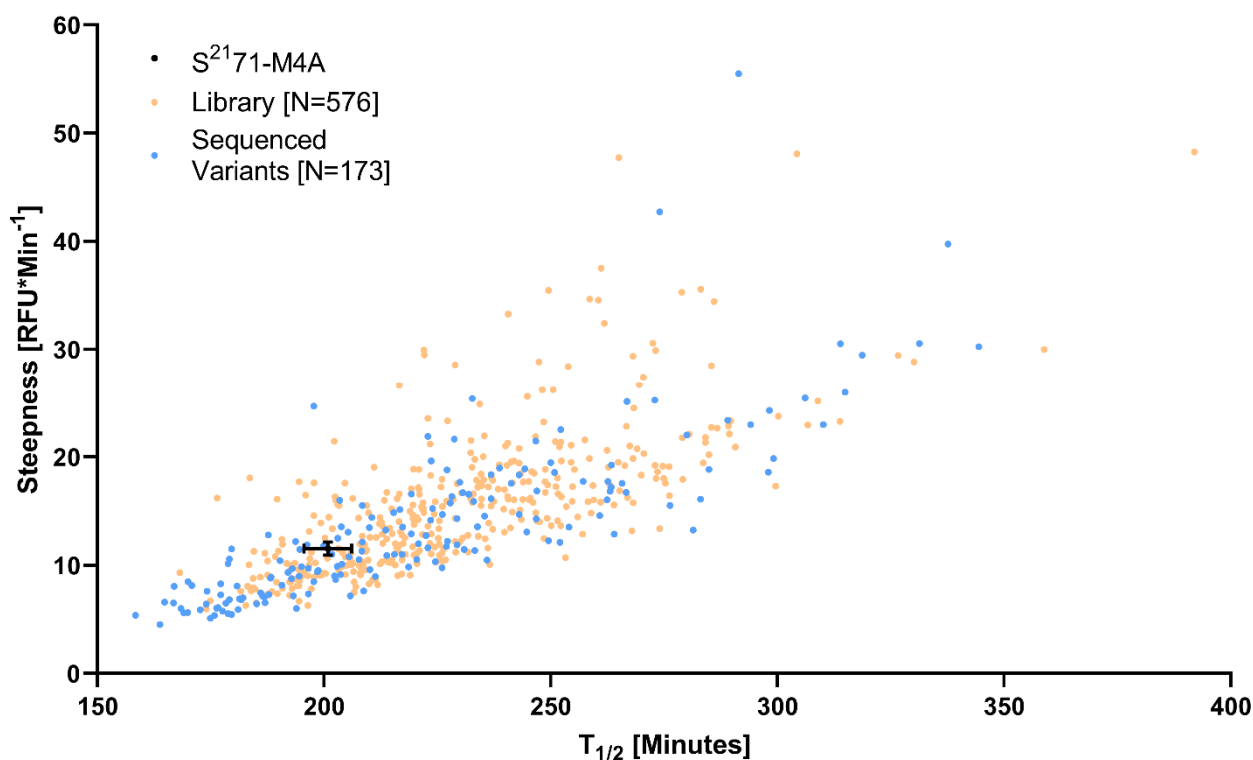


**Figure 34 Library screen with the T7.100.sRBS promoter.** The whole library marked in orange (N=576; n=1) is spread around the control variant S<sup>2171</sup>-M4A (black; error bars indicate SD, n=18). Sequenced variants are marked in blue (Datapoints represent mean values; N=173; n=3)

The sequenced variants were grouped (according to aliphatic, positive, negative, aromatic, polar and small residues) and analysed according to their properties and position. Both parameters  $T_{1/2}$  and steepness were plotted individually in a median displaying heatmap (**Figure 35**). Detailed information on the distribution of single amino acids on each position as well as the total number of amino acids can be found in the appendix (**Supplementary Table 1**; **Supplementary Figure 13**; **Supplementary Figure 14**; **Supplementary Figure 15**). Variants containing amino acids with special characteristics like methionine (potential new reading frame), proline (helix breaker), cysteine (disulfide bonds) and stop-codons were not included in the analysis resulting in 139 variants that were evaluated.

The variance in the signal output was high due to the holistic selection condition. Nevertheless, a range of interesting information could be extracted from the screening data. First of all, the signal has an overall large dynamic range and demonstrates that changes of single amino acids within a nanopore forming protein can be detected. Furthermore, while most of the substituted residues lead to inferior pore forming properties, some changes had a positive effect and yielded fast forming pores. In particular, a negative amino acid on position three led to low  $T_{1/2}$  and high steepness values. Aromatic residues on position two had a similar change on the  $T_{1/2}$  parameter, but did not display the same change in steepness as observed for negatively charged amino acids in position three (**Figure 35 A B**). On the other hand, aromatic amino acids on position one and three as well as a Gly on position two had an opposite effect. Those variants retained the pore forming even longer than the natural antiholin.

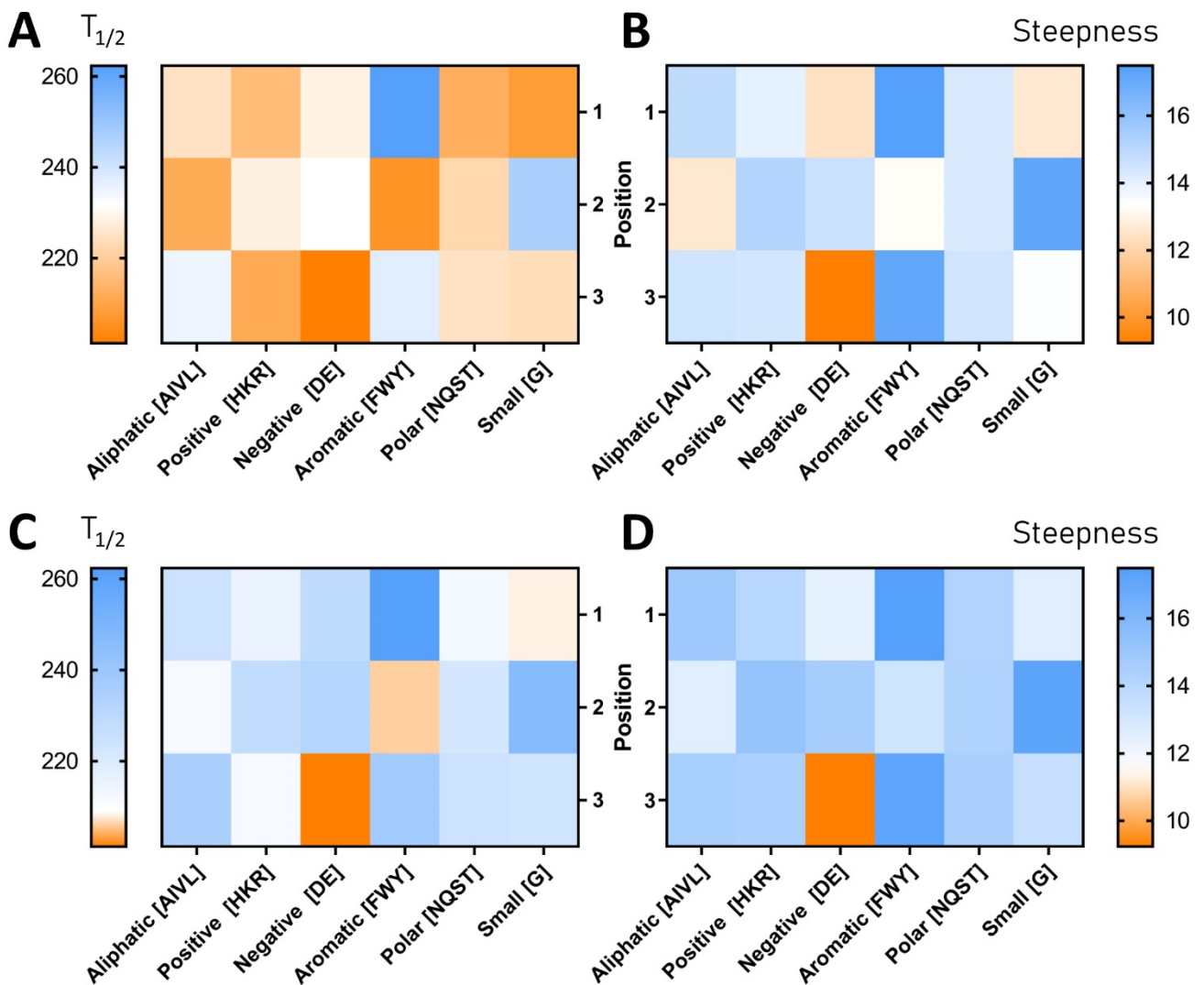


**Figure 35 Heatmap of grouped amino acids on different positions.** (A)  $T_{1/2}$  (Minutes) and (B) Steepness (Minutes\*RFU<sup>-1</sup>) measurements display a high variance in pore forming abilities. (C-D) Same values as in (A) and (B) but normalized on the control S<sup>2171</sup>-M4A (white colour) to highlight changes. Negative amino acids in position 3 lead to fast forming pores, while aromatic residues in position 1 and 3 cause the opposite. The colour code in (A-B) represents the median (95% CI; N=139; n=3).

By taking a closer look into the single amino acids of the previous highlighted groups, some residues seem to be more influential than others (**Supplementary Figure 14**). For the faster pore forming variants, this is quite easy as there are only the two residues Asp and Glu. Both seem to behave similar in terms of  $T_{1/2}$  and steepness. Although these two amino acids are charged, they seem to pass the membrane quite easily. A possible explanation can be found in the negative-not-inside or negative-outside rule (Baker et al., 2017). This rule particularly applies to short and single-pass membrane proteins and states that a significant number of membrane proteins are biased towards negative residues in the periplasm, but not the cytoplasm. Furthermore, the membrane itself is composed of 75-80% phosphatidylethanolamine (PE), 20% phosphatidylglycerol (PG) and 1-5% cardiolipin (CL) of which the latter is negatively charged (Raetz, 1978). Those lipids seem to facilitate electrostatic interactions with positively charged residues, but not as much with negative ones (de Vrije et al., 1990; Raetz, 1978). The retaining mutations caused by aromatic residues in position one and position three are not caused by the same amino acids. In position one, the delay is mainly introduced through Phe and Trp while in position three Trp and Tyr are responsible for retardation. It is important to note that, particularly in position three the data points for Phe and Tyr are very low (n=2) and the following statements have to be treated with caution. Nevertheless, the group of aromatic amino acids near the interfacial region is consistent with ‘the aromatic belt’ as the hydrophobic section is rich in aliphatic residues and flanked on

---

both sides of the membrane by aromatic residues (**Figure 23**) that are thought to interact with the lipid headgroups (Killian & von Heijne, 2000). In particular, Trp and Tyr are often found near the interfacial region. Trp has a large hydrophobic aromatic ring in the indole side chain which might get buried in the hydrophobic region of the bilayer and the attached amide group could be expected to interact with the polar environment. Tyr has a similar structure with its smaller hydrophobic aromatic ring and the attached polar hydroxyl group. Both residues seem to be responsible for polar-apolar interfacial interactions and are predicted to stabilize certain conformations (Killian & von Heijne, 2000; Mbaye et al., 2019; H. Sun et al., 2008). This stabilization could be the driving factor for the retardation of pore formation.

But there are also variants with aromatic amino acids in position two which behave contrary to the predicted role of those residues. The leading amino acids here are Phe and Trp. Phe is known to be preferably buried in the hydrophobic core (Wallin et al., 1997) and therefore could remove the barrier for flipping of the TMD1. Trp on the other hand, is also known to allow a faster penetration of the bilayer as shown for the transcription factor Antp where the exchange of tryptophan inhibited cell permeation (Derossi et al., 1996; W. Zhang et al., 2006).

One last mutation which seemed to slow down pore formation is Gly in position two. In membrane proteins, Gly is known to participate in close helix-helix packing (Dong et al., 2012). These structures are called glycine zippers and the sequence patterns are variable but based on (G,A,S)xxxGxxxG or GxxxGxxx(G,S,T) motifs (S. Kim et al., 2005). They facilitate intrinsic TM dimer formation and are generally overrepresented in membrane proteins (Russ & Engelman, 2000). In case of the pinholin mutation, several factors come together: S<sup>21</sup>68 as well as its antiholin S<sup>21</sup>71 form TMD1-TMD2 dimers prior pore formation via TMD2-TMD2 dimerization. Both interactions are presumably based on glycine zippers (T. Pang et al., 2010b). The introduction of another glycine could lead to zipper-like structures that favour the TMD1-TMD2 interaction or make TMD2-TMD2 interactions less likely.

In addition to all previous theories, the AT nucleotide count of the N-terminal mutations could also be important. One major role in protein expression is fulfilled by the translation initiation region (TIR). This region is about ~30 nucleotides long and recognised by the 30s ribosomal subunit during translation (Laursen et al., 2005; McCarthy & Gualerzi, 1990; Milón & Rodnina, 2012). In native *E. coli* mRNA, the TIR is composed of the Shine Dalgarno sequence, a spacer region of about 5-9 nucleotides (H. Chen et al., 1994; Osterman et al., 2013) and the first five codons of the coding sequence (Ingolia et al., 2009; Reeve et al., 2014). Usually, the lack of secondary structure is thought to promote accessibility of the ribosome subunit during translation initiation (Bentele et al., 2013; Goodman et al., 2013). Similar effects could also play a role in the FuN screen as there could be a correlation between faster pore formation and the amount of AT nucleotides in the mutated region (**Figure 36**). Notably, there seems to be a trend towards a faster signal increase when more than 2-3 AT nucleotides occur in the randomised region.

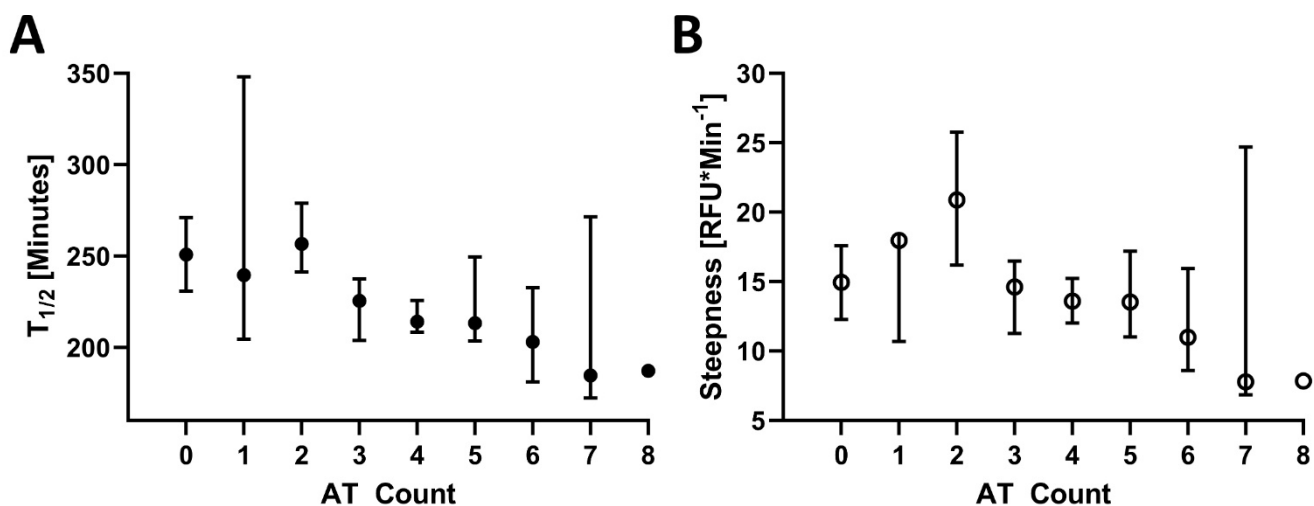


**Figure 36**  $T_{1/2}$  and steepness correlation to the AT count of the three mutated amino acids of  $S^{2171}$ -library. Dots represent the median with their 95% CI marked by the bars. The parameters (A)  $T_{1/2}$  and (B) steepness could be dependent on the number of AT nucleotides, as the overall pore formation accelerates with a higher AT count. The number of nucleotides of the sequenced variants (N=139) is 1251, of which 564 nucleotides were AT and 687 were GC. Data points represent median with 95% CI indicated as error bars (N=139).

This assay revealed a wide variety of new information regarding the N-terminus of the antiholin. It is important to note that out of a total of 8000 variants only 576 were assayed of which a further of 240 clones were verified via sequencing. Out of these 240 sequenced clones, 67 had frameshifts or contained mixed sequences. From the remaining subset of 173 sequences, only 139 met the conditions to be used in the analysis which corresponds to about 1.76% of the total library. Furthermore, all three amino acids were changed at once to get a holistic view of the distribution. Nevertheless, a favourable distribution in the library was visible and promising trends and phenomena of small transmembrane peptides could be revealed.

---

## Conclusion

---

The aim of this project was to develop a strategy to engineer protein nanopores and subsequently use these pores for biotechnological applications. The assay was required to (i) be usable in standard *E. coli* lab strains, (ii) the output signal had to be connected to the properties of the nanopores (genotype-phenotype linkage) and (iii) this assay should be scalable up to ultra-high-throughput formats. To this end, various nanopores with different properties, especially holins, were used and combined with a genetically encoded calcium sensor (GECO). This carried two advantages: First of all, holins are bacteriophage derived nanopores which are known to insert easily and without a distinct signal sequence into the *E. coli* inner membrane and they can form pores of different sizes. Secondly, the cytosolic  $\text{Ca}^{2+}$  concentration of *E. coli* cells is extremely low and can be increased by permeabilizing the membrane. Nanopore dependent calcium influx can then be measured by the GECO.

To establish the FuN screen, optimizing the right expression vectors proved absolutely critical. Nanopores are toxic proteins and especially holins form part of a naturally evolved system to kill the host and release its cytoplasmic content. This led to several complications with conventional protein expression vectors which are usually based on high copy oris and aim for strong protein expression. In this case, cells were not able to grow or under constant stress due to leaky expression. These problems were solved by choosing a low copy vector and adjusting the T7 promoter strength. In combination with a RNA polymerase utilizing high copy vector for the sensor and the choice of the G-GECO1, this system was sufficiently powerful to suppress and express highly toxic nanopores with a sufficient signal-to-noise ratio in the fluorescence output. Nanopores with different properties showed distinct and characteristic signals while the negative controls stayed dim. Furthermore, the two parameters  $T_{1/2}$  and steepness that were retrieved from the sigmoidal curve fit after nanopore induction enabled quantitative comparisons of pore forming properties based on their kinetics. Along with the  $\text{OD}_{600\text{nm}}$  measurements, one can also distinguish between lysing and non-lysing pores.

The FuN screen was then used to investigate the pore forming properties of the S<sup>2168</sup> pinholin which has previously been suggested to form defined heptameric pores. Systematic truncation experiments of the TMD1 revealed the key functions of the charged N-terminal region. This region naturally delays pore formation in the lytic cycle to ensure a sufficient production of bacteriophages upon release. The deletion of the Asp and especially Lys led to uncontrollable fast forming pores and rational mutagenesis of both amino acids showed that mainly Lys is responsible for the delayed pore formation. Further deletion of the TMD1 destabilized the pore and slowed the increase of the fluorescent signal. This behaviour was examined with several different platform assays, starting with high resolution *in vivo* spectrophotometric and *in vitro* bilayer measurements with chemically synthesized variants, followed by long time microfluidic measurements and low-tech colony screen on agar plates. Even ultra-high-throughput FACS selections for model peptides could be demonstrated.

In the final set of experiments, the N-terminal region of S<sup>2171</sup> was studied in detail. A random mutagenesis library of the first three amino acids was created and examined with the FuN screen. Once again, the important role of a suitable promoter was exemplified and the large sequence space was revealed with a diverse spread of different pore functions. Sequencing analysis showed that on some positions key residues can change the pore forming ability drastically. While negative amino acids in position three accelerate pore formation, aromatic residues in position 1 and 3 delay pore formation.

In summary, the FuN screen demonstrated its viability of linking the genotype and phenotype for a successful screening system. Several functions and key components of the natural S<sup>2168</sup> and its antiholin S<sup>2171</sup> could be displayed within this assay on different platforms from low-technology available in most labs to high-technology systems. Simple assay conditions combined with high-resolution output exhibit the robustness and applicability of this system for further nanopore engineering strategies.

---

## Outlook

The construction of protein nanopores, channels and transporters with tailored functions and properties has great potential for a number of biotechnological applications and provides fundamental insight into their mechanisms of action. To date, the majority of construction efforts have been realised by means of rational, structure-guided approaches and systems to screen nanopores in high-throughput remain scarce. In particular, the field of DNA sequencing has accelerated the exploitation of pore proteins and led to several successful developments (S. Wang et al., 2018). But there are also other scenarios for protein nanopores in addition to DNA sequencing. Potential applications can be (i) in biosensing as highly sensitive sensors that can detect clinically or biotechnologically relevant molecules in complex environments (Varongchayakul et al., 2018), (ii) in the construction of artificial biosynthetic and metabolic pathways as well as in chemical reaction engineering as membrane transporters which enable the import of substrates or the export of products through impermeable phospholipid membranes, e.g. in natural cells as well as biomimetic cell compartments (Keyser, 2011), (iii) in processing technology to purify specific molecules from complex environments (e.g. directly from the environment or chemical reaction compartments) (G. Sun et al., 2013).

For every application a tailored nanopore has to be constructed. This can be either done by computational approaches creating artificial synthetic pores (Joh et al., 2014; C. Xu et al., 2020) or by engineering natural pores (S. Wang et al., 2018). However, each pore has to be adjusted in the context of its specific application which also requires to consider its membrane context. To date, most of the screening systems are either limited by means of their throughput capability or by the usage of expensive equipment. The FuN screen addresses these problems by providing a universal screening system which can be readily applied in any laboratory. Its focus was set on small pore forming peptides due to their accessibility and easy genetic manipulation. Especially holin nanopores are favourable candidates given their nature of fast and efficient nanopore forming proteins.

### Holins – Potential Ancestors of Transporter Systems

Holins comprise a family of self-assembling peptide pores that potentially promise a simpler route to engineer nanopores with tailored properties and functions due to their modular organisation where distinct regions confer elementary capacities to insert, form and stabilise nanopores in membranes. Yet so far, they received little attention as potential building blocks in nanopore engineering. They are represented in several lifeforms and in some cases those small pores are suspected to be ancestors of actual transporter systems.

*S. aureus* for example uses a genetic program for cell lysis to achieve biofilm formation, regulated by the antiholin-like gene *lrgA* and the holin-like gene *cidA* (Bayles, 2003). Homologues of this Cid/Lrg system can be found in a wide range of other bacteria, both gram-negative and gram-positive bacteria (Bayles, 2007). Gram-positive *B. subtilis* contains genes encoding for YwbH (CidA homologue) and YsbA (LrgA homologue) and both are part of a two-component regulatory system which does not play a role in programmed cell death but instead takes part in pyruvate utilization (Charbonnier et al., 2017; van den Esker et al., 2017a). It seems that the intracellular pyruvate level and thereby the metabolic state of the cell is regulated by holin-like nanopores and similar systems can be found in various other bacteria (van den Esker et al., 2017b). A hypothetical model suggests that these pore proteins could have been acquired through horizontal gene transfer in ancient bacteria. These bacteria then were acquired by eukaryotes leading to the apoptotic system in mitochondria and plants. While some of the programmed cell death functions were preserved, homologues diverged in function from cell death to metabolism (van den Esker et al., 2017b). The diversity of holins and holin-like proteins demonstrates the potential use of these pores and their simple, yet functional design is preferable in engineering approaches.

Understanding pore forming properties does help in fundamental research, but also allows the specific genetic manipulation for rational designed variants. Technologies like the portable DNA sequencer MinION (Oxford nanopore technologies) or the water filtering cartridge Aquaporin inside® (Aquaporin

A/S) demonstrate the need for tailored nanopores. Although most of the engineered nanopores underlie large barrel-like structures,  $\alpha$ -helical peptides provide many benefits in nanopore engineering. A recent study published in 2020 from Xu *et al.* illustrates the power behind small artificial  $\alpha$ -helical nanopores which were constructed in a computational approach (C. Xu *et al.*, 2020). *De novo* nanopores constructed with this method were extremely stable and yielded well-defined transmembrane proteins that were capable of conducting ions in a highly selective fashion. In addition, larger pores could be computationally designed to enable the transport of small-molecule fluorophores. Preliminary results of the FuN screen with artificially constructed nanopores show that it is possible to measure a signal of the largest pore TMH4C4 (Figure 37). This nanopore consists of four quadruple-helix bundles and is able to transport fluorophores of 1kDA size. A linear signal increase can be detected beginning around 300 minutes after induction for TMH4C4, but not for the K<sup>+</sup> selective hexamer TMHC6 or TMHC8. The latter was designed as an octameric pore, but also tended to form heptamers and was therefore redesigned to TMH4C4. Despite the late signal, this demonstrates the capacity of the FuN screen to assay computationally designed nanopores. At the same time, it also demonstrates the challenges associated with the design of artificial nanopores as these pores do not function as efficiently as naturally evolved nanopores. In this regard, the majority of computational protein designs including nanopores yield ultra-stable structures that ultimately may not function as efficiently in an *in vivo* context where additional factors such as membrane insertion efficiency play key roles, yet are not actively considered in computational design algorithms.

However, with a databank full of potential pores like the TCDB (Milton H. Saier Jr *et al.*, 2016) combined with the ability to design *de novo* nanopores, the FuN screen could provide a powerful platform to verify, investigate and engineer peptide pores and their *in vivo* functions.

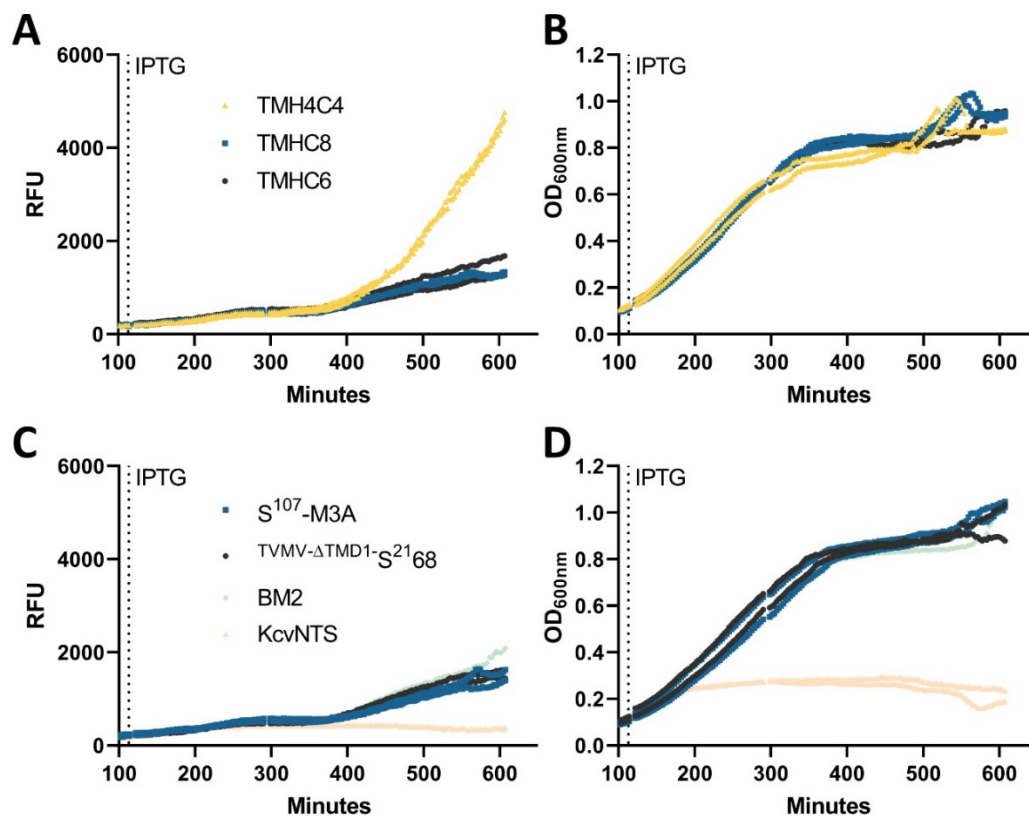


**Figure 37 Fluorescence and absorption measurement of artificial designed nanopores.** (A-B) The *de novo* designed large nanopore TMH4C4 is able to perforate the membrane 300 minutes after induction, while the TMHC6 and TMHC8 peptides do not show pore formation and behave like the (C-D) negative control nanopores S<sup>107</sup>-M3A, TVMV- $\Delta$ TMD1-S<sup>2168</sup> and BM2. KcvNTS actually kills the cells early and therefore the signal does not increase in the fluorescence, as well as absorption measurements. Preliminary results with n=2, each replicate is plotted individually.

---

## Developing new Biosensors with the FuN Screen

Beyond engineering nanopores, the FuN screen can also be applied to assay and engineer fluorescent protein sensors. These sensors are extremely useful tools to probe metabolism and therefore to understand the physiology of cells (DeBerardinis & Thompson, 2012; Heinemann & Sauer, 2010; Nadler et al., 2016). The problem is that every biosensor has to be tailor-made for the individual applications and often a new assay has to be established which is time consuming. Biosensors can be designed and tested in various ways. One way is to perform the whole construction directly in the cells they are made for, e.g. mammalian cells (Piljić et al., 2011). The sensor can then be optimized in the same context it will be finally applied, but the throughput of this screening is rather limited. A more convenient way is to use bacterial cells: They grow fast, can express proteins in a large scale and are cheap in sustainment. Even though *E. coli* lacks organelles for complex post translational modifications, several biosensors were successfully designed in bacteria and subsequently used in mammalian or other higher order cells (Ibraheem et al., 2011; Lindenburg, Hessels, et al., 2013; Lindenburg, Vinkenburg, et al., 2013; Marvin et al., 2013; Zhao et al., 2011).

The FuN screen was developed on the basis of the calcium sensing R- and G-GECO1 biosensors and used for nanopore screening. However, the screen can also be expanded for biosensor screening instead of nanopore evaluation. Each biosensor reacts to a specific ligand by a change in the output signal. This delta can be an increase or a decrease in the signal and is induced by addition or removal of the ligand. For ligands which are membrane permeable screening is rather easy. But membrane impermeable ligands are quite challenging and cells are usually lysed by auto-lysis cassettes, specific enzymes such as lysozyme or detergents (Menacho-Melgar et al., 2020) which however limits throughput. This limitation can be addressed with the FuN screen. The results of the FACS measurements demonstrate the ability to induce pores which make the membrane permeable, but leave the cell envelope intact allowing the sorting of the cells and retrieving of the DNA from positive variants. In addition, this can be also performed on colony agar plates with simple airbrush equipment which allows this technique to be used in nearly every lab.

Besides the inward flow of a ligand, which leads to a signal increase, also the outward flow of the ligand and therefore the signal decrease of a sensor can be measured with the FuN screen. Preliminary results with the iGluSnFR biosensor for glutamate detection demonstrate that under the right conditions the outflow of glutamate can be detected. **Figure 38** shows that the two pore forming peptides <sup>SGS-ΔTMD1</sup>-S<sup>2168</sup> and T4 lead to an outward flow of glutamate while the negative controls BM2 and <sup>TVMV-ΔTMD1</sup>-S<sup>2168</sup> contained the ligand in the cytoplasm. The addition of 25 mM glutamate into the medium leads then again to a partial increase of the signal.

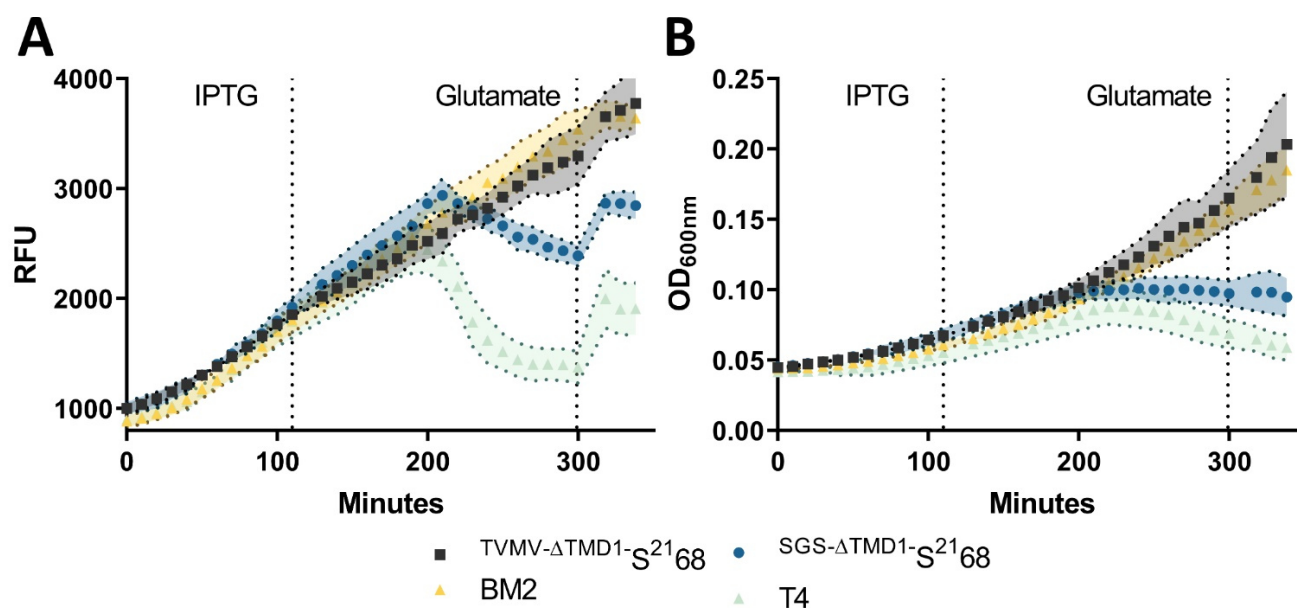


**Figure 38 Glutamic acid outward flow after nanopore induction. (A-B)** *E. coli* cells cultivated in defined minimal medium (M9) carrying the biosensor iGluSnFR for glutamate detection and the two negative controls BM2 and TVMV- $\Delta$ TMD1-S<sup>2168</sup>, as well as the two pore forming peptides SGS- $\Delta$ TMD1-S<sup>2168</sup> and T4. After pore induction only the two active pores lead to an outward flow of glutamate and therefore a signal decrease. The addition of 25 mM glutamate partially increases the signal again. Data points represent mean values with SD indicated as error area; n=4. Legend at the bottom refers to all graphs.

Every screening scenario has to be adjusted individually depending on the nanopore and biosensor combination, but especially on the host cell composition. For example, gram negative *E. coli* has two membranes which have to be crossed by the ligand. Although many compounds such as ions or amino acids can readily pass the outer membrane (OM) through porins and other relatively unselective transporters, some substances cannot surpass the OM (Krishnamoorthy et al., 2016; May & Grabowicz, 2018; Muheim et al., 2017; Nikaido, 2003).

This limitation was also found to be present in the FuN screen for the macrolide rapamycin, also known as sirolimus. Rapamycin has antifungal and immunosuppressive activity and is used as a therapeutic agent (Y. J. Yoo et al., 2017). It forms a strong interaction with FKBP12 (FK506-binding protein 12) and inhibits mTORC1 in the T-cells by binding to its FRB domain (FKBP12-rapamycin-binding domain) (Kolos et al., 2018; Y. J. Yoo et al., 2017). In the absence of rapamycin, the two domains FKBP12 and FRB show no protein interaction while the addition of the ligand leads to strong heterodimerization (Banaszynski et al., 2005). In synthetic biology, this inducible heterodimerization feature was utilized to study protein-protein interactions (Mabe et al., 2014; Putyrski & Schultz, 2012; Voß et al., 2015; Wu et al., 2020), in building artificial oligomers (Inobe & Nukina, 2016), used in integrated protease-based proximity sensors (Stein & Alexandrov, 2014) or in allosteric single-chain protein switches (Dagliyan et al., 2013, 2017; Gräwe et al., 2020).

A single-chain fluorescent protein sensor for rapamycin based on cpsfGFP created by Theresa Wörmann (data not shown) was used to investigate the usability of the FuN screen for larger molecules. The sensor exhibits a 2-3-fold increase in fluorescence in crude lysate screening experiments and was used analogous to the G-GECO1 screening conditions with the addition of rapamycin 2 hours after pore induction. Unfortunately, only the pores T4, S<sup>105</sup> and HokB which are able to lyse the cells led to an increased signal (Figure 39). Especially T4 under the strong T7 promoter had a fold change comparable to the crude lysate experiments. Otherwise, all other tested pores performed similar to the negative controls indicating that rapamycin cannot pass the outer or inner membrane even after pore induction.

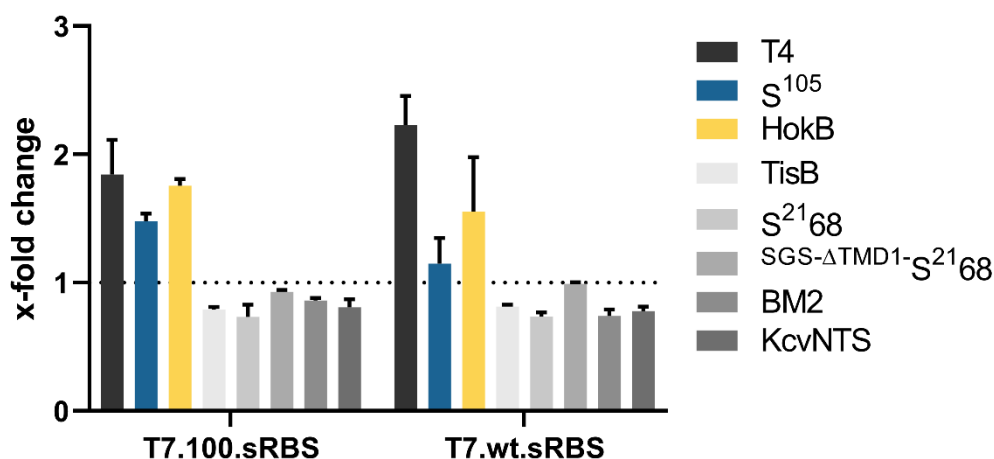


**Figure 39 Rapamycin sensor in combination with the FuN screen.** X-fold change was calculated with endpoint measurements before and after the addition of 250  $\mu$ M rapamycin. The rapamycin sensor showed an increase in fluorescence only in combination with the lysing nanopores T4, S<sup>105</sup> and T4. S<sup>2168</sup>, SGS- $\Delta$ TMD1-S<sup>2168</sup> and TisB did not show a fold change similar to the negative controls BM2 and KcvNTS. Bar graphs represent mean values with SD indicated as error bars; n=3.

Even though one lab could previously demonstrate that rapamycin could cross the membrane independent of a nanopore (Davis et al., 2011), this work demonstrates that in the context of the FuN screen it is not possible, at least not to a sufficient extent to induce fluorescence in the rapamycin-specific sensor. It remains unclear whether the cells were treated differently or the rapamycin had a different quality and therefore the results do not match. Nevertheless, the rapamycin sensor was responsive and did show a signal increase in lysed cells indicating that it cannot pass the membrane of intact cell envelopes.

The expression of a second pore in the OM could help to overcome this problem, but would lead to an additional physiological burden and probably to several other problems which then need to be addressed. Another solution might be to use other cell lines, like the gram-positive bacteria *Bacillus subtilis*. *B. subtilis* which has only one membrane, sophisticated tool boxes for protein expression systems (Guiziou et al., 2016; Y. Liu et al., 2019; Popp et al., 2017) and is a common organism in biotechnology due to its ability to secrete proteins in large quantities (Hohmann et al., 2017). Proteins of 25-50 kDA could potentially pass the peptidoglycan layer of *E. coli* and *B. subtilis* (Demchick & Koch, 1996) but the latter has the advantage of only one other membrane barrier.

In the end there are many potential applications for the FuN screen as it can be used to screen both nanopores or biosensors. Everything depends on the requirements and still has to be adjusted properly. However, the FuN screen provides a good foundation as a platform technology in terms of functionality, ease of use and expenses.

## Material and Methods

### Material

#### Microorganisms

Table 5 *E. Coli* strains used in this work.

Strain	Genotype	Usage	Originator
<i>E. coli</i> DH10 $\beta$	$\Delta$ (ara-leu) 7697 araD139 fhuA $\Delta$ lacX74 galK16 galE15 e14- $\phi$ 80dlacZ $\Delta$ M15 recA1 relA1 endA1 nupG rpsL (StrR) rph spoT1 $\Delta$ (mrr-hsdRMS-mcrBC)	Cloning and plasmid propagation	NEB, Massachusetts, USA
<i>E. coli</i> BL21(DE3)	fhuA2 [lon] ompT gal ( $\lambda$ DE3) [dcm] $\Delta$ hsdS $\lambda$ DE3 = $\lambda$ sBamHIo $\Delta$ EcoRI-B int::(lacI::PlacUV5::T7 gene1) i21 $\Delta$ in5	Expression of recombinant proteins; <i>In vivo</i> assays	NEB, Massachusetts, USA

#### DNA and Protein Standard Rulers

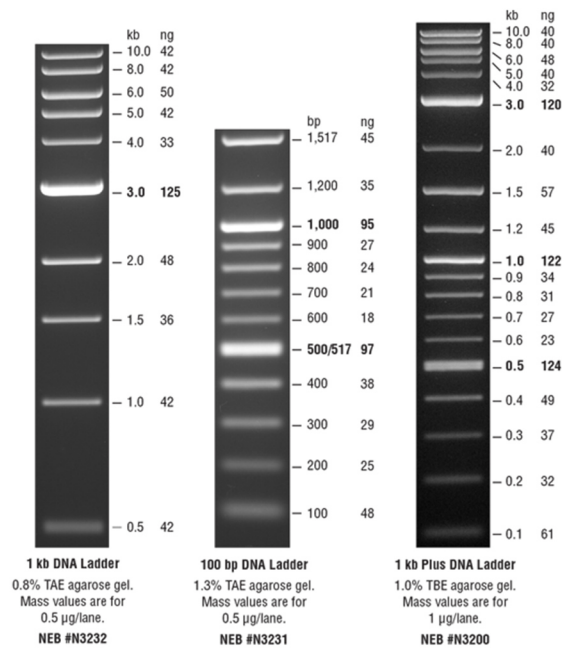
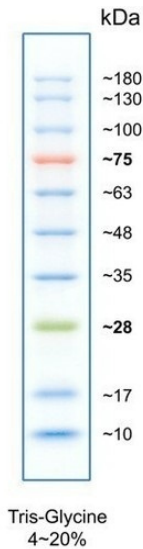


Figure 40 DNA-size ladders (NEB, Massachusetts, USA). Adapted from [https://www.nebiolabs.com.au/-/media/nebus/page-images/newsized-brochure-images/markers-and-ladders/dna\\_markers.png](https://www.nebiolabs.com.au/-/media/nebus/page-images/newsized-brochure-images/markers-and-ladders/dna_markers.png).



**Figure 41 BlueStar Prestained Protein Marker (Nippon Genetics, Tokio, Japan).** Adapted from [https://www.nippongenetics.eu/bilder/products/protein-elektrophorese/prestained-protein-marker/blue-star0\\_500x5200\\_481x500.jpg](https://www.nippongenetics.eu/bilder/products/protein-elektrophorese/prestained-protein-marker/blue-star0_500x5200_481x500.jpg).

## Enzymes

**Table 6 Enzymes used in this work.**

<b>Enzyme</b>	<b>Supplier</b>
BamHI	NEB, Massachusetts, USA
EcoRI	NEB, Massachusetts, USA
KpnI	NEB, Massachusetts, USA
MfeI	NEB, Massachusetts, USA
NdeI	NEB, Massachusetts, USA
SalI	NEB, Massachusetts, USA
XhoI	NEB, Massachusetts, USA
T4 DNA Ligase	NEB, Massachusetts, USA
T4 Polynucleotide Kinase	NEB, Massachusetts, USA
Shrimp Alkaline Phosphatase (rSAP)	NEB, Massachusetts, USA
Phusion® High-Fidelity DNA Polymerase	Produced in house
myTAQ polymerase NEB	NEB, Massachusetts, USA
Gibson Assembly Master Mix	NEB, Massachusetts, USA

## Equipment

**Table 7** Equipment used in this work.

<b>Instrument</b>	<b>Model</b>	<b>Manufacturer</b>
Airbrush	Fengda airbrush BD-130	Fenghua Bida Machinery Manufacture, Nigbo, China
Airbrush compressor	Fengda compressor FD-186	Fenghua Bida Machinery Manufacture, Nigbo, China
Agarose gel chamber	Perfectblue Mini S/M	Peqlab, Erlangen, Germany
Benchtop centrifuge	Microstar 17 Minispin plus	VWR, Pennsylvania, USA Eppendorf, Hamburg, Germany
Benchtop incubator	HT Ecotron	Infors, Bottmingen, Switzerland
Benchtop rocker	Rocker 3D digital	IKA, Staufen, Germany
Benchtop vortex	Vortex genie 2	Scientific industries
Block Heater	Touchscreen block heater Cooling Thermal Shaker Touch	Thermo Fisher Scientific, Massachusetts, USA VWR, Pennsylvania, USA
Blue light LED table	Illuminator	Nippon Genetics, Düren, Germany
Cell density meter	ULTRASPEC © 10 cell density meter	Biochrom, Berlin, Germany
Cell homogenizer with External air compressor	EmulsiFlex-C3 Super silent compressor	Avestin, Mannheim, Germany Aerotec, Seligenstadt, Germany
Electroporation device	Gene pulser II with capacitance extender plus	Bio-Rad, California, USA
FPLC	Äkta Pure	GE Healthcare, Illinois, USA
Gel documentation	E-BOX Amersham Imager 600 RGB	Vilber, Eberhardzell, Germany GE Healthcare, Illinois, USA
Incubator for microtiter plates	Titramax 1000 & Inkubator 1000	Heidolph, Schwabach, Germany
Incubator	HT Unitron, converted with a cooling device	Infors, Bottmingen, Switzerland
Laboratory scale	Se 1202	VWR, Pennsylvania, USA
L/M-EPC-7	Patch-clamp amplifier	List-Medical, Darmstadt, Germany
LIH 1600	16-bit A/D converter	HEKA Elektronik, Lambrecht, Germany
Low volume UV/Vis spectrophotometer	Nanodrop ND-1000	Peqlab, Erlangen, Germany
Magnetic stirrer	LabDisc S040 LabDisc VMS-A S040	VWR, Pennsylvania, USA
Microwave oven	Inverter	Sharp, Osaka, Japan
PCR cycler	Labcycler	Sensoquest, Göttingen, Germany
pH meter	pHenomenal pH1102	VWR, Pennsylvania, USA
Piston pipettes	Research Plus (2.5 µL, 10 µl, 100 µl, 1000 µl, 5 ml) 10 µl and 100 µl multipipette	Eppendorf, Hamburg, Germany
Platform shaker	Cetromat R/HK	B.Braun, Melsungen, Germany
Power Supply for agarose and SDS gels	PowerPac Basic	Bio-Rad, California, USA
Refrigerator and Freezer	(4°C) iQ500 KS36VAI41	Siemens, München, Germany

	(4°C) Super 520 (-20°C) GNP 3755 (-20°C) Froster 520 (-80°C) UFV500	Kirsch, Willstätt-Sand, Germany Liebherr, Bulle FR, Switzerland Kirsch, Willstätt-Sand, Germany Binder, Neckarsulm, Germany
Refrigerated centrifuge	Allegra X-30R Centrifuge	Beckman Coulter, California, USA
Sonicator	CL-18	Qsonica sonicators, Newtown, USA
Spectrophotometer	Spark	Tecan, Männedorf, Switzerland
Stereomicroscope		Novex, Netherlands
Vacuum pump	Diaphragm pump	Vacuubrand, Wertheim, Germany
Vertical bilayer setup		IonoVation, Osnabrück, Germany

Equipment for microfluidics microscopy and FACS measurements can be found in the associated chapter under experimental procedure.

**Table 8 Software used in this work.**

Software	Originator	Reference
Affinity Designer	Serif, Nottingham, UK	
GraphPad Prism	GraphPad Software, San Diego, USA	
ImageJ - Fiji		(Schindelin et al., 2012; Schneider et al., 2012)
Microsoft® Office	Microsoft ,Redmond, USA)	
Nest-o-Patch	V.Nesterov	
NIS-Elements 5.0	Nikon Instruments, Tokio, Japan	
PatchMaster	HEKA Elektronik, Lambrecht, Germany	
SnapGene®	GSL Biotech LLC, San Diego, USA	
UCSF Chimera	University of California San Francisco	(C. C. Huang et al., 2014; Pettersen et al., 2004)

## Chemicals

**Table 9 Chemicals used in this work.**

Chemical	Supplier
Acetone, synthesis grade	Carl Roth, Karlsruhe, Germany
Acetic acid, glacial	Carl Roth, Karlsruhe, Germany
Agar-Agar, Bioscience grade	Carl Roth, Karlsruhe, Germany
Agarose	Sigma Aldrich, St. Louis, USA
Ammonium chloride (NH <sub>4</sub> Cl)	Merck, Darmstadt, Germany
Ammonium heptamolybdate ((NH <sub>4</sub> ) <sub>6</sub> Mo <sub>7</sub> O <sub>24</sub> )	Carl Roth, Karlsruhe, Germany
Ammonium persulfate	Carl Roth, Karlsruhe, Germany
Ampicillin sodium salt, Bioscience grade	Carl Roth, Karlsruhe, Germany
L(+)-Arabinose	Carl Roth, Karlsruhe, Germany
Boric acid (H <sub>3</sub> BO <sub>3</sub> )	AppliChem, Darmstadt, Germany
Brilliant Blue G 250 (Coomassie®)	Carl Roth, Karlsruhe, Germany
Bromophenol blue	Merck, Darmstadt, Germany
Calcium chloride (CaCl <sub>2</sub> )	Carl Roth, Karlsruhe, Germany
Chloramphenicol	Carl Roth, Karlsruhe, Germany

Cobalt(II) chloride (CoCl <sub>2</sub> )	Merck, Darmstadt, Germany
Copper(II) sulfate (CuSO <sub>4</sub> )	AppliChem, Darmstadt, Germany
Dimethyl sulfoxide (DMSO)	Carl Roth, Karlsruhe, Germany
1,2-diphytanoyl- <i>sn</i> -glycero-3-phosphocholine (DPhPC)	Avanti Polar Lipids, Alabaster, AL, USA
DNase	Roche, Basel, Switzerland
dNTP mix (10 mM each)	Bioline, Luckenwalde, Germany
Ethanol (EtOH) denatured	Richter Chemie, Dockweiler, Germany
EtOH pure	Merck, Darmstadt, Germany
Ethylenediaminetetraacetic acid (EDTA)	Carl Roth, Karlsruhe, Germany
D(+)-Glucose, monohydrate	Carl Roth, Karlsruhe, Germany
Glycerol	Carl Roth, Karlsruhe, Germany
Glycine, Bioscience grade	Carl Roth, Karlsruhe, Germany
Hydrochloric acid 37%	Carl Roth, Karlsruhe, Germany
Imidazole	Sigma Aldrich, St. Louis, USA
n-Hexadecane	Merck, Darmstadt, Germany
n-Hexan	Merck, Darmstadt, Germany
Iron(II) sulfate (FeSO <sub>4</sub> )	Carl Roth, Karlsruhe, Germany
Isopropanol	Carl Roth, Karlsruhe, Germany
Isopropyl β-D-1-thiogalactopyranoside (IPTG)	Carl Roth, Karlsruhe, Germany
Lysozyme	Carl Roth, Karlsruhe, Germany
Magnesium chloride (MgCl <sub>2</sub> )	Carl Roth, Karlsruhe, Germany
Magnesium sulfate (MgSO <sub>4</sub> )	Merck, Darmstadt, Germany
Manganese(II) chloride (MnCl <sub>2</sub> )	Merck, Darmstadt, Germany
Midori Green Advance	Nippon Genetics, Tokio, Japan
Nickel(II) sulfate (NiSO <sub>4</sub> )	Carl Roth, Karlsruhe, Germany
β-Mercaptoethanol	Carl Roth, Karlsruhe, Germany
n-Pentane	Merck, Darmstadt, Germany
Peptone from casein	Carl Roth, Karlsruhe, Germany
Potassium chloride (KCl)	Carl Roth, Karlsruhe, Germany
Potassium hydroxide pellets (KOH)	Carl Roth, Karlsruhe, Germany
Potassium phosphate (KH <sub>2</sub> PO <sub>4</sub> /K <sub>2</sub> HPO <sub>4</sub> )	Carl Roth, Karlsruhe, Germany
Rapamycin	Hölzel Diagnostika, Köln, Germany
Rotiphorese® Gel 30 (37.5:1)	Carl Roth, Karlsruhe, Germany
Sodium acetate (NaCH <sub>3</sub> COO)	Carl Roth, Karlsruhe, Germany
Sodium chloride (NaCl)	Carl Roth, Karlsruhe, Germany
Sodium dodecyl sulfate (SDS)	Carl Roth, Karlsruhe, Germany
Sodium hydroxide pellets (NaOH)	Carl Roth, Karlsruhe, Germany
Sodium phosphate (NaH <sub>2</sub> PO <sub>4</sub> /Na <sub>2</sub> HPO <sub>4</sub> )	Carl Roth, Karlsruhe, Germany
Sodium propionate (CH <sub>3</sub> CH <sub>2</sub> CO <sub>2</sub> Na)	Carl Roth, Karlsruhe, Germany
Spectinomycin	Carl Roth, Karlsruhe, Germany
Tetramethylethylenediamine (TEMED)	Carl Roth, Karlsruhe, Germany
Tris(hydroxymethyl)-aminomethan (Tris)	Carl Roth, Karlsruhe, Germany
Triton® X 100 / IGEPAL	Carl Roth, Karlsruhe, Germany
Tween®20	Carl Roth, Karlsruhe, Germany
Yeast extract, micro granulated	Carl Roth, Karlsruhe, Germany
Zinc sulfate (ZnSO <sub>4</sub> )	Carl Roth, Karlsruhe, Germany

## Buffers and Solutions

Table 10 Buffers and solutions used in this work.

Buffer or solutions	Composition
<b>Antibiotics stock solutions (1000x)</b>	100 mg/ml ampicillin in ddH <sub>2</sub> O 25 mg/ml chloramphenicol in EtOH 50 mg/ml spectinomycin in ddH <sub>2</sub> O
<b>M9 salts 10x</b>	60 g/L Na <sub>2</sub> PO <sub>4</sub> , 30 g/L KH <sub>2</sub> PO <sub>4</sub> , 5 g/L NaCl, 10 g/L NH <sub>4</sub> Cl
<b>Micronutrients for M9 medium (1000x)</b>	3 mM (NH <sub>4</sub> ) <sub>6</sub> Mo <sub>7</sub> O <sub>24</sub> , 400 mM H <sub>3</sub> BO <sub>3</sub> , 30 mM CoCl <sub>2</sub> , 10 mM CuSO <sub>4</sub> , 80 mM MnCl <sub>2</sub> , 10 mM ZnSO <sub>4</sub>
<b>Protein loading dye</b>	200 mM Na <sub>3</sub> PO <sub>4</sub> , 4% SDS, 20% Glycerol, 0.002% Bromophenol Blue
<b>10x SDS-Page running buffer</b>	500 mM Tris-HCl, 1.9 M Glycine, 1 <sup>80</sup> g/L SDS, pH 8.8
<b>50x TAE buffer for DNA electrophoresis</b>	2 M Tris-HCl, 0.5 M Acetic Acid, 50 mM EDTA, pH 8.0
<b>10x PBS</b>	40 mM KH <sub>2</sub> PO <sub>4</sub> , 160 mM Na <sub>2</sub> HPO <sub>4</sub> , 1.15M NaCl, pH 7.4
<b>Chemical competent cell solutions</b>	
CaCl <sub>2</sub> solution for competent cells	80 mM CaCl <sub>2</sub> (sterile)
Cryo-CaCl <sub>2</sub> solution for competent cells	CaCl <sub>2</sub> , 20% (v/v) Glycerol (sterile)
<b>Protein Purification Buffers Phusion® High-Fidelity DNA Polymerase</b>	
Buffer A	50 mM Tris pH 7.4, 10% (v/v) glycerol autoclaved
Buffer B	50 mM Tris pH 7.4, 300 mM NaCl, 30 mM Imidazole, sterile filtered and degassed
Buffer B2	50 mM Tris pH 7.4, 1 M NaCl, 30 mM Imidazole, sterile filtered and degassed
Buffer C	50 mM Tris pH 7.4, 300 mM NaCl, 300 mM Imidazole, sterile filtered and degassed
Buffer D	100 mM Tris pH 8.2, 0.1 mM EDTA, 1 mM DTT
Buffer E	0.1 mM EDTA, 1 mM DTT, 0.4% (v/v) IGEPAL® CA-630 (or Triton X-100), 0.4% (v/v) Tween 20 100% Glycerol
<b>SDS PAGE solutions</b>	
Stacking buffer	1.5 M Tris, 0.4% (v/v) SDS, pH 8.8
Separation buffer	0.5 M Tris, 0.4% (v/v) SDS, pH 6.6
10x SDS Running Buffer	30.2 g/l Tris, 144 g/l glycine, 1% (v/v) SDS
2x loading dye	200 mM Na <sub>3</sub> PO <sub>4</sub> , 4% (v/v) SDS, 20% (v/v) Glycerol, 0.002% (w/v) Bromophenol Blue, 5% (v/v) β-mercaptoethanol
Coomassie staining solution	25 mg Brilliant Blue G 250, 3 ml HCl 37% in 1 L ddH <sub>2</sub> O
<b>DNA precipitation solutions</b>	
Sodium-Acetate	3M Na-Acetate pH 5.2 in ddH <sub>2</sub> O
70% EtOH	70% EtOH in ddH <sub>2</sub> O
<b>Bilayer solution</b>	100 mM KCl, 10 mM HEPES, pH 7

---

## Cultivation Medium

Sterilization of media was performed at 121°C for 15 minutes. Sterile filter antibiotics were added after sterilization in cooled down medium with a final concentration of 100 µg/ml for ampicillin, 25 µg/ml for chloramphenicol and 50 µg/ml spectinomycin.

### **Lysogenic broth (LB) medium** (“LB (Luria-Bertani) Liquid Medium,” 2006)

0.5% (w/v) yeast extract, 1% (w/v) peptone, 1% (w/v) NaCl, pH 7.4 adjusted with NaOH. Stored at 4 °C after antibiotics were added.

### **Terrific broth (TB) medium** (“Terrific Broth,” 2015)

TB-A: Tryptone 12 g, yeast extract 24 g, glycerol 4 g; ingredients were combined in a final volume of 900 ml ddH<sub>2</sub>O and sterilized. TB-B: KH<sub>2</sub>PO<sub>4</sub> 2.3 g, K<sub>2</sub>HPO<sub>4</sub> 16.4 g; ingredients were combined in a final volume of 100 ml ddH<sub>2</sub>O and sterilized. For final TB-medium TB-A (900 ml) and TB-B (100 ml) were mixed. Stored at 4 °C after antibiotics were added.

### **LB agar** (“LB Agar,” 2009)

0.5% (w/v) yeast extract, 1% (w/v) peptone, 1% (w/v) NaCl, 1.5% agar, pH 7.4 adjusted with NaOH. Stored at 4 °C after antibiotics were added.

### **Super optimal broth with catabolite repression (SOC) medium** (“SOC Medium for E. Coli,” 2012)

2% (w/v) peptone, 0.5% (w/v) yeast extract, 10 mM NaCl, 2.5 mM KCl, 5 mM MgCl<sub>2</sub>, 5 mM MgSO<sub>4</sub> and 20 mM glucose. Sterile filtered MgCl<sub>2</sub>, MgSO<sub>4</sub>, and glucose were added after sterilization in cooled down medium. Stored at room temperature.

### **M9 medium with arabinose**

6 g/L Na<sub>2</sub>PO<sub>4</sub>, 3 g/L KH<sub>2</sub>PO<sub>4</sub>, 0.5 g/L NaCl, 1 g/L NH<sub>4</sub>Cl, pH 7.4 (Diluted 1:10 from M9 Salts 10x). After sterilization 3 nM (NH<sub>4</sub>)<sub>6</sub>Mo<sub>7</sub>O<sub>24</sub>, 0.4 µM H<sub>3</sub>BO<sub>3</sub>, 30 nM CoCl<sub>2</sub>, 10 nM CuSO<sub>4</sub>, 80 nM MnCl<sub>2</sub>, 10 nM ZnSO<sub>4</sub>, 1 mM MgSO<sub>4</sub>, 100 µM CaCl<sub>2</sub> (Diluted 1:1000 from micronutrients M9 1000x solution), 0.2% (w/v) arabinose, and 1 µM FeSO<sub>4</sub> were added. Stored at 4 °C after antibiotics were added.

---

## Methods

### *E. coli* DH10 $\beta$ Cultivation

Required solutions:

LB medium and LB agar with appropriate antibiotics

*E. coli* cells were cultivated in LB medium containing the appropriate antibiotics at 37°C in a shaking incubator at 180 rpm or on LB agar plates with appropriate antibiotics. Cell density was determined by measuring the optical density at 600 nm (OD<sub>600nm</sub>) using a cell density meter (OD<sub>600nm</sub> of 1 equals  $\sim 8 \times 10^8$  cells/ml). For long term storage, 500  $\mu$ l of overnight culture in LB medium was mixed with 500  $\mu$ l sterile glycerol, shock frozen in liquid nitrogen and stored at -80°C.

### Preparing Chemically Competent Cells

Required solutions:

LB medium, LB agar, CaCl<sub>2</sub> solution for competent cells, Cryo-CaCl<sub>2</sub> solution for competent cells (both precooled to 4°C)

A single colony from a LB agar plate was used to inoculate a 10 ml culture of *E. coli* cells in LB medium (if necessary with appropriate antibiotics) and grown overnight at 37°C in a shaking incubator at 180 rpm. The next day 200 ml LB medium was inoculated with the overnight culture to an OD<sub>600nm</sub> of 0.1 and grown at 37°C in a shaking incubator at 180 rpm until it reached an OD<sub>600nm</sub> of  $\sim 0.6$ . The culture was split into 50 ml reaction tubes and chilled on ice for 20 minutes. After cooling cells were centrifuged (2500xg, 4 °C, 15 min) and the supernatant was decanted. All following steps were performed on ice. Cells were washed in 50 ml CaCl<sub>2</sub> solution for competent cells and chilled for another 30 minutes on ice. Cells were then centrifuged (2500xg, 4 °C, 15 min), the supernatant decanted and the pellet was carefully resuspended in 5.5 ml cryo-CaCl<sub>2</sub> solution for competent cells. Aliquots of 150  $\mu$ l were made, flash frozen in liquid nitrogen and stored at -80°C. Competent cells were used up to 6 months after preparation.

### Heat-Shock Transformation of *E. coli* Cells

Required solutions:

SOC medium, LB agar with appropriate antibiotics

Chemically-competent cells were thawed on ice and split into 50  $\mu$ l aliquots and 20 ng DNA was added carefully. This mixture was incubated on ice for 30 minutes and subsequently heat shocked at 42°C for 45 seconds. Tubes were then placed on ice for 2 minutes. Afterwards, 450  $\mu$ l SOC medium was added and the cells recovered at 37°C in a shaking incubator at 180 rpm for 1 hour. Cells were then plated onto LB agar plates with appropriate antibiotics and incubated overnight at 37°C.

### Electro-Competent *E. Coli* Cells and Electroporation Transformation

Required solutions:

Sterile ddH<sub>2</sub>O (RT), SOC medium (37°C), LB medium and LB agar with appropriate antibiotics

A single colony from a LB agar plate was used to inoculate a 10 ml culture of *E. coli* cells in LB medium (if necessary with appropriate antibiotics) and grown overnight at 37°C in a shaking incubator at 180 rpm. The next day 200 ml LB medium was inoculated with the overnight culture to an OD<sub>600nm</sub> of 0.1

---

and grown at 37°C in a shaking incubator at 180 rpm until it reached an OD<sub>600nm</sub> of ~0.6. The culture was split into 50 ml reaction tubes, centrifuged (2500xg, 21 °C, 15 min), the supernatant was decanted and the cells were then washed with 50 ml sterile ddH<sub>2</sub>O. This step was performed twice. After the second wash, cells were centrifuged (2500xg, 21 °C, 15 min) again and resuspended in 1 ml ddH<sub>2</sub>O.

For electroporation 1 µl of 20 ng/µl DNA solution in ddH<sub>2</sub>O was mixed with 100 µl electrocompetent cell suspension in a 1 mm electroporation cuvet. The cell/DNA mixture was electroporated with a Gene pulser II with a capacitance extender plus with the following conditions: 300 Ω, 25 µF, 1.8 kV. Usually time constants of around 6-7 ms were achieved. Transformations with visible electrical discharge and unusual time constants were discarded. Immediately after the pulse, 900 µl SOC medium (prewarmed at 37°C) were added to the cells and the suspension was transformed into a fresh tube and cells recovered at 37°C in a shaking incubator at 180 rpm for 1 hour. Cells were then plated onto LB agar plates with appropriate antibiotics and incubated overnight at 37°C.

### **Isolation of Plasmid DNA from *E. Coli***

Plasmid DNA was prepared from overnight cultures of *E. coli* using a NucleoSpin kit for plasmid DNA from Macherey-Nagel (MN, Düren, Germany). For small cultures from 5-20 ml NucleoSpin® NoLid Mini-Prep kit was used and for larger cultures > 100 ml the NucleoBond® Xtra Midi kit was used. Preparations were performed according to manufacturer's instructions. Isolated DNA was stored at -20°C.

### **DNA Clean-Up from PCR and Gel electrophoresis**

DNA from polymerase chain reactions and agarose gels was purified using the Nucleospin Gel and PCR clean-up Kit from Macherey-Nagel. Preparations were performed according to manufacturer's instructions. Isolated DNA was stored at -20°C

### **Determination of DNA Concentration**

DNA concentration measurements were performed with the NanoDrop ND-1000. DNA concentration was determined at A<sub>260nm</sub>. Quotients of A<sub>260nm</sub>/A<sub>280nm</sub> and A<sub>260nm</sub>/A<sub>230nm</sub> were calculated to estimate the purity of the sample.

## Polymerase Chain Reaction (PCR)

PCR reactions were performed with Phusion® High-Fidelity DNA polymerase. **Table 11** shows the PCR mixture for a single reaction of 50  $\mu$ l suggested by the manufacturer (NEB, Massachusetts, USA) for Phusion® High-Fidelity DNA polymerase. For this work all volumes were scaled up to 4-8 times depending on the need of DNA yield. **Table 12** shows the PCR cyclers program.

**Table 11** Thermocycler program for Phusion® High-Fidelity DNA Polymerase.

Component	Reaction volume ( $\mu$ l)	Final concentration
5x HF Buffer	10	1x
dNTP mix 10 mM	1	200 $\mu$ M
Forward primer 10 $\mu$ M	2.5	500 nM
Reverse primer 10 $\mu$ M	2.5	500 nM
DNA template 20 ng/ $\mu$ l	1	400 pg
Phusion® High-Fidelity DNA Polymerase 2 U/ $\mu$ l	0.5	0.04 U
ddH <sub>2</sub> O	ad 50	-

**Table 12** Thermocycler program for Phusion® High-Fidelity DNA Polymerase.

Step	Temperature [°C]	Time [s]	Cycles
Initial denaturation	98	30	1
Denaturation	98	30	30
Annealing	60-70 Depending on primer pair	20	
Elongation	72	30 per kb	
Final Elongation	72	300	1
Hold	4	$\infty$	

## Colony PCR after Fluorescence Activated Cell Sorting (FACS)

For colony PCR after FACS OneTaq® DNA polymerase was used according to manufacturer's (NEB, Massachusetts, USA) instructions (**Table 13**). For sorted cells, a maximum of 6  $\mu$ l PBS cell suspension can be used as excessive PBS interferes with the PCR. **Table 14** shows the PCR cyclers program. Primers were designed to bind on the T7 promoter (forward: 5'-CCATGGGCTGCCTAATACGA) and after the second terminator (reverse: 5'-TTATTGCTCAGCGGTGGCAG).

**Table 13** OneTaq® DNA polymerase PCR mix.

Component	Reaction volume ( $\mu$ l)	Final concentration
5x OneTaq standard reaction buffer	10	1x
dNTP mix 10 mM	1	200 $\mu$ M
Forward primer 10 $\mu$ M	2.5	500 nM
Reverse primer 10 $\mu$ M	2.5	500 nM
DNA template (cells in PBS)	6	-
OneTaq® DNA polymerase	0.25	1.25 U
ddH <sub>2</sub> O	ad 50	-

**Table 14 Thermocycler program for OneTaq® DNA polymerase.**

Step	Temperature [°C]	Time [s]	Cycles
Initial denaturation	94	300	1
Denaturation	94	30	30
Annealing	55-65 Depending on primer pair	30	
Elongation	68	60 per kp	
Final Elongation	68	300	1
Hold	4	∞	

## Agarose Gel Electrophoresis

Required Solutions: 0.5-1.5% (w/v) agarose in 1xTAE buffer, Midori Green

Agarose gel electrophoresis was performed for visual analysis and purification of restricted DNA samples. Depending on the DNA sample size 0.5-1.5% (w/v) agarose in 1xTAE buffer (0.5% for fragments >4kb to 1.5% for fragments <500 bp) was used for DNA separation. 50 ml agarose in 1xTAE buffer was melted in the microwave and 1.5  $\mu$ l Midori Green was added to the agarose under stirring and casted in the agarose gel chambers. DNA was mixed with 6x QuickLoad® purple loading dye prior loading. DNA ladder was chosen according to sample size. Electrophoresis was performed at a constant voltage of 100-120 V for 40-90 minutes. DNA was visualized using the E-BOX geld documentation or a blue light LED table.

## Restriction of DNA

The digestion protocol for enzymes is summarized in **Table 15**. Digestion time was prolonged to 1 hour for all enzymes (Exception NdeI: 1.5 hours). Plasmid backbones were additionally incubated with shrimp alkaline phosphatase to reduce religation events due to dephosphorylation.

**Table 15 Components of a DNA restriction reaction.**

Component	Reaction Volume
DNA	2.5 $\mu$ g
10x CutSmart	10 $\mu$ l
Enzyme I	1.5 $\mu$ l
Enzyme II	1.5 $\mu$ l
rSAP	0.5 (only for backbones) $\mu$ l
Nuclease-free ddH <sub>2</sub> O	ad 100 $\mu$ l

## Gibson Assembly

Synthetic double stranded DNA (gBlocks - ordered from Integrated DNA Technologies (IDT, Iowa, USA)) was cloned via Gibson assembly into the destination vectors. For this purpose, gBlocks were designed with a 50 bp overhang compatible with the insert area in the backbone. Gibson assembly was performed at 50°C for 50 minutes according to **Table 16**. For transformation, a volume of 2  $\mu$ l of the final mixture was used.

**Table 16 Components of Gibson assembly reaction.**

<b>Component</b>	<b>Reaction Volume</b>
Backbone DNA	10-20 nM
Insert DNA (gBlock)	50 nM
Gibson Master mix (2x)	3 $\mu$ l
ddH <sub>2</sub> O	ad 6 $\mu$ l

## Oligo Cloning

For oligo cloning, two overlapping oligos up to 80 bp with compatible overhangs for specific restrictions sites were designed and annealed. For annealing, both oligos were mixed with equal volumes (10  $\mu$ M each) and heated up to 95°C for 5 minutes. The mixture was then cooled down for 30 minutes at room temperature.

## Ligation and Sequencing

Ligation of insert and vector DNA was performed according to **Table 17** either for 1 hour at room temperature or for 16 hours at 16°C. Heat inactivation was performed for 10 minutes at 65°

**Table 17 Components of ligation reaction.**

<b>Component</b>	<b>Reaction Volume</b>
Backbone DNA	0.02 pmol
Insert DNA	0.06-0.1 pmol
T4 Buffer	1 $\mu$ l
T4 Ligase	0.5 $\mu$ l
ddH <sub>2</sub> O	ad 10 $\mu$ l

## DNA Precipitation

Required solutions:

3M Na-Acetate pH 5.2, 100% ice-cold EtOH (pure), 70% EtOH (pure)

For DNA precipitation 1/10 volume of 3M Na-Acetate pH 5.2 and 2.5 volumes of ice-cold 100% EtOH were added to the DNA sample. The solution was vortexed and kept for 1 hour at -20°C to precipitate the DNA. DNA was recovered by centrifugation (25000xg, 4°C, 20 minutes). EtOH was poured off and the pellets were washed once with 70% EtOH. DNA pellets were then air-dried until excessive EtOH was vanished. Precipitated DNA was usually resuspended in nuclease free ddH<sub>2</sub>O.

## Fast Protein Liquid Chromatography (FPLC) for Phusion® High Fidelity Polymerase

All credit for this protocol belongs to A. Gräwe.

Required solutions: TB medium, IPTG, Glycerol, Phusion® High-Fidelity Polymerase Buffer A-E, Lysozyme, DNase, Triton X-100

---

### Protein expression

*E. coli* BL21(DE3) cells were co-transformed with plasmids pPhusion and pSJS1240 following the regular protocol for the transformation of chemo-competent *E. coli* cells with a prolonged regeneration phase of 2 hours. A single colony was picked from the Agar plate and used to inoculate 10 ml TB-Amp/Spec medium. This preculture was used to inoculate three flask 500 ml TB-Amp/Spec medium. Cultures were grown until an OD<sub>600nm</sub> of 1 and induced with a final concentration of 1 mM IPTG. Protein expression was performed at 37°C in a shaking incubator at 160 rpm for 12 hours. Cells were harvested by centrifugation (3500xg, 4°C, 20 min). Cells were resuspended in 25 ml buffer A per litre culture volume and transferred in 25 ml aliquots to 50 ml reaction tubes.

### Cell lysis

The following ingredients were added to the cell suspension in buffer A: Triton X-100 0.1% (v/v); MgSO<sub>4</sub> 5 mM; Lysozyme 300 µg/ml; 10 µg/ml DNase. Cells were then lysed by sonication (4x 1 min 75% amplitude intercepted by 1 min pauses), while being kept on ice. Cell debris was precipitated by centrifugation (25000xg, 4°C, 30 min). The supernatant was transferred into a fresh tube and endogenous host proteins were denatured at 85°C for 30 min and subsequently centrifuged (25000xg, 4°C, 30 min). Supernatant was filtered through a 0.45 µm sterile filter to remove excessive particles and transferred to a fresh 50 ml tube.

### Purification

A 5 ml Ni-NTA sepharose column (MN, Düren, Germany) was equilibrated with 10 column volumes (CV) of buffer B with a flow rate of 1 ml/min. All previous supernatant samples were pooled and loaded on the column with a constant flow of 1 ml/min. After the loading, the column was washed with 3 CV buffer B, followed by 2 CV of buffer B2 and again 3 CV of buffer B. Elution was performed with buffer C in 500 µl fractions. All protein containing fractions were pooled and the buffer was exchanged with buffer D with Vivaspin 20 (MWCO 10 kDA, Sartorius, Göttingen, Germany) columns. According to manufacturer's instructions, two concentration steps were performed for complete buffer exchange. Protein concentration was measured with the NanoDrop ND-1000 at an absorption of A<sub>280nm</sub>. Phusion® High-Fidelity Polymerase was diluted to a concentration of 0.4 mg/ml with buffer D. Finally, this diluted solution was mixed with one volume equivalent of buffer E. This solution was then mixed with one volume equivalent of 100% glycerol, resulting in approximately 2 U/µl. 1 ml aliquots were snap frozen in liquid nitrogen. For long term storage aliquots were stored at -80 °C. The working aliquots were stored at -20 °C.

### SDS Polyacrylamide Gel Electrophoresis (SDS-PAGE)

#### Required solutions:

Separation buffer, Stacking buffer, Rotiphorese® Gel 30, APS 15% in ddH<sub>2</sub>O, TEMED, ddH<sub>2</sub>O, SDS running buffer 1x, 2x loading dye.

Sodium dodecyl sulfate (SDS) polyacrylamide gel electrophoresis was used to examine protein expression efficiency. SDS-gels of 12% acrylamide were casted with the Mini-PROTEAN® system according to (Table 18). Separation gels were casted first and covered with isopropanol for top edge smoothing. After the separation gels were fully polymerized, isopropanol was removed and stacking gels were casted on top. Immediately after casting a comb was inserted into the chamber. Fully polymerized gels were either directly used or stored in moist paper towels for up to 3 weeks at 4°C.

**Table 18 Composition of 12 % polyacrylamide gels.** Volumes are for two gels.

Component	Stacking gel (5%)	Separation gel (12%)
ddH <sub>2</sub> O	2.65 ml	3.49 ml
Separation buffer	-	2.7 ml
Stacking buffer	1.25 ml	-
Rotiphorese® Gel 30	830 $\mu$ l	4.6 ml
APS (15%, freshly prepared)	200 $\mu$ l	200 $\mu$ l
TEMED	10 $\mu$ l	10 $\mu$ l

Equal volumes of sample were mixed with 2x loading dye and denatured for 10 min at 95°C. 20  $\mu$ l of the prepared sample was loaded per well with a protein ladder. Electrophoresis was performed at 120 V for 90 minutes in a 1x running buffer. SDS gels were stained with a Coomassie staining solution in a microwave for about 30 seconds. Afterwards the gels were shaken for 30 minutes and detained several times with ddH<sub>2</sub>O. Image acquisition was performed with E-BOX gel documentation.

## Experimental Procedure

### Vectors

All vectors used and generated in this work can be found in **Table 19**.

**Table 19 Vectors used in this work.**

Name	Promoter-Repressor/Activator (inducer)	Ori (class)	Selection marker	Usage	Originator
pPRO24	P <sub>P<sub>prpB</sub></sub> -PrpR (Propionate)	ColE1 + F1 (A)	AmpR	Expression of R-GECO1 and G-GECO1	Addgene #17805 (S. K. Lee & Keasling, 2006)
pACYCT2	P <sub>T7</sub> and P <sub>tac</sub> – LacI (IPTG)	p15A (B)	CmR	Basis for creation of pCTRL2	Addgene #45799 (Ponchon et al., 2013)
pTorPE-R-GECO1	P <sub>BAD</sub> - AraC (Arabinose)	ColE1	AmpR	R-GECO1 template	Addgene #32465 (Zhao et al., 2011)
pTorPE-G-GECO1	P <sub>BAD</sub> - AraC (Arabinose)	ColE1	AmpR	G-GECO1 template	Addgene #32466 (Zhao et al., 2011)
pCTRL2.T7.wt.sRBS	P <sub>T7</sub> - LacI (IPTG)	p15A (B)	CmR	pCTRL2 variant	This work
pCTRL2.T7.03.sRBS	P <sub>T7</sub> - LacI (IPTG)	p15A (B)	CmR	pCTRL2 variant	This work
pCTRL2.T7.03.U6	P <sub>T7</sub> - LacI (IPTG)	p15A (B)	CmR	pCTRL2 variant	This work

pCTRL2.T7.03.U9	P <sub>T7</sub> - LacI (IPTG)	p15A (B)	CmR	pCTRL2 variant	This work
pCTRL2.T7.14.sRBS	P <sub>T7</sub> - LacI (IPTG)	p15A (B)	CmR	pCTRL2 variant	This work
pCTRL2.T7.14.U6	P <sub>T7</sub> - LacI (IPTG)	p15A (B)	CmR	pCTRL2 variant	This work
pCTRL2.T7.14.U9	P <sub>T7</sub> - LacI (IPTG)	p15A (B)	CmR	pCTRL2 variant	This work
pCTRL2.T7.100.sRBS	P <sub>T7</sub> - LacI (IPTG)	p15A (B)	CmR	pCTRL2 variant	This work
pCTRL2.T7.100.U9	P <sub>T7</sub> - LacI (IPTG)	p15A (B)	CmR	pCTRL2 variant	This work
pPhusion	P <sub>T7</sub> - LacI (IPTG)	ColE1	AmpR	Pfu-Sso7d (Phusion® High-Fidelity DNA Polymerase)	Brought by Alexander Gräwe into the laboratory
pSJS 1240	unknown	p15A (B)	SmR	Encodes rare argenyl and isoleucyl tRNAs	Addgene #12234 (R. Kim et al., 1998)

### Plasmid Construction: pPRO24-G-GECO1 and pPRO24-R-GECO1

The plasmid pPRO24, pTorPE-G-GECO1 and pTorPE-R-GECO1 were obtained from Addgene (Zhao et al., 2011). Sequences for G-GECO1 and R-GECO1 were amplified with oligos introducing a N-terminal EcoRI and a C-terminal BamHI restriction site. PCR product and pPRO24 backbone were digested with EcoRI/BamHI and ligated. The final product was verified by sequencing.

#### G-GECO1 (M13-cpeGFP-CaM)

MVDSSRRKWNKTGHAVRAIGRLSSLEENVYIKADKQKNGIKANFKIRHNIEDGGVQLAYHYQQNTPIGDGPVLLPD  
 NHYLSVQSILSKDPNEKRDHMLLEFVTAAGITLGMDELYKGGTGGSMVSKGEELFTGVVPIQVELDGDVNGHKF  
 SVSGEGEGDATYGKLTCLKFICTTGKLPVPWPTLVTTLYGVQCFSRYPDHMKQHDFFKSAMPEGYIQERTIFFKD  
 DGNKTRAEVKFEGDTLVNRIELKGIIDFKEDGNILGHKLEYNTRDQLTEEQIAEFKEAFSLFDKGDGTITTKEL  
 GTVMRSLGQNPTEAELQDMINEVDADGDGTIDFPEFLTMMARKMKDSEEEIREAFRVFDKDGNGYIGAAELRH  
 VMTNLGEKLTDEEVDEMIRVADIDGGQVNYEEFVQMMTAK

#### R-GECO1 (M13-cpRFP-CaM)

MVDSSRRKWNKTGHAVRAIGRLSSPVVSEMYPEDGALKSEIKKGLRLKDGGHYAAEVKTTYKAKKPVQLPGAYI  
 VDIKLDIVSHNEDYTIVEQCERAEGRHSTGGMDELYKGGTGGSLVSKGEEDNMAIIEKFMRFKVHMEGSVNGHEF  
 EIEGEGEGRPYEAFTAKLKVTKGGPLPFAWDILSPQFMYGSKAYIKHPADIPDYFKLSFPEGFRWERVMNFEDG  
 GIIHVNQDSSLQDGVFIYKVKLRGTNFPDGPVMQKKTMGWEATRDQLTEEQIAEFKEAFSLFDKGDGTITTKEL  
 LGTVMRSLGQNPTEAELQDMINEVDADGDGTIDFPEFLTMMARKMKDSEEEIREAFRVFDKDGNGYIGAAELR  
 HVMTNLGEKLTDEEVDEMIRVADIDGGQVNYEEFVQMMTAK

---

## Plasmid Construction: pCTRL2

The pCTRL2 vector is based on the pACYCT2 plasmid obtained from Addgene (Ponchon et al., 2013). Single expression/repression elements were changed in a multistep approach. First of all, the *lacI* gene mutation W220F introduced by site directed mutagenesis to ensure better repression (Gatti-Lafranconi et al., 2013). Then the tac promoter was exchanged with a T7.wt.sRBS cassette (Elowitz & Leibler, 2000; Studier, 1991; Studier et al., 1990) flanked by several terminators (Mairhofer et al., 2015) with a combination of Gibson assembly and oligo cloning.

pCTRL2.T7.wt.sRBS nucleotide sequence between the *lacI* and the *cmr* (chloramphenicol acetyltransferase) gene

(rrnB T1 terminator-T7 terminator-T7 promoter-lac operator-RBS-T3 terminator-rrnB T1 terminator-T7 terminator)

```
CGGGATCTCGACGCTCTCCCTTATGCGACTCCTGCATTAGGAAATTAATACGACTCACTATCAATTCAAATAAAA
CGAAAGGCTCAGTCGAAAGACTGGGCCTTTCGTTTTATCTGTTGTTTGTCTGGTGAACGCTCTCGTCGACCTGCAG
CTAGCATAACCCCTTGGGGCCTCTAAACGGGTCTTGAGGGTTTTTTTGCCATGCTGATGAGCCATGGGCTGCCTA
ATACGACTCACTATAGGGGAATTGTGAGCGGATAACAATTCCCTCTAGAAATAATTTTGTTTAACTTTAAGAAG
GAGATATACATATGACCGCTGGTACTAGTGGAGGTGGTACCGGATCCCTAGCATAACCCCGCGGGGCCTCTTCGG
GGGTCTCGCGGGTTTTTTTGCTGAAAGGAGCTCCAAATAAAACGAAAGGCTCAGTCGAAAGACTGGGCCTTTCGT
TTTATCTCGAGCTGCCACCGCTGAGCAATAACTAGCATAACCCCTTGGGGCCTCTAAACGGGTCTTGAGGGTTTT
TTTGCTGAAACCTCAGGCATTTGAGAAGCACACGGTCACACTGCTTCCGGTAGTCAATAAACCGGTAAACCAGCA
ATAGACATAAGCGGCTATTTAACGACCCTGCCCTGAACCGACGACCGGGTTCGAATTTGCTTTTGAATTTCTGCCA
TTCATCCGCTTATTATCACTTATTCAGGCGTAGCACCAGGCGTTTAAGGGCACCAATAACTGCCTTAAAAAAA
```

New promoter strength combinations were then assembled by oligo cloning which changed the spacing between the terminator, promoter, lacO and RBS sequence. In addition, the fluorescent protein mKO<sub>K</sub> was introduced into the multiple cloning site with a 5' NdeI and 3' KpnI restriction site. This made the cloning easier as the differences between cut and uncut plasmid were clearly visible and also helped to find possible religands in library cloning. The following sequence shows the pCTRL2.T7.100.sRBS expression cassette. Functional elements were changed with components of **Table 20**.

pCTRL2.T7.100.sRBS nucleotide sequence between the *lacI* and the *cmr* (chloramphenicol acetyltransferase) gene

(rrnB T1 terminator-T7 terminator-T7 promoter-lac operator-RBS-mKO<sub>K</sub>-T3 terminator-rrnB T1 terminator-T7 terminator)

CGGGATCTCGACGCTCTCCCTTATGCGACTCCTGCATTAGGAAATTAATACGACTCACTATCAATTCAAATAAAA  
 CGAAAGGCTCAGTCGAAAGACTGGGCCTTTCGTTTTATCTGTTGTTTGTGCGGTGAACGCTCTCGTCGACCTGCAG  
 CTAGCATAACCCCTTGGGGCCTCTAACGGGTCTTGAGGGTTTTTTGTCATGCTGATGAGCCATGGTAATACGAC  
 TCACTATAGGGGAATTGTGAGCGGATAACAATTCCACCGGTAAGAGGAGAAAAGGAGCATATGGTGTCTGTAATT  
 AAGCCAGAAATGAAGATGCGTTATTACATGGACGGAAGCGTTAATGGCCATGAGTTTACTATCGAGGGGGAGGGA  
 ACCGGGCGTCCGTATGAGGGCCACCAAGAAATGACATTACGCGTACTATGGCTGAGGGTGGACCTATGCCGTTT  
 GCCTTCGATCTGGTTTCCACGTCTTTTGTACGGCCACCGTGTGTTCCAAAAATATCCCGAAGAGATCCCGGAC  
 TATTTCAAACAGGCGTTCCAGAGGGTCTTAGCTGGGAACGTAGCCTGGAATTTGAGGACGGAGGATCAGCCAGT  
 GTATCGGCTCATATCTCTCTGCGCGGTAATACCTTCTATCATAAGAGCAAATTTACTGGTGTAAACTTTCCTGCT  
 GATGGTCCGATTATGCAAAATCAAAGTGTGGACTGGGAACCATCGACAGAGAAAATCACAGCCTCCGACGGAGTC  
 CTGAAAGGAGACGTAACGATGTACTTAAAGTTAGAAGGGGGCGGCAATCACAAGTGCCAGTTTAAGACAACCTAC  
 AAAGCGGCTAAAGAAATTTGGAAATGCCGGGTGACCACTACATCGGGCACCGCTTGTACGTAAGACCGAGGGT  
 AATTAATGTAACAGGTGGAGGATGCGGTGCGCCATTCTAAAGGTACCGGATCCCTAGCATAACCCCGCGGGGCC  
 TCTTCGGGGGTCTCGCGGGTTTTTTGCTGAAAGGAGCTCAAATAAAACGAAAGGCTCAGTCGAAAGACTGGGC  
 CTTTCGTTTTATCTCGAGCTGCCACCGCTGAGCAATAACTAGCATAACCCCTTGGGGCCTCTAACGGGTCTTGA  
 GGGTTTTTTGCTGAAACCTCAGGCATTTGAGAAGCACACGGTCACACTGCTTCCGGTAGTCAATAAACCGGTAA  
 ACCAGCAATAGACATAAGCGGCTATTTAACGACCCTGCCCTGAACCGACGACCGGGTCAATTTGCTTTCGAATT  
 TCTGCCATTCATCCGCTTATTATCACTTATTCAGGCGTAGCACCGGCGTTTAAGGGCACCAATAACTGCCTTAA  
 AAAAA

**Table 20** Exchangeable parts of the different expression vectors (T7 promoter-lac operator-RBS).

Part	Nucleotide sequence
pT7.03 (Imburgio et al., 2000)	TAATACGACTCACTACAGG
pT7.14 (Imburgio et al., 2000)	TGATACGACTCACTATAGG
pT7.100 (Imburgio et al., 2000)	TAATACGACTCACTATAGG
lac operator (Dubendorff & Studier, 1991)	GGAATTGTGAGCGGATAACAATTCC
sRBS (Elowitz & Leibler, 2000)	AAAGAGGAGAAAG
U6 (Neupert et al., 2008)	GATCCTCTCCTTCACTAGTAAAAAAAAAAAA AAAAAAAAAAAAAAAAAAGGAGATATA
U9 (Neupert et al., 2008)	GATCCCTCCTTACTAGTCTGCAGAAGGAGAT ATA

---

## Nanopore Sequences

The following nanopores and their corresponding amino acid sequences were used in this study. All variants were amplified with NdeI/KpnI introducing primer by classic restriction ligation, if not stated otherwise.

S<sup>2168</sup>

MDKISTGAIYGTSAAGSAGYWFLQWLDQVSPSQWAAIGVLGSLVVGFLTYLTNLYFKIREDRRKAARGE

S<sup>2171</sup>

MKSMDKISTGAIYGTSAAGSAGYWFLQWLDQVSPSQWAAIGVLGSLVVGFLTYLTNLYFKIREDRRKAARGE

S<sup>2171</sup>-M4A

MKSADKISTGAIYGTSAAGSAGYWFLQWLDQVSPSQWAAIGVLGSLVVGFLTYLTNLYFKIREDRRKAARGE

SGS-ΔTMD1-S<sup>2168</sup> ([Linker](#))

MSGSMWAAIGVLGSLVVGFLTYLTNLYFKIREDRRKAARGE

TVMV-ΔTMD1-S<sup>2168</sup> ([Linker](#); **TVMV cleavage site**)

MSSSGGSETVRFQSGSMWAAIGVLGSLVVGFLTYLTNLYFKIREDRRKAARGE

S<sup>105</sup>

MPEKHDLLAAILAAKEQGIGAILAFAMAYLRGRYNGGAFTKTVIDATMCAIIAWFIRDLLDFAGLSSNLAYITSV  
FIGYIGTDSIGSLIKRFAAKKAGVEDGRNQ

S<sup>107</sup>

MKMPEKHDLLAAILAAKEQGIGAILAFAMAYLRGRYNGGAFTKTVIDATMCAIIAWFIRDLLDFAGLSSNLAYIT  
SVFIGYIGTDSIGSLIKRFAAKKAGVEDGRNQ

S<sup>107</sup>-M3A

MKAPEKHDLLAAILAAKEQGIGAILAFAMAYLRGRYNGGAFTKTVIDATMCAIIAWFIRDLLDFAGLSSNLAYIT  
SVFIGYIGTDSIGSLIKRFAAKKAGVEDGRNQ

T4

MAAPRISFSPSDILFGVLDRLFKNATGKVLASRVAVVILLFIMAIWYRGDSFFEYKQSKYETYSEIIEKERT  
ARFESVALEQLQIVHISSEADFSVAVSFRPKNLNYFVDIIAYEGKLPSTISEKSLGGYPVDKTMDEYTVHLNGRH  
YYSNLKFAFLPTKPTPEINMYSCPYFNLDNIYAGTITMYWYRNDHISNDRLESICAQAARILGRAK

HokB

MKHNPLVVCLLIICITILTFTLLTRQTLYELRFRDGDKEVAALMACTSR

TisB

MNLVDIAAILILKLIVAALQLLDAVLKYLK

BM2

MLEPFQILSISSFILSALHFIAWTIGHLNQIKR

KcvNTS

MLLLIIHLSILVIFTAIYKMLPGGMFSNTDPTWVDCLYFSASTHTTVGYGDLTPKSPVAKLTATAHMLIVFAIVI  
SGFTFPW

---

## S<sup>2168</sup> Truncated Variants

S<sup>2166</sup>

MKISTGAIYGTSAAGSAGYWFLQWLDQVSPSQWAAIGVLGSLVLGFLTYLTNLYFKIREDRRKAARGE

S<sup>2164</sup>

MSTGAIYGTSAAGSAGYWFLQWLDQVSPSQWAAIGVLGSLVLGFLTYLTNLYFKIREDRRKAARGE

S<sup>2162</sup>

MGIAYGTSAAGSAGYWFLQWLDQVSPSQWAAIGVLGSLVLGFLTYLTNLYFKIREDRRKAARGE

S<sup>2160</sup>

MAYGTSAAGSAGYWFLQWLDQVSPSQWAAIGVLGSLVLGFLTYLTNLYFKIREDRRKAARGE

S<sup>2158</sup>

MGTSAAGSAGYWFLQWLDQVSPSQWAAIGVLGSLVLGFLTYLTNLYFKIREDRRKAARGE

S<sup>2156</sup>

MSAGSAGYWFLQWLDQVSPSQWAAIGVLGSLVLGFLTYLTNLYFKIREDRRKAARGE

S<sup>2154</sup>

MGSAGYWFLQWLDQVSPSQWAAIGVLGSLVLGFLTYLTNLYFKIREDRRKAARGE

S<sup>2152</sup>

MAGYWFLQWLDQVSPSQWAAIGVLGSLVLGFLTYLTNLYFKIREDRRKAARGE

S<sup>2150</sup>

MYWFLQWLDQVSPSQWAAIGVLGSLVLGFLTYLTNLYFKIREDRRKAARGE

S<sup>2148</sup>

MFLQWLDQVSPSQWAAIGVLGSLVLGFLTYLTNLYFKIREDRRKAARGE

S<sup>2146</sup>

MQWLDQVSPSQWAAIGVLGSLVLGFLTYLTNLYFKIREDRRKAARGE

S<sup>2144</sup>

MLDQVSPSQWAAIGVLGSLVLGFLTYLTNLYFKIREDRRKAARGE

S<sup>2142</sup>

MQVSPSQWAAIGVLGSLVLGFLTYLTNLYFKIREDRRKAARGE

S<sup>2140</sup>

MSPSQWAAIGVLGSLVLGFLTYLTNLYFKIREDRRKAARGE

S<sup>2138</sup>

MSQWAAIGVLGSLVLGFLTYLTNLYFKIREDRRKAARGE

---

## S<sup>2168</sup> Asp and Lys Mutagenesis

S<sup>2168</sup>-X<sub>AA</sub>K

MX<sub>AA</sub>KISTGIAYGTSAGSAGYWFLQWLDQVSPSQWAAIGVLGSLVLGFLTYLTNLYFKIREDRRKAARGE

X<sub>AA</sub> = R, H, K, E, G, P, A, V, I, L, F, Y, W, S, T, N, Q

S<sup>2168</sup>-DX<sub>AA</sub>

MDX<sub>AA</sub>ISTGIAYGTSAGSAGYWFLQWLDQVSPSQWAAIGVLGSLVLGFLTYLTNLYFKIREDRRKAARGE

X<sub>AA</sub> = R, H, D, E, G, P, A, V, I, L, F, Y, W, S, T, N, Q

## S<sup>2171</sup>-Library Construction

The S<sup>2171</sup>-library was constructed by PCR with a degenerate N-terminal primer. The primer had NNK codons for the first three amino acids after the Met. NNK codons encode for all 20 amino acids with 32 codons, from which only one is a stop codon. Fully randomized NNN codons would encode for all 64 codons and 3 stop codons and are therefore not ideal. The total possible library contained 8000 combinations.

Amino acid sequence:	M	K	S	M	D	K	I	S	T	(...)	
Nucleotide sequence:	ATG	AAA	TCT	ATG	GAC	AAA	ATC	TCA	ACT		
Degenerate primer:	TGATGAGG	CAT	ATG	NNK	NNK	NNK	GAC	AAA	ATC	TCA	ACT

The degenerate primer introduced a NdeI restriction site and the reverse primer introduced a KpnI site. PCR was performed as previously described, but in a larger volume of 16x50  $\mu$ l reactions. Pooled reactions were purified and digested for 1.5 hours with NdeI. Thereafter, KpnI was added and again digested for 1.5 hours. The same reaction was performed with the pCTRL2.T7.wt.sRBS and pCTRL2.T7.100.sRBS backbones, except rSAP was added. Ligation was performed in a 100  $\mu$ l reaction volume. DNA was precipitated and resuspended in a nuclease free ddH<sub>2</sub>O to 20 ng/ $\mu$ l. This DNA mix was then used for electroporation. Colonies were counted the day after the transformation and the grown-out cells in LB-medium were centrifuged (3500xg, 21°C, 15 minutes) and stored at -20°C. Several iterations were performed until a sufficient number of variants was pooled, followed by DNA preparation. The pCTRL2.T7.wt.sRBS-S<sup>2171</sup> library contained 270.000 clones and the pCTRL2.T7.100.sRBS-S<sup>2171</sup> library contained 300.000 clones.

## FRB FKBP Sensor

FRB-Linker-cpsfGFP-Linker-FKBP-Linker-6xHis

MGILWHEMWHEGLEEASRLYFGERNVKGMEVLEPLHAMMERGPQTLKETSFNQAYGRDLMEAEQWCRKYMKSGN  
VKDLTQAWDLYYHVFRRI GPPPPPGSHNVYITADKQKNGIKANFKIRHNVEDGSQLADHYQQNTPIGDGPVLLP  
DNHYLSTQSVLSKDPNEKRDHMLLEFVTAAGITLGMDELYKGGTGGSSMSKGEELFTGVVPILVELDGDVNGHKF  
SVRGEGEGDATNGKLT LKFICTTGKLPVPWPTLVTTLYGVQCF SRYPDHMKQHDFFKSAMPEGYVQERTISFKD  
DGTYKTRAEVKFEGDTLVNRIELKGIIDFKEDGNILGHKLEYNFN GPPPPPPPGVQVETISPGDGRTFPKRGQTCV  
VHYTGMLEDGKKFDSSRDRNKPFKMLGKQEVIRGWEEGVAQMSVGRRAKLTISPDIYAGATGHPGIIPPHATLV  
FDVELLKLEAS HHHHHH

## S<sup>2168</sup>, S<sup>2158</sup>, S<sup>2138</sup> Chemical Synthesis

Full length pinholin S<sup>2168</sup> and the truncated versions S<sup>2158</sup> and S<sup>2138</sup> were chemically synthesized by the Alesia Tietze group according to (Baumrueck et al., 2018). Lyophilized peptides were stored at -20°C up to 3 months. Prior usage, peptides were solved in DMSO (50 mg/ml) and stored at 4°C for up to two weeks.

## BL21(DE3) pPRO24-G-GECO1/R-GECO1 Competent Cell Preparation

BL21(DE3) cells were transformed with either pPRO24-G-GECO1 or pPRO24-R-GECO1 plasmid. These cells were then made chemical competent again and used for further nanopore containing vector transformation. The subsequent single transformation yielded more colonies compared to double transformation.

## BL21(DE3) pPRO24-G-GECO1/R-GECO1 transformation with pCTRL2

Chemical competent BL21(DE3) containing pPRO24-G-GECO1/R-GECO1 were transformed with a nanopore (or mKO<sub>K</sub>) containing pCTRL2 vector. The promoter strength used for the respective experiment is annotated in the results part. Table 21 contains the expression strength measured with the fluorescent mKO<sub>K</sub> (normalized on pCTRL2.T7.wt.sRBS).

Table 21 Expression strength measured with mKO<sub>K</sub>.

Promoter	Expression strength normalized on pCTRL2.T7.wt.sRBS
pCTRL2.T7.wt.sRBS	100%
pCTRL2.T7.03.sRBS	1.02%
pCTRL2.T7.14.sRBS	0.17%
pCTRL2.T7.100.sRBS	3.56%
pCTRL2.T7.03.U6	undetectable
pCTRL2.T7.14.U6	undetectable
pCTRL2.T7.03.U9	0.12%
pCTRL2.T7.14.U9	undetectable
pCTRL2.T7.100.U9	0.52%

---

## Spectrophotometer Screening for Nanopore Activity

Spectrophotometer (Tecan Spark) measurements were performed in 96-well black plates with transparent bottom. For this purpose, BL21(DE3) cells carrying the pPRO24-G-GECO1 or pPRO24-R-GECO1 vector were transformed with a nanopore containing pCTRL2 vector, plated on LB-agar cam/amp plates and grown overnight at 37°C. The next day, at least three colonies per combination were picked and inoculated in 300  $\mu$ l LB cam/amp medium in a 96-deepwell plate and incubated in a heated shaker at 37°C and 1300 rpm overnight. Thereafter, the OD<sub>600nm</sub> of three randomly chosen variants was measured to control growth (OD<sub>600nm</sub> was usually around 5-6). A black 96-well plate with transparent bottom was filled with 189.5  $\mu$ l medium and inoculated with 3.5  $\mu$ l pre-cultures which corresponds to an OD<sub>600nm</sub> of  $\sim$ 0.1. This plate was then incubated in a heated shaker at 900 rpm for 30 minutes at 37°C to warm up the plate and the cells. Cells were then induced with 25 mM Na-Propionate (5  $\mu$ l of a 1 M Na-Propionate solution) for biosensor expression and measurement was started. The measurement was paused at 113 minutes (if not stated otherwise) and 0.5 mM IPTG (2  $\mu$ l of a 50 mM IPTG solution) was added to induce nanopore expression. In some experiments, 2 mM EDTA (2  $\mu$ l of a 50 mM EDTA solution) was added at 312 minutes (if not stated otherwise) to diminish the signal. The kinetic measurement cycle was set to either 10 minutes or 3 minutes. Temperature was set to 30°C and each cycle started with double orbital shaking at 180 rpm followed by OD<sub>600nm</sub> and fluorescence read-out. Z-height was adjusted automatically and gain was set to 60 for pPRO24-G-GECO1 (excitation: 485 $\pm$ 20 nm; emission:525 $\pm$ 20) and 100 for pPRO24-R-GECO1 (excitation: 555 $\pm$ 20 nm; emission:600 $\pm$ 20). Medium blanks were subtracted, data analysis was performed with Excel and plotted in GraphPad Prism 8.

## Cell Lysis Experiments

Cell lysis analysis was performed in 96-deep-well plates. For this purpose, BL21(DE3) cells carrying the pPRO24-G-GECO1 vector were transformed with a nanopore containing pCTRL2 vector, plated on LB-agar cam/amp plates and grown overnight at 37°C. The next day, at least three colonies per combination were picked and inoculated in 300  $\mu$ l LB cam/amp medium in a 96-deep-well plate and incubated in a heated shaker at 37°C and 1300 rpm overnight. Thereafter, the OD<sub>600nm</sub> of three randomly chosen variants was measured to control growth (OD<sub>600nm</sub> was usually around 5-6). A fresh 96-deep-well plate was filled with 285  $\mu$ l medium and inoculated with 5  $\mu$ l pre-cultures which corresponds to an OD<sub>600nm</sub> of  $\sim$ 0.1. This plate was then incubated in a heated shaker at 1300 rpm for 30 minutes at 37°C to warm up the plate and the cells. Cells were then induced with 25 mM Na-Propionate (7.5  $\mu$ l of a 1 M Na-Propionate solution) for biosensor expression in a heated shaker at 30°C and 1300 rpm. After 113 minutes 0.5 mM IPTG (3.5  $\mu$ l of a 50 mM IPTG solution) was added to induce nanopore expression for another 3 hours in a heated shaker at 30°C and 1300 rpm. Cell suspension was then centrifuged (3500 xg, 21°C, 30 min) and supernatant (300  $\mu$ l) was separated from the pellet. The pellet was resuspended in 300  $\mu$ l fresh medium. Equal amounts of the supernatant and the resuspended pellet (200  $\mu$ l) were measured separately in the spectrophotometer in a 96-well black plate with transparent bottom. Z-height was adjusted automatically and gain was set to 60 for pPRO24-G-GECO1 (excitation: 485 $\pm$ 20 nm; emission:525 $\pm$ 20). Medium blanks were subtracted, data analysis was performed with Excel and plotted in GraphPad Prism 8.

## In Vitro Bilayer Measurements

Planar lipid bilayer experiments were done with a conventional, vertical bilayer setup (Braun, Baer, et al., 2014) and a stereomicroscope for optical monitoring. The setup for vertical *in vitro* bilayer measurements consists of two chambers called *cis* and *trans*. Both chambers contained an Ag/AgCl electrode, whereas the *trans* chamber was also grounded. Both chambers were separated by a 25  $\mu$ m thick Teflon foil with a small hole introduced by pre-penetrating the foil with a pin and enlarged to about

---

100  $\mu\text{m}$  by three electrical sparks while rotating the foil. After assembling the chamber, the Teflon foil around the hole was hydrophobized with 0.5  $\mu\text{l}$  of 1% (v/v) n-Hexadecane in n-Hexane. Both chambers were then filled with 800  $\mu\text{l}$  100 mM KCl 10 mM HEPES pH 7 solution and 35  $\mu\text{l}$  15 mg/ml 1,2-diphytanoyl-sn-glycero-3-phosphocholine (DPhPC) in n-Pentane was pipetted in each chamber. After 7.5 minutes of incubation at room temperature to evaporate the solvent, each chamber was filled with another 1.7 ml of the 100 mM KCl with 10 mM HEPES pH 7 solution. A bilayer was painted by sealing the aperture with an air bubble in the *trans* chamber. After the stability of the bilayer was verified, protein was added near the bilayer in the *trans* chamber. Nanopore peptides were solved in DMSO with a concentration of 50 mg/ml and stored at 4°C for up to two weeks. This 50 mg/ml solution was diluted 1:10 up to 1:1000 in 100 mM KCl with 10 mM HEPES, pH 7 prior usage in bilayer experiments. Usually 1-2  $\mu\text{l}$  protein samples were added with a bent 25- $\mu\text{l}$  Hamilton syringe and a voltage protocol (-120 mV to +120 mV and in reverse in 20 mV steps for 5 seconds) was applied. This process was repeated until a nanopore incorporated into the membrane. A current protocol with -100 mV to +100 mV and vice versa was applied when nanopores were incorporated. Current between both chambers was recorded with L/M-EPC7 Patch clamp amplifier which is connected to a preamplifier with a gain of 10 mV/pA and filtered at 1kHz. Recordings were digitized by a 16-bit LIH 1600 A/D converter and saved on a computer via the Patchmaster software. Data analysis was performed with Nest-O-patch software by V.Nesterov and Excel and plotted in GraphPad Prism 8.

### Colony Based Screening for Nanopore Activity

For colony-based screening, BL21(DE3) cells carrying the pPRO24-G-GECO1 vector were transformed with a nanopore containing pCTRL2.T7.100.sRBS vector, plated on LB-agar cam/amp plates and grown overnight at 37°C. It is crucial that the colonies are evenly spread. Cells were then airbrushed with a Fengda airbrush BD-130 with a working pressure of 1.5 bar delivered by a Fengda compressor FD-186 with a 500 mM Na-Propionate pH 8 solution until all cells were covered. Plates were incubated for 3 hours at 20°C covered in aluminium foil to prevent bleaching. Afterwards, a 50 mM IPTG solution was applied like previously described. Images were acquired with constant exposure times with an E-BOX equipped with a blue light table (Ex: 470nm; Em: F-590.M58 UV-Filter) directly after IPTG application (0 minutes) and then in a 60 minute interval up to 4 hours. Between the acquisitions, plates were kept at 20°C covered in aluminium foil. For image analysis, maximum intensity measurements were computed with imageJ-Fiji (Schindelin et al., 2012) and data was plotted with GraphPad Prism 8.

### Microfluidic Microscopy

For microfluidic measurements BL21(DE3) cells carrying the pPRO24-G-GECO1 vector were transformed with a nanopore containing pCTRL2.T7.100.sRBS vector, plated on LB-agar cam/amp plates and grown overnight at 37°C. The next day, one colony per combination was picked and inoculated in 4 ml LB cam/amp medium in a glass culture tube and grown overnight in a heated shaker at 37°C and 180 rpm. Thereafter, the  $\text{OD}_{600\text{nm}}$  was measured and adjusted to 0.1 in fresh sterile filtered 2 ml LB cam/amp medium in a glass culture tube followed by cultivation in a heated shaker at 37°C and 180 rpm for 3 hours. The microfluidic chip (Wunderli Chips, Zuerich, Switzerland) from the Shaerli lab (Santos-Moreno et al., 2020) was flooded with LB cam/amp medium and cells were loaded into the chip with a constant flow rate of 1  $\mu\text{l}/\text{min}$  controlled by a Flow EZ device (Fluigent, Le Kremlin-Bicêtre, France) for 3 hours at 37°C to fill up the cavities with cells. G-GECO1 expression was induced by switching to LB cam/amp medium with 25 mM Na-Propionate pH 8 for 2 hours at 30°C with a constant flow rate of 4  $\mu\text{l}/\text{min}$ . Nanopore expression was induced by switching to LB cam/amp medium with 25 mM Na-Propionate pH 8 and 0.5 mM IPTG for 16 hours at 30°C with a constant flow rate of 4  $\mu\text{l}/\text{min}$ . Image acquisition started after the last medium change and according to the length of the tubing, IPTG needed about 20 minutes to arrive at the chamber with the cells. Imaging was performed with the help of Markus Röder (Heinz Koepl group) on the inverted microscope Nikon TI Eclipse with a 100x NA

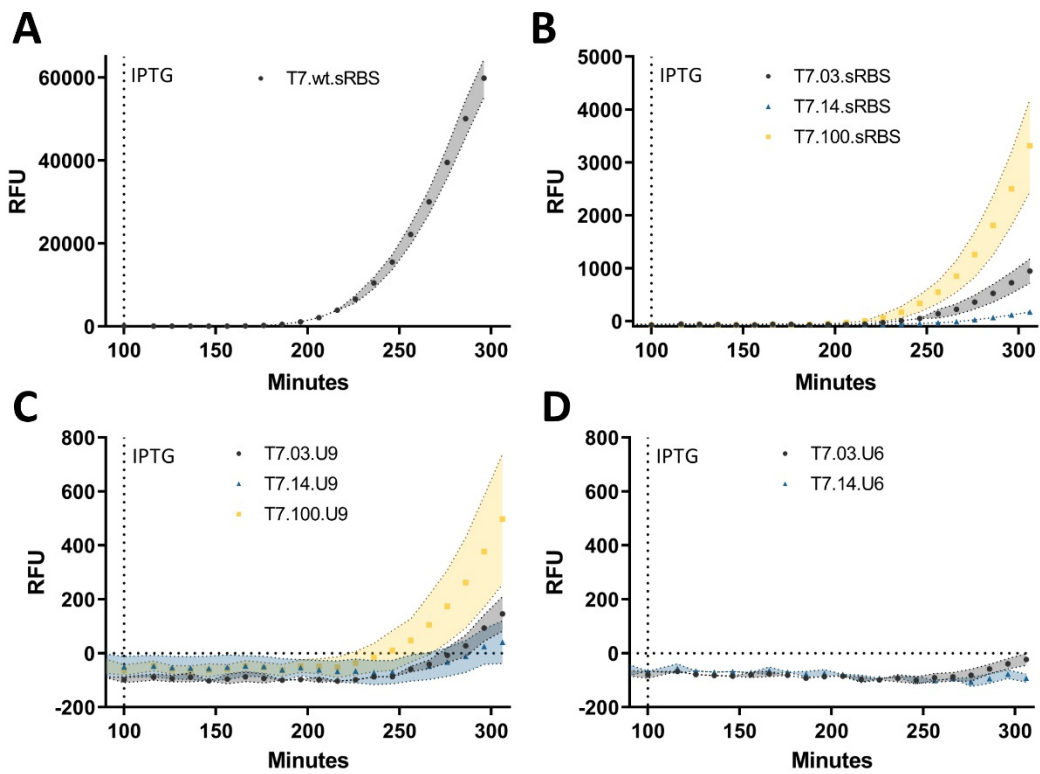
---

1.45 objective (Nikon instruments, Tokyo, Japan), an ORCA Fusion CMOS camera (Hamamatsu Photonics, Hamamatsu, Japan) and a 488/5 nm laser (Huebner GmbH, Kassel, Germany) with appropriate filters F58-019 (Dichroic Mirror) F57-019 (Emission Filter) (AHF Analysentechnik, Tübingen, Germany). The microscope chamber (Life image services, Basel, Switzerland) was kept to 30°C. NIS-Elements 5.0 (Nikon instruments, Tokyo, Japan) was used to command the microscope. Wide-field images were recorded at 3 min intervals with 7 z-stacks ( $\Delta z$  0.3  $\mu\text{m}$ ) and 100 ms exposure for 16 h. For image analysis, maximum intensity projections were computed with imageJ-Fiji (Schindelin et al., 2012) and data was plotted with GraphPad Prism 8.

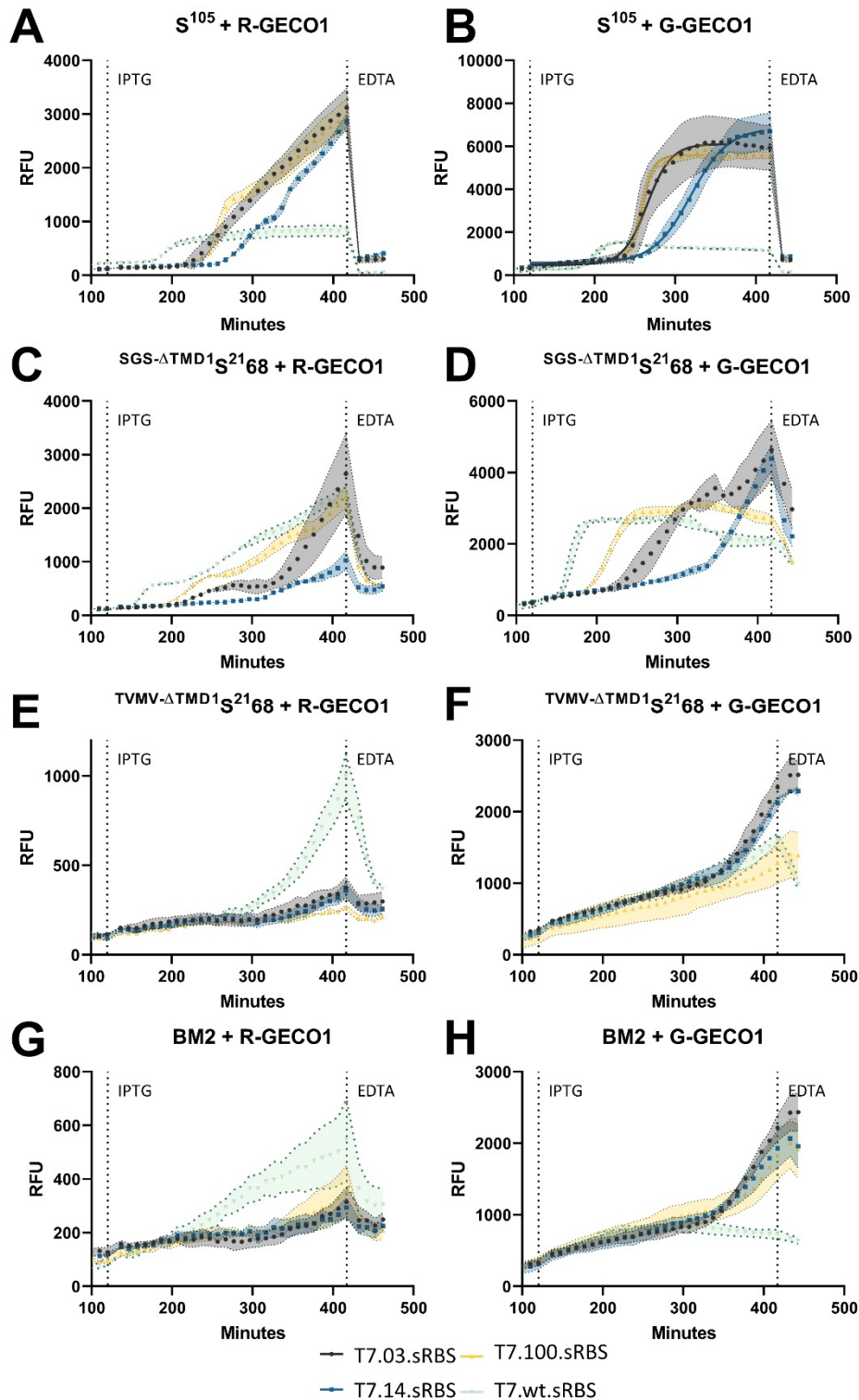
### Fluorescence Activated Cell Sorting (FACS)

For FACS measurements BL21(DE3) cells carrying the pPRO24-G-GECO1 vector were transformed via electroporation with pCTRL2.T7.wt.sRBS vector containing either  $^{SGS-\Delta TMD1-S^{2168}}$  (positive control),  $^{TVMV-\Delta TMD1-S^{2168}}$  (negative control) or a 1:10 mixture  $^{SGS-\Delta TMD1-S^{2168}}$  to  $^{TVMV-\Delta TMD1-S^{2168}}$  and grown in LB-medium with cam/amp overnight in a heated shaker at 37°C and 180 rpm. The next day, cells were inoculated to an  $OD_{600\text{nm}}$  of 0.1 in fresh 4 ml LB-medium with Cam/Amp in a glass culture tube and grown in a heated shaker at 37°C and 180 rpm for 30 minutes. Cells were then induced with 25 mM Na-Propionate for biosensor expression in a heated shaker at 30°C and 180 rpm for 113 minutes. Afterwards nanopore expression was induced with 0.5 mM IPTG at 30°C and 180 rpm for 60 minutes. Cells were then washed twice with PBS, diluted to an  $OD_{600\text{nm}}$  of 0.05 in PBS and kept on ice. FACS measurements were performed with a Sony SH800S (Sony, Minato, Japan) equipped with a 480 nm laser and 525 nm emission filter. A 100  $\mu\text{m}$  sorting chip (Sony, Minato, Japan) was calibrated after manufacturer's instructions and gating conditions were set as described in the results. In total 18500 events from the 1:10 mixture were sorted resulting in about 20  $\mu\text{l}$  PBS cell suspension.

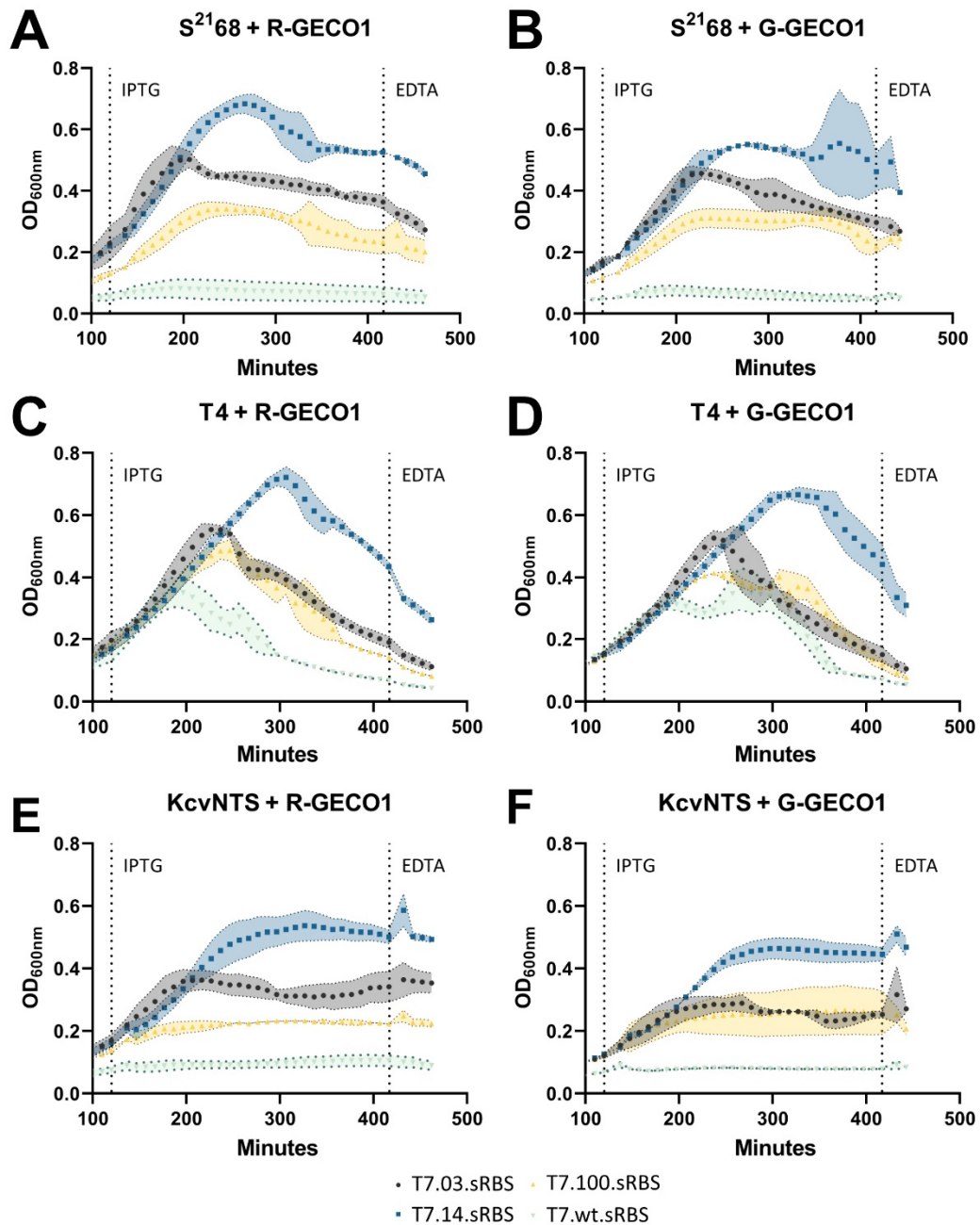
## Supplementary



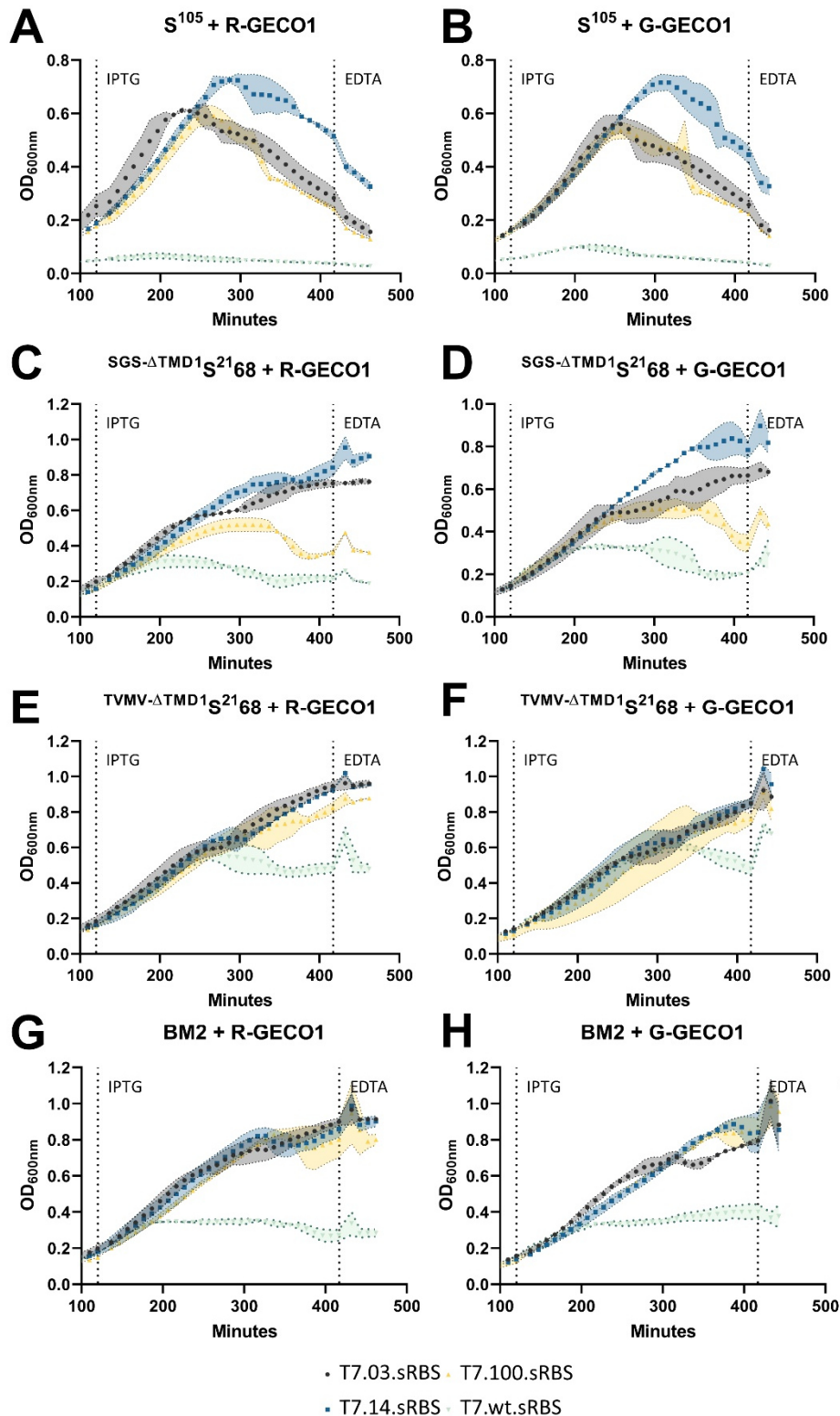
**Supplementary Figure 1** Expression kinetic of mKO<sub>k</sub> under different pCTRL2 promoter variants related to Figure 16. (A) pCTRL2.T7.wt.sRBS had the strongest expression comparable to the pET system. (B) The promoter variants pCTRL2.T7.03/14/100.sRBS exhibited a gradual increase in expression from the T7.14 with the lowest, over T7.03.sRBS to a higher strength in T7.100.sRBS. (C) pCTRL2.T7.03/14/100.U9 RNAT variants had very low expression strength and (D) the pCTRL2.T7.03/14/U6 combinations did not yield any detectable protein. Data points represent mean values with SD indicated as error area; n=3.



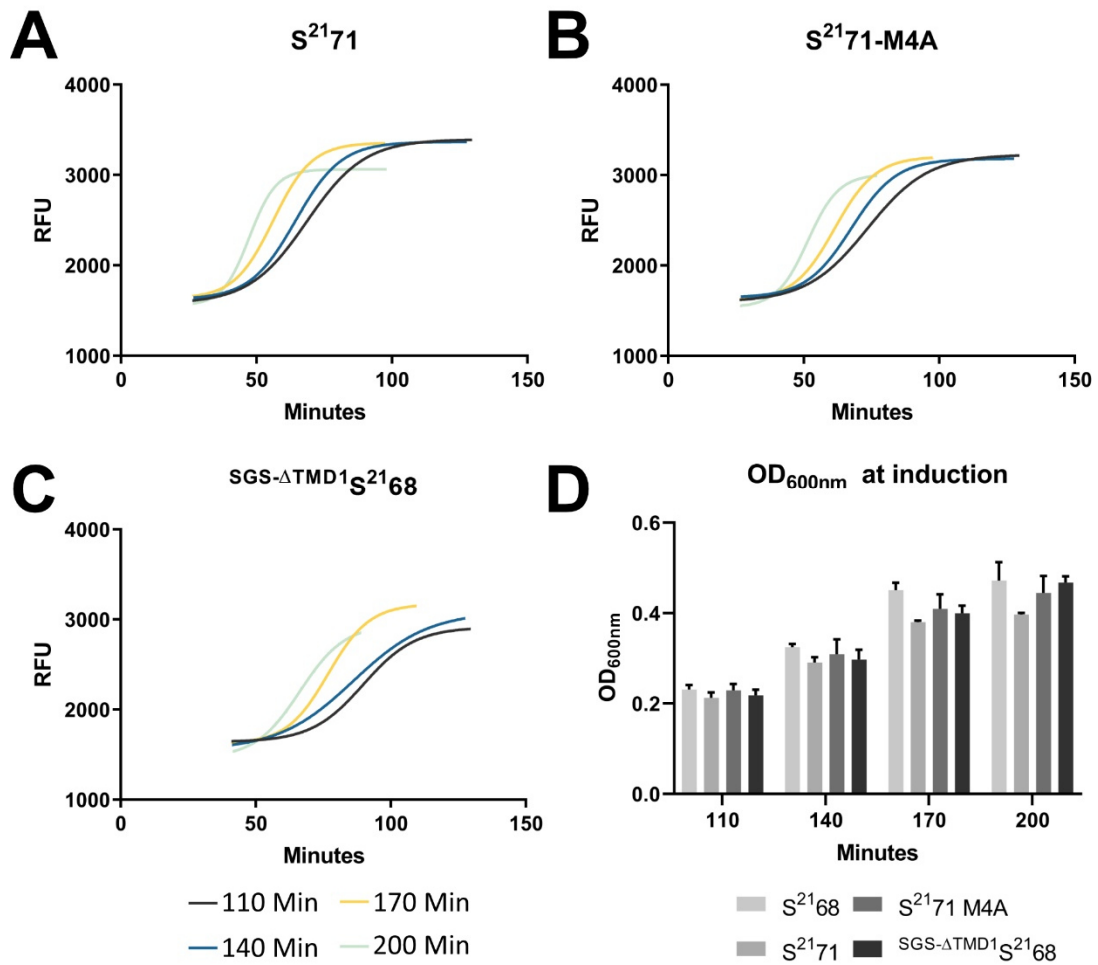
**Supplementary Figure 2** Fluorescence measurement over time of the pores  $S^{105}$ ,  $SGS-\Delta TMD1S^{2168}$ ,  $TVMV-\Delta TMD1S^{2168}$  and  $BM2$  in combination with R-GECO1 or G-GECO1 related to Figure 17. Sensors were expressed for 110 minutes followed by pore induction marked by the IPTG line and EDTA addition to diminish the signal. (A-B) Cells with  $S^{105}$  experience growth inhibition due to the leaky expression under the T7.100.sRBS promoter. In addition, R-GECO1 variants do not show a full sigmoid curve compared to G-GECO1. (C-D)  $SGS-\Delta TMD1S^{2168}$  nanopore shows a shifted answer depending on the promoter strength for R-GECO1 and G-GECO1, while R-GECO1 shows delayed maturation timings. (E-F) The  $TVMV-\Delta TMD1S^{2168}$  variant is not able to form pores for about 150-200 minutes after induction, but leads to minimal membrane perforation after 200 minutes under the T7.wt.sRBS for R-GECO1 and T7.03.sRBS/T7.14.sRBS for G-GECO1. (G-H)  $BM2$  shows no signal increase with R-GECO1 and a slight one after 300 minutes for every promoter strength except T7.wt.sRBS, where the growth is inhibited early. Data points represent mean values with SD indicated as error area; n=3.



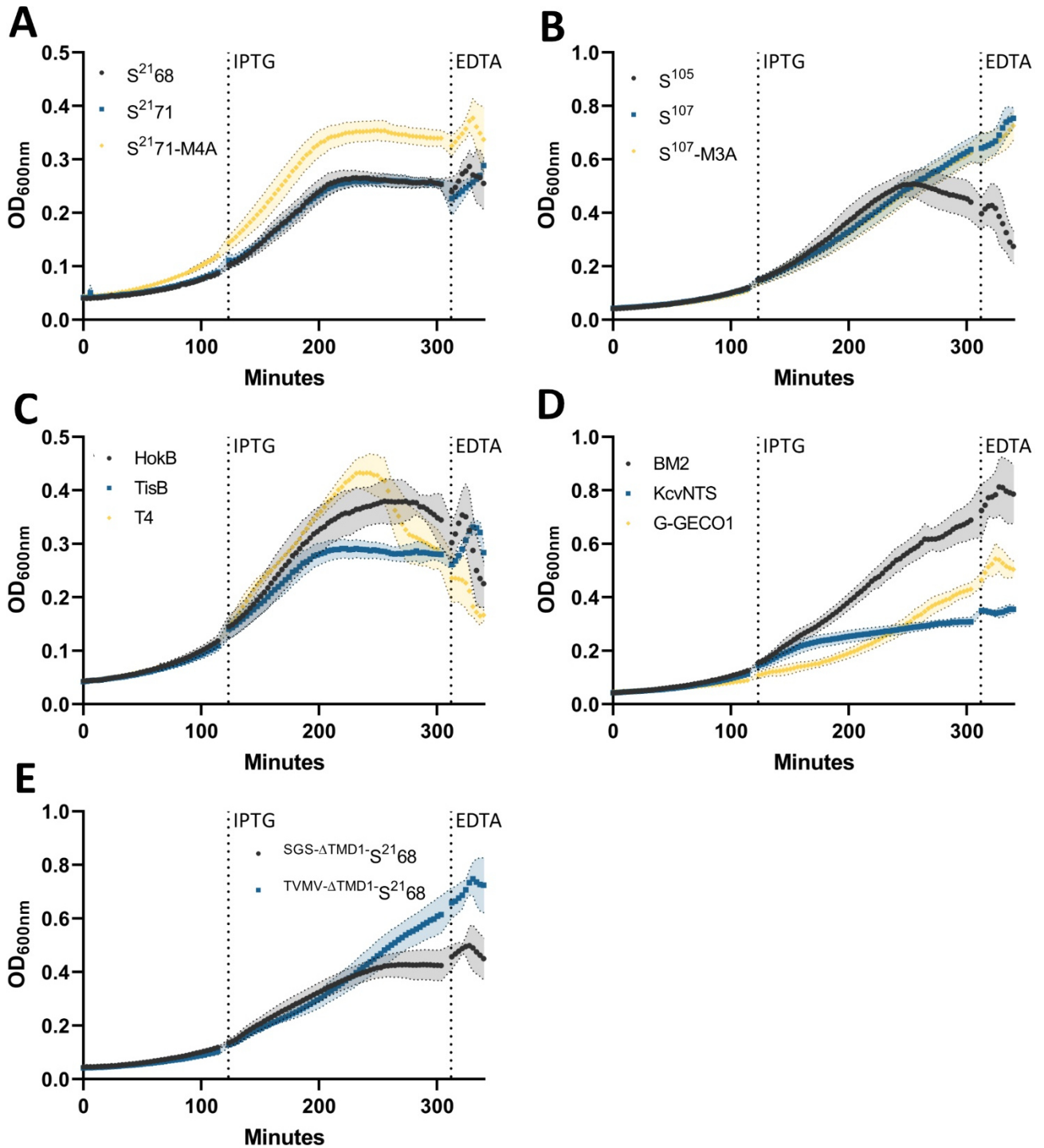
**Supplementary Figure 3 Absorption OD<sub>600nm</sub> measurements over time of the pores S<sup>21</sup>68, T4 and KcvNTS in combination with R-GECO1 or G-GECO1 related to Figure 17.** Sensors were expressed for 110 minutes followed by pore induction marked by the IPTG line and EDTA addition to diminish the fluorescence signal. (A-B) For S<sup>21</sup>68 the strongest promoter T7.wt.sRBS inhibits cell growth, while the curves for the other promoter strengths remain stable after induction (C-D) T4 holin expressions leads to a delayed cell death with weaker promoters, but exhibits a strong signal decrease indicating complete cell lysis (E-F) Cells with KcvNTS can grow under the every promoter except the T7.wt.sRBS. Data points represent mean values with SD indicated as error area; n=3.



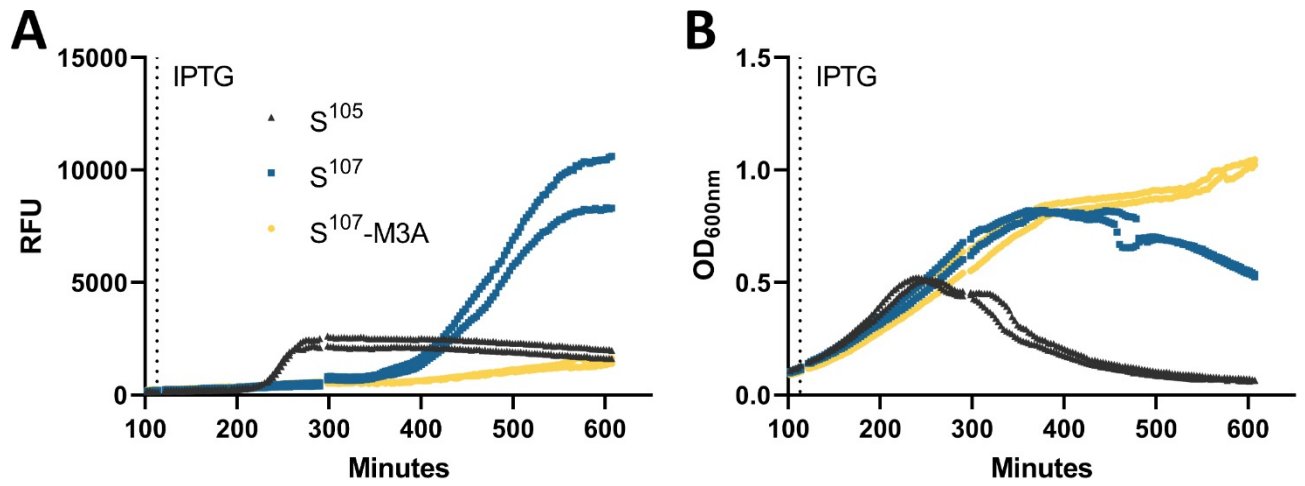
**Supplementary Figure 4** Absorption  $OD_{600nm}$  measurements over time of the pores  $S^{105}$ ,  $SGS-\Delta TMD1S^{2168}$ ,  $TVMV-\Delta TMD1S^{2168}$  and  $BM2$  in combination with R-GECO1 or G-GECO1 related to Figure 17. Sensors were expressed for 110 minutes followed by pore induction marked by the IPTG line and EDTA addition to diminish the fluorescence signal. (A-B) For  $S^{105}$  the strongest promoter T7.wt.sRBS inhibits the cell growth, while the decreasing curves for the other promoter strengths show typical cell lysis behaviour (C-D)  $SGS-\Delta TMD1S^{2168}$  grows under every promoter strength, while the curves remain stable after cell death (E-F) The negative control  $TVMV-\Delta TMD1S^{2168}$  inhibits cell growth after 180-200 minutes after nanopore induction under wildtype T7.wt.sRBS, while the others do not influence cell growth. (G-H) The other negative control  $BM2$  reacts similar to  $TVMV-\Delta TMD1S^{2168}$ , but with faster cell growth inhibition of 60-80 minutes after induction. Data points represent mean values with SD indicated as error area;  $n=3$ .



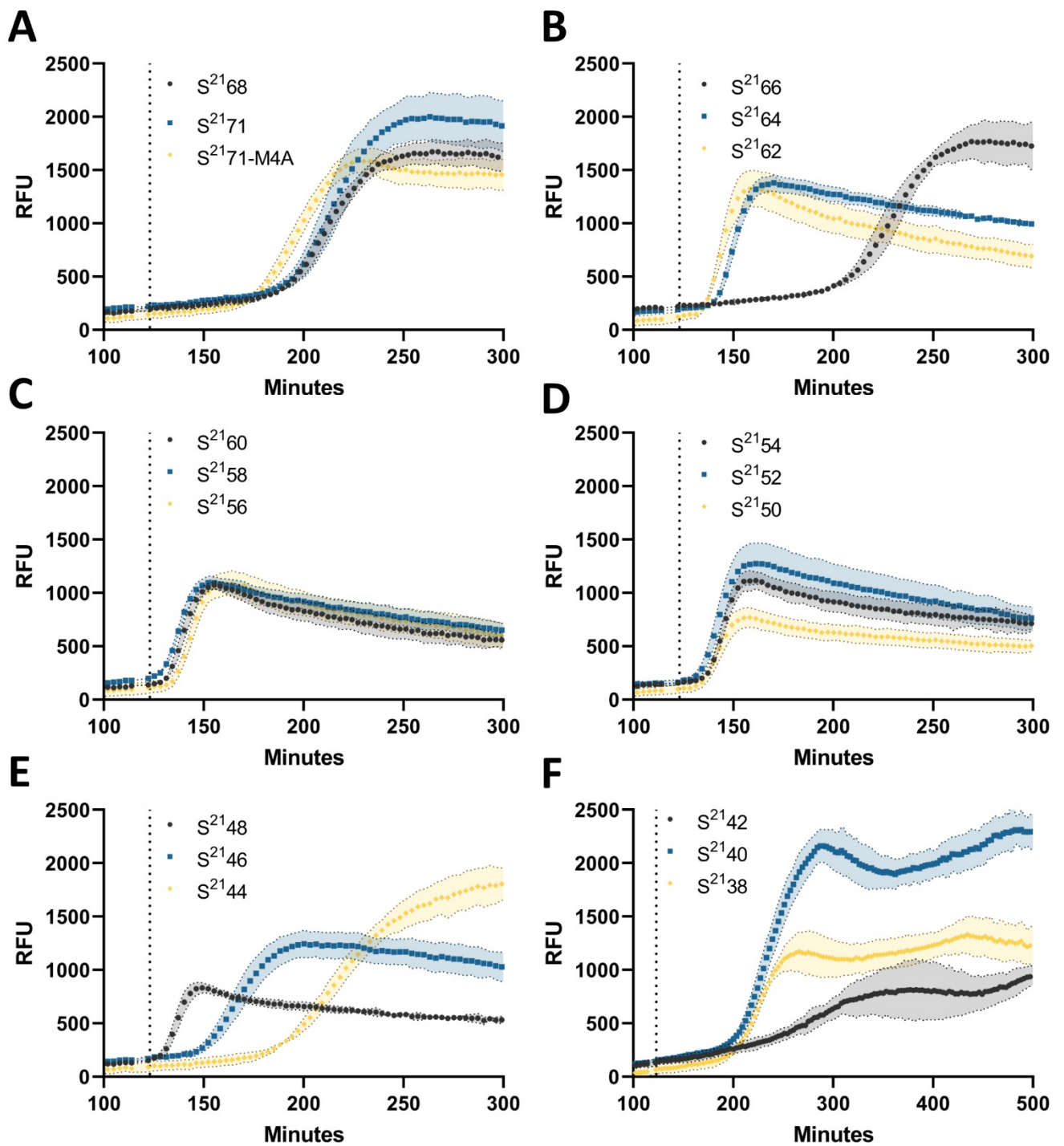
**Supplementary Figure 5** Variation of induction times for  $S^{2171}$ ,  $S^{2171}\text{-M4A}$  and  $\text{SGS-}\Delta\text{TMD1-}S^{2168}$  related to Figure 19. (A-C) Fluorescence measurements over time from different starting points were plotted by setting the induction point to 0 minutes and comparing the signal after induction. All variants behave similarly in their response, by having a fast signal increase with later nanopore induction. (D) The  $\text{OD}_{600\text{nm}}$  at the nanopore induction varied from 0.2 to 0.5. This number has to be multiplied by  $\sim 2$  to get the corresponding  $\text{OD}_{600\text{nm}}$  from UV-vis measurements in cuvettes. Graph bars represent mean values with SD indicated as error bars;  $n=3$ . Error bars missing in (A,B,C) for better visibility.



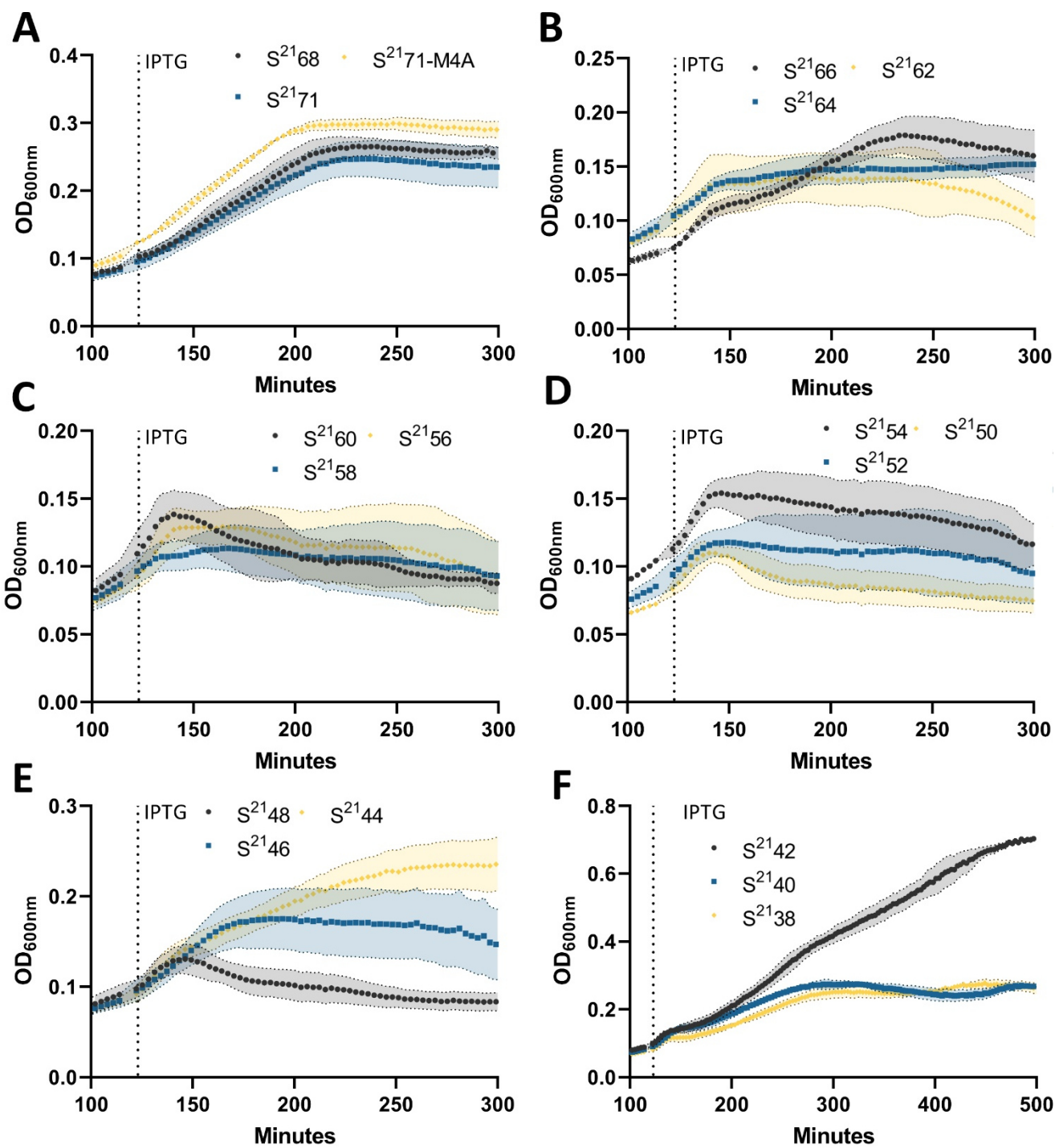
**Supplementary Figure 6 Absorption measurements of different nanopores related to Figure 20.** Induction was performed at 113 minutes and EDTA was added 312 min to diminish the G-GECO1 signal. (A) The pinholin  $S^{2168}$ , the antiholin  $S^{2171}$  and  $S^{2171-M4A}$  behave similarly in growth and stagnation after pore induction. (B) The canonical  $S^{105}$  holin is the only active variant with lysis capability compared to its antiholin variants  $S^{107}$  and  $S^{107-M3A}$ . (C). The T4 holin leads to strong lysis after induction, followed by HokB with minor cell lysis. TisB absorption remains stable after nanopore formation. (D) The negative control KcvNTS leads to a fast cell death, while BM2 growth is not inhibited upon nanopore expression. Cells without any pore grow slower but do not stagnate (E) Absorption curves do not decrease for  $TVMV-\Delta TMD1-S^{2168}$  but for the active version  $SGS-\Delta TMD1-S^{2168}$ . Data points represent mean values with SD indicated as error area;  $n=3$ .



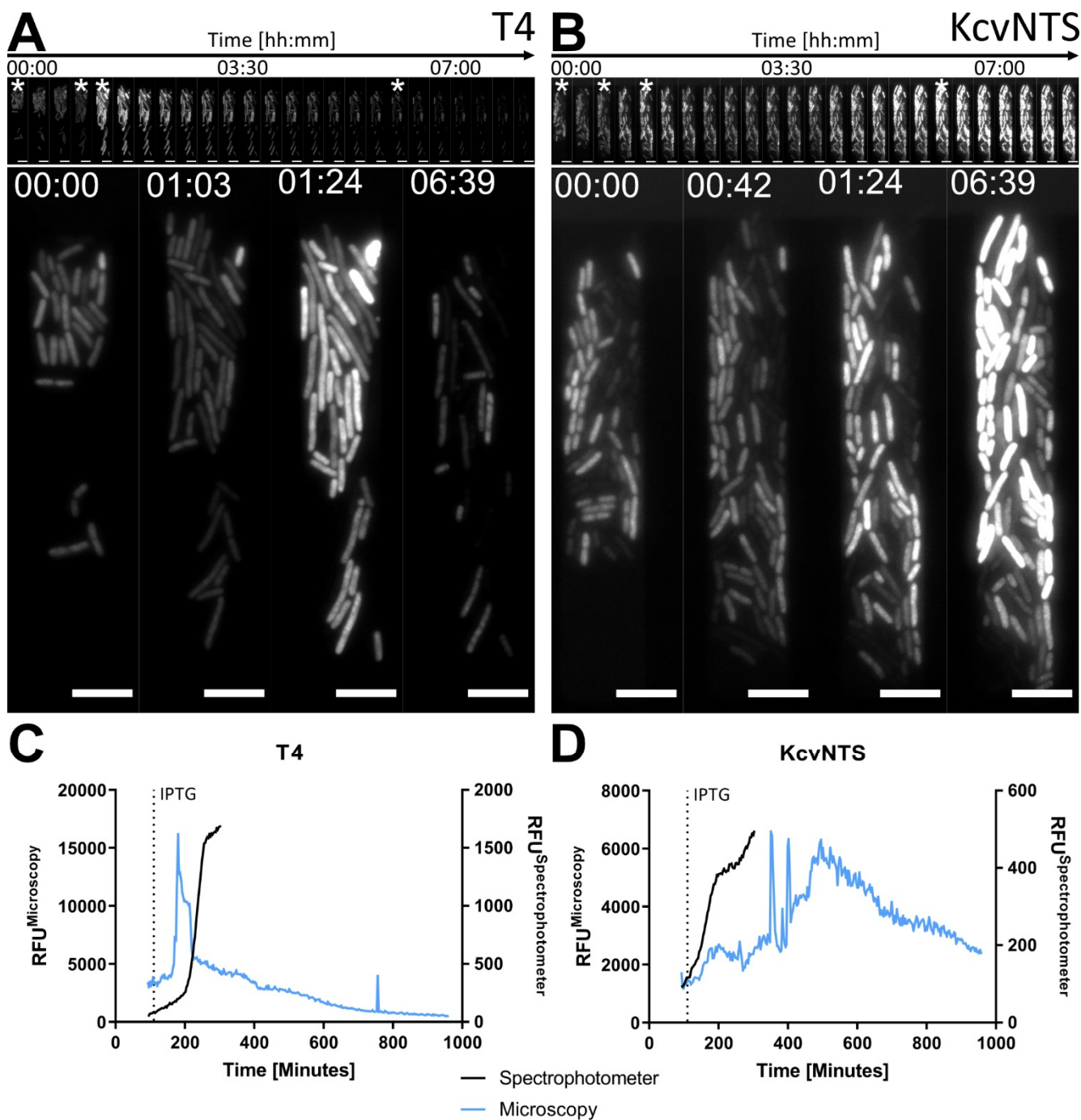
**Supplementary Figure 7 Fluorescence and absorption measurement of  $S^{105}$ ,  $S^{107}$   $S^{107}$ -M3A. (A-B)** Prolonged measurements with  $S^{107}$  demonstrate a delayed but large signal increase beginning with 300 minutes after induction. Preliminary results with  $n=2$ , each replicate is plotted individually.



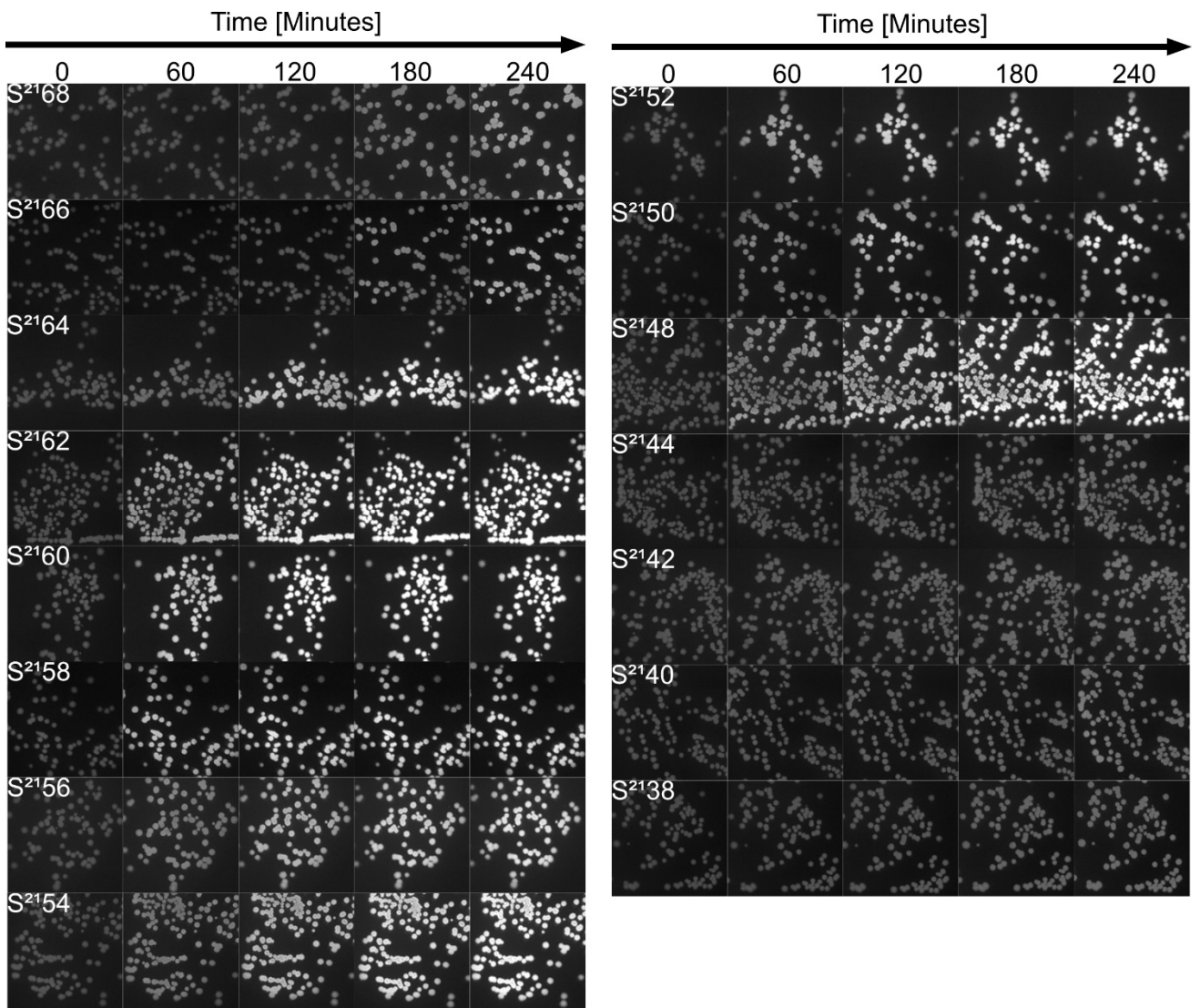
**Supplementary Figure 8** Truncation experiments of the first transmembrane domain of S<sup>2168</sup> related to Figure 22. (A-F) Steepness and  $T_{1/2}$  measurements of the truncated variants reveal two transition points, one between S<sup>2166</sup> and S<sup>2164</sup> to a faster and steeper signal increase and one between S<sup>2148</sup> and S<sup>2146</sup>, where the signal rise gets slower again. The variant S<sup>2142</sup> had extremely delayed and weak pore forming activity. Data points and graphs represent mean values with SD indicated as error area; n=3.



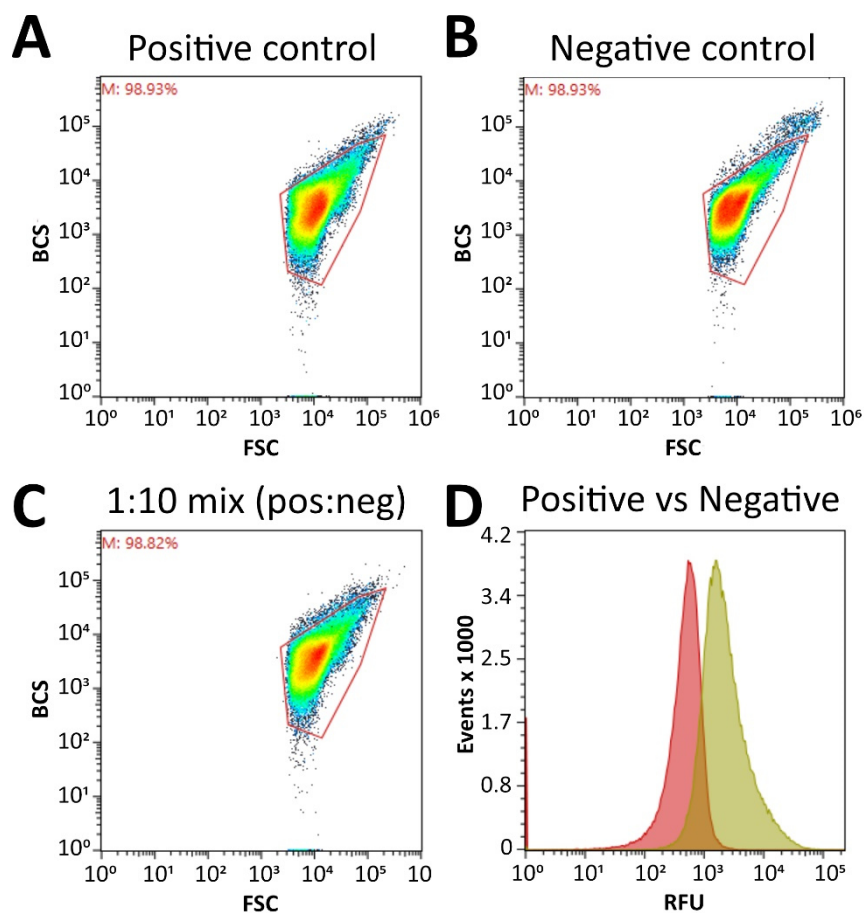
**Supplementary Figure 9** Truncation experiments of the first transmembrane domain of S<sub>2168</sub> related to Figure 22. (A-F) Absorption OD<sub>600nm</sub> measurements of the truncated variants show that fast pore forming variants also inhibit cell growth early, while slower variants lead to higher OD<sub>600nm</sub> values. Data points and graphs represent mean values with SD indicated as error area; n=3



**Supplementary Figure 10** Microfluidic microscopy measurements of the T4 holin and the negative control KcvNTS related to Figure 28. The images in the top bar are 21 minutes apart and show a time window of 08:24. Representative images marked with an asterisk are shown enlarged below. Scale bar 5  $\mu\text{m}$ . (A) Cells with T4 holin react with an accelerated signal rise, followed by exceptionally fast signal decrease. (B) KcvNTS leads to fast stop of cell division, but the signal increases over a long period of time. (C-D) T4 and KcvNTS curve overlay of spectrophotometer and microscopy measurements. Data points for spectrophotometer measurements represent mean values;  $n=3$ . Data points from microscopy measurements represent the max grey value of the whole cavity from (A-B).



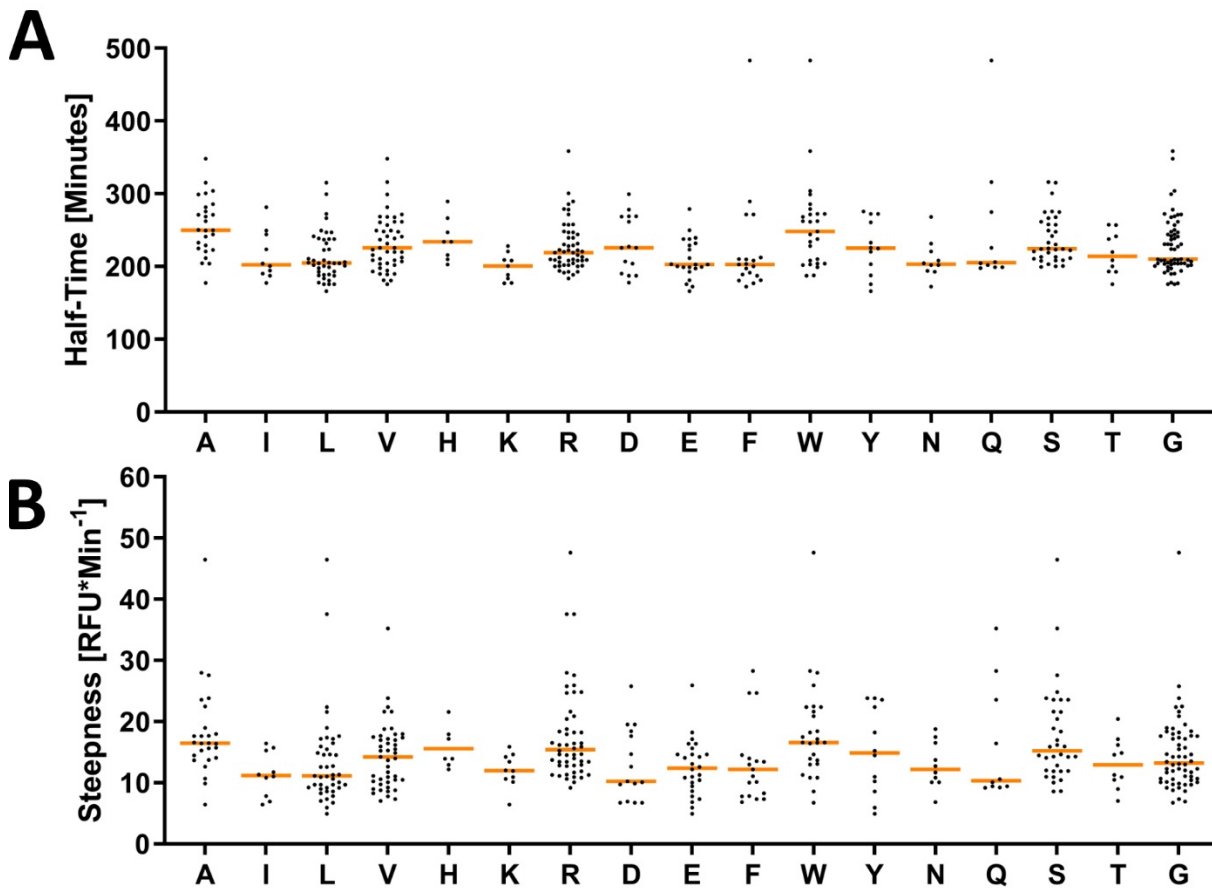
Supplementary Figure 11 Colony screening on agar plates for truncated variants related to Figure 30.



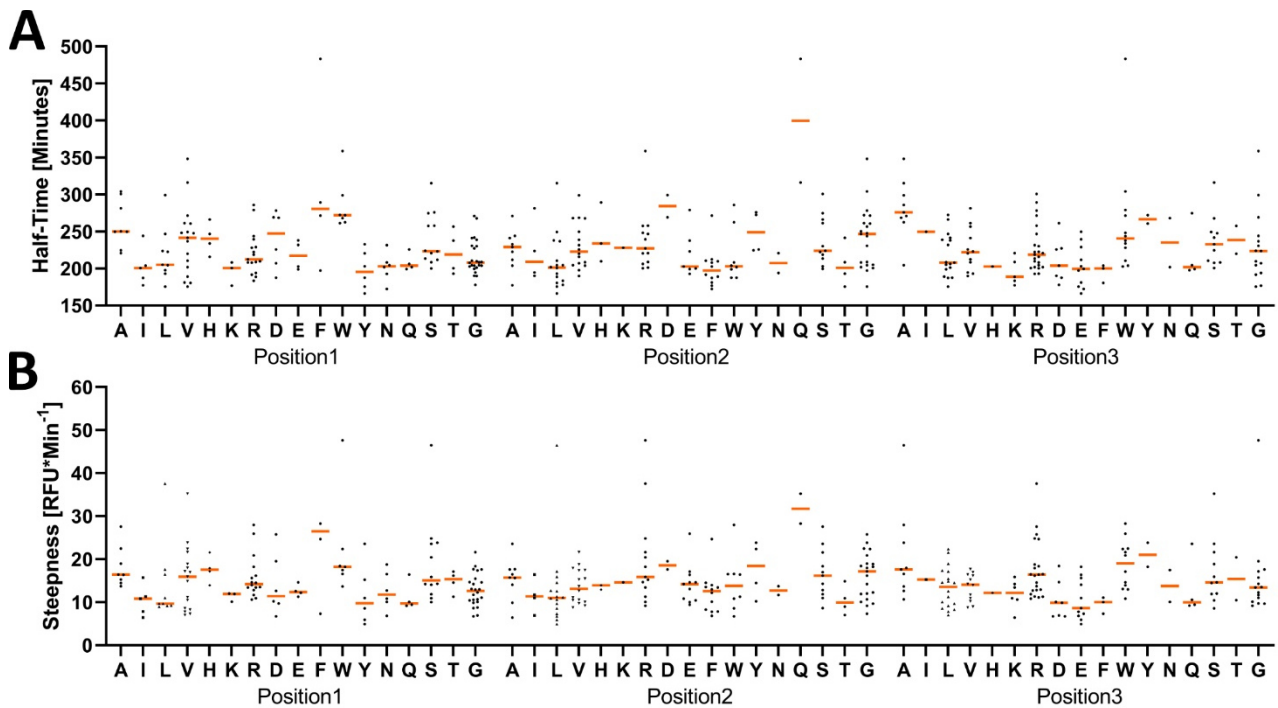
**Supplementary Figure 12** FACS dot plots and histograms of the sorting conditions for the model selection with <sup>SGS-ATMD1-S<sup>2168</sup></sup> and <sup>TVMV-ΔTMD1-S<sup>2168</sup></sup> under the pCTRL.wt.sRBS promoter related to Figure 31. Backward scatter against forward scatter dot plots of 100.000 recorded cells for the (A) positive control, (B) negative control and the (C) 1:10 mixture of positive to negative. (D) Histogram of all events against the RFU of the positive (green) and the negative (red) probe shows a ~10 times shift.

**Supplementary Table 1** Amino acid count of S<sup>2171</sup> library for every position. The residues M, C and P were not evaluated.

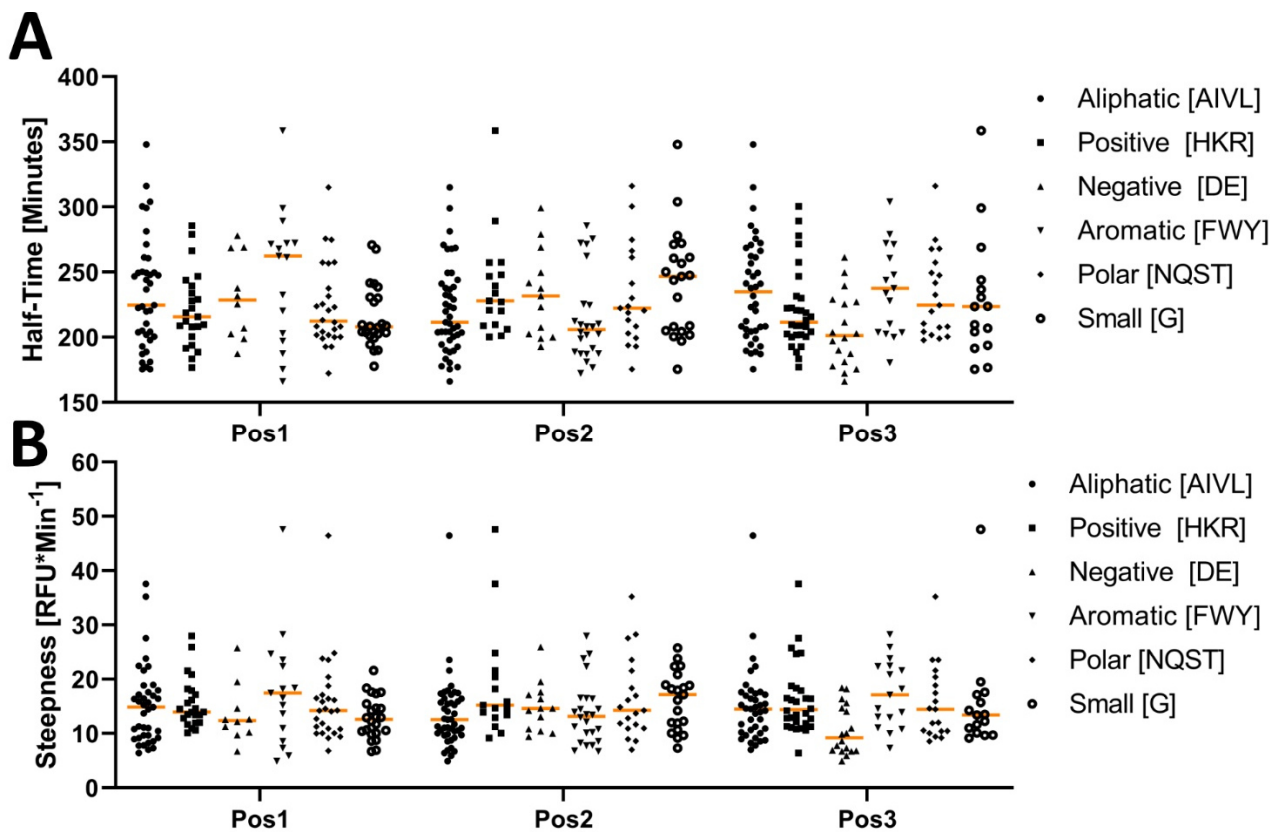
Amino Acid	Position 1	Position 2	Position 3	Total
I	5	4	1	10
V	17	16	12	45
L	9	16	18	43
K	3	1	5	9
R	16	13	22	51
H	4	3	1	8
D	6	1	7	14
E	4	11	11	26
F	4	11	3	18
W	7	7	11	25
Y	6	4	2	12
Q	4	2	3	9
N	6	2	2	10
S	12	11	11	34
T	4	3	2	9
G	24	18	10	52
A	8	6	8	22



Supplementary Figure 13 Impact of an amino acid on the (A) half-time and the (B) steepness without the discrimination of the residue position. Orange bars indicate the median (95% CI).



Supplementary Figure 14 Impact of an amino acid on the (A) half-time and the (B) steepness dependant on the position. Orange bars indicate the median (95% CI).



Supplementary Figure 15 Impact of grouped amino acids on the (A) half-time and the (B) steepness dependant on the position. Orange bars indicate the median (95% CI).

---

## References

---

- Agu, C. A., Klein, R., Lengler, J., Schilcher, F., Gregor, W., Peterbauer, T., Bläsi, U., Salmons, B., Günzburg, W. H., & Hohenadl, C. (2007). Bacteriophage-encoded toxins: the lambda-holin protein causes caspase-independent non-apoptotic cell death of eukaryotic cells. *Cellular Microbiology*, *9*(7), 1753–1765.
- Ahammad, T., Drew, D. L., Jr, Sahu, I. D., Serafin, R. A., Clowes, K. R., & Lorigan, G. A. (2019). Continuous Wave Electron Paramagnetic Resonance Spectroscopy Reveals the Structural Topology and Dynamic Properties of Active Pinholin S2168 in a Lipid Bilayer. *The Journal of Physical Chemistry. B*. <https://doi.org/10.1021/acs.jpcc.9b06480>
- Ahammad, T., Drew, D. L., Khan, R. H., Sahu, I. D., Faul, E., Li, T., & Lorigan, G. A. (2020). Structural Dynamics and Topology of the Inactive Form of S21 Holin in a Lipid Bilayer Using Continuous-Wave Electron Paramagnetic Resonance Spectroscopy. *The Journal of Physical Chemistry. B*, *124*(26), 5370–5379.
- Ahn, S.-J., Qu, M.-D., Roberts, E., Burne, R. A., & Rice, K. C. (2012). Identification of the *Streptococcus mutans* LytST two-component regulon reveals its contribution to oxidative stress tolerance. *BMC Microbiology*, *12*, 187.
- Akerboom, J., Rivera, J. D. V., Guilbe, M. M. R., Malavé, E. C. A., Hernandez, H. H., Tian, L., Hires, S. A., Marvin, J. S., Looger, L. L., & Schreier, E. R. (2009). Crystal structures of the GCaMP calcium sensor reveal the mechanism of fluorescence signal change and aid rational design. *The Journal of Biological Chemistry*, *284*(10), 6455–6464.
- Angius, F., Ilioaia, O., Amrani, A., Suisse, A., Rosset, L., Legrand, A., Abou-Hamdan, A., Uzan, M., Zito, F., & Miroux, B. (2018). A novel regulation mechanism of the T7 RNA polymerase based expression system improves overproduction and folding of membrane proteins. *Scientific Reports*, *8*(1), 8572.
- Araz, M. K., Tentori, A. M., & Herr, A. E. (2013). Microfluidic multiplexing in bioanalyses. *Journal of Laboratory Automation*, *18*(5), 350–366.
- Arnold, F. H. (1998). Design by Directed Evolution. *Accounts of Chemical Research*, *31*(3), 125–131.
- Arnold, F. H. (2019). Innovation by Evolution: Bringing New Chemistry to Life (Nobel Lecture). *Angewandte Chemie*, *58*(41), 14420–14426.
- Ast, C., Foret, J., Oltrogge, L. M., De Michele, R., Kleist, T. J., Ho, C.-H., & Frommer, W. B. (2017). Ratiometric Matryoshka biosensors from a nested cassette of green- and orange-emitting fluorescent proteins. *Nature Communications*, *8*(1), 431.
- Ayub, M., & Bayley, H. (2016). Engineered transmembrane pores. *Current Opinion in Chemical Biology*, *34*, 117–126.
- Baeza-Delgado, C., Marti-Renom, M. A., & Mingarro, I. (2013). Structure-based statistical analysis of transmembrane helices. *European Biophysics Journal: EBJ*, *42*(2-3), 199–207.
- Baird, G. S., Zacharias, D. A., & Tsien, R. Y. (1999). Circular permutation and receptor insertion within green fluorescent proteins. *Proceedings of the National Academy of Sciences of the United States of America*, *96*(20), 11241–11246.
- Baker, J. A., Wong, W.-C., Eisenhaber, B., Warwicker, J., & Eisenhaber, F. (2017). Charged residues next to transmembrane regions revisited: “Positive-inside rule” is complemented by the “negative inside depletion/outside enrichment rule.” *BMC Biology*, *15*(1), 66.
- Balaban, N. Q., Gerdes, K., Lewis, K., & McKinney, J. D. (2013). A problem of persistence: still more questions than answers? *Nature Reviews. Microbiology*, *11*(8), 587–591.
- Banaszynski, L. A., Liu, C. W., & Wandless, T. J. (2005). Characterization of the FKBP·Rapamycin·FRB Ternary Complex. *Journal of the American Chemical Society*, *127*(13), 4715–4721.
- Banghart, M., Borges, K., Isacoff, E., Trauner, D., & Kramer, R. H. (2004). Light-activated ion channels for remote control of neuronal firing. *Nature Neuroscience*, *7*(12), 1381–1386.
- Barboiu, M., & Gilles, A. (2013). From natural to bioassisted and biomimetic artificial water channel systems. *Accounts of Chemical Research*, *46*(12), 2814–2823.
- Baumruck, A. C., Tietze, D., Steinacker, L. K., & Tietze, A. A. (2018). Chemical synthesis of membrane proteins: a model study on the influenza virus B proton channel. *Chemical Science*, *9*(8), 2365–2375.
- Bayles, K. W. (2003). Are the molecular strategies that control apoptosis conserved in bacteria? *Trends in Microbiology*, *11*(7), 306–311.
- Bayles, K. W. (2007). The biological role of death and lysis in biofilm development. *Nature Reviews. Microbiology*, *5*(9), 721–726.
- Bayley, H., & Cremer, P. S. (2001). Stochastic sensors inspired by biology. *Nature*, *413*(6852), 226–230.
- Benner, S. A., & Sismour, A. M. (2005). Synthetic biology. *Nature Reviews. Genetics*, *6*(7), 533–543.
- Bentele, K., Saffert, P., Rauscher, R., Ignatova, Z., & Blüthgen, N. (2013). Efficient translation initiation dictates codon usage at gene start. *Molecular Systems Biology*, *9*, 675.

- Blake, S., Capone, R., Mayer, M., & Yang, J. (2008). Chemically reactive derivatives of gramicidin A for developing ion channel-based nanopores. *Bioconjugate Chemistry*, 19(8), 1614–1624.
- Bonhivers, M., Plançon, L., Ghazi, A., Boulanger, P., le Maire, M., Lambert, O., Rigaud, J. L., & Letellier, L. (1998). FhuA, an Escherichia coli outer membrane protein with a dual function of transporter and channel which mediates the transport of phage DNA. *Biochimie*, 80(5-6), 363–369.
- Bowden, R., Davies, R. W., Heger, A., Pagnamenta, A. T., de Cesare, M., Oikkonen, L. E., Parkes, D., Freeman, C., Dhalla, F., Patel, S. Y., Popitsch, N., Ip, C. L. C., Roberts, H. E., Salatino, S., Lockstone, H., Lunter, G., Taylor, J. C., Buck, D., Simpson, M. A., & Donnelly, P. (2019). Sequencing of human genomes with nanopore technology. *Nature Communications*, 10(1), 1869.
- Braha, O., Walker, B., Cheley, S., Kasianowicz, J. J., Song, L., Gouaux, J. E., & Bayley, H. (1997). Designed protein pores as components for biosensors. *Chemistry & Biology*, 4(7), 497–505.
- Brannigan, J. A., & Wilkinson, A. J. (2002). Protein engineering 20 years on. *Nature Reviews. Molecular Cell Biology*, 3(12), 964–970.
- Brantl, S., & Jahn, N. (2015). sRNAs in bacterial type I and type III toxin-antitoxin systems. *FEMS Microbiology Reviews*, 39(3), 413–427.
- Branton, D., Deamer, D. W., Marziali, A., Bayley, H., Benner, S. A., Butler, T., Di Ventra, M., Garaj, S., Hibbs, A., Huang, X., Jovanovich, S. B., Krstic, P. S., Lindsay, S., Ling, X. S., Mastrangelo, C. H., Meller, A., Oliver, J. S., Pershin, Y. V., Michael Ramsey, J., ... Schloss, J. A. (2008). The potential and challenges of nanopore sequencing. *Nature Biotechnology*, 26(10), 1146–1153.
- Braun, C. J., Baer, T., Moroni, A., & Thiel, G. (2014). Pseudo painting/air bubble technique for planar lipid bilayers. *Journal of Neuroscience Methods*, 233, 13–17.
- Braun, C. J., Lachnit, C., Becker, P., Henkes, L. M., Arrigoni, C., Kast, S. M., Moroni, A., Thiel, G., & Schroeder, I. (2014). Viral potassium channels as a robust model system for studies of membrane-protein interaction. *Biochimica et Biophysica Acta*, 1838(4), 1096–1103.
- Brogden, K. A. (2005). Antimicrobial peptides: pore formers or metabolic inhibitors in bacteria? *Nature Reviews. Microbiology*, 3(3), 238–250.
- Burns, J. R., Al-Juffali, N., Janes, S. M., & Howorka, S. (2014). Membrane-Spanning DNA Nanopores with Cytotoxic Effect. *Angewandte Chemie, International Edition*. <https://doi.org/10.1002/anie.201409587>
- Burns, J. R., Seifert, A., Fertig, N., & Howorka, S. (2016). A biomimetic DNA-based channel for the ligand-controlled transport of charged molecular cargo across a biological membrane. *Nature Nanotechnology*, 11(2), 152–156.
- Burns, J. R., Stulz, E., & Howorka, S. (2013). Self-assembled DNA nanopores that span lipid bilayers. *Nano Letters*, 13(6), 2351–2356.
- Cameron, D. E., Bashor, C. J., & Collins, J. J. (2014). A brief history of synthetic biology. *Nature Reviews. Microbiology*, 12(5), 381–390.
- Cárcel-Márquez, J., Flores, A., Martín-Cabello, G., Santero, E., & Camacho, E. M. (2019). Development of an inducible lytic system for functional metagenomic screening. *Scientific Reports*, 9(1), 3887.
- Carpenter, E. P., Beis, K., Cameron, A. D., & Iwata, S. (2008). Overcoming the challenges of membrane protein crystallography. *Current Opinion in Structural Biology*, 18(5), 581–586.
- Chang, C. Y., Nam, K., & Young, R. (1995). S gene expression and the timing of lysis by bacteriophage lambda. *Journal of Bacteriology*, 177(11), 3283–3294.
- Chang, G., Spencer, R. H., Lee, A. T., Barclay, M. T., & Rees, D. C. (1998). Structure of the MscL homolog from Mycobacterium tuberculosis: a gated mechanosensitive ion channel. *Science*, 282(5397), 2220–2226.
- Charbonnier, T., Le Coq, D., McGovern, S., Calabre, M., Delumeau, O., Aymerich, S., & Jules, M. (2017). Molecular and Physiological Logics of the Pyruvate-Induced Response of a Novel Transporter in Bacillus subtilis. *mBio*, 8(5). <https://doi.org/10.1128/mBio.00976-17>
- Chen, H., Bjerknes, M., Kumar, R., & Jay, E. (1994). Determination of the optimal aligned spacing between the Shine-Dalgarno sequence and the translation initiation codon of Escherichia coli mRNAs. *Nucleic Acids Research*, 22(23), 4953–4957.
- Chen, K., & Arnold, F. H. (1993). Tuning the activity of an enzyme for unusual environments: sequential random mutagenesis of subtilisin E for catalysis in dimethylformamide. *Proceedings of the National Academy of Sciences of the United States of America*, 90(12), 5618–5622.
- Chen, M., Khalid, S., Sansom, M. S. P., & Bayley, H. (2008). Outer membrane protein G: Engineering a quiet pore for biosensing. *Proceedings of the National Academy of Sciences of the United States of America*, 105(17), 6272–6277.
- Chen, X., Zaro, J. L., & Shen, W.-C. (2013). Fusion protein linkers: property, design and functionality. *Advanced Drug Delivery Reviews*, 65(10), 1357–1369.

- Chen, Y.-J., Groves, B., Muscat, R. A., & Seelig, G. (2015). DNA nanotechnology from the test tube to the cell. *Nature Nanotechnology*, *10*(9), 748–760.
- Chen, Y., & Young, R. (2016). The Last r Locus Unveiled: T4 RIII Is a Cytoplasmic Antiholin. *Journal of Bacteriology*, *198*(18), 2448–2457.
- Cherf, G. M., Lieberman, K. R., Rashid, H., Lam, C. E., Karplus, K., & Akeson, M. (2012). Automated forward and reverse ratcheting of DNA in a nanopore at 5-Å precision. *Nature Biotechnology*, *30*(4), 344–348.
- Cheung, P., Toda-Peters, K., & Shen, A. Q. (2012). In situ pressure measurement within deformable rectangular polydimethylsiloxane microfluidic devices. *Biomicrofluidics*, *6*(2), 26501–2650112.
- Cho, H., Jönsson, H., Campbell, K., Melke, P., Williams, J. W., Jedynek, B., Stevens, A. M., Groisman, A., & Levchenko, A. (2007). Self-organization in high-density bacterial colonies: efficient crowd control. *PLoS Biology*, *5*(11), e302.
- Cifu, A. S., Koeppe, R. E., 2nd, & Andersen, O. S. (1992). On the supramolecular organization of gramicidin channels. The elementary conducting unit is a dimer. *Biophysical Journal*, *61*(1), 189–203.
- Clayton, D., Shapovalov, G., Maurer, J. A., Dougherty, D. A., Lester, H. A., & Kochendoerfer, G. G. (2004). Total chemical synthesis and electrophysiological characterization of mechanosensitive channels from *Escherichia coli* and *Mycobacterium tuberculosis*. *Proceedings of the National Academy of Sciences of the United States of America*, *101*(14), 4764–4769.
- Cong, L., Ran, F. A., Cox, D., Lin, S., Barretto, R., Habib, N., Hsu, P. D., Wu, X., Jiang, W., Marraffini, L. A., & Zhang, F. (2013). Multiplex genome engineering using CRISPR/Cas systems. *Science*, *339*(6121), 819–823.
- Constantinou, A., & Polizzi, K. M. (2013). Opportunities for bioprocess monitoring using FRET biosensors. *Biochemical Society Transactions*, *41*(5), 1146–1151.
- Cornell, B. A., Braach-Maksvytis, V. L. B., King, L. G., Osman, P. D. J., Raguse, B., Wieczorek, L., & Pace, R. J. (1997). A biosensor that uses ion-channel switches. *Nature*, *387*(6633), 580–583.
- Cosentino, C., Alberio, L., Gazzarrini, S., Aquila, M., Romano, E., Cermenati, S., Zuccolini, P., Petersen, J., Beltrame, M., Van Etten, J. L., Christie, J. M., Thiel, G., & Moroni, A. (2015). Optogenetics. Engineering of a light-gated potassium channel. *Science*, *348*(6235), 707–710.
- Cowan, S. W., Schirmer, T., Rummel, G., Steiert, M., Ghosh, R., Pauptit, R. A., Jansonius, J. N., & Rosenbusch, J. P. (1992). Crystal structures explain functional properties of two *E. coli* porins. *Nature*, *358*(6389), 727–733.
- Cramer, A., Raillard, S. A., Bermudez, E., & Stemmer, W. P. (1998). DNA shuffling of a family of genes from diverse species accelerates directed evolution. *Nature*, *391*(6664), 288–291.
- Dagliyan, O., Karginov, A. V., Yagishita, S., Gale, M. E., Wang, H., DerMardirossian, C., Wells, C. M., Dokholyan, N. V., Kasai, H., & Hahn, K. M. (2017). Engineering Pak1 Allosteric Switches. *ACS Synthetic Biology*, *6*(7), 1257–1262.
- Dagliyan, O., Shirvanyants, D., Karginov, A. V., Ding, F., Fee, L., Chandrasekaran, S. N., Freisinger, C. M., Smolen, G. A., Huttenlocher, A., Hahn, K. M., & Dokholyan, N. V. (2013). Rational design of a ligand-controlled protein conformational switch. *Proceedings of the National Academy of Sciences of the United States of America*, *110*(17), 6800–6804.
- Dalbadie-McFarland, G., Cohen, L. W., Riggs, A. D., Morin, C., Itakura, K., & Richards, J. H. (1982). Oligonucleotide-directed mutagenesis as a general and powerful method for studies of protein function. *Proceedings of the National Academy of Sciences of the United States of America*, *79*(21), 6409–6413.
- Dal Peraro, M., & van der Goot, F. G. (2016). Pore-forming toxins: ancient, but never really out of fashion. *Nature Reviews. Microbiology*, *14*(2), 77–92.
- Danial, N. N., & Korsmeyer, S. J. (2004). Cell death: critical control points. *Cell*, *116*(2), 205–219.
- Davis, J. H., Baker, T. A., & Sauer, R. T. (2011). Small-molecule control of protein degradation using split adaptors. *ACS Chemical Biology*. <https://pubs.acs.org/doi/abs/10.1021/cb2001389>
- Deamer, D., Akeson, M., & Branton, D. (2016). Three decades of nanopore sequencing. *Nature Biotechnology*, *34*(5), 518–524.
- DeBerardinis, R. J., & Thompson, C. B. (2012). Cellular Metabolism and Disease: What Do Metabolic Outliers Teach Us? *Cell*, *148*(6), 1132–1144.
- Degnan, P. H., & Moran, N. A. (2008). Diverse phage-encoded toxins in a protective insect endosymbiont. *Applied and Environmental Microbiology*, *74*(21), 6782–6791.
- del Solar, G., Giraldo, R., Ruiz-Echevarría, M. J., Espinosa, M., & Díaz-Orejas, R. (1998). Replication and control of circular bacterial plasmids. *Microbiology and Molecular Biology Reviews: MMBR*, *62*(2), 434–464.
- Demchick, P., & Koch, A. L. (1996). The permeability of the wall fabric of *Escherichia coli* and *Bacillus subtilis*. *Journal of Bacteriology*. <https://jb.asm.org/content/178/3/768.short>
- Derossi, D., Calvet, S., Trembleau, A., Brunissen, A., Chassaing, G., & Prochiantz, A. (1996). Cell internalization of the third helix of the Antennapedia homeodomain is receptor-independent. *The Journal of Biological Chemistry*, *271*(30), 18188–18193.

- de Vrije, G. J., Batenburg, A. M., Killian, J. A., & de Kruijff, B. (1990). Lipid involvement in protein translocation in *Escherichia coli*. *Molecular Microbiology*, 4(1), 143–150.
- Diaz, R., Rech, J., & Bouet, J.-Y. (2015). Imaging centromere-based incompatibilities: Insights into the mechanism of incompatibility mediated by low-copy number plasmids. *Plasmid*, 80, 54–62.
- Diederichs, T., Nguyen, Q. H., Urban, M., Tampé, R., & Tornow, M. (2018). Transparent Nanopore Cavity Arrays Enable Highly Parallelized Optical Studies of Single Membrane Proteins on Chip. *Nano Letters*, 18(6), 3901–3910.
- Dong, H., Sharma, M., Zhou, H.-X., & Cross, T. A. (2012). Glycines: role in  $\alpha$ -helical membrane protein structures and a potential indicator of native conformation. *Biochemistry*, 51(24), 4779–4789.
- Douglas, S. M., Marblestone, A. H., Teerapittayanon, S., Vazquez, A., Church, G. M., & Shih, W. M. (2009). Rapid prototyping of 3D DNA-origami shapes with caDNAno. *Nucleic Acids Research*, 37(15), 5001–5006.
- Doyle, D. A., Morais Cabral, J., Pfuetzner, R. A., Kuo, A., Gulbis, J. M., Cohen, S. L., Chait, B. T., & MacKinnon, R. (1998). The structure of the potassium channel: molecular basis of K<sup>+</sup> conduction and selectivity. *Science*, 280(5360), 69–77.
- Drew, D. L., Jr, Ahammad, T., Serafin, R. A., Butcher, B. J., Clowes, K. R., Drake, Z., Sahu, I. D., McCarrick, R. M., & Lorigan, G. A. (2019). Solid phase synthesis and spectroscopic characterization of the active and inactive forms of bacteriophage S21 pinholin protein. *Analytical Biochemistry*, 567, 14–20.
- Dubendorff, J. W., & Studier, F. W. (1991). Controlling basal expression in an inducible T7 expression system by blocking the target T7 promoter with lac repressor. *Journal of Molecular Biology*, 219(1), 45–59.
- Eason, M. G., Damry, A. M., & Chica, R. A. (2017). Structure-guided rational design of red fluorescent proteins: towards designer genetically-encoded fluorophores. *Current Opinion in Structural Biology*, 45, 91–99.
- Elowitz, M. B., & Leibler, S. (2000). A synthetic oscillatory network of transcriptional regulators. *Nature*, 403(6767), 335–338.
- Faller, M., Niederweis, M., & Schulz, G. E. (2004). The structure of a mycobacterial outer-membrane channel. *Science*, 303(5661), 1189–1192.
- Fauvart, M., De Groote, V. N., & Michiels, J. (2011). Role of persister cells in chronic infections: clinical relevance and perspectives on anti-persister therapies. *Journal of Medical Microbiology*, 60(Pt 6), 699–709.
- Fehr, M., Okumoto, S., Deuschle, K., Lager, I., Looger, L. L., Persson, J., Kozhukh, L., Lalonde, S., & Frommer, W. B. (2005). Development and use of fluorescent nanosensors for metabolite imaging in living cells. *Biochemical Society Transactions*, 33(Pt 1), 287–290.
- Feng, Y., Zhang, Y., Ying, C., Wang, D., & Du, C. (2015). Nanopore-based fourth-generation DNA sequencing technology. *Genomics, Proteomics & Bioinformatics*, 13(1), 4–16.
- Focke, P. J., & Valiyaveetil, F. I. (2010). Studies of ion channels using expressed protein ligation. *Current Opinion in Chemical Biology*, 14(6), 797–802.
- Fujii, S., Matsuura, T., Sunami, T., Kazuta, Y., & Yomo, T. (2013). In vitro evolution of  $\alpha$ -hemolysin using a liposome display. *Proceedings of the National Academy of Sciences of the United States of America*, 110(42), 16796–16801.
- Fujii, S., Matsuura, T., Sunami, T., Nishikawa, T., Kazuta, Y., & Yomo, T. (2014). Liposome display for in vitro selection and evolution of membrane proteins. *Nature Protocols*, 9(7), 1578–1591.
- Funakoshi, K., Suzuki, H., & Takeuchi, S. (2006). Lipid bilayer formation by contacting monolayers in a microfluidic device for membrane protein analysis. *Analytical Chemistry*, 78(24), 8169–8174.
- Galonek, H. L., & Hardwick, J. M. (2006). Upgrading the BCL-2 network [Review of *Upgrading the BCL-2 network*]. *Nature Cell Biology*, 8(12), 1317–1319.
- Gangola, P., & Rosen, B. P. (1987). Maintenance of intracellular calcium in *Escherichia coli*. *The Journal of Biological Chemistry*, 262(26), 12570–12574.
- Garcia, P. A., Ge, Z., Moran, J. L., & Buie, C. R. (2016). Microfluidic Screening of Electric Fields for Electroporation. *Scientific Reports*, 6, 21238.
- Garrett, J., Bruno, C., & Young, R. (1990). Lysis protein S of phage lambda functions in *Saccharomyces cerevisiae*. *Journal of Bacteriology*, 172(12), 7275–7277.
- Gatti-Lafranconi, P., Dijkman, W. P., Devenish, S. R. A., & Hollfelder, F. (2013). A single mutation in the core domain of the lac repressor reduces leakiness. *Microbial Cell Factories*, 12, 67.
- Geng, J., Kim, K., Zhang, J., Escalada, A., Tunuguntla, R., Comolli, L. R., Allen, F. I., Shnyrova, A. V., Cho, K. R., Munoz, D., Wang, Y. M., Grigoropoulos, C. P., Ajo-Franklin, C. M., Frolov, V. A., & Noy, A. (2014). Stochastic transport through carbon nanotubes in lipid bilayers and live cell membranes. *Nature*, 514(7524), 612–615.
- George, R. A., & Heringa, J. (2002). An analysis of protein domain linkers: their classification and role in protein folding. *Protein Engineering*, 15(11), 871–879.
- Gokel, G. W., & Negin, S. (2013). Synthetic ion channels: from pores to biological applications. *Accounts of Chemical Research*, 46(12), 2824–2833.

- Goodman, D. B., Church, G. M., & Kosuri, S. (2013). Causes and effects of N-terminal codon bias in bacterial genes. *Science*, 342(6157), 475–479.
- Göpfrich, K., Li, C.-Y., Mames, I., Bhamidimarri, S. P., Ricci, M., Yoo, J., Mames, A., Ohmann, A., Winterhalter, M., Stulz, E., Aksimentiev, A., & Keyser, U. F. (2016). Ion Channels Made from a Single Membrane-Spanning DNA Duplex. *Nano Letters*, 16(7), 4665–4669.
- Göpfrich, K., Zettl, T., Meijering, A. E. C., Hernández-Ainsa, S., Kocabey, S., Liedl, T., & Keyser, U. F. (2015). DNA-Tile Structures Induce Ionic Currents through Lipid Membranes. *Nano Letters*, 15(5), 3134–3138.
- Goyal, P., Krasteva, P. V., Van Gerven, N., Gubellini, F., Van den Broeck, I., Troupiotis-Tsailaki, A., Jonckheere, W., Péhau-Arnaudet, G., Pinkner, J. S., Chapman, M. R., Hultgren, S. J., Howorka, S., Fronzes, R., & Remaut, H. (2014). Structural and mechanistic insights into the bacterial amyloid secretion channel CsgG. *Nature*, 516(7530), 250–253.
- Granseth, E., von Heijne, G., & Elofsson, A. (2005). A Study of the Membrane–Water Interface Region of Membrane Proteins. *Journal of Molecular Biology*, 346(1), 377–385.
- Gräwe, A., Ranglack, J., Weyrich, A., & Stein, V. (2020). iFLinkC: an iterative functional linker cloning strategy for the combinatorial assembly and recombination of linker peptides with functional domains. *Nucleic Acids Research*, 48(4), e24.
- Gründling, A., Manson, M. D., & Young, R. (2001). Holins kill without warning. *Proceedings of the National Academy of Sciences of the United States of America*, 98(16), 9348–9352.
- Guiziou, S., Sauveplane, V., & Chang, H. J. (2016). A part toolbox to tune genetic expression in *Bacillus subtilis*. *Nucleic Acids*. <https://academic.oup.com/nar/article-abstract/44/15/7495/2457776>
- Gu, L. Q., & Bayley, H. (2000). Interaction of the noncovalent molecular adapter, beta-cyclodextrin, with the staphylococcal alpha-hemolysin pore. *Biophysical Journal*, 79(4), 1967–1975.
- Gu, L. Q., Braha, O., Conlan, S., Cheley, S., & Bayley, H. (1999). Stochastic sensing of organic analytes by a pore-forming protein containing a molecular adapter. *Nature*, 398(6729), 686–690.
- Gu, L. Q., Cheley, S., & Bayley, H. (2001). Capture of a single molecule in a nanocavity. *Science*, 291(5504), 636–640.
- Guntas, G., Mansell, T. J., Kim, J. R., & Ostermeier, M. (2005). Directed evolution of protein switches and their application to the creation of ligand-binding proteins. *Proceedings of the National Academy of Sciences of the United States of America*, 102(32), 11224–11229.
- Guo, Z., Johnston, W. A., Stein, V., Kalimuthu, P., Perez-Alcala, S., Bernhardt, P. V., & Alexandrov, K. (2016). Engineering PQQ-glucose dehydrogenase into an allosteric electrochemical Ca(2+) sensor. *Chemical Communications*, 52(3), 485–488.
- Gurnev, P. A., Ortenberg, R., Dörr, T., Lewis, K., & Bezrukov, S. M. (2012). Persister-promoting bacterial toxin TisB produces anion-selective pores in planar lipid bilayers. *FEBS Letters*, 586(16), 2529–2534.
- Gutsmann, T., Heimburg, T., Keyser, U., Mahendran, K. R., & Winterhalter, M. (2015). Protein reconstitution into freestanding planar lipid membranes for electrophysiological characterization. *Nature Protocols*, 10(1), 188–198.
- Guzman, L. M., Belin, D., Carson, M. J., & Beckwith, J. (1995). Tight regulation, modulation, and high-level expression by vectors containing the arabinose PBAD promoter. *Journal of Bacteriology*, 177(14), 4121–4130.
- Heinemann, M., & Sauer, U. (2010). Systems biology of microbial metabolism. *Current Opinion in Microbiology*, 13(3), 337–343.
- Heins, A.-L., Johanson, T., Han, S., Lundin, L., Carlquist, M., Gernaey, K. V., Sørensen, S. J., & Eliasson Lantz, A. (2019). Quantitative Flow Cytometry to Understand Population Heterogeneity in Response to Changes in Substrate Availability in *Escherichia coli* and *Saccharomyces cerevisiae* Chemostats. *Frontiers in Bioengineering and Biotechnology*, 7, 187.
- Hindley, J. W., Zheleva, D. G., Elani, Y., Charalambous, K., Barter, L. M. C., Booth, P. J., Bevan, C. L., Law, R. V., & Ces, O. (2019). Building a synthetic mechanosensitive signaling pathway in compartmentalized artificial cells. *Proceedings of the National Academy of Sciences of the United States of America*, 116(34), 16711–16716.
- Hirel, P. H., Schmitter, M. J., Dessen, P., Fayat, G., & Blanquet, S. (1989). Extent of N-terminal methionine excision from *Escherichia coli* proteins is governed by the side-chain length of the penultimate amino acid. *Proceedings of the National Academy of Sciences of the United States of America*, 86(21), 8247–8251.
- Hladky, S. B., & Haydon, D. A. (1970). Discreteness of conductance change in bimolecular lipid membranes in the presence of certain antibiotics. *Nature*, 225(5231), 451–453.
- Hohmann, H.-P., van Dijl, J. M., Krishnappa, L., & Prágai, Z. (2017). Host Organisms: *Bacillus subtilis*. *Industrial Biotechnology*, 221–297.
- Howorka, S. (2017). Building membrane nanopores. *Nature Nanotechnology*, 12(7), 619–630.
- Howorka, S., Cheley, S., & Bayley, H. (2001). Sequence-specific detection of individual DNA strands using engineered nanopores. *Nature Biotechnology*, 19(7), 636–639.

- Howorka, S., & Siwy, Z. (2009). Nanopore analytics: sensing of single molecules. *Chemical Society Reviews*, 38(8), 2360–2384.
- Huang, C. C., Meng, E. C., Morris, J. H., Pettersen, E. F., & Ferrin, T. E. (2014). Enhancing UCSF Chimera through web services. *Nucleic Acids Research*, 42(Web Server issue), W478–W484.
- Huang, S., Romero-Ruiz, M., Castell, O. K., Bayley, H., & Wallace, M. I. (2015). High-throughput optical sensing of nucleic acids in a nanopore array. *Nature Nanotechnology*, 10(11), 986–991.
- Hwang, W. L., Chen, M., Cronin, B., Holden, M. A., & Bayley, H. (2008). Asymmetric droplet interface bilayers. *Journal of the American Chemical Society*, 130(18), 5878–5879.
- Ibraheem, A., Yap, H., Ding, Y., & Campbell, R. E. (2011). A bacteria colony-based screen for optimal linker combinations in genetically encoded biosensors. *BMC Biotechnology*, 11, 105.
- Imburgio, D., Rong, M., Ma, K., & McAllister, W. T. (2000). Studies of promoter recognition and start site selection by T7 RNA polymerase using a comprehensive collection of promoter variants. *Biochemistry*, 39(34), 10419–10430.
- Ingolia, N. T., Ghaemmighami, S., Newman, J. R. S., & Weissman, J. S. (2009). Genome-wide analysis in vivo of translation with nucleotide resolution using ribosome profiling. *Science*, 324(5924), 218–223.
- Inobe, T., & Nukina, N. (2016). Rapamycin-induced oligomer formation system of FRB-FKBP fusion proteins. *Journal of Bioscience and Bioengineering*, 122(1), 40–46.
- Ismail, N., Hedman, R., Lindén, M., & von Heijne, G. (2015). Charge-driven dynamics of nascent-chain movement through the SecYEG translocon. *Nature Structural & Molecular Biology*, 22(2), 145–149.
- Ismail, N., Hedman, R., Schiller, N., & von Heijne, G. (2012). A biphasic pulling force acts on transmembrane helices during translocon-mediated membrane integration. *Nature Structural & Molecular Biology*, 19(10), 1018–1022.
- Jiang, X., & Wang, X. (2004). Cytochrome C-mediated apoptosis. *Annual Review of Biochemistry*, 73, 87–106.
- Jinek, M., Chylinski, K., Fonfara, I., Hauer, M., Doudna, J. A., & Charpentier, E. (2012). A programmable dual-RNA-guided DNA endonuclease in adaptive bacterial immunity. *Science*, 337(6096), 816–821.
- Ji, Z., Wang, S., Zhao, Z., Zhou, Z., Haque, F., & Guo, P. (2016). Fingerprinting of Peptides with a Large Channel of Bacteriophage Phi29 DNA Packaging Motor. *Small*, 12(33), 4572–4578.
- Joh, N. H., Wang, T., Bhate, M. P., Acharya, R., Wu, Y., Grabe, M., Hong, M., Grigoryan, G., & DeGrado, W. F. (2014). De novo design of a transmembrane Zn<sup>2+</sup>-transporting four-helix bundle. *Science*, 346(6216), 1520–1524.
- Jones, P. T., Dear, P. H., Foote, J., Neuberger, M. S., & Winter, G. (1986). Replacing the complementarity-determining regions in a human antibody with those from a mouse. *Nature*, 321(6069), 522–525.
- Jung, Y., Bayley, H., & Movileanu, L. (2006). Temperature-responsive protein pores. *Journal of the American Chemical Society*, 128(47), 15332–15340.
- Kang, X.-F., Cheley, S., Guan, X., & Bayley, H. (2006). Stochastic detection of enantiomers. *Journal of the American Chemical Society*, 128(33), 10684–10685.
- Kasianowicz, J. J., Brandin, E., Branton, D., & Deamer, D. W. (1996). Characterization of individual polynucleotide molecules using a membrane channel. *Proceedings of the National Academy of Sciences of the United States of America*, 93(24), 13770–13773.
- Kawano, R., Osaki, T., Sasaki, H., Takinoue, M., Yoshizawa, S., & Takeuchi, S. (2011). Rapid detection of a cocaine-binding aptamer using biological nanopores on a chip. *Journal of the American Chemical Society*, 133(22), 8474–8477.
- Ketchum, R. R., Hu, W., & Cross, T. A. (1993). High-resolution conformation of gramicidin A in a lipid bilayer by solid-state NMR. *Science*, 261(5127), 1457–1460.
- Keyser, U. F. (2011). Controlling molecular transport through nanopores. *Journal of the Royal Society, Interface / the Royal Society*, 8(63), 1369–1378.
- Killian, J. A., & von Heijne, G. (2000). How proteins adapt to a membrane–water interface. *Trends in Biochemical Sciences*, 25(9), 429–434.
- Kim, R., Sandler, S. J., Goldman, S., Yokota, H., Clark, A. J., & Kim, S.-H. (1998). Overexpression of archaeal proteins in Escherichia coli. *Biotechnology Letters*, 20(3), 207–210.
- Kim, S., Jeon, T.-J., Oberai, A., Yang, D., Schmidt, J. J., & Bowie, J. U. (2005). Transmembrane glycine zippers: physiological and pathological roles in membrane proteins. *Proceedings of the National Academy of Sciences of the United States of America*, 102(40), 14278–14283.
- Klarenbeek, J. B., Goedhart, J., Hink, M. A., Gadella, T. W. J., & Jalink, K. (2011). A mTurquoise-based cAMP sensor for both FLIM and ratiometric read-out has improved dynamic range. *PloS One*, 6(4), e19170.
- Kleefen, A., Pedone, D., Grunwald, C., Wei, R., Firnkens, M., Abstreiter, G., Rant, U., & Tampé, R. (2010). Multiplexed parallel single transport recordings on nanopore arrays. *Nano Letters*, 10(12), 5080–5087.

- Koçer, A., Walko, M., Meijberg, W., & Feringa, B. L. (2005). A light-actuated nanovalve derived from a channel protein. *Science*, 309(5735), 755–758.
- Kochendoerfer, G. G., Salom, D., Lear, J. D., Wilk-Orescan, R., Kent, S. B., & DeGrado, W. F. (1999). Total chemical synthesis of the integral membrane protein influenza A virus M2: role of its C-terminal domain in tetramer assembly. *Biochemistry*, 38(37), 11905–11913.
- Kolos, J. M., Voll, A. M., Bauder, M., & Hausch, F. (2018). FKBP Ligands-Where We Are and Where to Go? *Frontiers in Pharmacology*, 9, 1425.
- Kongari, R., Rajaure, M., Cahill, J., Rasche, E., Mijalis, E., Berry, J., & Young, R. (2018). Phage spanins: diversity, topological dynamics and gene convergence. *BMC Bioinformatics*, 19(1), 326.
- Krishan, A. (1975). Rapid flow cytofluorometric analysis of mammalian cell cycle by propidium iodide staining. *The Journal of Cell Biology*, 66(1), 188–193.
- Krishnamoorthy, G., Wolloscheck, D., Weeks, J. W., Croft, C., Rybenkov, V. V., & Zgurskaya, H. I. (2016). Breaking the Permeability Barrier of Escherichia coli by Controlled Hyperporination of the Outer Membrane. *Antimicrobial Agents and Chemotherapy*, 60(12), 7372–7381.
- Krishnan R, S., Satheesan, R., Puthumadathil, N., Kumar, K. S., Jayasree, P., & Mahendran, K. R. (2019). Autonomously Assembled Synthetic Transmembrane Peptide Pore. *Journal of the American Chemical Society*, 141(7), 2949–2959.
- Krishnan, S., Ziegler, D., Arnaut, V., Martin, T. G., Kapsner, K., Henneberg, K., Bausch, A. R., Dietz, H., & Simmel, F. C. (2016). Molecular transport through large-diameter DNA nanopores. *Nature Communications*, 7, 12787.
- Krogh, A., Larsson, B., von Heijne, G., & Sonnhammer, E. L. (2001). Predicting transmembrane protein topology with a hidden Markov model: application to complete genomes. *Journal of Molecular Biology*, 305(3), 567–580.
- Kusters, I., van Oijen, A. M., & Driessen, A. J. M. (2014). Membrane-on-a-chip: microstructured silicon/silicon-dioxide chips for high-throughput screening of membrane transport and viral membrane fusion. *ACS Nano*, 8(4), 3380–3392.
- Langecker, M., Arnaut, V., Martin, T. G., List, J., Renner, S., Mayer, M., Dietz, H., & Simmel, F. C. (2012). Synthetic lipid membrane channels formed by designed DNA nanostructures. *Science*, 338(6109), 932–936.
- Laszlo, A. H., Derrington, I. M., Brinkerhoff, H., Langford, K. W., Nova, I. C., Samson, J. M., Bartlett, J. J., Pavlenok, M., & Gundlach, J. H. (2013). Detection and mapping of 5-methylcytosine and 5-hydroxymethylcytosine with nanopore MspA. *Proceedings of the National Academy of Sciences of the United States of America*, 110(47), 18904–18909.
- Laursen, B. S., Sørensen, H. P., Mortensen, K. K., & Sperling-Petersen, H. U. (2005). Initiation of protein synthesis in bacteria. *Microbiology and Molecular Biology Reviews: MMBR*, 69(1), 101–123.
- LB agar. (2009). *Cold Spring Harbor Protocols*, 2009(3), db.rec11683.
- LB (Luria-Bertani) liquid medium. (2006). *Cold Spring Harbor Protocols*, 2006(1), db.rec8141.
- Lee, J., & Bayley, H. (2015). Semisynthetic protein nanoreactor for single-molecule chemistry. *Proceedings of the National Academy of Sciences of the United States of America*, 112(45), 13768–13773.
- Lee, S. K., & Keasling, J. D. (2005). A propionate-inducible expression system for enteric bacteria. *Applied and Environmental Microbiology*, 71(11), 6856–6862.
- Lee, S. K., & Keasling, J. D. (2006). Propionate-regulated high-yield protein production in Escherichia coli. *Biotechnology and Bioengineering*, 93(5), 912–918.
- Leitgeb, B., Szekeres, A., Manczinger, L., Vágvölgyi, C., & Kredics, L. (2007). The history of alamethicin: a review of the most extensively studied peptaibol. *Chemistry & Biodiversity*, 4(6), 1027–1051.
- Levin-Reisman, I., Ronin, I., Gefen, O., Braniss, I., Shores, N., & Balaban, N. Q. (2017). Antibiotic tolerance facilitates the evolution of resistance. *Science*, 355(6327), 826–830.
- Liang, S., Bipatnath, M., Xu, Y., Chen, S., Dennis, P., Ehrenberg, M., & Bremer, H. (1999). Activities of constitutive promoters in Escherichia coli. *Journal of Molecular Biology*, 292(1), 19–37.
- Lin, C.-Y., & Liu, J. C. (2016). Modular protein domains: an engineering approach toward functional biomaterials. *Current Opinion in Biotechnology*, 40, 56–63.
- Lindenburg, L. H., Hessels, A. M., Ebberink, E. H. T. M., Arts, R., & Merkx, M. (2013). Robust red FRET sensors using self-associating fluorescent domains. *ACS Chemical Biology*, 8(10), 2133–2139.
- Lindenburg, L. H., Vinkenburg, J. L., Oortwijn, J., Aper, S. J. A., & Merkx, M. (2013). MagFRET: the first genetically encoded fluorescent Mg<sup>2+</sup> sensor. *PloS One*, 8(12), e82009.
- Littleton, J. T., & Ganetzky, B. (2000). Ion channels and synaptic organization: analysis of the Drosophila genome. *Neuron*, 26(1), 35–43.
- Litvinchuk, S., Tanaka, H., Miyatake, T., Pasini, D., Tanaka, T., Bollot, G., Mareda, J., & Matile, S. (2007). Synthetic pores with reactive signal amplifiers as artificial tongues. *Nature Materials*, 6(8), 576–580.

- Litzlbauer, J., Schifferer, M., Ng, D., Fabritius, A., Thestrup, T., & Griesbeck, O. (2015). Large Scale Bacterial Colony Screening of Diversified FRET Biosensors. *PLoS One*, *10*(6), e0119860.
- Liu, L., & Wu, H.-C. (2016). DNA-Based Nanopore Sensing. *Angewandte Chemie*, *55*(49), 15216–15222.
- Liu, Y., Liu, L., Li, J., Du, G., & Chen, J. (2019). Synthetic biology toolbox and chassis development in *Bacillus subtilis*. *Trends in Biotechnology*. <https://www.sciencedirect.com/science/article/pii/S0167779918303019>
- Lobato-Márquez, D., Díaz-Orejas, R., & García-Del Portillo, F. (2016). Toxin-antitoxins and bacterial virulence. *FEMS Microbiology Reviews*, *40*(5), 592–609.
- Lo, C. S., Prewett, P. D., Davies, G. J., Bowen, J., & Vanner, K. (2008). A micromagnetoflowcell for microfluidic measurements. *Microelectronic Engineering*, *85*(5), 1062–1065.
- Loudwig, S., & Bayley, H. (2006). Photoisomerization of an individual azobenzene molecule in water: an on-off switch triggered by light at a fixed wavelength. *Journal of the American Chemical Society*, *128*(38), 12404–12405.
- Lu, S., Li, W.-W., Rotem, D., Mikhailova, E., & Bayley, H. (2010). A primary hydrogen-deuterium isotope effect observed at the single-molecule level. *Nature Chemistry*, *2*(11), 921–928.
- Mabe, S., Nagamune, T., & Kawahara, M. (2014). Detecting protein-protein interactions based on kinase-mediated growth induction of mammalian cells. *Scientific Reports*, *4*, 6127.
- Macrae, M. X., Blake, S., Jiang, X., Capone, R., Estes, D. J., Mayer, M., & Yang, J. (2009). A semi-synthetic ion channel platform for detection of phosphatase and protease activity. *ACS Nano*, *3*(11), 3567–3580.
- Maglia, G., Heron, A. J., Hwang, W. L., Holden, M. A., Mikhailova, E., Li, Q., Cheley, S., & Bayley, H. (2009). Droplet networks with incorporated protein diodes show collective properties. *Nature Nanotechnology*, *4*(7), 437–440.
- Mahendran, K. R., Niitsu, A., Kong, L., Thomson, A. R., Sessions, R. B., Woolfson, D. N., & Bayley, H. (2017). A monodisperse transmembrane  $\alpha$ -helical peptide barrel. *Nature Chemistry*, *9*(5), 411–419.
- Mahendran, K. R., Romero-Ruiz, M., Schlösinger, A., Winterhalter, M., & Nussberger, S. (2012). Protein translocation through Tom40: kinetics of peptide release. *Biophysical Journal*, *102*(1), 39–47.
- Maingi, V., Lelimosin, M., Howorka, S., & Sansom, M. S. P. (2015). Gating-like Motions and Wall Porosity in a DNA Nanopore Scaffold Revealed by Molecular Simulations. *ACS Nano*, *9*(11), 11209–11217.
- Mairhofer, J., Wittwer, A., Cserjan-Puschmann, M., & Striedner, G. (2015). Preventing T7 RNA polymerase read-through transcription-A synthetic termination signal capable of improving bioprocess stability. *ACS Synthetic Biology*, *4*(3), 265–273.
- Majumder, S., Garamella, J., Wang, Y.-L., DeNies, M., Noireaux, V., & Liu, A. P. (2017). Cell-sized mechanosensitive and biosensing compartment programmed with DNA. *Chemical Communications*, *53*(53), 7349–7352.
- Mandala, V. S., Loftis, A. R., Shcherbakov, A. A., Pentelute, B. L., & Hong, M. (2020). Atomic structures of closed and open influenza B M2 proton channel reveal the conduction mechanism. *Nature Structural & Molecular Biology*, *27*(2), 160–167.
- Mank, M., & Griesbeck, O. (2008). Genetically encoded calcium indicators. *Chemical Reviews*, *108*(5), 1550–1564.
- Manrao, E. A., Derrington, I. M., Laszlo, A. H., Langford, K. W., Hopper, M. K., Gillgren, N., Pavlenok, M., Niederweis, M., & Gundlach, J. H. (2012). Reading DNA at single-nucleotide resolution with a mutant MspA nanopore and phi29 DNA polymerase. *Nature Biotechnology*, *30*(4), 349–353.
- Marvin, J. S., Borghuis, B. G., Tian, L., Cichon, J., Harnett, M. T., Akerboom, J., Gordus, A., Renninger, S. L., Chen, T.-W., Bargmann, C. I., Orger, M. B., Schreier, E. R., Demb, J. B., Gan, W.-B., Hires, S. A., & Looger, L. L. (2013). An optimized fluorescent probe for visualizing glutamate neurotransmission. *Nature Methods*, *10*(2), 162–170.
- Matson, E. G., Thompson, M. G., Humphrey, S. B., Zuerner, R. L., & Stanton, T. B. (2005). Identification of genes of VSH-1, a prophage-like gene transfer agent of *Brachyspira hyodysenteriae*. *Journal of Bacteriology*, *187*(17), 5885–5892.
- Mayer, M., & Yang, J. (2013). Engineered ion channels as emerging tools for chemical biology. *Accounts of Chemical Research*, *46*(12), 2998–3008.
- May, K. L., & Grabowicz, M. (2018). The bacterial outer membrane is an evolving antibiotic barrier [Review of *The bacterial outer membrane is an evolving antibiotic barrier*]. *Proceedings of the National Academy of Sciences of the United States of America*, *115*(36), 8852–8854.
- Mbaye, M. N., Hou, Q., Basu, S., Teheux, F., Pucci, F., & Rooman, M. (2019). A comprehensive computational study of amino acid interactions in membrane proteins. *Scientific Reports*, *9*(1), 12043.
- McCarthy, J. E., & Gualerzi, C. (1990). Translational control of prokaryotic gene expression. *Trends in Genetics: TIG*, *6*(3), 78–85.
- Meillon, J.-C., & Voyer, N. (1997). A Synthetic Transmembrane Channel Active in Lipid Bilayers. *Angewandte Chemie*, *36*(9), 967–969.

- 
- Menacho-Melgar, R., Moreb, E. A., Efromson, J. P., Yang, T., Hennigan, J. N., Wang, R., & Lynch, M. D. (2020). Improved two-stage protein expression and purification via autoinduction of both autolysis and auto DNA/RNA hydrolysis conferred by phage lysozyme and DNA/RNA endonuclease. *Biotechnology and Bioengineering*, *117*(9), 2852–2860.
- Merx, M., Golynskiy, M. V., Lindenburg, L. H., & Vinkenborg, J. L. (2013). Rational design of FRET sensor proteins based on mutually exclusive domain interactions. *Biochemical Society Transactions*, *41*(5), 1201–1205.
- Michiels, J. E., Van den Bergh, B., Verstraeten, N., & Michiels, J. (2016). Molecular mechanisms and clinical implications of bacterial persistence. *Drug Resistance Updates: Reviews and Commentaries in Antimicrobial and Anticancer Chemotherapy*, *29*, 76–89.
- Midkiff, D., & San-Miguel, A. (2019). Microfluidic Technologies for High Throughput Screening Through Sorting and On-Chip Culture of *C. elegans*. *Molecules*, *24*(23). <https://doi.org/10.3390/molecules24234292>
- Milón, P., & Rodnina, M. V. (2012). Kinetic control of translation initiation in bacteria. *Critical Reviews in Biochemistry and Molecular Biology*, *47*(4), 334–348.
- Miyawaki, A., Llopis, J., Heim, R., McCaffery, J. M., Adams, J. A., Ikura, M., & Tsien, R. Y. (1997). Fluorescent indicators for Ca<sup>2+</sup> based on green fluorescent proteins and calmodulin. *Nature*, *388*(6645), 882–887.
- Molle, G., Dugast, J. Y., Spach, G., & Duclouier, H. (1996). Ion channel stabilization of synthetic alamethicin analogs by rings of inter-helix H-bonds. *Biophysical Journal*, *70*(4), 1669–1675.
- Montal, M., & Mueller, P. (1972). Formation of bimolecular membranes from lipid monolayers and a study of their electrical properties. *Proceedings of the National Academy of Sciences of the United States of America*, *69*(12), 3561–3566.
- Montenegro, J., Ghadiri, M. R., & Granja, J. R. (2013). Ion channel models based on self-assembling cyclic peptide nanotubes. *Accounts of Chemical Research*, *46*(12), 2955–2965.
- Moreau, C. J., Dupuis, J. P., Revilloud, J., Arumugam, K., & Vivaudou, M. (2008). Coupling ion channels to receptors for biomolecule sensing. *Nature Nanotechnology*, *3*(10), 620–625.
- Movileanu, L., Howorka, S., Braha, O., & Bayley, H. (2000). Detecting protein analytes that modulate transmembrane movement of a polymer chain within a single protein pore. *Nature Biotechnology*, *18*(10), 1091–1095.
- Mueller, M., Grauschopf, U., Maier, T., Glockshuber, R., & Ban, N. (2009). The structure of a cytolitic alpha-helical toxin pore reveals its assembly mechanism. *Nature*, *459*(7247), 726–730.
- Mueller, P., Rudin, D. O., Tien, H. T., & Wescott, W. C. (1962). Reconstitution of cell membrane structure in vitro and its transformation into an excitable system. *Nature*, *194*, 979–980.
- Muheim, C., Götzke, H., Eriksson, A. U., Lindberg, S., Lauritsen, I., Nørholm, M. H. H., & Daley, D. O. (2017). Increasing the permeability of *Escherichia coli* using MAC13243. *Scientific Reports*, *7*(1), 17629.
- Mulkidjanian, A. Y., Galperin, M. Y., & Koonin, E. V. (2009). Co-evolution of primordial membranes and membrane proteins. *Trends in Biochemical Sciences*, *34*(4), 206–215.
- Nadler, D. C., Morgan, S.-A., Flamholz, A., Kortright, K. E., & Savage, D. F. (2016). Rapid construction of metabolite biosensors using domain-insertion profiling. *Nature Communications*, *7*, 12266.
- Nagai, T., Sawano, A., Park, E. S., & Miyawaki, A. (2001). Circularly permuted green fluorescent proteins engineered to sense Ca<sup>2+</sup>. *Proceedings of the National Academy of Sciences of the United States of America*, *98*(6), 3197–3202.
- Nakai, J., Ohkura, M., & Imoto, K. (2001). A high signal-to-noise Ca(2+) probe composed of a single green fluorescent protein. *Nature Biotechnology*, *19*(2), 137–141.
- Nallamsetty, S., Kapust, R. B., Tözsér, J., Cherry, S., Tropea, J. E., Copeland, T. D., & Waugh, D. S. (2004). Efficient site-specific processing of fusion proteins by tobacco vein mottling virus protease in vivo and in vitro. *Protein Expression and Purification*, *38*(1), 108–115.
- Neher, E., & Sakmann, B. (1976). Single-channel currents recorded from membrane of denervated frog muscle fibres. *Nature*, *260*(5554), 799–802.
- Nehra, A., Ahlawat, S., & Singh, K. P. (2019). A biosensing expedition of nanopore: A review. *Sensors and Actuators. B, Chemical*, *284*, 595–622.
- Neuberger, M. S., Williams, G. T., & Fox, R. O. (1984). Recombinant antibodies possessing novel effector functions. *Nature*, *312*(5995), 604–608.
- Neupert, J., Karcher, D., & Bock, R. (2008). Design of simple synthetic RNA thermometers for temperature-controlled gene expression in *Escherichia coli*. *Nucleic Acids Research*, *36*(19), e124.
- Newman, R. H., Fosbrink, M. D., & Zhang, J. (2011). Genetically encodable fluorescent biosensors for tracking signaling dynamics in living cells. *Chemical Reviews*, *111*(5), 3614–3666.
- Newmeyer, D. D., & Ferguson-Miller, S. (2003). Mitochondria: releasing power for life and unleashing the machineries of death. *Cell*, *112*(4), 481–490.

- 
- Nicoletti, I., Migliorati, G., Pagliacci, M. C., Grignani, F., & Riccardi, C. (1991). A rapid and simple method for measuring thymocyte apoptosis by propidium iodide staining and flow cytometry. *Journal of Immunological Methods*, 139(2), 271–279.
- Nikaido, H. (2003). Molecular basis of bacterial outer membrane permeability revisited. *Microbiology and Molecular Biology Reviews: MMBR*, 67(4), 593–656.
- Nilsson, J., Persson, B., & von Heijne, G. (2005). Comparative analysis of amino acid distributions in integral membrane proteins from 107 genomes. *Proteins*, 60(4), 606–616.
- Novick, R. P. (1987). Plasmid incompatibility. *Microbiological Reviews*, 51(4), 381–395.
- Ohba, Y., Fujioka, Y., Nakada, S., & Tsuda, M. (2013). Fluorescent protein-based biosensors and their clinical applications. *Progress in Molecular Biology and Translational Science*, 113, 313–348.
- Osterman, I. A., Evfratov, S. A., Sergiev, P. V., & Dontsova, O. A. (2013). Comparison of mRNA features affecting translation initiation and reinitiation. *Nucleic Acids Research*, 41(1), 474–486.
- Overington, J. P., Al-Lazikani, B., & Hopkins, A. L. (2006). How many drug targets are there? *Nature Reviews. Drug Discovery*, 5(12), 993–996.
- Pagliuca, C., Goetze, T. A., Wagner, R., Thiel, G., Moroni, A., & Parcej, D. (2007). Molecular properties of Kcv, a virus encoded K<sup>+</sup> channel. *Biochemistry*, 46(4), 1079–1090.
- Palmer, A. E., Qin, Y., Park, J. G., & McCombs, J. E. (2011). Design and application of genetically encoded biosensors. *Trends in Biotechnology*, 29(3), 144–152.
- Pang, T., Fleming, T. C., Pogliano, K., & Young, R. (2013). Visualization of pinholin lesions in vivo. *Proceedings of the National Academy of Sciences of the United States of America*, 110(22), E2054–E2063.
- Pang, T., Park, T., & Young, R. (2010a). Mutational analysis of the S21 pinholin. *Molecular Microbiology*, 76(1), 68–77.
- Pang, T., Park, T., & Young, R. (2010b). Mapping the pinhole formation pathway of S21. *Molecular Microbiology*, 78(3), 710–719.
- Pang, T., Savva, C. G., Fleming, K. G., Struck, D. K., & Young, R. (2009). Structure of the lethal phage pinhole. *Proceedings of the National Academy of Sciences of the United States of America*, 106(45), 18966–18971.
- Pang, X., Moussa, S. H., Targy, N. M., Bose, J. L., George, N. M., Gries, C., Lopez, H., Zhang, L., Bayles, K. W., Young, R., & Luo, X. (2011). Active Bax and Bak are functional holins. *Genes & Development*, 25(21), 2278–2290.
- Park, S.-Y., Lee, J.-Y., Chang, W.-S., Choy, H. E., & Kim, G.-J. (2011). A coupling process for improving purity of bacterial minicells by holin/lysin. *Journal of Microbiological Methods*, 86(1), 108–110.
- Park, T., Struck, D. K., Deaton, J. F., & Young, R. (2006). Topological dynamics of holins in programmed bacterial lysis. *Proceedings of the National Academy of Sciences of the United States of America*, 103(52), 19713–19718.
- Payet, L., Martinho, M., Pastoriza-Gallego, M., Betton, J.-M., Auvray, L., Pelta, J., & Mathé, J. (2012). Thermal unfolding of proteins probed at the single molecule level using nanopores. *Analytical Chemistry*, 84(9), 4071–4076.
- Peters, R. (1983). Nuclear envelope permeability measured by fluorescence microphotolysis of single liver cell nuclei. *The Journal of Biological Chemistry*, 258(19), 11427–11429.
- Peters, R. (2003). Optical single transporter recording: transport kinetics in microarrays of membrane patches. *Annual Review of Biophysics and Biomolecular Structure*, 32, 47–67.
- Peters, R., Sauer, H., Tschopp, J., & Fritzsche, G. (1990). Transients of perforin pore formation observed by fluorescence microscopic single channel recording. *The EMBO Journal*, 9(8), 2447–2451.
- Pettersen, E. F., Goddard, T. D., Huang, C. C., Couch, G. S., Greenblatt, D. M., Meng, E. C., & Ferrin, T. E. (2004). UCSF Chimera—a visualization system for exploratory research and analysis. *Journal of Computational Chemistry*, 25(13), 1605–1612.
- Pick, T. R., Bräutigam, A., Schulz, M. A., Obata, T., Fernie, A. R., & Weber, A. P. M. (2013). PLGG1, a plastidic glycolate glycerate transporter, is required for photorespiration and defines a unique class of metabolite transporters. *Proceedings of the National Academy of Sciences of the United States of America*, 110(8), 3185–3190.
- Pielak, R. M., & Chou, J. J. (2011). Influenza M2 proton channels. *Biochimica et Biophysica Acta*, 1808(2), 522–529.
- Pieta, P., Mirza, J., & Lipkowski, J. (2012). Direct visualization of the alamethicin pore formed in a planar phospholipid matrix. *Proceedings of the National Academy of Sciences of the United States of America*, 109(52), 21223–21227.
- Piguet, F., Ouldali, H., Pastoriza-Gallego, M., Manivet, P., Pelta, J., & Oukhaled, A. (2018). Identification of single amino acid differences in uniformly charged homopolymeric peptides with aerolysin nanopore. *Nature Communications*, 9(1), 966.
-

- Piljić, A., de Diego, I., Wilmanns, M., & Schultz, C. (2011). Rapid development of genetically encoded FRET reporters. *ACS Chemical Biology*, 6(7), 685–691.
- Pinheiro, A. V., Han, D., Shih, W. M., & Yan, H. (2011). Challenges and opportunities for structural DNA nanotechnology. *Nature Nanotechnology*, 6(12), 763–772.
- Ponchon, L., Catala, M., Seijo, B., El Khouri, M., Dardel, F., Nonin-Lecomte, S., & Tisné, C. (2013). Co-expression of RNA-protein complexes in *Escherichia coli* and applications to RNA biology. *Nucleic Acids Research*, 41(15), e150.
- Popp, P. F., Dotzler, M., Radeck, J., Bartels, J., & Mascher, T. (2017). The Bacillus BioBrick Box 2.0: expanding the genetic toolbox for the standardized work with *Bacillus subtilis*. *Scientific Reports*. <https://www.nature.com/articles/s41598-017-15107-z>
- Pulcu, G. S., Mikhailova, E., Choi, L.-S., & Bayley, H. (2015). Continuous observation of the stochastic motion of an individual small-molecule walker. *Nature Nanotechnology*, 10(1), 76–83.
- Putyrski, M., & Schultz, C. (2012). Protein translocation as a tool: The current rapamycin story. *FEBS Letters*, 586(15), 2097–2105.
- Quick, J., Loman, N. J., Duraffour, S., Simpson, J. T., Severi, E., Cowley, L., Bore, J. A., Koundouno, R., Dudas, G., Mikhail, A., Ouédraogo, N., Afrough, B., Bah, A., Baum, J. H., Becker-Ziaja, B., Boettcher, J.-P., Cabeza-Cabrerizo, M., Camino-Sanchez, A., Carter, L. L., ... Carroll, M. W. (2016). Real-time, portable genome sequencing for Ebola surveillance. *Nature*, 530(7589), 228–232.
- Raab, R., Neal, G., Garrett, J., Grimaila, R., Fusselman, R., & Young, R. (1986). Mutational analysis of bacteriophage lambda lysis gene S. *Journal of Bacteriology*, 167(3), 1035–1042.
- Raetz, C. R. (1978). Enzymology, genetics, and regulation of membrane phospholipid synthesis in *Escherichia coli*. *Microbiological Reviews*, 42(3), 614–659.
- Rajesh, T., Anthony, T., Saranya, S., Pushpam, P. L., & Gunasekaran, P. (2011). Functional characterization of a new holin-like antibacterial protein coding gene *tmp1* from goat skin surface metagenome. *Applied Microbiology and Biotechnology*, 89(4), 1061–1073.
- Ramanculov, E., & Young, R. (2001a). Genetic analysis of the T4 holin: timing and topology. *Gene*, 265(1-2), 25–36.
- Ramanculov, E., & Young, R. (2001b). Functional analysis of the phage T4 holin in a lambda context. *Molecular Genetics and Genomics: MGG*, 265(2), 345–353.
- Ranjit, D. K., Endres, J. L., & Bayles, K. W. (2011). Staphylococcus aureus CidA and LrgA proteins exhibit holin-like properties. *Journal of Bacteriology*, 193(10), 2468–2476.
- Rathinakumar, R., Walkenhorst, W. F., & Wimley, W. C. (2009). Broad-spectrum antimicrobial peptides by rational combinatorial design and high-throughput screening: the importance of interfacial activity. *Journal of the American Chemical Society*, 131(22), 7609–7617.
- Real, G., Pinto, S. M., Schyns, G., Costa, T., Henriques, A. O., & Moran, C. P., Jr. (2005). A gene encoding a holin-like protein involved in spore morphogenesis and spore germination in *Bacillus subtilis*. *Journal of Bacteriology*, 187(18), 6443–6453.
- Reddy, B. L., & Saier, M. H., Jr. (2013). Topological and phylogenetic analyses of bacterial holin families and superfamilies. *Biochimica et Biophysica Acta*, 1828(11), 2654–2671.
- Reeve, B., Hargest, T., Gilbert, C., & Ellis, T. (2014). Predicting translation initiation rates for designing synthetic biology. *Frontiers in Bioengineering and Biotechnology*, 2, 1.
- Reimer, J. M., Aloise, M. N., Harrison, P. M., & Schmeing, T. M. (2016). Synthetic cycle of the initiation module of a formylating nonribosomal peptide synthetase. *Nature*, 529(7585), 239–242.
- Restrepo-Pérez, L., Joo, C., & Dekker, C. (2018). Paving the way to single-molecule protein sequencing. *Nature Nanotechnology*, 13(9), 786–796.
- Roach, D. R., & Donovan, D. M. (2015). Antimicrobial bacteriophage-derived proteins and therapeutic applications. *Bacteriophage*, 5(3), e1062590.
- Rosenberg, A. H., Lade, B. N., Chui, D. S., Lin, S. W., Dunn, J. J., & Studier, F. W. (1987). Vectors for selective expression of cloned DNAs by T7 RNA polymerase. *Gene*, 56(1), 125–135.
- Roth, B. L., Poot, M., Yue, S. T., & Millard, P. J. (1997). Bacterial viability and antibiotic susceptibility testing with SYTOX green nucleic acid stain. *Applied and Environmental Microbiology*, 63(6), 2421–2431.
- Rothemund, P. W. K. (2006). Folding DNA to create nanoscale shapes and patterns. *Nature*, 440(7082), 297–302.
- Roux, B. (2017). Ion channels and ion selectivity. *Essays in Biochemistry*, 61(2), 201–209.
- Russ, W. P., & Engelman, D. M. (2000). The GxxxG motif: a framework for transmembrane helix-helix association. *Journal of Molecular Biology*, 296(3), 911–919.
- Russwurm, M., Mullershausen, F., Friebe, A., Jäger, R., Russwurm, C., & Koesling, D. (2007). Design of fluorescence resonance energy transfer (FRET)-based cGMP indicators: a systematic approach. *Biochemical Journal*, 407(1), 69–77.

- Rutberg, B., & Rutberg, L. (1965). Role of superinfecting phage in lysis inhibition with phage T4 in *Escherichia coli*. *Journal of Bacteriology*, *90*(4), 891–894.
- Saha, S., Ghosh, A., Tiwari, N., Kumar, A., Kumar, A., & Goswami, C. (2017). Preferential selection of Arginine at the lipid-water-interface of TRPV1 during vertebrate evolution correlates with its snorkeling behaviour and cholesterol interaction. *Scientific Reports*, *7*(1), 16808.
- Saier, M. H., Jr. (2000). A functional-phylogenetic classification system for transmembrane solute transporters. *Microbiology and Molecular Biology Reviews: MMBR*, *64*(2), 354–411.
- Saier, M. H., Jr, Reddy, V. S., Tsu, B. V., Ahmed, M. S., Li, C., & Moreno-Hagelsieb, G. (2016). The Transporter Classification Database (TCDB): recent advances. *Nucleic Acids Research*, *44*(D1), D372–D379.
- Saier, M. H., Jr, Tran, C. V., & Barabote, R. D. (2006). TCDB: the Transporter Classification Database for membrane transport protein analyses and information. *Nucleic Acids Research*, *34*(Database issue), D181–D186.
- Saier, M. H., & Reddy, B. L. (2014). Holins in Bacteria, Eukaryotes and Archaea: Multifunctional Xenologues with Potential Biotechnological and Biomedical Applications. *Journal of Bacteriology*. <https://doi.org/10.1128/JB.02046-14>
- Sakai, N., Mareda, J., & Matile, S. (2008). Artificial beta-barrels. *Accounts of Chemical Research*, *41*(10), 1354–1365.
- San Martín, A., Ceballo, S., Ruminot, I., Lerchundi, R., Frommer, W. B., & Barros, L. F. (2013). A genetically encoded FRET lactate sensor and its use to detect the Warburg effect in single cancer cells. *PloS One*, *8*(2), e57712.
- Santos-Moreno, J., Tasiudi, E., Stelling, J., & Schaerli, Y. (2020). Multistable and dynamic CRISPRi-based synthetic circuits. *Nature Communications*, *11*(1), 2746.
- Schindelin, J., Arganda-Carreras, I., Frise, E., Kaynig, V., Longair, M., Pietzsch, T., Preibisch, S., Rueden, C., Saalfeld, S., Schmid, B., Tinevez, J.-Y., White, D. J., Hartenstein, V., Eliceiri, K., Tomancak, P., & Cardona, A. (2012). Fiji: an open-source platform for biological-image analysis. *Nature Methods*, *9*(7), 676–682.
- Schleifenbaum, A., Stier, G., Gasch, A., Sattler, M., & Schultz, C. (2004). Genetically encoded FRET probe for PKC activity based on pleckstrin. *Journal of the American Chemical Society*, *126*(38), 11786–11787.
- Schmidt, J. (2016). Membrane platforms for biological nanopore sensing and sequencing. *Current Opinion in Biotechnology*, *39*, 17–27.
- Schneider, C. A., Rasband, W. S., & Eliceiri, K. W. (2012). NIH Image to ImageJ: 25 years of image analysis. *Nature Methods*, *9*(7), 671–675.
- Schönrock, M., Thiel, G., & Laube, B. (2019). Coupling of a viral K<sup>+</sup>-channel with a glutamate-binding-domain highlights the modular design of ionotropic glutamate-receptors. *Communications Biology*, *2*, 75.
- Schoppa, N. E., & Sigworth, F. J. (1998). Activation of shaker potassium channels. I. Characterization of voltage-dependent transitions. *The Journal of General Physiology*, *111*(2), 271–294.
- Schumacher, M. A. (2012). Bacterial plasmid partition machinery: a minimalist approach to survival. *Current Opinion in Structural Biology*, *22*(1), 72–79.
- Sebastian, J., Swaminath, S., Nair, R. R., Jakkala, K., Pradhan, A., & Ajitkumar, P. (2017). De Novo Emergence of Genetically Resistant Mutants of *Mycobacterium tuberculosis* from the Persistence Phase Cells Formed against Antituberculosis Drugs In Vitro. *Antimicrobial Agents and Chemotherapy*, *61*(2). <https://doi.org/10.1128/AAC.01343-16>
- Seifert, A., Göpfrich, K., Burns, J. R., Fertig, N., Keyser, U. F., & Howorka, S. (2015). Bilayer-spanning DNA nanopores with voltage-switching between open and closed state. *ACS Nano*, *9*(2), 1117–1126.
- Shaner, N. C., Lambert, G. G., Chammas, A., Ni, Y., Cranfill, P. J., Baird, M. A., Sell, B. R., Allen, J. R., Day, R. N., Israelsson, M., Davidson, M. W., & Wang, J. (2013). A bright monomeric green fluorescent protein derived from *Branchiostoma lanceolatum*. *Nature Methods*, *10*(5), 407–409.
- Sharpe, H. J., Stevens, T. J., & Munro, S. (2010). A comprehensive comparison of transmembrane domains reveals organelle-specific properties. *Cell*, *142*(1), 158–169.
- Shimizu, Y., Inoue, A., Tomari, Y., Suzuki, T., Yokogawa, T., Nishikawa, K., & Ueda, T. (2001). Cell-free translation reconstituted with purified components. *Nature Biotechnology*, *19*(8), 751–755.
- Shin, S.-H., Steffensen, M. B., Claridge, T. D. W., & Bayley, H. (2007). Formation of a chiral center and pyrimidal inversion at the single-molecule level. *Angewandte Chemie*, *46*(39), 7412–7416.
- Shi, W., Friedman, A. K., & Baker, L. A. (2017). Nanopore Sensing. *Analytical Chemistry*, *89*(1), 157–188.
- Sigal, I. S., Harwood, B. G., & Arentzen, R. (1982). Thiol-beta-lactamase: replacement of the active-site serine of RTEM beta-lactamase by a cysteine residue. *Proceedings of the National Academy of Sciences of the United States of America*, *79*(23), 7157–7160.
- Silhavy, T. J., Kahne, D., & Walker, S. (2010). The bacterial cell envelope. *Cold Spring Harbor Perspectives in Biology*, *2*(5), a000414.

- Simons, K. T., Bonneau, R., Ruczinski, I., & Baker, D. (1999). Ab initio protein structure prediction of CASP III targets using ROSETTA. *Proteins, Suppl 3*, 171–176.
- Singh, P. R., Bárcena-Uribarri, I., Modi, N., Kleinekathöfer, U., Benz, R., Winterhalter, M., & Mahendran, K. R. (2012). Pulling peptides across nanochannels: resolving peptide binding and translocation through the hetero-oligomeric channel from *Nocardia farcinica*. *ACS Nano*, 6(12), 10699–10707.
- Smeets, R. M. M., Kowalczyk, S. W., Hall, A. R., Dekker, N. H., & Dekker, C. (2009). Translocation of RecA-coated double-stranded DNA through solid-state nanopores. *Nano Letters*, 9(9), 3089–3096.
- Smolke, C. (2018). *Synthetic Biology: Parts, Devices and Applications*. John Wiley & Sons.
- SOC Medium for *E. coli*. (2012). *Cold Spring Harbor Protocols*, 2012(6), db.rec069732.
- Song, L., Hobaugh, M. R., Shustak, C., Cheley, S., Bayley, H., & Gouaux, J. E. (1996). Structure of staphylococcal alpha-hemolysin, a heptameric transmembrane pore. *Science*, 274(5294), 1859–1866.
- Sørensen, C. S., & Kjaergaard, M. (2019). Effective concentrations enforced by intrinsically disordered linkers are governed by polymer physics. *Proceedings of the National Academy of Sciences of the United States of America*, 116(46), 23124–23131.
- Soskine, M., Biesemans, A., De Maeyer, M., & Maglia, G. (2013). Tuning the size and properties of ClyA nanopores assisted by directed evolution. *Journal of the American Chemical Society*, 135(36), 13456–13463.
- Soskine, M., Biesemans, A., Moeyaert, B., Cheley, S., Bayley, H., & Maglia, G. (2012). An engineered ClyA nanopore detects folded target proteins by selective external association and pore entry. *Nano Letters*, 12(9), 4895–4900.
- Spicer, C. D., & Davis, B. G. (2014). Selective chemical protein modification. *Nature Communications*, 5, 4740.
- Stein, V., & Alexandrov, K. (2014). Protease-based synthetic sensing and signal amplification. *Proceedings of the National Academy of Sciences of the United States of America*, 111(45), 15934–15939.
- Stemmer, W. P. (1994). Rapid evolution of a protein in vitro by DNA shuffling. *Nature*, 370(6488), 389–391.
- Studier, F. W. (1991). Use of bacteriophage T7 lysozyme to improve an inducible T7 expression system. *Journal of Molecular Biology*, 219(1), 37–44.
- Studier, F. W., Rosenberg, A. H., Dunn, J. J., & Dubendorff, J. W. (1990). Use of T7 RNA polymerase to direct expression of cloned genes. *Methods in Enzymology*, 185, 60–89.
- Sun, G., Chung, T.-S., Jeyaseelan, K., & Armugam, A. (2013). Stabilization and immobilization of aquaporin reconstituted lipid vesicles for water purification. *Colloids and Surfaces. B, Biointerfaces*, 102, 466–471.
- Sun, H., Greathouse, D. V., Andersen, O. S., & Koeppe, R. E., 2nd. (2008). The preference of tryptophan for membrane interfaces: insights from N-methylation of tryptophans in gramicidin channels. *The Journal of Biological Chemistry*, 283(32), 22233–22243.
- Sun, Q., Kutty, G. F., Arockiasamy, A., Xu, M., Young, R., & Sacchettini, J. C. (2009). Regulation of a muralytic enzyme by dynamic membrane topology. *Nature Structural & Molecular Biology*, 16(11), 1192–1194.
- Suzuki, Y. (2020). Advent of a new sequencing era: long-read and on-site sequencing. *Journal of Human Genetics*, 65(1), 1.
- Tarasov, A. I., Girard, C. A. J., & Ashcroft, F. M. (2006). ATP sensitivity of the ATP-sensitive K<sup>+</sup> channel in intact and permeabilized pancreatic beta-cells. *Diabetes*, 55(9), 2446–2454.
- Terrific Broth. (2015). *Cold Spring Harbor Protocols*, 2015(7), db.rec087874.
- Te Winkel, J. D., Gray, D. A., Seistrup, K. H., Hamoen, L. W., & Strahl, H. (2016). Analysis of Antimicrobial-Triggered Membrane Depolarization Using Voltage Sensitive Dyes. *Frontiers in Cell and Developmental Biology*, 4, 29.
- Thakur, A. K., & Movileanu, L. (2018). Real-time measurement of protein-protein interactions at single-molecule resolution using a biological nanopore. *Nature Biotechnology*. <https://doi.org/10.1038/nbt.4316>
- Thiel, G., Baumeister, D., Schroeder, I., Kast, S. M., Van Etten, J. L., & Moroni, A. (2011). Minimal art: Or why small viral K<sup>+</sup> channels are good tools for understanding basic structure and function relations. *Biochimica et Biophysica Acta (BBA) - Biomembranes*, 1808(2), 580–588.
- Thompson, A. N., Posson, D. J., Parsa, P. V., & Nimigeon, C. M. (2008). Molecular mechanism of pH sensing in KcsA potassium channels. *Proceedings of the National Academy of Sciences of the United States of America*, 105(19), 6900–6905.
- Thomson, A. R., Wood, C. W., Burton, A. J., Bartlett, G. J., Sessions, R. B., Brady, R. L., & Woolfson, D. N. (2014). Computational design of water-soluble  $\alpha$ -helical barrels. *Science*, 346(6208), 485–488.
- To, K. H., & Young, R. (2014). Probing the structure of the S105 hole. *Journal of Bacteriology*, 196(21), 3683–3689.
- Tripathy, A., Sreedharan, S., Bhaskarla, C., Majumdar, S., Peneti, S. K., Nandi, D., & Sen, P. (2017). Enhancing the Bactericidal Efficacy of Nanostructured Multifunctional Surface Using an Ultrathin Metal Coating. *Langmuir: The ACS Journal of Surfaces and Colloids*, 33(44), 12569–12579.
- Tsien, R. Y. (1998). The green fluorescent protein. *Annual Review of Biochemistry*, 67, 509–544.

- Uyeda, A., Nakayama, S., Kato, Y., Watanabe, H., & Matsuura, T. (2016). Construction of an in Vitro Gene Screening System of the E. coli EmrE Transporter Using Liposome Display. *Analytical Chemistry*, 88(24), 12028–12035.
- van den Esker, M. H., Kovács, Á. T., & Kuipers, O. P. (2017a). YsbA and LytST are essential for pyruvate utilization in *Bacillus subtilis*. *Environmental Microbiology*, 19(1), 83–94.
- van den Esker, M. H., Kovács, Á. T., & Kuipers, O. P. (2017b). From Cell Death to Metabolism: Holin-Antiholin Homologues with New Functions. *mBio*, 8(6). <https://doi.org/10.1128/mBio.01963-17>
- Varongchayakul, N., Song, J., Meller, A., & Grinstaff, M. W. (2018). Single-molecule protein sensing in a nanopore: a tutorial. *Chemical Society Reviews*, 47(23), 8512–8524.
- Varshavsky, A. (1997). The N-end rule pathway of protein degradation. *Genes to Cells: Devoted to Molecular & Cellular Mechanisms*, 2(1), 13–28.
- Velappan, N., Sblattero, D., Chasteen, L., Pavlik, P., & Bradbury, A. R. M. (2007). Plasmid incompatibility: more compatible than previously thought? *Protein Engineering, Design & Selection: PEDS*, 20(7), 309–313.
- Volfson, D., Cookson, S., Hasty, J., & Tsimring, L. S. (2008). Biomechanical ordering of dense cell populations. *Proceedings of the National Academy of Sciences of the United States of America*, 105(40), 15346–15351.
- von Heijne, G. (1986). The distribution of positively charged residues in bacterial inner membrane proteins correlates with the trans-membrane topology. *The EMBO Journal*. <https://www.embopress.org/doi/abs/10.1002/j.1460-2075.1986.tb04601.x>
- von Heijne, G. (1989). Control of topology and mode of assembly of a polytopic membrane protein by positively charged residues. *Nature*, 341(6241), 456–458.
- Voß, S., Klewer, L., & Wu, Y.-W. (2015). Chemically induced dimerization: reversible and spatiotemporal control of protein function in cells. *Current Opinion in Chemical Biology*, 28, 194–201.
- Walker, B., & Bayley, H. (1995). Key Residues for Membrane Binding, Oligomerization, and Pore Forming Activity of Staphylococcal  $\alpha$ -Hemolysin Identified by Cysteine Scanning Mutagenesis and Targeted Chemical Modification. *THE JOURNAL OF BIOLOGICAL CHEMISTRY*, 270(39), 23065–23071.
- Wallin, E., Tsukihara, T., Yoshikawa, S., von Heijne, G., & Elofsson, A. (1997). Architecture of helix bundle membrane proteins: an analysis of cytochrome c oxidase from bovine mitochondria. *Protein Science: A Publication of the Protein Society*, 6(4), 808–815.
- Wang, H.-Y., & Lu, C. (2006). High-throughput and real-time study of single cell electroporation using microfluidics: effects of medium osmolarity. *Biotechnology and Bioengineering*, 95(6), 1116–1125.
- Wang, I.-N., Deaton, J., & Young, R. (2003). Sizing the Holin Lesion with an Endolysin- $\beta$ -Galactosidase Fusion. *JBR-BTR: Organe de La Societe Royale Belge de Radiologie*, 185(3), 779–787.
- Wang, J., & Bayles, K. W. (2013). Programmed cell death in plants: lessons from bacteria? *Trends in Plant Science*, 18(3), 133–139.
- Wang, P., Robert, L., Pelletier, J., Dang, W. L., Taddei, F., Wright, A., & Jun, S. (2010). Robust growth of *Escherichia coli*. *Current Biology: CB*, 20(12), 1099–1103.
- Wang, S., Zhao, Z., Haque, F., & Guo, P. (2018). Engineering of protein nanopores for sequencing, chemical or protein sensing and disease diagnosis. *Current Opinion in Biotechnology*, 51, 80–89.
- Wang, Y., Zheng, D., Tan, Q., Wang, M. X., & Gu, L.-Q. (2011). Nanopore-based detection of circulating microRNAs in lung cancer patients. *Nature Nanotechnology*, 6(10), 668–674.
- Watson, C., & Senyo, S. E. (2019). All-in-one automated microfluidics control system. *HardwareX*, 5. <https://doi.org/10.1016/j.ohx.2019.e00063>
- Wen, S., Zeng, T., Liu, L., Zhao, K., Zhao, Y., Liu, X., & Wu, H.-C. (2011). Highly sensitive and selective DNA-based detection of mercury(II) with  $\alpha$ -hemolysin nanopore. *Journal of the American Chemical Society*, 133(45), 18312–18317.
- White, R., Chiba, S., Pang, T., Dewey, J. S., Savva, C. G., Holzenburg, A., Pogliano, K., & Young, R. (2011). Holin triggering in real time. *Proceedings of the National Academy of Sciences of the United States of America*, 108(2), 798–803.
- White, R., Tran, T. A. T., Dankenbring, C. A., Deaton, J., & Young, R. (2010). The N-Terminal Transmembrane Domain of  $\lambda$  S Is Required for Holin but Not Antiholin Function. *Journal of Bacteriology*, 192(3), 725–733.
- Willems, K., Van Meervelt, V., Wloka, C., & Maglia, G. (2017). Single-molecule nanopore enzymology. *Philosophical Transactions of the Royal Society of London. Series B, Biological Sciences*, 372(1726). <https://doi.org/10.1098/rstb.2016.0230>
- Wilmaerts, D., Bayoumi, M., Dewachter, L., Knapen, W., Mika, J. T., Hofkens, J., Dedecker, P., Maglia, G., Verstraeten, N., & Michiels, J. (2018). The Persistence-Inducing Toxin HokB Forms Dynamic Pores That Cause ATP Leakage. *mBio*, 9(4). <https://doi.org/10.1128/mBio.00744-18>

- Wilmaerts, D., Dewachter, L., De Loose, P.-J., Bollen, C., Verstraeten, N., & Michiels, J. (2019). HokB Monomerization and Membrane Repolarization Control Persister Awakening. *Molecular Cell*, 75(5), 1031–1042.e4.
- Winter, G., Fersht, A. R., Wilkinson, A. J., Zoller, M., & Smith, M. (1982). Redesigning enzyme structure by site-directed mutagenesis: tyrosyl tRNA synthetase and ATP binding. *Nature*, 299(5885), 756–758.
- Winter, G., & Milstein, C. (1991). Man-made antibodies. *Nature*, 349(6307), 293–299.
- Wloka, C., Mutter, N. L., Soskine, M., & Maglia, G. (2016). Alpha-Helical Fragaceatoxin C Nanopore Engineered for Double-Stranded and Single-Stranded Nucleic Acid Analysis. *Angewandte Chemie*, 55(40), 12494–12498.
- Wu, H. D., Kikuchi, M., Dagliyan, O., Aragaki, A. K., Nakamura, H., Dokholyan, N. V., Umehara, T., & Inoue, T. (2020). Rational design and implementation of a chemically inducible hetero-trimerization system (p. 2020.03.16.994277). <https://doi.org/10.1101/2020.03.16.994277>
- Xu, C., Lu, P., Gamal El-Din, T. M., Pei, X. Y., Johnson, M. C., Uyeda, A., Bick, M. J., Xu, Q., Jiang, D., Bai, H., Reggiano, G., Hsia, Y., Brunette, T. J., Dou, J., Ma, D., Lynch, E. M., Boyken, S. E., Huang, P.-S., Stewart, L., ... Baker, D. (2020). Computational design of transmembrane pores. *Nature*. <https://doi.org/10.1038/s41586-020-2646-5>
- Xu, M., Struck, D. K., Deaton, J., Wang, I.-N., & Young, R. (2004). A signal-arrest-release sequence mediates export and control of the phage P1 endolysin. *Proceedings of the National Academy of Sciences of the United States of America*, 101(17), 6415–6420.
- Yang, Y., Jin, H., Chen, Y., Lin, W., Wang, C., Chen, Z., Han, N., Bian, H., Zhu, M., & Wang, J. (2012). A chloroplast envelope membrane protein containing a putative LrgB domain related to the control of bacterial death and lysis is required for chloroplast development in *Arabidopsis thaliana*. *The New Phytologist*, 193(1), 81–95.
- Yasir, M., Dutta, D., & Willcox, M. D. P. (2019). Mode of action of the antimicrobial peptide Mel4 is independent of *Staphylococcus aureus* cell membrane permeability. *PloS One*, 14(7), e0215703.
- Yoo, J., & Aksimentiev, A. (2015). Molecular Dynamics of Membrane-Spanning DNA Channels: Conductance Mechanism, Electro-Osmotic Transport, and Mechanical Gating. *Journal of Physical Chemistry Letters*, 6(23), 4680–4687.
- Yoo, Y. J., Kim, H., Park, S. R., & Yoon, Y. J. (2017). An overview of rapamycin: from discovery to future perspectives. *Journal of Industrial Microbiology & Biotechnology*, 44(4-5), 537–553.
- Young, R. (2002). Bacteriophage holins: deadly diversity. *Journal of Molecular Microbiology and Biotechnology*, 4(1), 21–36.
- Young, R. (2013). Phage lysis: do we have the hole story yet? *Current Opinion in Microbiology*, 16(6), 790–797.
- Young, R. (2014). Phage lysis: three steps, three choices, one outcome. *Journal of Microbiology*, 52(3), 243–258.
- Zakharian, E. (2013). Recording of ion channel activity in planar lipid bilayer experiments. *Methods in Molecular Biology*, 998, 109–118.
- Zhang, J., Ma, Y., Taylor, S. S., & Tsien, R. Y. (2001). Genetically encoded reporters of protein kinase A activity reveal impact of substrate tethering. *Proceedings of the National Academy of Sciences of the United States of America*, 98(26), 14997–15002.
- Zhang, W., Sato, T., & Smith, S. O. (2006). NMR spectroscopy of basic/aromatic amino acid clusters in membrane proteins. *Progress in Nuclear Magnetic Resonance Spectroscopy*, 48(4), 183–199.
- Zhang, Y., Bartz, R., Grigoryan, G., Bryant, M., Aaronson, J., Beck, S., Innocent, N., Klein, L., Procopio, W., Tucker, T., Jadhav, V., Tellers, D. M., & DeGrado, W. F. (2015). Computational design and experimental characterization of peptides intended for pH-dependent membrane insertion and pore formation. *ACS Chemical Biology*, 10(4), 1082–1093.
- Zhao, Y., Araki, S., Wu, J., Teramoto, T., Chang, Y.-F., Nakano, M., Abdelfattah, A. S., Fujiwara, M., Ishihara, T., Nagai, T., & Campbell, R. E. (2011). An expanded palette of genetically encoded Ca<sup>2+</sup> indicators. *Science*, 333(6051), 1888–1891.
- Zhong, C., & Schleifenbaum, J. (2019). Genetically Encoded Calcium Indicators: A New Tool in Renal Hypertension Research. *Frontiers of Medicine*, 6, 128.

## List of Abbreviations

Table 22 Amino acid abbreviations as 1- and 3-letter code.

Amino Acid	1-Letter code	3-Letter code
Alanine	A	Ala
Arginine	R	Arg
Asparagine	N	Asn
Aspartic acid	D	Asp
Cysteine	C	Cys
Glutamine	Q	Gln
Glutamic acid	E	Glu
Glycine	G	Gly
Histidine	H	His
Isoleucine	I	Ile
Leucine	L	Leu
Lysine	K	Lys
Methionine	M	Met
Phenylalanine	F	Phe
Proline	P	Pro
Serine	S	Ser
Threonine	T	Thr
Tryptophane	W	Trp
Tyrosine	Y	Tyr
Valine	V	Val

Table 23 Abbreviations.

(DiSC <sub>3</sub> (5))	3,3' Dipropylthiadicyanone
ΔTMD	Delta transmembrane domain
Amp	Ampicillin
AmpR	Ampicillin resistance
AT	Adenine thymine
ATP	Adenosine triphosphate
Avg	Average
<i>B. subtilis</i>	<i>Bacillus subtilis</i>
B-GECO	Blue-calcium indicators for optical imaging
BLINK1	Blue-light-inducible potassium channel 1
BLM	Black lipid membrane
BSC	Backscatter
Ca <sup>2+</sup>	Calcium
Cam	Chloramphenicol
CaM	Calmodulin
CBP	Calmodulin binding peptide
CCD	Charge-coupled device
CL	Cardiolipin
ClyA	Cytotoxic cytolysin A

CmR	Chloramphenicol resistance
cpeGFP	circular permuted eGFP (enhanced green fluorescent protein)
CsgG	Curli specific gene G
CV	Column volumes
DNA	Deoxyribonucleic acid
dNTP	Deoxyribose nucleoside triphosphates
<i>E. coli</i>	<i>Escherichia coli</i>
<i>E. coli</i>	<i>Escherichia coli</i>
EDTA	Ethylenediaminetetraacetic acid
FACS	Fluorescence-activated cell sorting
FPLC	Fast protein liquid chromatography
FraC	Fragaceatoxin C
FRET	Förster energy transfer
FSC	Forward scatter
FuN	Functional nanopore
GFP	Green fluorescent protein
G-GECO	Green-calcium indicators for optical imaging
GUV	Giant unilamellar vesicle
IM	inner membrane
IPTG	isopropyl- $\beta$ -D-thiogalactopyranosid
K <sup>+</sup>	Potassium
L	Lysogenic broth
M13	Myosin light chain kinase
mKO <sub>K</sub>	mKusabira-Orange-kappa
mRNA	Messenger RNA
MspA	<i>Mycobacterium smegmatis</i> porin A
Nfp	<i>Nocardia farcinica</i> porin
OD <sub>600nm</sub>	Optical density at 600 nm
OM	outer membrane
OmpF	Outer membrane protein F
OmpG	Outer membrane protein G
OTSR	Optical single transporter recordings
PBS	Phosphate buffered saline
PCR	Polymerase chain reaction
PE	Phosphatidylethanolamine
PG	Phosphatidylglycerol
PLGG1	plastidic glycolate/glycerate transporters
PMF	proton motive force
P <sub>prpB</sub>	<i>prpBCDE</i> promoter
P <sub>T7</sub>	T7 promoter
RBS	Ribosome binding site
RFU	Relative fluorescent units
R-GECO	Red-calcium indicators for optical imaging
RNA	Ribonucleic acid

RNAT	RNA thermometer
SAR	Signal-anchor-release
sCMOS	Scientific complementary metal–oxide–semiconductor
SD	Standard deviation
SDS PAGE	Sodium dodecyl sulfate polyacrylamide gel electrophoresis
SmR	Spectinomycin resistance
SOC	Super optimal broth with catabolite repression
Spec	Spectinomycin
sRBS	Strong ribosome binding site
SynBio	Synthetic biology
T <sub>1/2</sub>	Half-time
TA	Toxin-antitoxin
TAE	Tris base, acetic acid, EDTA
TB	Terrific broth
TCDB	Transporter classification database
TIR	Translation initiation region
TMD	Transmembrane domain
TVMV	Tobacco Vein Mottling Virus Protease
αHL	Alpha Hemolysin

---

---

## List of Figures

---

Figure 1 Gramicidin A forming a dual $\beta$ -helix ion channel in a lipid bilayer.....	5
Figure 2 Demonstration of the size of different Nanopores. ....	7
Figure 3 Structure of a bilayer chamber used in electrophysiological measurements. ....	9
Figure 4 Schematic overview of different analytes passing a protein pore.....	10
Figure 5 Schematic drawing of a modern chip with possible scenarios during $\alpha$ -hemolysin mediated transport.....	11
Figure 6 Schematic overview of the in vitro evolution of $\alpha$ HL in the liposome display technique. ....	14
Figure 7 Insertion theory of a folded water soluble $\alpha$ -helical hairpin into the lipid membrane by ‘inside-out’ transition. ....	15
Figure 8 Overview of the pore forming mechanisms of canonical and non-canonical holins. ....	17
Figure 9 Illustration of S <sup>105</sup> pore formation and topology. ....	18
Figure 10 Illustration of S <sup>2168</sup> pore formation and topology. ....	19
Figure 11 Illustration of T4 pore formation and topology.....	19
Figure 12 Principle of the circular permuted GFP based biosensor G-GECO. ....	23
Figure 13 Principle of the FuN screen.....	25
Figure 14 Schematic overview of pPRO24 carrying the gene for G-GECO1. ....	26
Figure 15 Schematic overview of pCTRL2 carrying the gene for a holin.....	27
Figure 16 Endpoint fluorescence measurements for different promoter and RBS combinations 200 min after induction. ....	28
Figure 17 Fluorescence measurement over time of the three pores S <sup>2168</sup> , T4 and KcvNTS in combination with R-GECO1 or G-GECO1.....	29
Figure 18 Example sigmoidal curve for parameter explanation.....	31
Figure 19 Variation of induction times leads to different signal patterns. ....	32
Figure 20 FuN screen verification with a variety of different nanopores.....	34
Figure 21 Total fluorescence measurements of the supernatant and the cell pellet 3 hours after nanopore induction. ....	37
Figure 22 Truncation experiments of the first transmembrane domain of S <sup>2168</sup> . ....	38
Figure 23 Schematic illustration of the different lipid bilayer regions and the amino acids groups occurrence in those areas. ....	39
Figure 24 Lipid bilayer measurements with selected and chemically synthesized variants.....	41
Figure 25 Schematic illustration of the different antimicrobial peptide pore forming models....	42
Figure 26 Individual mutations of the two N-terminal amino acids Asp and Lys. ....	43
Figure 27 Illustration of the microfluidic device used to validate the FuN screen. ....	44
Figure 28 Microfluidic microscopy measurements of the pinholin S <sup>2168</sup> and the truncation variants S <sup>2158</sup> , S <sup>2146</sup> and S <sup>2138</sup> .....	46
Figure 29 Comparison of spectrophotometer and microscopy measurements of the pinholin S <sup>2168</sup> and the truncation variants S <sup>2158</sup> , S <sup>2146</sup> and S <sup>2138</sup> . ....	47
Figure 30 Colony screening on agar plates. ....	48
Figure 31 FACS dot plots and histograms of the sorting conditions for the model selection with SGS-ATMD1-S <sup>2168</sup> and TVMV-ATMD1-S <sup>2168</sup> under the pCTRL.wt.sRBS promoter. ....	50
Figure 32 Colony PCR of the model selection steps compared to the positive and negative control.....	50
Figure 33 Comparison of the promoter strength of T7.wt.sRBS and T7.100sRBS with the S <sup>2171</sup> -library. ....	52
Figure 34 Library screen with the T7.100.sRBS promoter. ....	53
Figure 35 Heatmap of grouped amino acids on different positions. ....	54
Figure 36 T <sub>1/2</sub> and steepness correlation to the AT count of the three mutated amino acids of S <sup>2171</sup> -library.....	56
Figure 37 Fluorescence and absorption measurement of artificial designed nanopores. ....	59
Figure 38 Glutamic acid outward flow after nanopore induction. ....	61

Figure 39 Rapamycin sensor in combination with the FuN screen. ....	62
Figure 40 DNA-size ladders (NEB, Massachusetts, USA).....	63
Figure 41 BlueStar Prestained Protein Marker (Nippon Genetics, Tokyo, Japan).....	64
Supplementary Figure 1 Expression kinetic of mKO <sub>k</sub> under different pCTRL2 promoter variants related to Figure 16. ....	87
Supplementary Figure 2 Fluorescence measurement over time of the pores S <sup>105</sup> , SGS-ΔTMD1-S <sup>2168</sup> , TVMV-ΔTMD1-S <sup>2168</sup> and BM2 in combination with R-GECO1 or G-GECO1 related to Figure 17. ..	88
Supplementary Figure 3 Absorption OD <sub>600nm</sub> measurements over time of the pores S <sup>2168</sup> , T4 and KcvNTS in combination with R-GECO1 or G-GECO1 related to Figure 17. ....	89
Supplementary Figure 4 Absorption OD <sub>600nm</sub> measurements over time of the pores S <sup>105</sup> , SGS-ΔTMD1-S <sup>2168</sup> , TVMV-ΔTMD1-S <sup>2168</sup> and BM2 in combination with R-GECO1 or G-GECO1 related to Figure 17. ....	90
Supplementary Figure 5 Variation of induction times for S <sup>2171</sup> , S <sup>2171</sup> -M4A and SGS-ΔTMD1-S <sup>2168</sup> related to Figure 19. ....	91
Supplementary Figure 6 Absorption measurements of different nanopores related to Figure 20. ....	92
Supplementary Figure 7 Fluorescence and absorption measurement of S <sup>105</sup> , S <sup>107</sup> S <sup>107</sup> -M3A. ....	93
Supplementary Figure 8 Truncation experiments of the first transmembrane domain of S <sup>2168</sup> related to Figure 22. ....	94
Supplementary Figure 9 Truncation experiments of the first transmembrane domain of S <sub>2168</sub> related to Figure 22. ....	95
Supplementary Figure 10 Microfluidic microscopy measurements of the T4 holin and the negative control KcvNTS related to Figure 28. ....	96
Supplementary Figure 11 Colony screening on agar plates for truncated variants related to Figure 30. ....	97
Supplementary Figure 12 FACS dot plots and histograms of the sorting conditions for the model selection with SGS-ΔTMD1-S <sup>2168</sup> and TVMV-ΔTMD1-S <sup>2168</sup> under the pCTRL.wt.sRBS promoter related to Figure 31. ....	98
Supplementary Figure 13 Impact of an amino acid on the (A) half-time and the (B) steepness without the discrimination of the residue position. ....	99
Supplementary Figure 14 Impact of an amino acid on the (A) half-time and the (B) steepness dependant on the position. ....	99
Supplementary Figure 15 Impact of grouped amino acids on the (A) half-time and the (B) steepness dependant on the position. ....	100

---

## List of Tables & Equations

---

Table 1 Characteristics of holin superfamilies. ....	16
Table 2 Promoter and RBS systems used in this work. ....	27
Table 3 T <sub>1/2</sub> and steepness values from the fitted curves from Figure 20. ....	36
Table 4 Mutated amino acids of the S <sup>2171</sup> -library. ....	51
Table 5 <i>E. Coli</i> strains used in this work. ....	63
Table 6 Enzymes used in this work. ....	64
Table 7 Equipment used in this work. ....	65
Table 8 Software used in this work. ....	66
Table 9 Chemicals used in this work. ....	66
Table 10 Buffers and solutions used in this work. ....	68
Table 11 Thermocycler program for Phusion® High-Fidelity DNA Polymerase. ....	72
Table 12 Thermocycler program for Phusion® High-Fidelity DNA Polymerase. ....	72
Table 13 OneTaq® DNA polymerase PCR mix. ....	72
Table 14 Thermocycler program for OneTaq® DNA polymerase. ....	73

---

Table 15 Components of a DNA restriction reaction.....	73
Table 16 Components of Gibson assembly reaction.....	74
Table 17 Components of ligation reaction. ....	74
Table 18 Composition of 12 % polyacrylamide gels. ....	76
Table 19 Vectors used in this work.....	76
Table 20 Exchangeable parts of the different expression vectors (T7 promoter-lac operator-RBS). .....	79
Table 21 Expression strength measured with mKO <sub>K</sub> .....	83
Table 22 Amino acid abbreviations as 1- and 3-letter code.....	116
Table 23 Abbreviations.....	116
 Supplementary Table 1 Amino acid count of S <sup>21</sup> 71 library for every position.....	 98
 Equation 1 Non-linear regression equation used to fit sigmoid curves.....	 30

---

## Own Work

---

Experiments, data analysis and writing were exclusively done by myself with the exception of:

- Microfluidic microscopy measurements and image analysis (**Figure 28**; **Figure 29**; **Supplementary Figure 10**) were performed together with Markus Röder (TU Darmstadt, group member of Prof. Dr. Heinz Köppl).
- Rapamycin biosensor construction and FuN screen measurements with different nanopores for rapamycin (**Figure 39**) were performed by Theresa Wörmann under my supervision.
- Synthetic peptides S<sup>21</sup>68, S<sup>21</sup>58 and S<sup>21</sup>38 were chemically synthesized by the group of Prof. Dr. Alesia Tietze (University of Gothenburg, Sweden)

---

---

## Declaration – Ehrenwörtliche Erklärung

---

Ehrenwörtliche Erklärung:

Ich erkläre hiermit ehrenwörtlich, dass ich die vorliegende Arbeit entsprechend den Regeln guter wissenschaftlicher Praxis selbstständig und ohne unzulässige Hilfe Dritter angefertigt habe.

Sämtliche aus fremden Quellen direkt oder indirekt übernommenen Gedanken sowie sämtliche von Anderen direkt oder indirekt übernommenen Daten, Techniken und Materialien sind als solche kenntlich gemacht. Die Arbeit wurde bisher bei keiner anderen Hochschule zu Prüfungszwecken eingereicht.

Darmstadt, 15.10.2020



.....  
Wadim Weber